https://www.sciltp.com/journals/mi
Online ISSN: 2982-2394
Volume 2, Issue 4, 2025

Materials and Interfaces

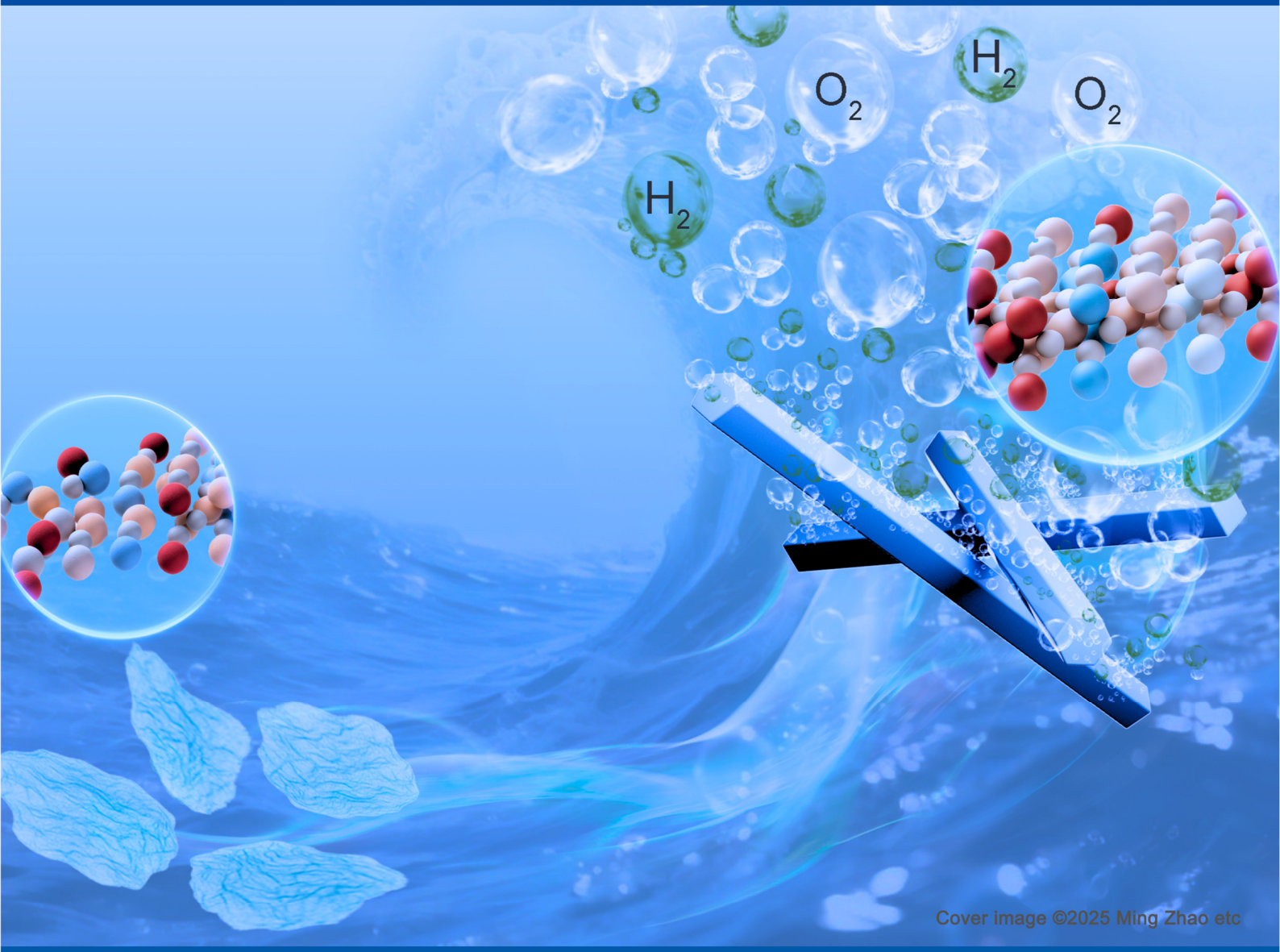

Cover image ©2025 Ming Zhao etc

Morphological Transformation of NiCoMoSeOx from Nanosheets to Nanorods for Enhanced Oxygen Evolution

Scilight

Contents

Vol. 2 No. 4, December 2025

Article

Morphological Transformation of $NiCoMoSeO_x$ from Nanosheets to Nanorods for Enhanced Oxygen Evolution

Jianbin Luo [1,†], Xiaofei Long [1,2,†], Biao Huang [1], Lei Huang [1,3], Jing Cao [1], Qingdian Yan [1], Mao Wu [1], and Ming Zhao [1,3,*]

[1] Department of Materials Science & Engineering, National University of Singapore, Singapore 117575, Singapore
[2] Key Laboratory of Low-Grade Energy Utilization Technologies and Systems, Ministry of Education of China, Chongqing University, Chongqing 400044, China
[3] Centre for Hydrogen Innovations, National University of Singapore, Singapore 117580, Singapore
* Correspondence: mingzhao@nus.edu.sg
† These authors contributed equally to this work.
Received: 10 August 2025; Revised: 29 September 2025; Accepted: 10 October 2025; Published: 13 October 2025

Abstract: Green hydrogen production via water electrolysis has emerged as a promising technology to address the environmental crisis and to achieve sustainability. However, the anodic oxygen evolution reaction (OER) of water electrolysis is kinetically sluggish, which requires the development of highly efficient catalysts to materialize this technology. Herein, we report the facile synthesis of two-dimensional $NiCoMoSeO_x$ nanosheets, which can be further transformed into one-dimensional nanorods. Structural characterizations confirm the existence of amorphous and crystalline domains in the nanosheets while the nanorods feature high crystallinity. The progressive nanosheets-to-nanorods transformation was also accompanied with composition variation and further oxidation. Excitingly, when employed as catalysts for alkaline OER, the nanorods exhibit a dramatic overpotential drop of 123 and 158 mV at 10 and 200 mA cm^{-2}, respectively, relative to the nanosheet counterpart. Moreover, the nanorods also exhibit superior durability than the nanosheets at various current density and could largely maintain its performance for 200 h at 300 mA cm^{-2}. In situ spectroscopic analysis confirms the critical role of low-valence Mo species in suppressing the Se leaching from nanorods, which greatly stabilizes the structure for improved durability. This work offers an effective approach to produce nanorods via structural transformation, together with valuable insights into the structure-performance relation for enhanced electrocatalysis.

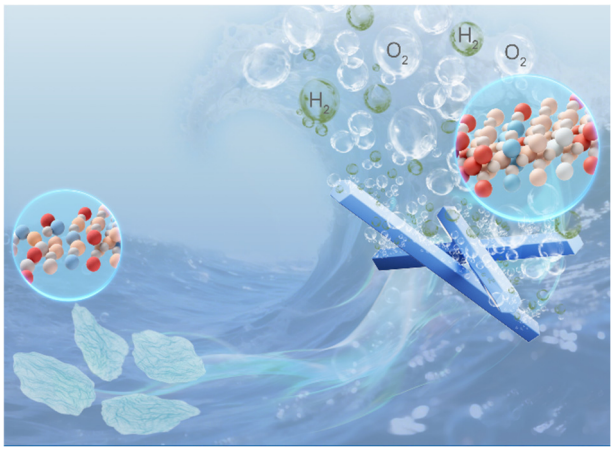

Keywords: oxygen evolution reaction; nanosheets; nanorods; structural transformation; structure-performance relationship

1. Introduction

Water electrolysis using green electricity has received considerable attention owing to the capability to produce green hydrogen and the potential to integrate with renewable energy devices for value-added chemicals synthesis [1–5]. However, the sluggish kinetics of the anodic oxygen evolution reaction (OER) of water electrolysis, which involves a complex four-electron pathway and thus impose a substantial activation energy barrier, largely retarding the practical application of this technology [6–8]. To this end, tremendous efforts have been devoted to the development of OER catalysts, with effective methods encompassing phase engineering [9–11], composition optimization [12–14], and morphological control [15–18].

Among various catalysts, noble metal-based catalysts, such as RuO_2 and IrO_2, have demonstrated exceptional OER performance. However, their extremely low abundance and notoriously high cost hinder their large-scale

Copyright: © 2025 by the authors. This is an open access article under the terms and conditions of the Creative Commons Attribution (CC BY) license (https://creativecommons.org/licenses/by/4.0/).
Publisher's Note: Scilight stays neutral with regard to jurisdictional claims in published maps and institutional affiliations.

applications [13]. To address these limitations, extensive efforts have been invested in exploring earth-abundant transition metal-based catalysts, such as Ni and Co. Notably, the catalytic activity of those catalysts is highly sensitive to the morphology [19–21], which defines the nature of catalytically active sites involved in reactant adsorption and electron transfer [22–24]. As a compelling example, Sun and co-worker reported a porous nanoscale NiO/$NiCo_2O_4$ heterostructure which optimize the mass transfer process and significantly increases the electrochemically active surface area (ECSA) compared to NiO particles, collectively contributing to the improved catalytic activity [25]. Despite the progress, the catalytic performance of the abundant metal-based catalysts is still unsatisfactory, which calls for the further improvement of highly efficient catalysts. One promising strategy for enhancing the efficiency of catalysts is to engineer the morphology and dimensionality of nanocatalysts. However, the current understanding of dimensionality-controlled nanomaterials remains insufficient, and their structure-performance relationships necessitate further investigation.

Herein, we successfully synthesized the two-dimensional (2D) $NiCoMoSeO_x$ nanosheets and subsequently, the one-dimensional (1D) $NiCoMoSeO_x$ nanorods via the dimensional transformation from 2D nanosheets. Specifically, Ni, Co, and Mo were employed owing to their outstanding activity toward OER [19–21], while Se nanoparticles serve as the reductant to induce the formation of multi-metallic oxides, which also plays a key role in the morphological transformation. The nanosheets were proven to consist of both amorphous and crystalline domains while the nanorods were highly crystallized. The transformation mechanism from nanosheets to nanorods was also investigated through the time-dependent monitoring of products and composition analysis. When used as catalysts toward OER in alkaline conditions, the 1D nanorods show greatly enhanced activity and durability than the 2D nanosheets. Additionally, in situ attenuated total reflection surface-enhanced infrared absorption spectroscopy (ATR-SEIRAS) was conducted to rationalize the enhanced catalytic performance and reaction mechanisms.

2. Methods and Characterizations

2.1. Chemicals and Materials

Ethanol (C_2H_5OH, 99%) was obtained from J.T. Baker. Sodium sulfite (Na_2SO_3, 98%) was obtained from Thermo Fisher Scientific. Pt/C (20 wt.%) was obtained from Johnson Matthey. Sodium tetrachloroaurate (III) ($NaAuCl_4$, 99.9%) was obtained from Macklin. Selenous acid (H_2SeO_3, 98%), hydrazine hydrate ($N_2H_4{\cdot}H_2O$, 50–60% in H_2O) and potassium hydroxide (KOH, 99.99%) were obtained from Sigma Aldrich. Nickel chloride hexahydrate ($NiCl_2{\cdot}6H_2O$, 99.9%), sodium molybdate (Na_2MoO_4, 99%), cobalt chloride ($CoCl_2$, 99%), sodium thiosulfate pentahydrate ($Na_2S_2O_3{\cdot}5H_2O$, 99.99%), ammonium chloride (NH_4Cl), hydrofluoric acid (HF, 2% aqueous solution), polyvinylpyrrolidone (PVP, MW ≈ 55,000) were all obtained from Aladdin. Nafion® aqueous solution (N–117, 5wt.%, Dupont), nickel foam (Sinero) and carbon paper (Toray) were used as received. Millipore deionized (DI) water with resistivity of 18 MΩ cm was used for preparing all solutions unless specified.

2.2. Syntheses of $NiCoMoSeO_x$ Nanosheets and Nanorods

The synthesis of $NiCoMoSeO_x$ nanosheets include two major steps. In the first step, Se nanoparticles were prepared based on a reported protocol [26,27]. Typically, 0.3 mmol of H_2SeO_3 and 10 mg of PVP were mixed and dissolved in 10 mL of DI water under magnetic stirring for 10 min, followed by a one-shot injection of 414 μL of $N_2H_4{\cdot}H_2O$ at room temperature. After 3 h, the as-synthesized Se nanoparticles were collected via centrifugation at 12,000 rpm for 20 min and washed three times with DI water and then dispersed in 10 mL of DI water for further use. In the second step, 0.6 mmol of $NiCl_2$, 0.2 mmol of $CoCl_2$, and 0.2 mmol of Na_2MoO_4 were dissolved in 10 mL DI water in a 20-mL glass vial and stirred for 10 min, followed by one-shot injection of 2 mL of the as-prepared Se nanoparticles suspension. The mixture was heated at 70 °C for 3 h in oil bath. The products were collected via centrifugation at 10,000 rpm for 5 min and then washed with DI water three times. The synthesis of $NiCoMoSeO_x$ nanorods follows the same protocol except extending the reaction to 24 h.

2.3. Characterizations

Scanning transmission electron microscope (STEM) and energy-dispersive X-ray spectroscopy (EDS) elemental mapping images were acquired on a JEOL JEM-F200 microscope. TEM images and selected area electron diffraction (SAED) patterns were acquired on a JEOL JEM-2010F microscope. X-ray photoelectron spectroscopy (XPS) spectra were measured using a Thermo scientific ESCALAB 250Xi XPS microprobe. All photochromic tests were conducted under ambient conditions.

2.4. Electrochemical Measurements

All the electrochemical measurements were conducted in a three-electrode cell using an electrochemical workstation (CS310X, Corrtest). A carbon rod and saturated calomel electrode (SCE) were used as the counter and reference electrode, respectively. Working electrodes were prepared by dropping various catalyst inks on the carbon paper. Specifically, catalyst inks were prepared as follows: 15 mg of as-synthesized $NiCoMoSeO_x$ was dispersed in the mixture of 2 mL ethanol and 1 mL DI water. The mixed solution was treated with ultrasonication for 5 min, followed by the addition of 60 μL 5wt.% Nafion solution. After an additional 1-h ultrasonication, 200 μL of prepared ink was dropped onto the carbon paper, forming a working electrode with active aera of 0.5 cm^2.

Linear sweep voltammograms (LSVs), cyclic voltammograms (CVs), electrochemical impedance spectroscopy (EIS), and chronopotentiometric tests were conducted in a 1 M KOH aqueous solution. For LSVs, the potential range was set at 1.0–1.9 V vs. RHE at a scan rate of 5 mV s^{-1}. The potentials were derived from *E*(SCE) and presented as *E*(RHE), according to the formula:

$$E(\mathrm{RHE}) = E(\mathrm{SCE}) + 0.2412 + 0.05916 * pH \quad (1)$$

CVs were conducted at scan rates of 10, 20, 40, 60, 100 mV s^{-1} within the non-Faradaic region (0.1–0.2 V) to calculate the double layer capacity (C_{dl}). The C_{dl} were calculated using the following formula:

$$C_{\mathrm{dl}} = \frac{\Delta i}{2\nu} \quad (2)$$

where $\Delta i/2$ represents the capacitive current at a specific potential, and ν is the CV scan rate.

To quantify the ECSA and specific activity (i_s), the specific capacitance (C_s) with typical value of 40 μF cm^{-2} for NiCo-based alloys, and the current density measured by LSV (i_{LSV}) are introduced in the following equation [28]:

$$\mathrm{ECSA} = \frac{C_{\mathrm{dl}}}{C_{\mathrm{s}}} \quad (3)$$

$$i_{\mathrm{s}} = \frac{i_{\mathrm{LSV}}}{\mathrm{ECSA}} \quad (4)$$

EIS was conducted in the three-electrode system at 1.75 V vs. RHE which falls in the active reaction region. Herein, both Nyquist and Bode plots were obtained with frequency range from 10,000 to 1 Hz and sinusoidal potential perturbation amplitude of 5 mV.

To accommodate long-term stability testing, the working electrode substrates were replaced with nickel foam, while all other experimental conditions remained unchanged. The as-synthesized catalysts were subjected to stepwise chronopotentiometric stability tests at 10, 20, and 50 mA cm^{-2}, with each step lasting 20 h. In addition, to evaluate the durability of the nanorods under high current density, an extended chronopotentiometric test was performed at 300 mA cm^{-2} for 200 h.

2.5. In Situ ATR-SEIRAS Study

All in situ ATR-SEIRAS spectra were recorded on a Fourier-transform infrared (FTIR) spectrometer (iS50, Thermo Fisher Scientific) equipped with a liquid-nitrogen-cooled MCT detector. Unless otherwise noted, measurements were conducted at an incident angle of 60°, with a spectral resolution of 8 cm^{-1} and averaged over 100 scans. The obtained spectra are presented in terms of reflectance, as defined by:

$$\frac{\Delta R}{R} = \frac{R(E_1) - R(E)}{R(E)} \quad (5)$$

where $R(E_1)$ and $R(E)$represent the reflectivity from the electrode at the applied potential E_1 and open circuit potential, respectively.

The homemade reaction cell was set as the Kretschmann configuration, with the catalyst drop-casting onto the Si prism coated with an Au film. The protocol for coating an approximately 50 nm Au film on Si prism follows previous report [29]. Residual material on the prism surface was removed by aqua regia, after which the prism was rinsed with deionized water and polished using 0.05 μm abrasive powder. A 40% NH_4F solution was then applied to the surface for several minutes to remove the native oxide layer [30]. Au deposition was performed at 60 °C by drop-casting a plating solution (0.015 M $NaAuCl_4 \cdot 2H_2O$, 0.15 M Na_2SO_3, 0.05 M $Na_2S_2O_3 \cdot 5H_2O$, and 0.05 M NH_4Cl) mixed with 2% HF in a 2:1 volume ratio onto the Si surface. Using the CHI 660e electrochemical workstation, the potentials ranged from 1.0 to 1.9 V vs. RHE were applied to induce OER while the spectra were recorded from 4000 to 650 cm^{-1}. Each infrared spectrum was collected after holding the potential constant for 5 min.

3. Results and Discussion

3.1. Synthesis and Characterizations of $NiCoMoSeO_x$ Nanosheets

The one-pot synthesis of $NiCoMoSeO_x$ nanosheets was accomplished by the galvanic replacement reaction between Se nanoparticles and Ni(II), Co(II), and Mo(VI) precursors. First, Se nanoparticles were synthesized as the template, with an average diameter of 37.5 ± 1.4 nm (Figure S1) [26,27]. After the galvanic replacement reaction at 70 °C for 3 h, nanosheets with abundant wrinkles and basal planes were obtained, as evidenced by the TEM images (Figure 1a,b). The lattice fringe spacings of 2.21 and 2.59 Å can be indexed to the (200) and (111) plane, close to 2.10 Å of the (200) plane and 2.41 Å of the (111) plane in $Ni_{0.5}Co_{0.5}$ oxide [31], suggesting the formation of multi-metallic oxides ($NiCoMoSeO_x$, Figure 1c). The wrinkles within the nanosheets presented an average size of 2.9 ± 0.8 nm in width (Figure 1d). Regarding the basal plane, high-resolution STEM image showed a mix of amorphous and crystalline domains (Figures 1e and S2). Within the crystalline domains, the lattice fringe spacings of 2.17 and 2.56 Å correspond to the (111) and (110) planes of $NiCoMoSeO_x$, similar to those of the wrinkles and suggesting identical compositions (Figure 1e). In addition, the presence of crystalline structure was also confirmed by the SAED rings indexed to (110), (111), and (200) reflections of the crystalline constituents of $NiCoMoSeO_x$ (Figure 1f), consistent with the results shown in Figure 1e. To analyze the composition of the nanosheets, we conducted EDS elemental mapping. As shown in Figure 1g, the atomic proportions of Ni, Co, Mo, Se, and O are 12.46%, 11.51%, 16.50%, 0.03%, and 59.50%, respectively, revealing the oxide structure of the nanosheets. Moreover, the extremely low composition of Se in the nanosheets validates the role of Se nanoparticles as a sacrificial template for the galvanic replacement, where Se atoms were oxidized and dissolved in the solution as cations (Figure S3). It is worth noting that the Se nanoparticles cannot be completely oxidized without the Mo^{6+} precursor (Figure S4). The galvanic replacement reaction can be further supported by the thermodynamic potential of Se^0/Se^{4+} (−0.74 V vs. standard hydrogen electrode or SHE), which is lower than those of Mo^{6+}/MoO_2 (+0.02 V), Ni^{2+}/Ni (−0.257 V), and Co^{2+}/Co (−0.277 V). Moreover, UV-Vis spectroscopic analysis suggest that the absorption peak intensity of Se nanoparticles at 283 nm shows a clear decay over the reaction time upon the addition of the Ni^{2+} precursor (Figure S3), further confirming the occurrence of galvanic replacement. Figures 1h and S5 shows the EDS mapping of Ni, Co, Mo, Se, and O distributions, indicating uniform distributions across the nanosheet.

3.2. Synthesis of Characterizations of $NiCoMoSeO_x$ Nanorods

Excitingly, when the standard synthesis was extended from 3 to 24 h, the obtained products were switched from nanosheets to nanorods, as shown in Figure 2a. Specifically, the nanorods are uniform and in high quality, with an average size of 36.4 ± 14.8 nm (Figures 2a–d, and S6). Different from the mixed amorphous/crystalline structure in the nanosheets, the as-obtained nanorods possess a well crystalline structure (Figure 2b–e). Specifically, the lattice fringes in the nanorods are derived as 1.75, 1.83, and 2.98 Å, corresponding to the (200), (111), and (110) planes of $NiCoMoSeO_x$ (Figure 2e). The structural ordering was further corroborated by the SAED pattern, which displays sharp, discrete diffraction rings indexed to the (100), (110), (111), and (200) planes that are indicative of a highly crystalline lattice (Figure 2f). It is worth noting that compared to nanosheets, the nanorods show slightly reduced (200) and (111) lattice fringe spacings, which we attribute to the higher crystallinity and thus more compact atom packing in nanorods [32]. XRD patterns of nanosheets and nanorods indicate the low and high crystallinity (Figure S8), respectively, with the characteristic peaks close to those of NiO, MoO_3, Co_3O_4 and SeO_2. Moreover, the composition difference could also contribute to the variation of lattice fringe spacings. As shown in Figure 2g, the atomic proportions of Ni, Co, Mo, Se, and O are 6.06%, 9.03%, 15.95%, 0.16%, and 68.80%, respectively, showing a higher O proportion than that of nanosheets. The increased O portion in the nanorods suggests the continuous oxidation of the nanosheets over the extended reaction time. EDS mapping results show the uniform distributions of Ni, Co, Mo, Se, and O in the nanorods, confirming the homogeneous composition across the nanorods (Figures 2h and S8).

3.3. Dynamic Structural Evolution from Nanosheets to Nanorods

To elucidate the transformation mechanism from nanosheets to nanorods, we collected the products synthesized via the standard protocol except for reaction at 3, 6, 12, 18, and 24 h, as summarized in Figure 3a–e. After 3 h of reaction, i.e., the standard synthesis, the as-obtained products were predominant by nanosheets. Upon extending the reaction to 6 h, nanorods started to appear, showing a proportion of 44% (Figure 3b). Other than the nanorods with large sizes, we also observed some small nanorods mixed with nanosheets, suggesting the ongoing transformation from nanosheets to nanorods (Figure 3b). Especially, these intermediate small nanorods show similar structure and size to those of the wrinkles in the nanosheets (Figures 1b,c and 3a,b), suggesting that the

structural transformation might start from the wrinkles. When the reaction was extended for 12 and further to 18 h, the proportion of nanorods in the product increased remarkably to 84% and 86%, respectively (Figure 3c,d,f). Eventually, highly pure and uniform nanorods with almost 100% were obtained after 24 h of reaction (Figure 3e,f).

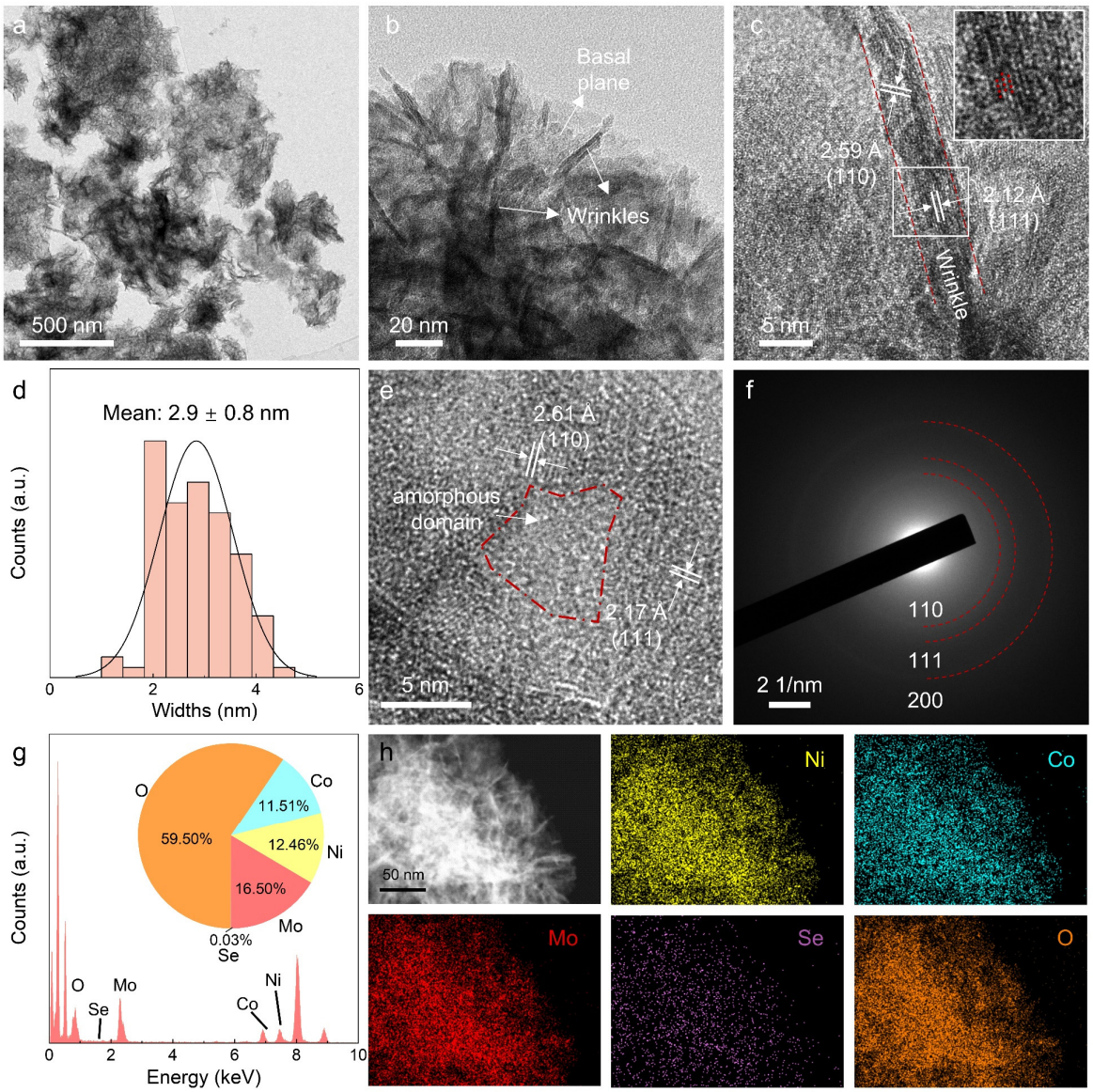

Figure 1. Synthesis and characterizations of $NiCoMoSeO_x$ nanosheets. (**a–c**) STEM images of $NiCoMoSeO_x$ nanosheets at different magnifications. The two parallel red dashed lines define the width of wrinkles. (**d**) The width distribution of wrinkles, which is 2.9 ± 0.8 nm. (**e**) High-resolution STEM and (**f**) SAED pattern of $NiCoMoSeO_x$ nanosheets displaying mixed domains with different lattice phases. (**g**) EDS survey of Ni, Co, Mo, Se, and O. (**h**) EDS elemental mapping of Ni, Co, Mo, Se, and O distributions in the $NiCoMoSeO_x$ nanosheets. The scale bar applies to all panels in (**h**).

To investigate the electronic structures of $NiCoMoSeO_x$ nanosheets and nanorods, we conducted XPS analysis. The survey spectra reveal the presence of Ni 2*p*, Co 2*p*, Mo 3*d*, Se 3*d* and O 1*s* in both nanosheets and nanorods (Figure 4a). In the high-resolution Ni 2*p* spectrum of nanosheets, two characteristic peaks at 873.4 and 875.1 eV are observed, corresponding to Ni^{2+} $2p_{1/2}$ and Ni^{3+} $2p_{1/2}$, respectively (Figure 4b) [33]. Notably, the Ni^{3+} $2p_{1/2}$ peak shifts by +0.8 eV from nanosheets to nanorods, which we attribute to that Ni was coordinated by a greater proportion of oxygen atoms (Figure 4b). Similarly, Co 2*p* spectrum reveals presences of Co^{2+} and Co^{3+} at 780.6 and 782.9 eV, respectively (Figure 4c). In comparison, the major peaks at 235.5 and 232.3 eV are assigned to the Mo^{4+} $3d_{3/2}$ and $3d_{5/2}$, respectively, rather than Mo^{6+}. This suggests that Mo^{6+} in the precursors was predominately reduced to Mo^{4+} during the formation of $NiCoMoSeO_x$ nanosheets and nanorods (Figure 4d). Moreover, both Mo^{4+} $3d_{3/2}$ and $3d_{5/2}$ peaks negatively shift by 0.1 eV after transforming into nanorods, the electron transfer from Mo to the neighboring atoms (Figure 4d). We also found that there exists Se^0 in the nanosheets, as

evidenced by the characteristic peaks at 56.4 eV and 55.8 eV, suggesting that the residual of Se^0 in the nanosheets (Figure 4e). Surprisingly, only characteristic peaks of SeO_x were observed in the nanorods after morphological transformation (Figure 4e). This sharp contrast indicates that the residual Se^0 atoms were further oxidized during transformation of nanosheets into nanorods. Additionally, the metal oxide lattice oxygen (O_m) peak shows a negative shift of 0.5 eV after nanosheets-to-nanorods transformation while the surface –OH/–OOH peak (O_{OH}) suggest a positive shift of 0.5 eV. This observation likely results from the strengthened interaction between high-valence metal centers and hydroxyl species in the more crystallized nanorods (Figure 4f).

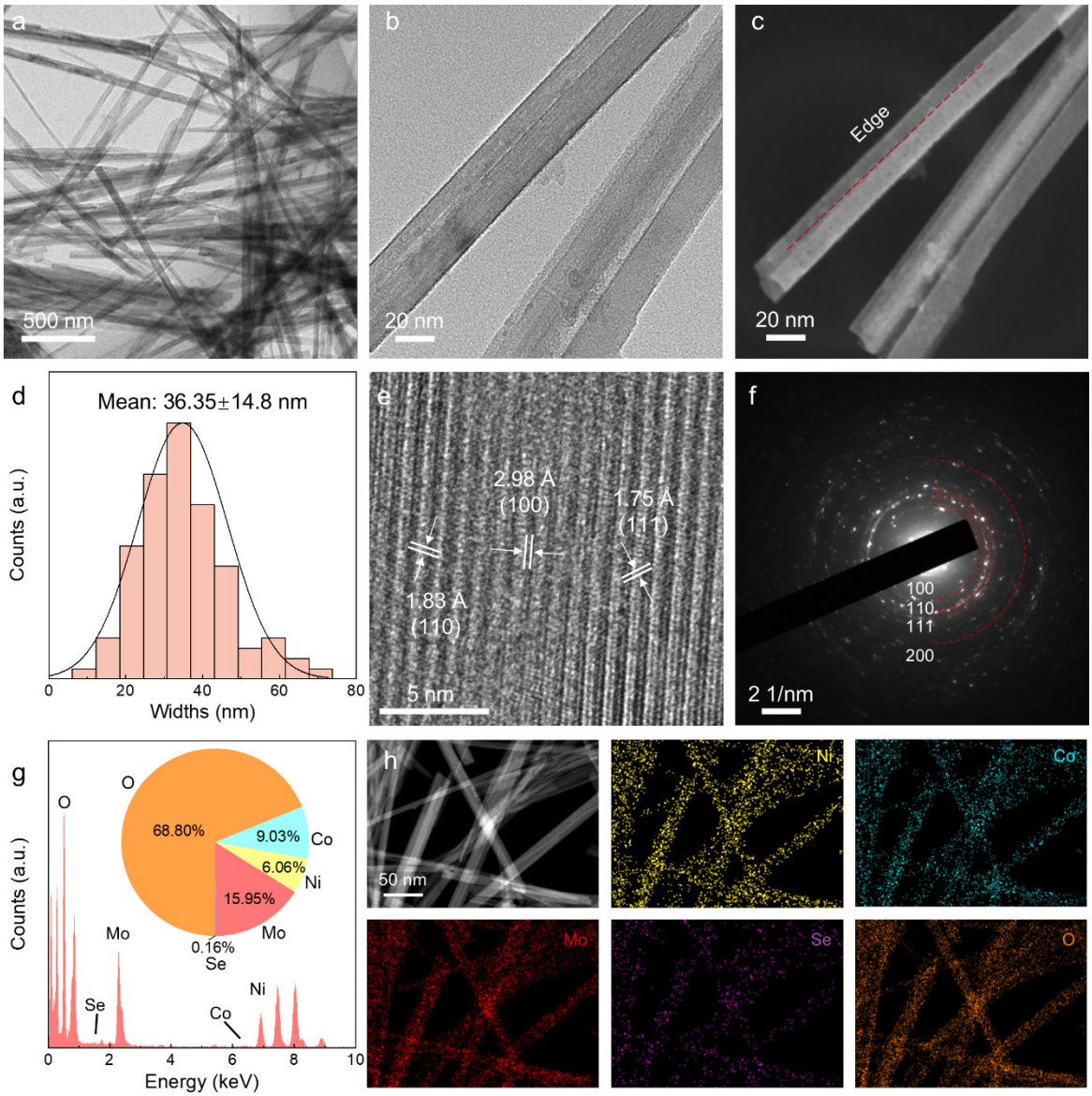

Figure 2. Synthesis and characterizations of $NiCoMoSeO_x$ nanorods. (**a–c**) STEM images of $NiCoMoSeO_x$ nanorods at different magnifications. (**d**) Size distribution of nanorods, which is derived as 36.4 ± 14.8 nm. (**e**) High-resolution STEM and (**f**) SAED pattern of a representative local plane structure in $NiCoMoSeO_x$ nanorods. (**g**) EDS survey of Ni, Co, Mo, Se, and O elements. (**h**) EDS elemental mapping of Ni, Co, Mo, Se, and O distributions in the $NiCoMoSeO_x$ nanorods. The scale bar applies to all panels in (**h**).

3.4. Enhanced Performance and Stability After the Transformation

The synthesis of $NiCoMoSeO_x$ nanosheets and nanorods allows us to study the structure-dependent catalytic properties toward alkaline OER in 1 M KOH electrolyte. As shown in the LSV curves, the nanorods demonstrate markedly enhanced OER activity compared to the nanosheets, requiring lower overpotentials to reach the same current density (Figure 5a). Specifically, the overpotential at 10 mA cm^{-2} was reduced from 383 to 260 mV after the nanosheets-to-nanorods transformation, showing a dramatic drop of 123 mV. This notable overpotential drop was maintained and even enlarged at high current density of 50, 100, and 200 mA cm^{-2}, with the overpotential drop of

119, 126, and 158 mV, respectively, further confirming the superior OER performance of the nanorods (Figure 5b). Moreover, the Tafel slope analysis suggests that the nanorods exhibit a Tafel slope of 119.45 mV dec^{-1}, which is lower than 147.06 mV dec^{-1} for the nanosheets, indicating faster reaction kinetics during OER (Figure 5c). Notably, a distinct current peak appears in the potential range of 1.2–1.5 V vs. RHE for nanorods, whereas no such response is observed for nanosheets (Figure 5a). This difference likely stems from the lower initial oxidation states of Mo in nanorods than in nanosheets, making it vulnerable to be further oxidized under high positive potentials (Figure 4d).

To uncover the origin of enhanced OER activity, we analyzed the ECSAs of nanorods and nanosheets by measuring the C_{dl} (Figure S9a,b). The calculated results show that the C_{dl} of nanosheets and nanorods is 2.1 and 4.6 mF cm^{-2}, respectively, suggesting that more active sites are exposed on the nanorods than on the nanosheets, thus leading to the enhanced OER activity (Figure 5d). Figure S7c shows the C_{dl}-normalized LSV curves, where the nanorods still exhibit higher specific activity than nanosheets, implying that the performance enhancement could not be exclusively attributed to the larger ECSA. We then conducted EIS to investigate the conductivity and the charge transfer kinetics of both $NiCoMoSeO_x$ nanosheets and nanorods, with the resulting Nyquist plots fitted using the equivalent circuit (Figure 5e) [34]. Specifically, the charge transfer resistance R_{ct} of nanorods is 7.15 Ω cm^2, much lower than 13.26 Ω cm^2 for the nanosheets. This lower charge transfer resistance could promote electron transfer during OER, resulting in faster reaction kinetics and thus higher current density. To further understand the role of R_{ct} in affecting the OER activity, we conducted EIS measurements under operando OER conditions in a potential range of 1.65 to 1.9 V, where the OER kinetics are notable (Figures 5a and S10). Especially, the nanorods exhibited a R_{ct} value of 18 Ω cm^2 at 1.65 V, which is ~5.8 times lower than that of the nanosheets (105 Ω cm^2). In addition, the Bode-phase diagram shows that the nanorods exhibit a phase angle peak at a higher frequency (286 Hz) compared to the nanosheets (112 Hz, Figure 5f). Since in an equivalent circuit the characteristic frequency inversely correlates to R_{ct}, the higher peak frequency enabled by the nanorods suggests accelerated charge-transfer dynamics. which is attributed to the highly crystalline lattice and the 1D structure and continuous electron pathways with minimal boundary/defects scattering (Figure 5e) [35,36]. In contrast, the nanosheets exhibit a mixed crystalline/amorphous microstructure that disrupts long-range electron conduction, leading to increased charge transfer resistance [37].

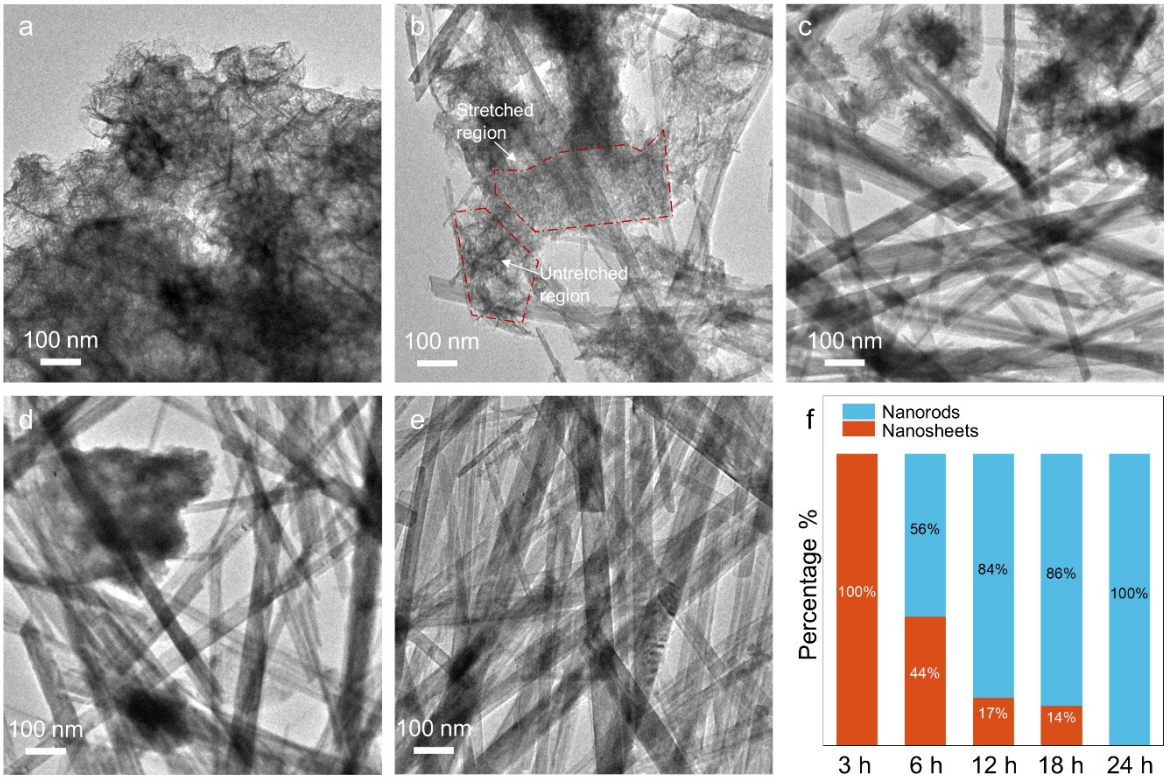

Figure 3. Time-dependent morphological evolution of $NiCoMoSeO_x$. (**a**–**e**) TEM images of the products obtained using the standard protocol but after reaction for (**a**) 3 h, (**b**) 6 h, (**c**) 12 h, (**d**) 18 h, and (**e**) 24 h. (**f**) Time-dependent distributions of nanosheets and nanorod in the products. The percentage of nanorods and nanosheets was estimated based on their projected areas in the TEM images.

To assess long-term durability, chronopotentiometric testing was conducted at 10, 20, and 50 mA cm^{-2} for 20 h (Figure 5g). Under all current densities, the nanorods show lower potentials than the nanosheets, validating the superior OER activity. Moreover, the nanorods exhibited decay rates of 3.1, 3.8, and 5.1 mV h^{-1} at 10, 20, and 50 mA cm^{-2}, respectively, lower than 4.0, 4.7 and 6.3 mV h^{-1} for nanosheets, validating the enhanced stability of nanorods. Notably, the nanosheets display notable voltage fluctuations during the potential switching, which we attributed to structural instability of the amorphous domains that are more susceptible to reconstruct under high potentials. To further assess the stability of nanorods, we conducted a durability test at 300 mA cm^{-2} for 200 h (Figures 5h and S11). The nanorods could well maintain both its rod structure and activity over the long-term test (Figure S11), showing a decay rate of only 1.468 mV h^{-1}, demonstrating its great promise for practical applications [38–42].

3.5. Investigation for the Enhancement Attributed to the Transformation via In Situ ATR-SEIRAS

To investigate the reaction mechanisms, in situ ATR-SEIRAS analysis was conducted for nanosheets and nanorods in the potential range of 1.0–1.9 V vs. RHE. As shown in Figure 6a,b, the nanosheets exhibit no discernible O–H stretching signals at potentials below 1.4 V, whereas the nanorods display a distinct peak at ~3384 cm^{-1} corresponding to the adsorption of free OH groups. This contrast indicates that nanorods possess stronger OH adsorption than nanosheets and thus results in the presence of more available OH groups for enhanced OER kinetics. When the applied potential was gradually increased to 1.8 V, both the nanosheets and nanorods display a pronounced hydrogen-bonded water adsorption band, with the nanorods exhibiting a much higher intensity. Moreover, the band of nanorods undergoes a progressive redshift from 3284 to 3248 cm^{-1}, indicative of hydrogen-bond network disruption and reorganization under OER conditions. As comparison, the commercial Pt/C and RuO_2 exhibits only the free-water peak during OER, suggesting the weak interaction among the absorbed *OH species without hydrogen bond (Figures S12 and S13). Concurrently, the δ(H–O–H) peaks at 1626 cm^{-1} for $NiCoMoSeO_x$ nanorods is significantly stronger than that of nanosheets, confirming a stronger interaction of the nanorod catalyst with water and other *OH species and thereby facilitate the initialization of oxygen evolution (Figure 6a,b).

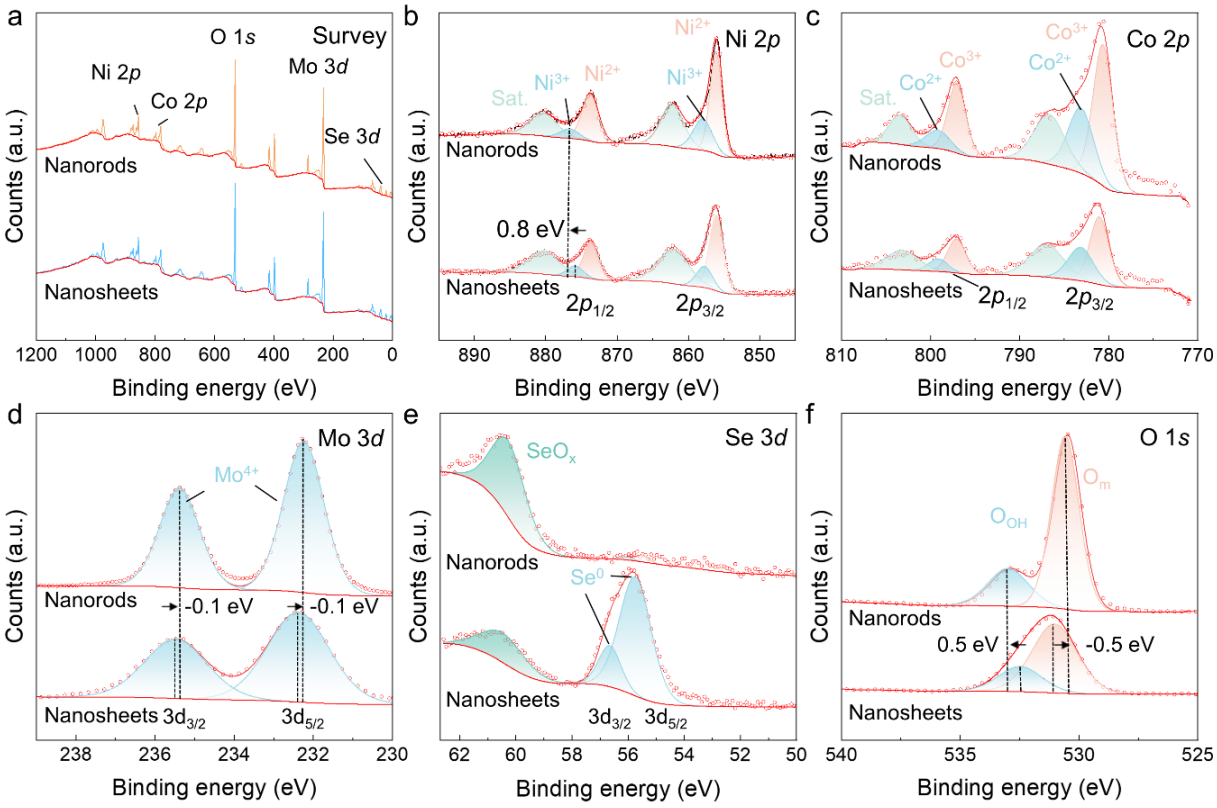

Figure 4. XPS of $NiCoMoO_x$ in nanosheets and nanorods morphologies. (**a**) Survey scan showing Ni, Co, Mo, Se and O signals. (**b**) Ni 2*p*, (**c**) Co 2*p*, (**d**) Mo 3*d*, (**e**) Se 3*d* and (**f**) O 1*s*. Black dashed vertical lines mark binding energy shifts in the nanosheets relative to nanorods.

In addition, M–O stretching vibrations were also observed in the low wavenumber region (Figure 6a–d). Both nanosheets and nanorods exhibited increasingly strong negative bands at 1242 cm^{-1} corresponding to Se–O vibrations with increasing potential. This indicated that Se–O species were partially leached from the lattice into the electrolyte

during OER, forming SeO_3^{2-} species that adsorbed onto the catalyst surface (Figure 6a–d). Importantly, due to the lower initial oxidation status of Mo content in the nanorods, distinct MoO_3^{2-} features appeared at 888 cm^{-1} during OER (Figure 6d). The greater proportion of relatively lower-valence Mo species in nanorods appeared to suppress Se leaching, helping to stabilize the structure and thereby improve the electrochemical durability. Moreover, the Raman spectroscopic analysis also indicates a characteristic Se–O peak at 283 cm^{-1} for the the $NiCoMoSeO_x$ nanorods after the durability test (Figure S14), with an intensity comparable to that of the pristine $NiCoMoSeO_x$ nanorods, confirming the suppressed leaching under long-term electrochemical tests.

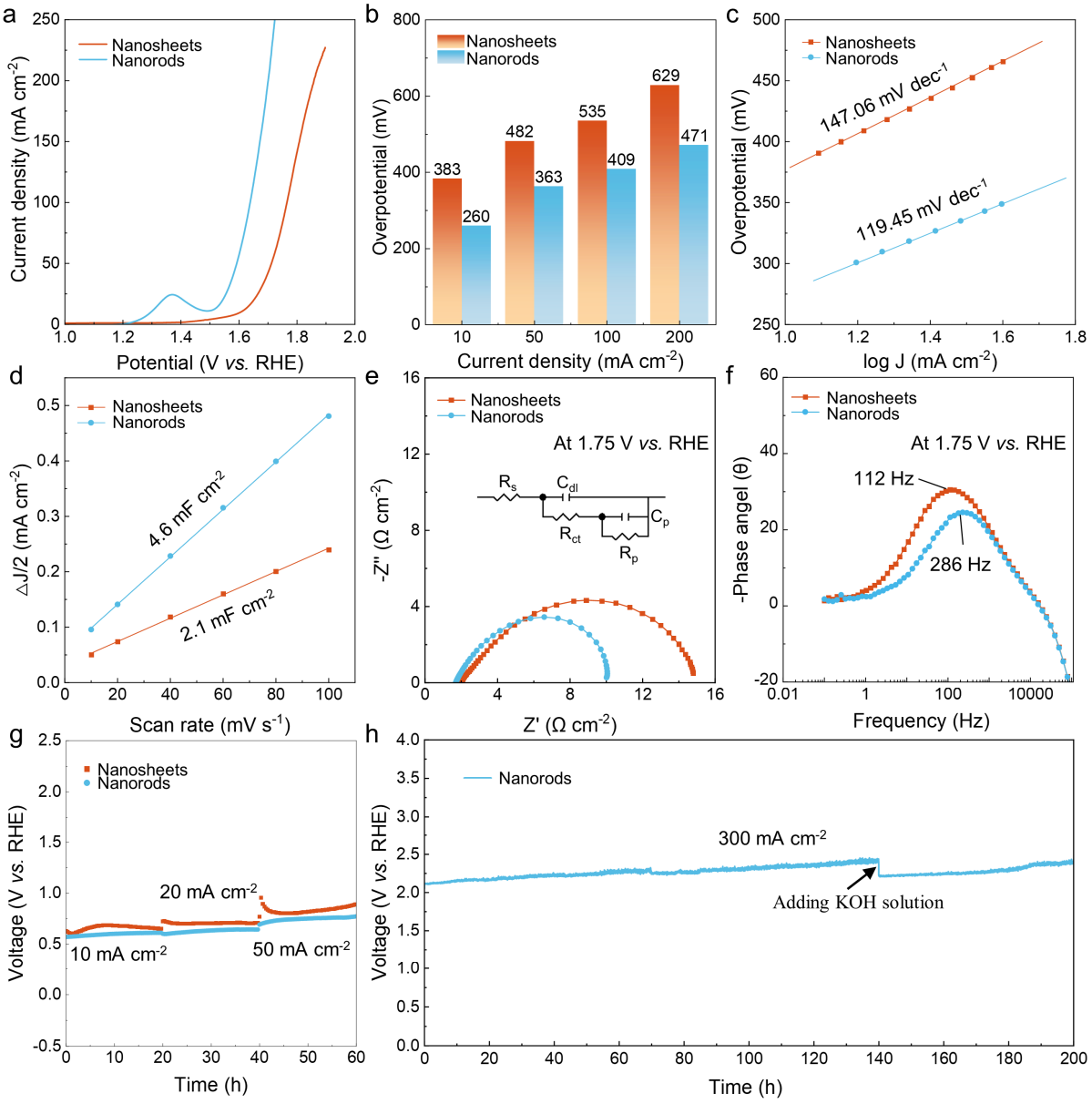

Figure 5. Electrochemical performance of nanosheets and nanorods in 1 M KOH. (**a**) LSV polarization curves (scan rate 5 mV s^{-1}, iR–corrected). (**b**) Overpotentials required to reach 10, 50, 100 and 200 mA cm^{-2}. (**c**) Tafel plots derived from (**a**). (**d**) Δj/2 vs. scan rate for C_{dl} determination. (**e**) Nyquist plots from EIS at 1.75 V vs. RHE and its equivalent circuit. (**f**) Bode-phase diagram from EIS at 1.75 V vs. RHE. (**g**) Chronopotentiometric stability at 10, 20 and 50 mA cm^{-2} over 60 h. (**h**) 200 h of durability test at 300 mA cm^{-2}, with KOH replenishment at 140 (**h**).

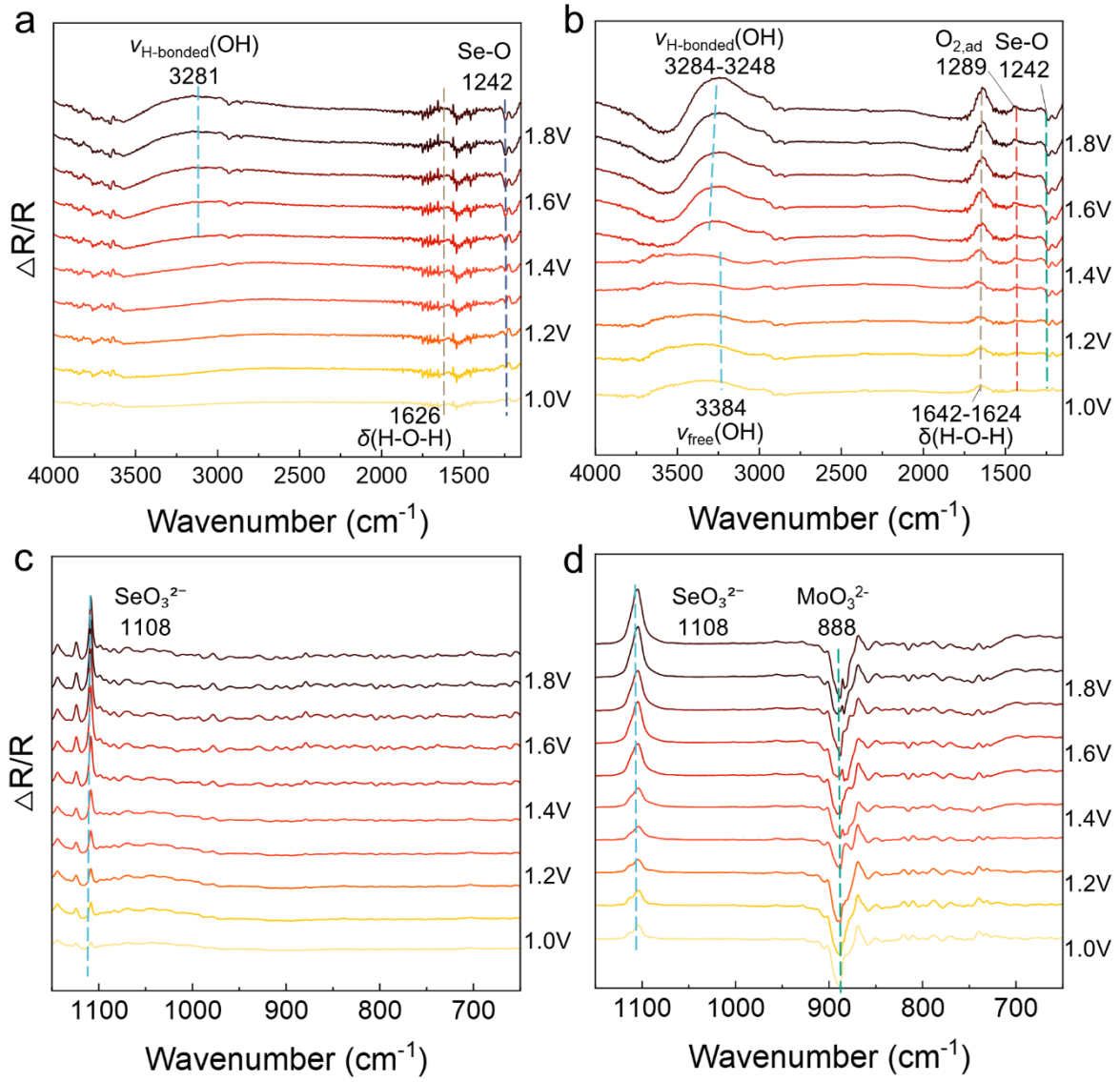

Figure 6. In situ ATR-SEIRAS ΔR/R spectra recorded at 1.0–1.9 V vs. RHE for $NiCoMoSeO_x$ nanosheets and nanorods: (**a**,**c**) nanosheets; (**b**,**d**) nanorods. (**a**,**b**) Full spectra in the range of 4000–1150 cm^{-1}. (**c**,**d**) Spectra of the fingerprint region (1150–650 cm^{-1}). Spectra are vertically offset for clarity.

4. Conclusions

In summary, we have demonstrated the successful synthesis of 2D $NiCoMoSeO_x$ nanosheets via galvanic replacement and their morphological transformation into 1D nanorods, simply by extending the reaction time. Accompanied with the dimensional transformation, the structure of the nanoparticles also evolved from mixed amorphous/crystalline structure in nanosheets to a highly crystallized structure in nanorods. Time-dependent analysis of the synthesis suggests that the structural transformation likely starts from the wrinkles of nanosheets, accompanied with the variations of composition and valence states of metal atoms. Significantly, this dimensional transformation resulted in a significant reduction of the overpotential from 383 to 260 mV at 10 mA cm^{-2}, when employed as catalysts for OER under alkaline conditions. EIS further revealed a pronounced decrease in charge transfer resistance from 13.26 for nanosheets to 7.15 Ω·cm^2 for nanorods, confirming the accelerated electron transfer kinetics in the 1D nanorod structure for enhanced catalysis. Long-term stability tests validated the excellent durability of $NiCoMoSeO_x$ nanorods, exhibiting insignificant performance degradation after 200 h of continuous operation at a high current density of 300 mA cm^{-2}. In situ ATR-SEIRAS study validates that the suppressed Se leaching by low-valence Mo species and thus a stabilized structure, lead to the superior electrochemical stability. We believe this work offers a new approach to regulate the dimension of nanocatalysts for enhanced OER and provides necessary insights into the structure-performance relationships, which collective contributes to the rational design of highly efficient electrocatalysts for sustainability applications.

Supplementary Materials: The following supporting information can be downloaded at: https://media.sciltp.com/articles/others/2510131446053079/MI-2508000264-Supplementary-Materials.pdf, Figure S1. TEM images of Se nanoparticles in low magnification (a) and high magnification (b) synthesized following reported studies [26,27]. The size of Se nanoparticles is 37.5 ± 1.4 nm. Figure S2. TEM images of $NiCoMoSeO_x$ nanosheets at low magnification (a) and high magnification (b). Figure S3. STEM image (a) and EDS elemental mapping of (b) Ni, (c) Co, (d) Mo, (e) Se, and (f) O distributions in the $NiCoMoSeO_x$ nanosheets. The scale bar applies to all panels in a. Figure S4. STEM images of $NiCoMoSeO_x$ nanorods at low magnification (a) and high magnification (b). Figure S5. HADDF-STEM image (a) and EDS elemental mapping of (b) Ni, (c) Co, (d) Mo, (e) Se, and (f) O distributions in the $NiCoMoSeO_x$ nanorods. The scale bar applies to all panels in a. Figure S6. CVs of (a) nanorods and (b) nanosheets in the non-active potential range with scan rates of 10, 20, 40, 60, 80, 100 mV s^{-1}. (c) Specific activity of nanosheets and nanorods normalized by C_{dl}. Figure S7. The Nyquist plots of nanosheets (a) and nanorods (b) measured at the range of 1.65–1.9 V. (c) The changes of R_{ct} upon different potentials derived from panel a and b. Figure S8. In situ ATR-SEIRAS spectra of RuO_2 during the OER at various potentials (1.0 V to 1.9 V). The spectra highlight key vibrational bands: the free OH stretching at 3384 cm^{-1}, H-O-H bending at 1643 cm^{-1}, and adsorbed *OOH at 1213 cm^{-1}. Figure S9. In situ ATR-SEIRAS spectra of Pt during the OER at various potentials (1.0–1.9 V). The spectra highlight key vibrational bands: the free OH stretching at 3384 cm^{-1}, H-O-H bending at 1642 cm^{-1}, and adsorbed O_2 at 1289 cm^{-1}. References [43,44] are cited in the Supplementary Materials.

Author Contributions: J.L. and X.L. conducted the nanoparticle synthesis and characterizations, electrochemical measurements, and data analysis. J.L. performed the in situ ATR-SEIRAS measurements. J.L. and M.Z. wrote the manuscript. M.Z. directed research. All authors contributed to discussions. All authors have read and agreed to the published version of the manuscript.

Funding: This work was supported by the National University of Singapore start–up grant, National Research Foundation, Prime Minister's Office, Singapore under its Campus for Research Excellence and Technological Enterprise (CREATE) programme (Development of advanced catalysts for electrochemical carbon abatement, project Code: 370184872), and Ministry of Education (grant no. 24-1770-A0002).

Data Availability Statement: The data that support the findings of this study are available from the corresponding author upon reasonable request.

Conflicts of Interest: The authors declare no conflict of interest.

References

1. Qian, Q.; Zhu, Y.; Ahmad, N.; Feng, Y.; Zhang, H.; Cheng, M.; Liu, H.; Xiao, C.; Zhang, G.; Xie, Y. Recent Advancements in Electrochemical Hydrogen Production via Hybrid Water Splitting. *Adv. Mater.* **2024**, *36*, 2306108. https://doi.org/10.1002/adma.202306108.
2. Sharshir, S.; Joseph, A.; Elsayad, M.; Tareemi, A.; Kandeal, A.; Elkadeem, M. A Review of Recent Advances in Alkaline Electrolyzer for Green Hydrogen Production: Performance Improvement and Applications. *Int. J. Hydrogen Energy* **2024**, *49*, 458–488. https://doi.org/10.1016/j.ijhydene.2023.08.107.
3. Tüysüz, H. Alkaline Water Electrolysis for Green Hydrogen Production. *Acc. Chem. Res.* **2024**, *57*, 558–567. https://doi.org/10.1021/acs.accounts.3c00709.
4. Sebbahi, S.; Assila, A.; Belghiti, A.; Laasri, S.; Kaya, S.; Hlil, E.; Rachidi, S.; Hajjaji, A. A Comprehensive Review of Recent Advances in Alkaline Water Electrolysis for Hydrogen Production. *Int. J. Hydrogen Energy* **2024**, *82*, 583–599. https://doi.org/10.1016/j.ijhydene.2024.07.428.
5. He, X.; Deng, B.; Lang, J.; Zheng, Z.; Zhang, Z.; Chang, H.; Wu, Y.; Yang, C.; Zhao, W.; Lei, M.; et al. Interfacial-Free-Water-Enhanced Mass Transfer to Boost Current Density of Hydrogen Evolution. *Nano Lett.* **2025**, *25*, 6780–6787. https://doi.org/10.1021/acs.nanolett.5c01235.
6. Lin, Y.; Dong, Y.; Wang, X.; Chen, L. Electrocatalysts for the Oxygen Evolution Reaction in Acidic Media. *Adv. Mater.* **2023**, *35*, 2210565. https://doi.org/10.1002/adma.202210565.
7. Li, H.; Lin, Y.; Duan, J.; Wen, Q.; Liu, Y.; Zhai, T. Stability of Electrocatalytic OER: From Principle to Application. *Chem. Soc. Rev.* **2024**, *53*, 10709–10740. https://doi.org/10.1039/d3cs00010a.
8. Chen, M.; Kitiphatpiboon, N.; Feng, C.; Abudula, A.; Ma, Y.; Guan, G. Recent Progress in Transition-Metal-Oxide-Based Electrocatalysts for the Oxygen Evolution Reaction in Natural Seawater Splitting: A Critical Review. *eScience* **2023**, *3*, 100111. https://doi.org/10.1016/j.esci.2023.100111.
9. Zhao, M.; Chen, Z.; Shi, Y.; Hood, Z.D.; Lyu, Z.; Xie, M.; Chi, M.; Xia, Y. Kinetically Controlled Synthesis of Rhodium Nanocrystals with Different Shapes and a Comparison Study of Their Thermal and Catalytic Properties. *J. Am. Chem. Soc.* **2021**, *143*, 6293–6302. https://doi.org/10.1021/jacs.1c02734.
10. Zhou, S.; Liu, Y.; Li, J.; Liu, Z.; Shi, J.; Fan, L.; Cai, W. Surface-Neutralization Engineered NiCo-LDH/Phosphate Hetero-Sheets toward Robust Oxygen Evolution Reaction. *Green Energy Environ.* **2024**, *9*, 1151–1158. https://doi.org/10.1016/j.gee.2022.12.003.
11. Xie, J.; Zhang, Q.; Gu, L.; Xu, S.; Wang, P.; Liu, J.; Ding, Y.; Yao, Y.F.; Nan, C.; Zhao, M.; et al. Ruthenium–Platinum Core–Shell Nanocatalysts with Substantially Enhanced Activity and Durability towards Methanol Oxidation. *Nano Energy* **2016**, *21*, 247–257. https://doi.org/10.1016/j.nanoen.2016.01.013.

12. Wu, C.-Y.; Hsiao, Y.-C.; Chen, Y.; Lin, K.-H.; Lee, T.-J.; Chi, C.-C.; Lin, J.-T.; Hsu, L.-C.; Tsai, H.-J.; Gao, J.-Q.; et al. A Catalyst Family of High-Entropy Alloy Atomic Layers with Square Atomic Arrangements Comprising Iron- and Platinum-Group Metals. *Sci. Adv.* **2024**, *10*, eadl3693. https://doi.org/10.1126/sciadv.adl3693.
13. Qin, R.; Chen, G.; Feng, X.; Weng, J.; Han, Y. Ru/Ir-Based Electrocatalysts for Oxygen Evolution Reaction in Acidic Conditions: From Mechanisms, Optimizations to Challenges. *Adv. Sci.* **2024**, *11*, 2309364. https://doi.org/10.1002/advs.202309364.
14. Kumar, H.; Yan, M. Quantification of Nanomaterial Surfaces. *Mater. Interfaces* **2025**, *2*, 66–83. https://doi.org/10.53941/mi.2025.100007.
15. Hou, Y.; Cui, S.; Wen, Z.; Guo, X.; Feng, X.; Chen, J. Strongly Coupled 3D Hybrids of N-Doped Porous Carbon Nanosheet/CoNi Alloy-Encapsulated Carbon Nanotubes for Enhanced Electrocatalysis. *Small* **2015**, *11*, 5940–5948. https://doi.org/10.1002/smll.201502297.
16. Yan, Q.; Li, X.; Luo, J.; Zhao, M. Single-Molecule Fluorescence Imaging of Energy-Related Catalytic Reactions. *Chem. Biomed. Imaging* **2025**, *3*, 280–300. https://doi.org/10.1021/cbmi.4c00112.
17. Hammons, J.A.; Kang, S.; Ferron, T.J.; Aydin, F.; Lin, T.Y.; Seung, K.; Chow, P.; Xiao, Y.; Davis, J.T. Nanobubble Formation and Coverage during High Current Density Alkaline Water Electrolysis. *Nano Lett.* **2024**, *24*, 13695–13701. https://doi.org/10.1021/acs.nanolett.4c03657.
18. Wang, J.; Gao, Y.; Kong, H.; Kim, J.; Choi, S.; Ciucci, F.; Hao, Y.; Yang, S.; Shao, Z.; Lim, J. Non-Precious-Metal Catalysts for Alkaline Water Electrolysis: Operando Characterizations, Theoretical Calculations, and Recent Advances. *Chem. Soc. Rev* **2020**, *49*, 9154–9196. https://doi.org/10.1039/d0cs00575d.
19. Wang, J.; Xu, F.; Jin, H.; Chen, Y.; Wang, Y. Non-Noble Metal-Based Carbon Composites in Hydrogen Evolution Reaction: Fundamentals to Applications. *Adv. Mater.* **2017**, *29*, 1605838. https://doi.org/10.1002/adma.201605838.
20. Li, X.; Huang, C.; Han, W.; Ouyang, T.; Liu, Z. Transition Metal-Based Electrocatalysts for Overall Water Splitting. *Chin. Chem. Lett.* **2021**, *32*, 2597–2616. https://doi.org/10.1016/j.cclet.2021.01.047.
21. Pan, Q.; Wang, L. Recent Perspectives on the Structure and Oxygen Evolution Activity for Non-Noble Metal-Based Catalysts. *J. Power Sources* **2021**, *485*, 229335. https://doi.org/10.1016/j.jpowsour.2020.229335.
22. Gao, F.; Zhang, Y.; Wu, Z.; You, H.; Du, Y. Universal Strategies to Multi-Dimensional Noble-Metal-Based Catalysts for Electrocatalysis. *Coord. Chem. Rev.* **2021**, *436*, 213825. https://doi.org/10.1016/j.ccr.2021.213825.
23. Zubair, M.; Ul Hassan, M.; Mehran, M.; Baig, M.; Hussain, S.; Shahzad, F. 2D MXenes and Their Heterostructures for HER, OER and Overall Water Splitting: A Review. *Int. J. Hydrogen Energy* **2022**, *47*, 2794–2818. https://doi.org/10.1016/j.ijhydene.2021.10.248.
24. Wang, C.; Lin, Y.; Cui, L.; Zhu, J.; Bu, X. 2D Metal-Organic Frameworks as Competent Electrocatalysts for Water Splitting. *Small* **2023**, *19*, 2207342. https://doi.org/10.1002/smll.202207342.
25. Sun, S.; Jin, X.; Cong, B.; Zhou, X.; Hong, W.; Chen, G. Construction of Porous Nanoscale NiO/NiCo2O4 Heterostructure for Highly Enhanced Electrocatalytic Oxygen Evolution Activity. *J. Catal.* **2019**, *379*, 1–9. https://doi.org/10.1016/j.jcat.2019.09.010.
26. Cheng, H.; Wang, C.; Lyu, Z.; Zhu, Z.; Xia, Y. Controlling the Nucleation and Growth of Au on A-Se Nanospheres to Enhance Their Cellular Uptake and Cytotoxicity. *J. Am. Chem. Soc.* **2023**, *145*, 1216–1226. https://doi.org/10.1021/jacs.2c11053.
27. Cheng, H.; Zhou, S.; Xie, M.; Gilroy, K.D.; Zhu, Z.; Xia, Y. Colloidal Nanospheres of Amorphous Selenium: Facile Synthesis, Size Control, and Optical Properties. *Chem. Nano. Mater.* **2021**, *7*, 620–625. https://doi.org/10.1002/cnma.202100115.
28. Zheng, W.; Liu, M.; Lee, L.Y.S. Best Practices in Using Foam-Type Electrodes for Electrocatalytic Performance Benchmark. *ACS Energy Lett.* **2020**, *5*, 3260–3264. https://doi.org/10.1021/acsenergylett.0c01958.
29. Miyake, H.; Ye, S.; Osawa, M. Electroless Deposition of Gold Thin Films on Silicon for Surface-Enhanced Infrared Spectroelectrochemistry. *Electrochem. Commun.* **2002**, *4*, 973–977. https://doi.org/10.1016/S1388-2481(02)00510-6.
30. Ye, S.; Ichihara, T.; Uosaki, K. Spectroscopic Studies on Electroless Deposition of Copper on a Hydrogen-Terminated Si(111) Surface in Fluoride Solutions. *J. Electrochem. Soc.* **2001**, *148*, C421. https://doi.org/10.1149/1.1370964.
31. Mukherjee, S.; Mukhopadhyay, N.K.; Basu, J. Structural Modulation, Oriented Growth of Rock Salt, and Spinel in (Co(Cr/Mg)FeMnNi) Multicomponent Oxide and Derivatives. *J. Am. Ceram. Soc.* **2025**, *108*, e20619. https://doi.org/10.1111/jace.20619.
32. Park, J.; Kim, H.K.; Park, J.; Kim, B.; Baik, H.; Baik, M.-H.; Lee, K. Flattening Bent Janus Nanodiscs Expands Lattice Parameters. *Chem* **2023**, *9*, 948–962. https://doi.org/10.1016/j.chempr.2022.12.004.
33. Abidat, I.; Morais, C.; Comminges, C.; Canaff, C.; Rousseau, J.; Guignard, N.; Napporn, T.W.; Habrioux, A.; Kokoh, K.B. Three Dimensionally Ordered Mesoporous Hydroxylated NixCo3-xO4 Spinels for the Oxygen Evolution Reaction: On the Hydroxyl-Induced Surface Restructuring Effect. *J. Mater. Chem. A* **2017**, *5*, 7173–7183. https://doi.org/10.1039/c7ta00185a.

34. Anantharaj, S.; Noda, S. Appropriate Use of Electrochemical Impedance Spectroscopy in Water Splitting Electrocatalysis. *Chem. Electro. Chem.* **2020**, *7*, 2297–2308. https://doi.org/10.1002/celc.202000515.
35. Ruiz-Fresneda, M.A.; Eswayah, A.S.; Romero-González, M.; Gardiner, P.H.; Solari, P.L.; Merroun, M.L. Chemical and Structural Characterization of Se IV Biotransformations by Stenotrophomonas Bentonitica into Se^0 Nanostructures and Volatiles Se Species. *Environ. Sci. Nano* **2020**, *7*, 2140–2155. https://doi.org/10.1039/D0EN00507J.
36. Ariyoshi, K.; Siroma, Z.; Mineshige, A.; Takeno, M.; Fukutsuka, T.; Abe, T.; Uchida, S. Electrochemical Impedance Spectroscopy Part 1: Fundamentals. *Electrochemistry* **2022**, *90*, 102007. https://doi.org/10.5796/electrochemistry.22-66071.
37. Ding, J.; Du, M.; Wang, S.; Zhang, L.; Yue, Y.; Smedskjaer, M.M. Amorphous Material Based Heterostructures with Disordered Heterointerfaces for Advanced Rechargeable Batteries. *Energy Environ. Sci.* **2025**, *18*, 1587–1611. https://doi.org/10.1039/D4EE04566A.
38. Zou, X.; Liu, Y.; Li, G.; Wu, Y.; Liu, D.; Li, W.; Li, H.; Wang, D.; Zhang, Y.; Zou, X. Ultrafast Formation of Amorphous Bimetallic Hydroxide Films on 3D Conductive Sulfide Nanoarrays for Large-Current-Density Oxygen Evolution Electrocatalysis. *Adv. Mater.* **2017**, *29*, 1700404. https://doi.org/10.1002/adma.201700404.
39. Sun, J.; Xue, H.; Guo, N.; Song, T.; Hao, Y.; Sun, J.; Zhang, J.; Wang, Q. Synergetic Metal Defect and Surface Chemical Reconstruction into NiCo2S4/ZnS Heterojunction to Achieve Outstanding Oxygen Evolution Performance. *Angew. Chem. Int. Ed.* **2021**, *60*, 19435–19441. https://doi.org/10.1002/anie.202107731.
40. Jiang, J.; Sun, F.; Zhou, S.; Hu, W.; Zhang, H.; Dong, J.; Jiang, Z.; Zhao, J.; Li, J.; Yan, W.; et al. Atomic-Level Insight into Super-Efficient Electrocatalytic Oxygen Evolution on Iron and Vanadium Co-Doped Nickel (Oxy)Hydroxide. *Nat. Commun.* **2018**, *9*, 2885. https://doi.org/10.1038/s41467-018-05341-y.
41. Xue, Z.; Li, X.; Liu, Q.; Cai, M.; Liu, K.; Liu, M.; Ke, Z.; Liu, X.; Li, G. Interfacial Electronic Structure Modulation of NiTe Nanoarrays with NiS Nanodots Facilitates Electrocatalytic Oxygen Evolution. *Adv. Mater.* **2019**, *31*, 1900430. https://doi.org/10.1002/adma.201900430.
42. Niu, S.; Jiang, W.-J.; Wei, Z.; Tang, T.; Ma, J.; Hu, J.-S.; Wan, L.-J. Se-Doping Activates FeOOH for Cost-Effective and Efficient Electrochemical Water Oxidation. *J. Am. Chem. Soc.* **2019**, *141*, 7005–7013. https://doi.org/10.1021/jacs.9b01214.
43. Chen, J.; Qi, M.; Yang, Y.; Xiao, X.; Li, Y.; Jin, H.; Wang, Y. Chloride Residues in RuO2 Catalysts Enhance Its Stability and Efficiency for Acidic Oxygen Evolution Reaction. *Angew. Chem. Int. Ed.* **2025**, *64*, e202420860. https://doi.org/10.1002/anie.202420860.
44. Liu, X.; Zhao, P.; Liu, F.; Lin, R.; Yao, H.; Zhu, S. Attenuated Total Reflection Infrared Spectroscopy for Studying Electrochemical Cycling of Hydrogen, Carbon, and Nitrogen-Containing Molecules. *J. Energy Chem.* **2024**, *99*, 495–511. https://doi.org/10.1016/j.jechem.2024.08.008.

Article

Seeded Growth of Large Gold Nanorods Modulated by Halide-Mediated Kinetics

Francisco Bevilacqua [1,2] and Luis M. Liz-Marzán [1,2,3,4,*]

[1] CIC biomaGUNE, Basque Research and Technology Alliance (BRTA), 20014 Donostia-San Sebastián, Spain
[2] Biomedical Networking Center of Bioengineering, Biomaterials and Nanomedicine, CIBER-BBN, 20014 Donostia-San Sebastián, Spain
[3] Ikerbasque, Basque Foundation for Science, 48009 Bilbao, Spain
[4] CINBIO, University of Vigo, 36310 Vigo, Spain
* Correspondence: llizmarzan@cicbiomagune.es

Received: 24 September 2025; Revised: 23 October 2025; Accepted: 3 November 2025; Published: 4 November 2025

Abstract: We report a robust and versatile method to overgrow pentatwinned gold nanorods using a combination of cetyltrimehylammonium chloride (CTAC) and bromide (CTAB), thereby expanding current protocols to the production of larger nanorod dimensions. When increasing CTAB content in the reaction medium, the aspect ratio of the resulting nanorods was found to decrease, due to the higher binding energy of bromide on gold surfaces, compared to chloride. A further handle to tailor the dimensions of larger nanorods can be achieved by tuning the Au^{3+}/Au^{0} ratio. At a fixed CTAB concentration, increasing Au^{3+}/Au^{0} ratio resulted in larger nanorods with minor variation of the aspect ratio, which again highlights the central role of CTAB in the overgrowth process. Our findings highlight the effect of CTAB on both growth kinetics and facet stabilization, offering a simple approach to finely tune the dimensions of pentatwinned gold nanorods. We also demonstrate the versatile use of CTAB/CTAC ratio in a more standard synthesis method, again leading to fine tuning of nanorod dimensions.

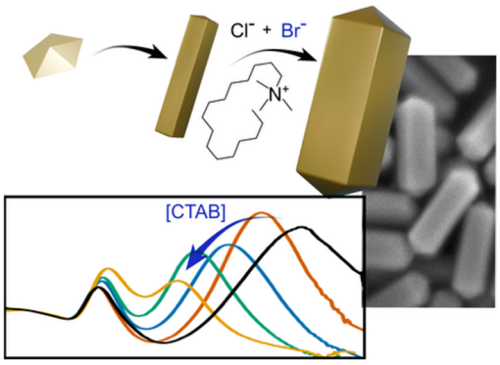

Keywords: gold; nanorods; CTAB; growth mechanism; plasmonic nanoparticles

1. Introduction

Since the early works by Murphy and El-Sayed [1,2], the synthesis of gold nanorods (AuNRs) has been repeatedly optimized and is currently one of the best-established fabrication procedures in nanomaterials research [3–5]. The superior quality of the nanomaterials obtained through these synthetic protocols allows precise tunability in the corresponding localized surface plasmon resonance (LSPR), in turn providing broad applicability in fields such as photothermal therapy, sensing, and imaging, among others [6–8]. The development of reliable synthetic protocols has been enabled by extensive studies of the involved growth mechanisms and detailed understanding of the influence of individual synthetic parameters, leading to a precise control over AuNR dimensions and, consequently, their optical properties [4,5,9,10]. The control over nanoparticle shape is achieved by performing nucleation and growth in separate reaction steps. First, small, quasi-spherical gold nanoparticles are formed by mixing $AuCl_4^-$ in solution with a strong reducing agent, most frequently sodium borohydride. Subsequently, these "seeds" are overgrown by further addition of $AuCl_4^-$, together with shape-directing reagents—quaternary ammonium surfactants, halide counter-ions, and often Ag^+ ions—and a weak reducing agent, usually ascorbic acid (AA). The use of a weak reductant promotes the initial reduction of Au^{3+} to Au^+, while avoiding complete reduction into Au^0 in the absence of seeds [1]. In this manner, reduction of Au^+ into Au^0 only occurs on the surface of the added gold seeds, leading to a more uniform growth and restricting homogeneous nucleation of gold particles. In this growth scheme the crystallinity of the seeds plays a key role in determining the morphology of the fully grown nanorods [4,11].

In broad terms, AuNRs can be synthesized using seeds with two different crystallographic habits, either single-crystalline (SC) [2,5] or pentatwinned (PT) [4,12]. On one hand, SC seeds have no crystal twin defects, and

Copyright: © 2025 by the authors. This is an open access article under the terms and conditions of the Creative Commons Attribution (CC BY) license (https://creativecommons.org/licenses/by/4.0/).
Publisher's Note: Scilight stays neutral with regard to jurisdictional claims in published maps and institutional affiliations.

are commonly employed to prepare single-crystal AuNRs (SC-AuNRs) in the presence of Ag^+ ions. On the other hand, PT seeds contain five twin boundaries, which propagate during (Ag-free) seeded growth, leading to the formation of pentatwinned AuNRs (PT-AuNRs) with 5-fold symmetry along the long axis. However, the formation of PT seeds in high yield has proven challenging and often requires extensive purification steps [12]. Albeit less commonly used than SC-AuNR, PT-AuNR allow the preparation of larger nanoparticles, with the additional advantage that silver is not present in their composition, thus reducing cytotoxicity and facilitating surface conjugation [4,12]. Typically, the preparation of SC-AuNRs requires a growth solution containing—apart from $HAuCl_4$ and AA—a high concentration of the surfactant hexadecyltrimethylammonium bromide (CTAB), HCl, and $AgNO_3$ [2,3,5], whereas PT-AuNRs solely require the presence of CTAB, which is also present in a smaller amount compared to SC-AuNRs. Standard SC-AuNRs are characterized by small dimensions and aspect ratios up to ~8, ranging from "minirods" (~20 nm length and diameter below 10 nm) to larger rods with lengths in the hundred nm range [5,13,14]. On the other hand, PT-AuNRs can be grown into larger dimensions (>100 nm length) and longer aspect ratios >20 [12,15,16]**.** Structurally, SC- and PT-AuNRs exhibit key differences in the Miller indices of their surface facets, which is relevant for various applications and processes, such as catalysis, bioconjugation, self-assembly, or seeded overgrowth: SC-AuNRs expose high-index {520} facets (combined with {100} and {110}) along their sides and a combination of {111}, {100}, and {110} facets at their tips [17]; whereas PT-AuNRs predominantly display low-index {100} lateral facets and {111} tip facets due to the presence of five twin planes that impose a pentagonal cross section [4,18].

The control over anisotropic growth of AuNRs depends on the shape-directing ability of the different reagents, involving effects on the thermodynamic stability of the resulting surface facets and on reaction kinetics. Surfactant molecules have an influence on three key aspects of particle growth: (i) stabilization of nanoparticles to prevent aggregation, (ii) formation of complexes with gold ions and modulation of their reduction potential and kinetics, and (iii) promotion of anisotropic growth by selective facet stabilization. Therefore, understanding their influence on the two latter aspects is crucial to gain control over the dimensions and quality of the resulting particles. Several studies reported the influence of various surfactants and other surface-binding ligands. Among these, CTAB and other quaternary ammonium salts—hexadecyltrimethylammonium chloride (CTAC) and others—have been the subject of extensive investigation [19–21]. These studies have emphasized the importance of the cetyltrimethylammonium (CTA^+) cationic surfactant for directing nanorod growth through two main mechanisms, namely the packing density and the organization of the organic surface layer, both influencing the accessibility of reactants to the Au surface to allow further Au reduction [18,20]. For example, in CTAB-mediated synthesis, CTA^+ molecules exhibit a higher packing density on {100} facets compared to {111} facets [18,20]. Interestingly, "patchy" structures on gold surfaces have been proposed at low CTA^+ concentrations, with more continuous layers at higher concentrations [18,22,23]. On the other hand, studies on CTAC showed weaker CTA^+ adsorption onto gold surfaces, creating a more diffuse surfactant layer that allows easier access to the gold surface [20,23]. An important component of the surfactant is thus the counterion—typically a halide—which plays a major role during anisotropic growth. Bromide ions ($Br^–$) have a higher binding energy to gold surfaces compared to chloride ($Cl^–$), thereby leading to a slower deposition rate of Au^0 on the growing seed facets [17]. Accordingly, the addition of $Br^–$ to the growth solution can be used to increase the local density of CTA^+ on the gold surface [20,24]. Overall, the differences in specific adsorption for CTAB and CTAC explain why CTAB is preferred in syntheses that require kinetic regulation and symmetry breaking [3–5], whereas CTAC is more commonly employed in the synthesis of isotropic nanoparticles [10].

Binary surfactant systems have been investigated for the preparation of high aspect ratio PT-AuNRs from SC seeds. For example, binary surfactant mixtures combining oleic acid and CTAB were employed to achieve high aspect ratio PT-NRs in relatively high yield (>70%) [15]. It is generally understood that a slower gold reduction rate leads to nanorods with higher aspect ratio; this can be achieved by decreasing the reaction pH (i.e., regulating the presence of the ascorbate anions responsible for reduction of Au^{3+} to Au^+), decreasing the concentration of reducing agent, or lowering the reaction temperature [5,24]. However, reducing reaction temperature can be challenging for syntheses employing high CTAB concentrations because of the low solubility of CTAB in water, which spontaneously crystallizes below ~25 °C. Our group has recently demonstrated that a suitable CTAB/CTAC ratio can be selected to enable seeded growth at low temperatures down to 8 °C, thereby expanding the accessible dimensions of PT-AuNRs [24]. We have also reported that the overgrowth of pre-formed PT-AuNRs in the presence of CTAC at 30 °C results in the formation of large PT bipyramids, eventually featuring a thicker equatorial belt [25].

Despite these developments, studies on PT-AuNR synthesis remain scarce compared to SC-AuNRs, for which numerous optimization procedures have been reported, resulting in great reproducibility and control over aspect ratio and dimensions. We thus aimed at identifying suitable conditions to obtain PT-AuNRs with larger dimensions while keeping a low aspect ratio (and LSPR modes within the visible or near-IR). Using pre-formed

PT-AuNRs as seeds, we focused on the role of CTAB in regulating the growth kinetics for different Au^{3+} to seed ratios. We thus hypothesized that, by using CTAB/CTAC surfactant mixtures with different ratios, we would modulate surface accessibility during growth and in turn the deposition of reduced Au atoms. As a result, we developed a robust method to overgrow pre-formed PT-AuNRs into larger PT-AuNRs with tunable aspect ratio, which we demonstrate for nanorods with dimensions (length × width) ranging from 126 nm × 60 nm to 266 nm × 76 nm. We additionally demonstrate that, by tailoring the CTAB/CTAC ratio, AuNR dimensions could also be tuned for PT-AuNRs grown from small PT seeds [24], thus offering a general strategy to tune the aspect ratio and expand the accessible sizes of PT-AuNRs.

2. Materials and Methods

2.1. Materials

Analytical grade reagents, $HAuCl_4 \cdot 3H_2O$ (≥99.9%), L-ascorbic acid (99%), cetyltrimethylammonium bromide (CTAB, ≥96.0%), cetyltrimethylammonium chloride (CTAC, 25 wt% in H_2O), citric acid (≥99.5%), sodium borohydride (≥99.0%), were all purchased from Merck, Darmstadt, Germany.

2.2. Preparation of pentatwinned seeds

PT Au seeds were prepared following a previously reported protocol [4]. Typically, 5 mL of 100 mM CTAC was first mixed with 0.5 mL of 100 mM citric acid and 4.2 mL of water. Subsequently, 50 µL of 50 mM $HAuCl_4$ was added under stirring. The solution was left under mild magnetic stirring (200–300 rpm) for 30 min to ensure homogeneous mixing. After this time, 250 µL of a freshly prepared ice-cold 25 mM $NaBH_4$ solution was quickly added under vigorous stirring (>1000 rpm) the color turned from light yellow to light brown. At this stage, a UV-vis spectrum was recorded to verify gold salt reduction through the absorbance at 400 nm (the value should be close to 0.6 for an optical pathlength of 1 cm). After borohydride addition, the solution was kept at room temperature for 15 min to ensure borohydride decomposition, followed by a heat treatment at 80 °C for 90 min, during which the color of the solution turned red. A larger amount of borohydride might result in extensive overgrowth during the heat treatment and thus a lower yield of twinning. At this stage the spectrum can be checked, and the peak should be below 529 nm; above this value no twinning could be observed.

2.3. Growth of 113 nm × 26 nm Au pentatwinned nanorods

The preparation of PT-AuNRs was based on the protocol reported in the same study as the PT seeds [4]. A 100 mL solution of 8 mM CTAB was prepared, to which 250 µL of 50 mM $HAuCl_4$ was added. The solution was left for 15 min under mild magnetic stirring to ensure the formation of [Br-Au-Br] complexes, followed by 15 additional minutes in a water bath at 20 °C. Thereafter, 250 µL of 100 mM AA solution and 230 µL of PT seeds were added under vigorous stirring. The solution was subsequently stored at 20 °C overnight without stirring. After synthesis, the obtained nanorods were centrifuged at 6,500 rpm for 15 min and redispersed in CTAC 100 mM. The particles were finally redispersed in 2 mL of MilliQ water, with a concentration (estimated from the absorbance at 400 nm) of 2.67 mM Au^0. A representative TEM image and UV-vis-NIR spectrum are shown in Figure S1. Statistical analysis from over 100 particles yielded average dimensions of 113 ± 6 nm in length, 26 ± 2 nm in width, and aspect ratio of 4.4 ± 0.5.

2.4. Overgrowth of PT-AuNRs

Typically, a 10 mL solution of 25 mM CTAC and a given concentration of CTAB was prepared by mixing 2.5 mL of 100 mM CTAC solution and the corresponding volume of a 100 mM CTAB solution and storing at 30 °C. To this mixed solution, 20 µL of 50 mM $HAuCl_4$ was added under mild stirring (200–300 rpm) and left for 15 min to stabilize the temperature. After 15 min, 20 µL of 100 mM AA and a selected amount of PT-AuNR seeds (see Tables S1 and S2) were added under vigorous stirring (700–800 rpm). The reaction was left to proceed at 30 °C under mild stirring for either 90 min ([CTAB] = 0.5–2 mM) or 2 h ([CTAB] = 5–10 mM). After this time, the particles were centrifuged at 2500 rpm for 8 min. The supernatant was discarded, and particles were redispersed in 2 mL of miliQ water.

2.5. Kinetic study

After the addition of gold salt in the reaction medium—initiation of the reaction, t_0—1 mL of the reaction mixture was poured in a plastic semi-microcuvette (1 cm path length) in the spectrometer holder, which was

connected to a water bath for temperature regulation at 30 °C. A spectrum was registered every 2 min for the first 10 min, then at 15 min, 20 min, and finally every 10 min for the remaining time of the reaction.

2.6. Growth from PT seeds

The growth of PT-AuNRs from PT seeds was adapted from a previously reported protocol [24]. Three 10 mL solutions of 100 mM CTAC containing, 4 mM CTAB, 6 mM CTAB, and 8 mM CTAB, were first prepared, to which 25 μL of 50 mM $HAuCl_4$ was added. The solutions were stirred for 15 min, and then placed in a water bath at 8 °C for 30 min. After this time, 25 μL of 100 mM AA was added, followed by 25 μL of PT seeds, both under vigorous stirring (700–800 rpm). After 90 min, the samples were centrifuged and purified by depletion separation using 100 mM CTAC, overnight. The pink supernatant was discarded and the particles were dispersed in 1 mL of miliQ water.

2.7. Optical characterization

Spectroscopic characterization was conducted with an Agilent 8453 UV−vis−NIR diode array spectrophotometer (Agilent Santa Clara, CA, USA) in the 350–1100 nm wavelength range. Typically, after synthesis, the particles were centrifuged (at 2500 rpm for 8 min), then redispersed in milliQ water and placed in a polystyrene cuvette (1 cm path length).

2.8. Electron microscopy

Transmission electron microscopy (TEM) images were captured with a JEOL JEM-1400PLUS (Tokyo, Japan) transmission electron microscope operating at 120 kV. Scanning electron microscopy (SEM) images were acquired using a JSM-IT800HL from JEOL (Tokyo, Japan) equipped with a secondary electron detector (SED) using 3–5 kV, under high vacuum.

2.9. Yield and measurement details

The yield in shape purity was estimated by counting 400–500 particles per sample. The particles were separated into three categories: “rods”, corresponding to pointy rods as the main product of the synthesis; “defective rods”, which exhibited anisotropy but with defects such as dumbbell shapes or protuberances; “non-rods” corresponding to the remaining minority shapes, as indicated in Tables S1 and S2. More than 150 particles were measured from each sample to determine the average length, width, and side length, as illustrated in Figure S2. Details on estimation of particle volume are provided in the Supporting Information.

3. Results and Discussion

On the basis of our previous experience in the growth of PT-AuNRs into large bipyramids [25], we first synthesized PT-AuNR seeds 113 ± 6 nm, 26 ± 2 nm (in short, 113 nm-PT-AuNRs) (Figure S1) using a previously reported protocol (see Section 2) [4]. In a first attempt, AA and 113 nm-PT-AuNR seeds were incubated with CTAC 25 mM and different CTAB concentrations, at 30 °C for 15 min, followed by addition of $HAuCl_4$ under vigorous stirring and allowing the reaction to proceed for 90 min. A summary of the obtained products using both 0.5 mM and 1 mM CTAB is presented in Figure S3. Although the obtained particles displayed a rod-like morphology, TEM images revealed a non-negligible proportion of dumbbell-like or defective rods. Therefore, we proceeded to alter the order of addition of reactants, to ensure complete pre-reduction of Au^{3+} into Au^{+}. The improved overgrowth procedure involved first mixing $HAuCl_4$ with a solution containing CTAC (25 mM) and selected concentrations of CTAB (0.5–10 mM), under mild stirring (200 rpm) at 30 °C for 15 min, followed by addition of AA and 113 nm PT-AuNR seeds, under vigorous stirring (800–1000 rpm). Thanks to this pre-reduction step, the quality of the products was significantly improved, with a yield of well-defined PT-AuNRs over 98% (see Figure S3). However, we found the AA/Au^{3+} ratio to have a moderate impact on the dimensions and quality of the final particles (Figure S4).

After establishing a reliable overgrowth protocol, we aimed at exploring the impact of CTAB concentration, keeping all other reagent concentrations constant, including an Au^{3+}/Au^{0} ratio = 12.5. The well-defined (longitudinal and transverse) LSPR modes in AuNRs allow for a quick initial characterization of seeded growth, simply by recording UV-Vis-NIR spectra of the prepared colloidal dispersions. The spectra for samples prepared at constant seed concentration and Au^{3+}/Au^{0} ratio, but varying CTAB/CTAC ratio (by increasing CTAB concentration) are displayed in Figure 1a. The position of the longitudinal LSPR peak exhibits a gradual blue shift (from 940 to 680 nm) for particles overgrown in the presence of increasing CTAB concentrations, as well as a relative increase in the

intensity of the transverse LSPR band. The corresponding TEM images (Figure 1b–f) reveal the formation of AuNRs with dimensions ranging from 203 nm × 66 nm to 145 nm × 84 nm, as CTAB concentration was increased (see histograms in Figure S5). The geometrical features measured from TEM images are summarized in Table S1 and confirm that the observed longitudinal LSPR blue shift correlates with a gradual decrease in aspect ratio, as expected for AuNRs [26]. Moreover, the small standard deviations in length and width reveal a low polydispersity (<10%) in all cases. Complementary scanning electron microscopy (SEM) measurements were conducted to unveil more detailed morphological features (Figures 1g,h and S6). SEM images evidence the presence of sharp tips on the obtained PT-AuNRs, with a well-defined pentagonal cross-section and sharp faceting. SEM analysis further confirms the low polydispersity of the samples produced. Finally, we demonstrate the feasibility of scaling the synthesis up to a total volume of 100 mL, using 5 mM CTAB. The produced particles showed high homogeneity in both shape and size (<10%), thus confirming the robustness of the synthesis protocol and potential upscaling to even larger volumes with no loss of sample quality (see Figure S7).

For consistency, we carried out optical simulations based on a quasi-analytical model for selected geometries [27]. We selected a cylindrical rod model for AuNRs with the average dimensions of our PT-AuNRs, as determined by TEM (Figure S8 and Table S1). The simulated spectra follow the same trend as the experimental ones, not only in the LSPR position, but also in the increased intensity of the transverse mode. However, the precise position of the LSPR band exhibits some discrepancies, which are minor for the samples obtained with [CTAB] ranging from 2 to 10 mM (~10–20 nm), but higher for the lowest CTAB concentration (~50 nm). Overall, these differences between experimental and simulated data are consistent among samples, supporting the idea that they are mainly due to the geometrical differences between the actual particles (pentagonal prisms with sharp tips) and the model (cylinder with hemispherical tips). However, the largest observed difference (50 nm for the 0.5 mM CTAB sample) suggests that the influence of these morphological features on the optical activity of the particles becomes more relevant for more elongated particles.

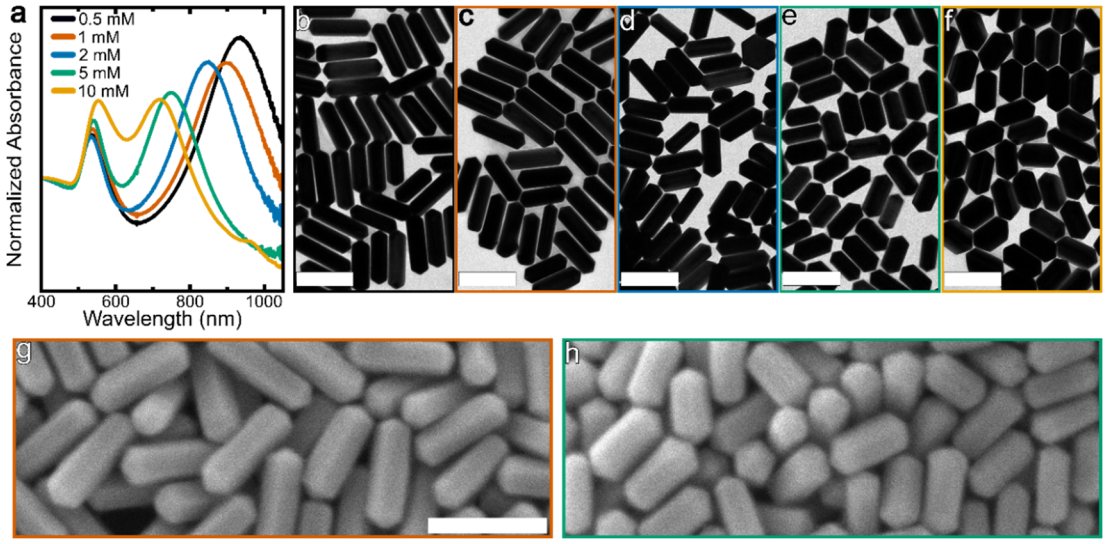

Figure 1. Overgrowth of PT-AuNRs at constant Au^{3+}/Au^0 = 12.5 and [CTAC] = 25 mM, with varying [CTAB] from 0.5 to 10 mM. (**a**) UV-vis-NIR spectra (normalized at 400 nm) for nanorods grown from 113 nm-PT-AuNR seeds at different CTAB concentrations. (**b**–**f**) TEM micrographs corresponding to the spectra in (**a**), with CTAB concentrations of 0.5 mM ((**b**), 202 nm × 60 nm), 1 mM ((**c**), 203 nm × 66 nm), 2 mM ((**d**), 171 nm × 70 nm), 5 mM ((**e**), 154 nm × 71 nm), and 10 mM ((**f**), 145 nm × 84 nm). SEM images of Pt-AuNRs obtained by seeded growth from 113 nm-PT-AuNR using Au^{3+}/Au^0 = 12.5 and different CTAB concentrations of 1 mM (**g**) and 5 mM (**h**). All scale bars represent 200 nm; the scale bar in (**g**) is also valid for (**h**).

To further assess the robustness of the synthesis, we estimated the average volume of the synthesized NRs using the calculation outlined in the Supporting Information (see Figure S2). Because a constant Au^{3+}/Au^0 ratio and PT-AuNR seed concentration were maintained for all syntheses with different CTAB concentrations, the initial AuNRs should have grown by the same proportion, and the final particles should reach approximately the same volume. The results are shown in Table S1 and confirm this hypothesis, albeit with minor deviations, from ~4% to ~15% for the 5–0.5 mM and 5–10 mM ranges, respectively. Although a 15% deviation lies slightly above the standard deviation of the sample dimensions (~10%), this difference may arise from deviations from the regular pentagonal cylinder geometry for some deformed nanorods. Overall, the synthesis proved to be effective and reproducible, resulting in high-quality nanorods at any of the selected CTAB concentrations.

We next employed UV-vis-NIR spectroscopy to investigate the effect of CTAB concentration on the kinetics of AuNR overgrowth. Two effects were expected from an increase in the concentration of CTAB in solution, namely an increase of the CTA^+ density at the AuNR surface and a higher density of bromide ions adsorbing on the gold surface, both effects contributing to a slower reduction and deposition of gold atoms [18,23]. Additionally, the CTA^+ and Br^- densities are also expected to be higher on {100} facets, thereby stabilizing them and favoring growth on {111} facets [20]. Shown in Figure 2a–e are the spectral traces during overgrowth, using an Au^{3+}/Au^0 ratio of 12.5, for the different CTAB concentrations, from 0.5 mM to 10 mM. During the overgrowth process, a spectrum was acquired every 2 min for the first 10 min (grey), followed by spectra at 15 and 20 min (brown), and then one spectrum every 10 min (green) until the absorbance at 400 nm reached a plateau. This strategy allowed us to identify differences in the growth rate, from the variations in both absorbance and LSPR position. The absorbance at 400 nm (mostly contributed by interband transitions in metallic gold [28]) can be used as a qualitative indicator of the reduction of Au^+ to Au^0. It should however be noted that, in the case of large nanoparticles, a significant contribution of scattering is expected, which hinders a quantitative analysis using this parameter [29]. Thus, to facilitate analysis of the kinetics we plotted in Figure 2f the absorbance at 400 nm as function of time. These plots clearly show differences in the initial increase of absorbance, as the slope decreases with increasing CTAB concentration. Moreover, a longer time is required for the absorbance to reach a plateau in the case of the higher CTAB concentrations (120 min for 10 mM CTAB versus 50 min for 0.5 mM CTAB). The time evolution of the longitudinal LSPR maximum is more complex (see Figure S9) because of the relative contributions of absorption and scattering during the morphological evolution of the NRs. These kinetic experiments confirmed the expected impact of Br^-, and CTA^+ on gold reduction kinetics, in agreement with previous literature reports [18,20,23].

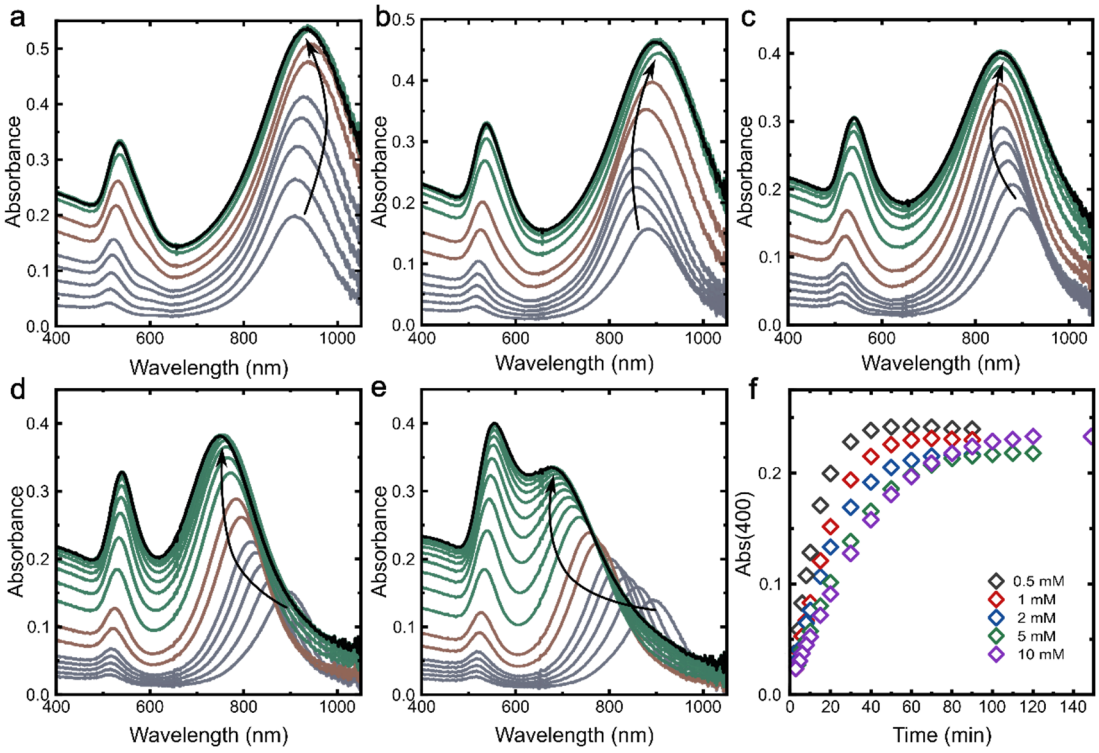

Figure 2. Effect of CTAB concentration on overgrowth kinetics. Spectral evolution during the overgrowth of 113 nm-PT-AuNRs using Au^{3+}/Au^0 = 12.5, for different CTAB concentrations: 0.5 mM (**a**), 1 mM (**b**), 2 mM (**c**), 5 mM (**d**), and 10 mM (**e**). A UV-vis-NIR spectrum was acquired every 2 min for the first 10 min (grey lines), then at 15 min, 20 min (brown), and every 10 min (green). (**f**) Evolution of the absorbance at 400 nm during the overgrowth of 113 nm-PT-AuNRs, as a function of CTAB concentration. Arrows are a guide for the eye showing the LSPR shift.

Aiming at a further range of particle dimensions, we carried out overgrowth experiments at constant CTAB concentrations, but increasing the Au^{3+}/Au^0 ratio (Figure 3). In all cases, when decreasing seed concentration in the growth solution, a red shift was observed in the longitudinal LSPR band, which should be related to an increase in aspect ratio [26]. The average dimensions for the different samples, obtained from TEM measurements are listed in Table S2. When using 0.5 mM CTAB, a small increase in aspect ratio was observed, from 3.28 to 3.47, a difference

that was within the standard deviations. Similarly, the aspect ratios for other samples were not found to show a clear increase or decrease, consistently remaining within the standard deviation range. For example, at 1 mM we observed a maximum aspect ratio of 2.98 at Au^{3+}/Au^0 = 18.75, and a smaller aspect ratio of 2.78 at Au^{3+}/Au^0 = 6.25. On the other hand, at the higher CTAB concentrations—5 mM and 10 mM—the aspect ratio appeared to slightly decrease for higher Au^{3+}/Au^0 ratios, but again remaining within the range of the standard deviation. Thus, we hypothesize that, under these synthetic conditions, the influence of CTAB concentration on the overgrowth process largely defines the aspect ratio, whereas the Au^{3+}/Au^0 ratio affects the final dimensions but not the aspect ratio. These optical changes were again supported by theoretical modeling using the cylindrical NR model, as shown in Figure S10, Table S2. Additionally, estimations of the average volume for the various samples was carried out to confirm complete overgrowth. As summarized in Figure S11, the values obtained for the volumes are within a narrow range for each Au^{3+}/Au^0 ratio and a high R^2 value of 0.99 was determined in a linear regression through the values for different Au^{3+}/Au^0 ratios, evidencing a linear evolution of rod volume as expected.

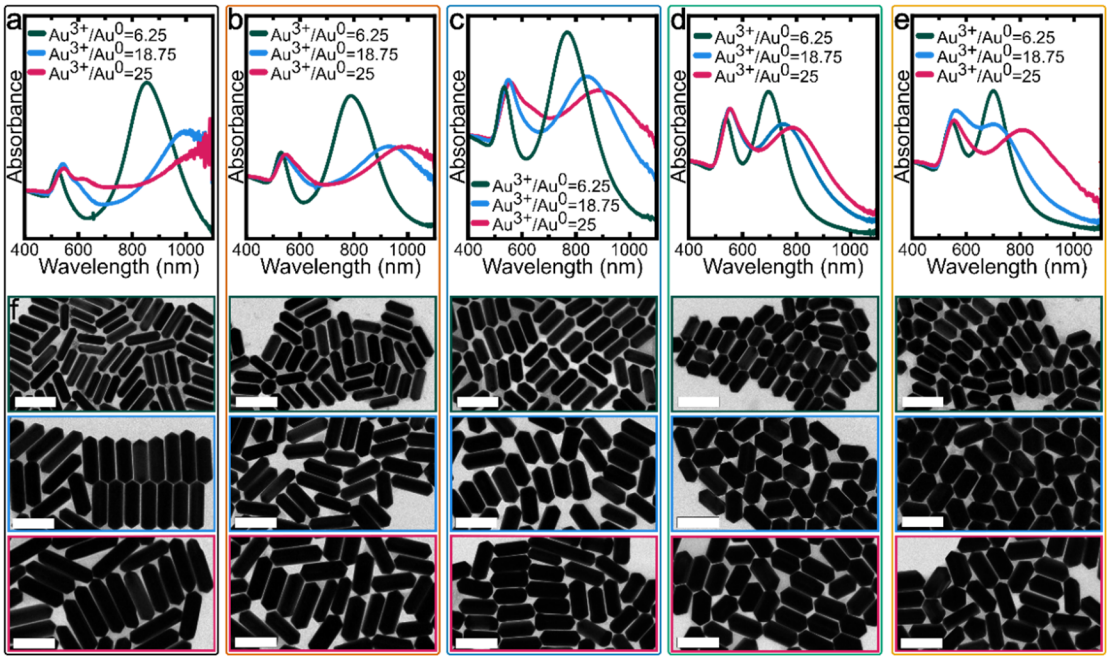

Figure 3. Study of the effect of Au^{3+}/Au^0 at different [CTAB] = 0.5 mM–10 mM. The top row shows UV-vis-NIR spectra for the produced particles using [CTAB] = 0.5 mM (**a**), 1 mM (**b**), 2 mM (**c**), 5 mM (**d**), and 10 mM (**e**). All spectra were normalized at 400 nm. (**f**) TEM micrographs are shown for the particles prepared using Au^{3+}/Au^0 ratios of 6.25 (**upper row**), 18.75 (**middle row**), and 25 (**bottom row**), for every CTAB concentration. All scale bars are 200 nm.

Finally, we aimed to demonstrate the general application of CTAB concentration as a versatile parameter for modulation of growth kinetics and dimensions of PT-AuNRs. Therefore, we investigated the effect of CTAB concentration on a previously reported low-temperature synthesis protocol, using small decahedral seeds (see Section 2) [24]. The reported protocol was previously optimized for a mixture of 2 mM CTAB and 100 mM CTAC. To show the versatility of the CTAB modification method, we simply varied CTAB concentration within the same protocol, carrying out the reaction at 8 °C. The results obtained for PT-AuNRs prepared in the presence of 4 mM, 6 mM, and 8 mM CTAB are summarized in Figure 4. UV-vis-NIR spectra showed the expected blue shift of the longitudinal LSPR band while increasing CTAB concentration, from 958 to 867, and finally 831 nm, for 4, 6, and 8 mM, respectively. Accordingly, TEM characterization of the resulting nanorods revealed a gradually smaller aspect ratio, arising from the following dimensions, 134 ± 10 nm × 28 ± 1 nm (AR 4.8 ± 0.4) for 4 mM CTAB, 122 ± 9 nm × 31 ± 1 nm (AR 3.8 ± 0.4) for 6 mM CTAB, and 114 ± 8 nm × 32 ± 2 nm (AR 3.6 ± 0.4) for 8 mM CTAB.

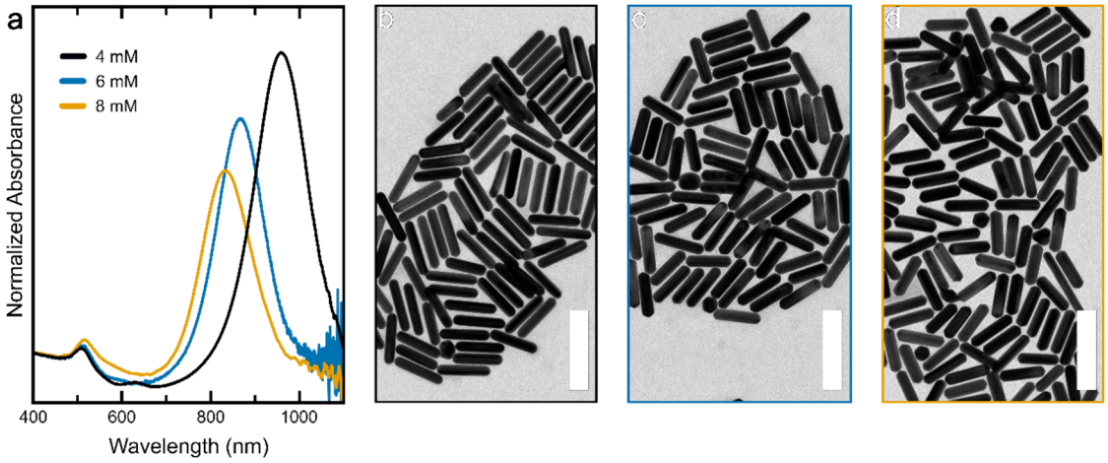

Figure 4. Application of CTAB-induced modulation of PT-AuNR growth from small PT Au seeds [24]. (**a**) Normalized UV-vis-NIR spectra of nanorods prepared using 4 mM, 6 mM, and 8 mM CTAB with $Au^{3+}/Au^{0} = 200$. TEM micrographs of the corresponding products for 4 mM (**b**), 6 mM (**c**), and 8 mM (**d**) CTAB. Spectra are normalized at 400 nm; scale bars are 200 nm.

4. Conclusions

The ratio between bromide and chloride counter-ions can be used to modulate the shape-directing effect of quaternary ammonium surfactants. By using a combination of CTAC and CTAB, the overgrowth of pre-formed PT-AuNRs can be tuned for the preparation of larger nanorods (up to several hundred nm), while maintaining the high monodispersity of the initial nanorod seeds. When increasing CTAB concentration, we consistently achieved a decrease in the aspect ratio of the resulting PT-AuNRs, while maintaining the same average volume per particle. The obtained nanorods featured well-defined pointy tips and lateral facets, maintaining the original pentagonal cross section. These morphological features are attributed to slower gold reduction kinetics due to the stronger surface binding of CTA^{+} and Br^{-}. We additionally found that more extensive overgrowth, achieved by increasing the Au^{3+}/Au^{0} ratio, leads to particles with similar aspect ratios, suggesting a dominating influence of CTAB concentration. Lastly, we demonstrated that this approach can also be applied to other synthetic methods, such as the direct growth of PT-AuNRs from decahedral seeds, thus allowing a fine tuning of AuNR aspect ratio.

Supplementary Materials: The following supporting information can be downloaded at: https://media.sciltp.com/articles/others/2511041613079794/MI-25090103-Supplementary-Materials.pdf.

Author Contributions: F.B.: data curation, visualization, investigation, writing—original draft preparation; L.M.L.-M.: conceptualization, supervision, validation, writing—reviewing and editing. All authors have read and agreed to the published version of the manuscript.

Funding: This work was supported by KU Leuven internal funds (C14/22/085) and by the European Research Council (ERC Synergy Grant no. 101166855, Chiral-Pro). The authors thank Dr. Gail A. Vinnacombe-Willson for her contributions to the organization and editing of the manuscript.

Institutional Review Board Statement: Not applicable.

Data Availability Statement: The data that support the findings of this study are available from the corresponding author upon reasonable request.

Conflicts of Interest: The authors declare no conflict of interest.

Use of AI and AI-assisted Technologies: No AI tools were utilized for this paper.

References

1. Jana, N.R.; Gearheart, L.; Murphy, C.J. Seed-Mediated Growth Approach for Shape-Controlled Synthesis of Spheroidal and Rod-like Gold Nanoparticles Using a Surfactant Template. *Adv. Mater.* **2001**, *13*, 1389–1393.
2. Nikoobakht, B.; El-Sayed, M.A. Preparation and Growth Mechanism of Gold Nanorods (NRs) Using Seed-Mediated Growth Method. *Chem. Mater.* **2003**, *15*, 1957–1962.
3. Scarabelli, L.; Sánchez-Iglesias, A.; Pérez-Juste, J.; Liz-Marzán, L.M. "Tips and Tricks" Practical Guide to the Synthesis of Gold Nanorods. *J. Phys. Chem. Lett.* **2015**, *6*, 4270–4279.
4. Sánchez-Iglesias, A.; Winckelmans, N.; Bals, S.; Grzelczak, M.; Liz-Marzán, L.M. High Yield Seeded Growth of Monodisperse Pentatwinned Gold Nanoparticles Through Thermally-Induced Seed Twinning. *J. Am. Chem. Soc.* **2017**, *139*, 107–110.

5. González-Rubio, G.; Kumar, V.; Llombart, P.; Díaz-Núñez, P.; Bladt, E.; Altantzis, T.; Bals, S.; Peña-Rodríguez, O.; Noya, E.G.; MacDowell, L.G.; et al. Disconnecting Symmetry Breaking from Seeded Growth for the Reproducible Synthesis of High Quality Gold Nanorods. *ACS Nano* **2019**, *13*, 4424–4435.
6. Huang, X.; El-Sayed, I.H.; El-Sayed, M.A. In *Cancer Nanotechnology*; Humana Press: Totowa, NJ, USA, 2010; pp. 343–357.
7. Langer, J.; De Aberasturi, D.J.; Aizpurua, J.; Alvarez-Puebla, R.A.; Auguié, B.; Baumberg, J.J.; Bazan, G.C.; Bell, S.E.J.; Boisen, A.; Brolo, A.G.; et al. Present and Future of Surface-Enhanced Raman Scattering. *ACS Nano* **2020**, *14*, 28–117.
8. Troncoso-Afonso, L.; Vinnacombe-Willson, G.A.; García-Astrain, C.; Liz-Márzan, L.M. SERS in 3D Cell Models: A Powerful Tool in Cancer Research. *Chem. Soc. Rev.* **2024**, *53*, 5118–5148.
9. Canbek, Z.C.; Cortes-Huerto, R.; Testard, F.; Spalla, O.; Moldovan, S.; Ersen, O.; Wisnet, A.; Wang, G.; Goniakowski, J.; Noguera, C.; et al. Twinned Gold Nanoparticles under Growth: Bipyramids Shape Controlled by Environment. *Cryst. Growth Des.* **2015**, *15*, 3637–3644.
10. Hanske, C.; González-Rubio, G.; Hamon, C.; Formentín, P.; Modin, E.; Chuvilin, A.; Guerrero-Martínez, A.; Marsal, L.F.; Liz-Marzán, L.M. Large-Scale Plasmonic Pyramidal Supercrystals via Templated Self-Assembly of Monodisperse Gold Nanospheres. *J. Phys. Chem. C* **2017**, *121*, 10899–10906.
11. González-Rubio, G.; Scarabelli, L.; Guerrero-Martínez, A.; Liz-Marzán, L.M. Surfactant-Assisted Symmetry Breaking in Colloidal Gold Nanocrystal Growth. *ChemNanoMat* **2020**, *6*, 698–707.
12. Jana, N.R.; Gearheart, L.; Murphy, C.J. Wet Chemical Synthesis of High Aspect Ratio Cylindrical Gold Nanorods. *J. Phys. Chem. B* **2001**, *105*, 4065–4067.
13. Chang, H.-H.; Murphy, C.J. Mini Gold Nanorods with Tunable Plasmonic Peaks beyond 1000 Nm. *Chem. Mater.* **2018**, *30*, 1427–1435.
14. González-Rubio, G.; Llombart, P.; Zhou, J.; Geiss, H.; Peña-Rodríguez, O.; Gai, H.; Ni, B.; Rosenberg, R.; Cölfen, H. Revisiting the Role of Seed Size for the Synthesis of Highly Uniform Sub-10 nm Length Gold Nanorods. *Chem. Mater.* **2024**, *36*, 1982–1997.
15. Harper-Harris, J.; Kant, K.; Singh, G. Oleic Acid-Assisted Synthesis of Tunable High-Aspect-Ratio Multiply-Twinned Gold Nanorods for Bioimaging. *ACS Appl. Nano Mater.* **2021**, *4*, 3325–3330.
16. Wu, H.-Y.; Chu, H.-C.; Kuo, T.-J.; Kuo, C.-L.; Huang, M.H. Seed-Mediated Synthesis of High Aspect Ratio Gold Nanorods with Nitric Acid. *Chem. Mater.* **2005**, *17*, 6447–6451.
17. Almora-Barrios, N.; Novell-Leruth, G.; Whiting, P.; Liz-Marzán, L.M.; López, N. Theoretical Description of the Role of Halides, Silver, and Surfactants on the Structure of Gold Nanorods. *Nano Lett.* **2014**, *14*, 871–875.
18. Meena, S.K.; Sulpizi, M. Understanding the Microscopic Origin of Gold Nanoparticle Anisotropic Growth from Molecular Dynamics Simulations. *Langmuir* **2013**, *29*, 14954–14961.
19. Gómez-Graña, S.; Hubert, F.; Testard, F.; Guerrero-Martínez, A.; Grillo, I.; Liz-Marzán, L.M.; Spalla, O. Surfactant (Bi)Layers on Gold Nanorods. *Langmuir* **2012**, *28*, 1453–1459.
20. Zech, T.; Schmutzler, T.; Noll, D.M.; Appavou, M.-S.; Unruh, T. Effect of Bromide on the Surfactant Stabilization Layer Density of Gold Nanorods. *Langmuir* **2022**, *38*, 2227–2237.
21. Mosquera, J.; Wang, D.; Bals, S.; Liz-Marzán, L.M. Surfactant Layers on Gold Nanorods. *Acc. Chem. Res.* **2023**, *56*, 1204–1212.
22. González-Rubio, G.; Díaz-Núñez, P.; Rivera, A.; Prada, A.; Tardajos, G.; González-Izquierdo, J.; Bañares, L.; Llombart, P.; Macdowell, L.G.; Palafox, M.A.; et al. Femtosecond Laser Reshaping Yields Gold Nanorods with Ultranarrow Surface Plasmon Resonances. *Science* **2017**, *358*, 640–644.
23. Meena, S.K.; Celiksoy, S.; Schäfer, P.; Henkel, A.; Sönnichsen, C.; Sulpizi, M. The Role of Halide Ions in the Anisotropic Growth of Gold Nanoparticles: A Microscopic, Atomistic Perspective. *Phys. Chem. Chem. Phys.* **2016**, *18*, 13246–13254.
24. Sánchez-Iglesias, A.; Jenkinson, K.; Bals, S.; Liz-Marzán, L.M. Kinetic Regulation of the Synthesis of Pentatwinned Gold Nanorods below Room Temperature. *J. Phys. Chem. C* **2021**, *125*, 23937–23944.
25. Bevilacqua, F.; Girod, R.; Martín, V.F.; Obelleiro-Liz, M.; Vinnacombe-Willson, G.A.; Van Gordon, K.; Hofkens, J.; Taboada, J.M.; Bals, S.; Liz-Marzán, L.M. Additive-Free Synthesis of (Chiral) Gold Bipyramids from Pentatwinned Nanorods. *ACS Mater. Lett.* **2024**, *6*, 5163–5169.
26. Pérez-Juste, J.; Pastoriza-Santos, I.; Liz-Marzán, L.M.; Mulvaney, P. Gold Nanorods: Synthesis, Characterization and Applications. *Coord. Chem. Rev.* **2005**, *249*, 1870–1901.
27. Yu, R.; Liz-Marzán, L.M.; De Abajo, F.J.G. Universal Analytical Modeling of Plasmonic Nanoparticles. *Chem. Soc. Rev.* **2017**, *46*, 6710–6724.
28. Rangel, T.; Kecik, D.; Trevisanutto, P.E.; Rignanese, G.-M.; Van Swygenhoven, H.; Olevano, V. Band Structure of Gold from Many-Body Perturbation Theory. *Phys. Rev. B* **2012**, *86*, 125125.
29. Hendel, T.; Wuithschick, M.; Kettemann, F.; Birnbaum, A.; Rademann, K.; Polte, J. In Situ Determination of Colloidal Gold Concentrations with UV–Vis Spectroscopy: Limitations and Perspectives. *Anal. Chem.* **2014**, *86*, 11115–11124.

Article

Trimetallic Pd@Pt_xAu_{1-x} Core-Shell Nanocubes with Enhanced Selectivity toward H_2O_2 for the Oxygen Reduction Reaction

Zhiqi Wang [1], Kei Kwan Li [1], Yong Ding [2], and Younan Xia [1,3,*]

[1] School of Chemistry and Biochemistry, Georgia Institute of Technology, Atlanta, GA 30332, USA
[2] School of Materials Science and Engineering, Georgia Institute of Technology, Atlanta, GA 30332, USA
[3] The Wallace H. Coulter Department of Biomedical Engineering, Georgia Institute of Technology and Emory University, Atlanta, GA 30332, USA
* Correspondence: younan.xia@bme.gatech.edu

Received: 10 October 2025; Revised: 30 October 2025; Accepted: 7 November 2025; Published: 13 November 2025

Abstract: We report a versatile method based on seed-mediated growth for the facile synthesis of trimetallic Pd@Pt_xAu_{1-x} core-shell nanocubes. By simply varying the feeding ratio between the Pt(II) and Au(III) precursors, the atomic ratio of Pt to Au in the shell and thereby the ensemble state of Pt atoms on the surface can be tuned to control the binding configuration of O_2 molecules. Specifically, discrete Pt atoms on the surface promote the adsorption of O_2 molecules in the Pauling configuration to enhance the catalytic selectivity of the nanoparticles toward H_2O_2 via the two-electron oxygen reduction reaction, with the Pd@$Pt_{0.025}Au_{0.975}$ nanocubes showing selectivity as high as 91% at 0.45 V_{RHE}. This work offers a viable means to augment the electrocatalytic performance of alloy nanocrystals by controlling their surface compositions.

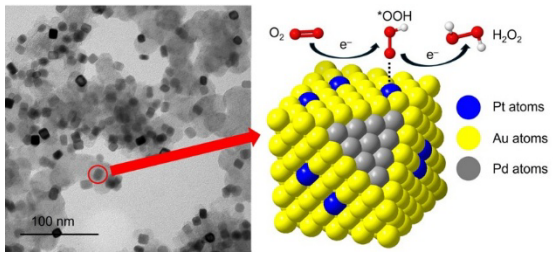

Keywords: alloy nanocrystals; core-shell nanocubes; H_2O_2 selectivity; oxygen reduction reaction; seed-mediated growth

1. Introduction

Electrochemical production of industrially valuable chemicals offers a viable way to fight the ever-increasing global climate crisis [1]. To this end, electrochemical synthesis of hydrogen peroxide (H_2O_2), a reagent widely used in healthcare, chemical synthesis, and paper bleaching sectors [2], has received great interest in recent years due to its reduced production of wastes and potentially lower cost than the commercial anthraquinone oxidation process [3]. Specifically, the oxygen reduction reaction (ORR) offers a promising route to the electrochemical production of H_2O_2. The success of this process critically depends on the availability of an electrocatalyst with high selectivity toward H_2O_2 because of the two competing pathways that involve two and four electrons ($2e^-$ vs. $4e^-$), respectively, to produce H_2O_2 and H_2O [3–5].

Various types of electrocatalysts have been explored to achieve $2e^-$ ORR [6–8], among which Pt- and Pd-based nanocrystals have proven to be the most successful candidates as they exhibit high activity toward ORR. In a prior study, our group developed a synthesis of bimetallic Pd@Pd_xAu_{1-x} core-shell nanocubes and demonstrated variation of Pd to Au ratio as an effective way to enhance selectivity toward $2e^-$ ORR [9]. In the present work, we seek to replace the Pd with Pt because the latter is known to have a higher activity toward ORR and has found commercial use in proton-exchange membrane fuel cells (PEMFCs) [10]. Similar to Pd, an extended surface made of Pt has a low selectivity toward $2e^-$ ORR [11], primarily due to the involvement of unfavorable intermediates. Specifically, the binding configuration of O_2 molecule has a direct impact on the type of intermediate and thus the ORR pathway. During ORR, O_2 molecules is expected to adsorb onto the metal surface to form *OOH (which then transforms to H_2O_2) or undergo O-O cleavage to generate *O. Typically, the adsorption of O_2 on a surface can take three different configurations: Pauling type (end-on coordination to one metal atom), Griffith type (side-on

Copyright: © 2025 by the authors. This is an open access article under the terms and conditions of the Creative Commons Attribution (CC BY) license (https://creativecommons.org/licenses/by/4.0/).
Publisher's Note: Scilight stays neutral with regard to jurisdictional claims in published maps and institutional affiliations.

coordination to one metal atom), and Yeager type (side-on bridge coordination to two adjacent metal atoms) [12]. Theoretical calculations suggest that the formation of *O species is thermodynamically favored on Pt{100} facets involving an array of touching Pt atoms [13,14]. As a result, it is critical to maintain Pt as discrete atoms on the surface to prevent the formation of *O species and thus augment the selectivity toward H_2O_2. To this end, coating the surface of a Pt catalyst with amorphous carbon was explored to limit the formation of large Pt ensembles and thus promote the Pauling type adsorption, enhancing the selectivity toward H_2O_2 [15]. Alloying Pt with another host metal has also proven to be effective in generating isolated Pt atoms on the surface [16]. In this approach, Siahrostami et al. have evaluated the performance of over 30 Pt-based alloys toward $2e^-$ ORR using density functional theory (DFT) calculation and identified $PtHg_4$ as a promising candidate [13]. However, the high toxicity of Hg limits the large-scale use of such catalysts. Alternatively, Brimaud et al. reported that the use of a Au-rich surface could shift the catalytic properties of Pt and thus increase its tendency toward H_2O_2 formation when tested with a model monolayer system [17]. Our previous work also demonstrated that co-deposition of Pd and Au atoms at different atomic ratios offered an effective means to improve the dispersity of Pd atoms on the surface and thus boost the selectivity toward $2e^-$ ORR [9].

Herein, we report the synthesis and characterizations of trimetallic $Pd@Pt_xAu_{1-x}$ core-shell nanocubes with high selectivity toward H_2O_2 by controlling the ensemble state of Pt atoms on the surface. We synthesized Pd nanocubes by reducing Na_2PdCl_4 in an aqueous solution, followed by co-titration of an aqueous mixture of K_2PtCl_4 and $HAuCl_4$ to simultaneously deposit Pt and Au on the Pd seeds. The feeding ratio between the Pt(II) and Au(III) precursors can be conveniently varied to control the ensemble state of Pt atoms on the surface. For convenience, the products are denoted by the feeding molar ratio between the Pt(II) and Au(III) precursors. For example, the $Pd@Pt_{0.025}Au_{0.975}$ sample indicates that the molar ratio of Pt(II) to Au(III) precursors is set to 0.025:0.975 during the synthesis. Our results indicate that the $Pd@Pt_{0.025}Au_{0.975}$ nanocubes have high (over 75%) selectivity toward H_2O_2 in the potential range of 0.05–0.45 V_{RHE}, much augmented than the commercial Pt/C catalyst.

2. Materials and Methods

2.1. Chemicals and Materials

Sodium tetrachloropalladate (Na_2PdCl_4), potassium tetrachloro-platinate(II) (K_2PtCl_4), gold(III) chloride trihydrate ($HAuCl_4 \cdot 3H_2O$), L-ascorbic acid (AA), poly(vinyl pyrrolidone) (PVP, MW ≈ 55,000) and potassium bromide (KBr) were all obtained from Sigma-Aldrich (St. Louis, MO, USA) and used as received. Deionized (DI) water with a resistivity of 18.2 MΩ·cm at room temperature was used for all the experiments.

2.2. Synthesis of the 10-nm Pd Nanocubes Serving as Seeds

The nanocubes were synthesized according to our previously published protocol [18]. In a typical process, 105 mg of PVP (MW ≈ 55,000), 60 mg of AA, and 300 mg of KBr were dissolved in 8 mL of water, preheated at 80 °C for 30 min, and 3 mL of aqueous Na_2PdCl_4 (19 $mg \cdot mL^{-1}$) was added in one shot. The reaction was allowed to proceed for 3 h. The solid products were collected by centrifugation, washed twice with ethanol and once with water, and then dispersed in water for further use.

2.3. Synthesis of $Pd@Pt_xAu_{1-x}$ Core-Shell Nanocubes

In a standard protocol, 66.5 mg of PVP (MW ≈ 55,000), 30 mg of AA and 19 mg of KBr were dissolved in 2.8 mL of water, and 0.3 mL of 10-nm Pd nanocubes was added as the seeds (1.34 $mg \cdot mL^{-1}$ as determined using ICP-MS). The mixture was preheated at 95 °C for 30 min. Different volumes of aqueous $HAuCl_4$ (40 mM) and aqueous K_2PtCl_4 (6.09 mM) were mixed in 10 mL of water. The specific volumes are 19 μL of aqueous $HAuCl_4$ for Pd@Au core-shell nanocubes, 18.52 μL of aqueous $HAuCl_4$ solution and 3.1 μL of aqueous K_2PtCl_4 for $Pd@Pt_{0.025}Au_{0.975}$, 18.05 μL of aqueous $HAuCl_4$ and 6.2 μL of aqueous K_2PtCl_4 for $Pd@Pt_{0.05}Au_{0.95}$, and 17 μL of aqueous $HAuCl_4$ and 12.4 μL of aqueous K_2PtCl_4 for $Pd@Pt_{0.1}Au_{0.9}$. For the synthesis of each sample, 4 mL of the mixture was injected into the reaction solution at a rate of 1 $mL \cdot h^{-1}$, and the reaction was allowed for another 10 min after the injection. The solid products were collected by centrifugation, washed twice with ethanol and once with water, and then dispersed in water for further use.

2.4. Characterizations

Transmission electron microscopy (TEM) images were taken using a Hitachi HT7700 microscope (Hitachi High-Technologies Corporation, Tokyo, Japan) operated at 120 kV. The elemental compositions of the samples

were determined using an inductively-coupled plasma mass spectrometer (ICP-MS, NexION 300 Q, PerkinElmer, Waltham, MA, USA). X-ray photoelectron spectroscopy (XPS) analyses were conducted using Thermo K-Alpha (Thermo Fisher Scientific, Waltham, MA, USA). Scanning transmission electron microscopy (STEM) images and energy- dispersive X-ray (EDX) spectroscopy data were acquired on a transmission electron microscope (FEI Tecnai F30 (FEI Company, Hillsboro, OR, USA; now part of Thermo Fisher Scientific)) equipped with a EDX detector. The high-angle annular dark-field scanning transmission electron microscopy (HAADF-STEM) images were captured using Hitachi HD 2700 (Hitachi High-Technologies Corporation, Tokyo, Japan) at an acceleration voltage of 200 kV. The samples for TEM analysis were prepared by drop casting the dispersions of nanoparticles on carbon-coated Cu grids, followed by drying under ambient conditions.

2.5. Preparation of a Working Electrode

The catalyst ink was prepared by mixing the as-prepared nanocrystals and carbon black (VXC72R, Cabot Corporation (Boston, MA, USA)) in ethanol under ultrasonication in an ice bath for 3 h. The carbon-supported catalyst was collected by centrifugation, and 1 mg of the catalyst was re-dispersed in 1 mL of water and isopropanol mixture (VH_2O/VIPA = 4/1) containing 10 μL Nafion (5% solution, Sigma-Aldrich). The metal contents in the ink were determined using ICP-MS. To benchmark the performance of Pd@Pt_xAu_{1-x}, a commercial Pt/C catalyst was used as the reference (3.2-nm Pt particles supported on Vulcan XC72, Premetek Co. (Cherry Hill, NJ, USA), with a Pt loading of 20 wt. %). The ink was prepared by mixing 2 mg of Pt/C, 1 mL of water, 1 mL of isopropanol, and 10 μL of Nafion under ultrasonication for 30 min. The working electrode was prepared by polishing with 0.3-μm Al_2O_3 slurry, washed with ethanol and water, and then polished by 0.05-μm Al_2O_3 slurry, followed by washing with ethanol and water. A proper amount of the suspension (10 μL) was deposited on a pre-cleaned glassy carbon rotating ring-disk electrode (RRDE, Pine Research Instrumentation (Durham, NC, USA)) with a geometric area of 0.237 cm^2 and then dried in air to give a total metal loading of around 2 μg.

2.6. Electrochemical Measurements

The electrochemical measurements were performed in a standard three-electrode cell using a WaveDriver 200 EIS Biopotentiostat electrochemical workstation. A standard size single junction Ag/AgCl reference electrode (+199 mV vs. NHE, PINE Research) and a Pt wire in a fritted isolation tube served as reference and counter electrodes. An aqueous $HClO_4$ solution (Baker) with a concentration of 0.1 M was used as an electrolyte. The catalyst was pre-cleaned by cycling between 0.05–1.20 V_{RHE} at a sweeping rate of 100 mV/s for 20 times. The cyclic voltammetry (CV) curve was then measured in an Ar-saturated electrolyte solution in the potential range of 0.05–1.00 V_{RHE} at a scan rate of 50 mV/s. The polarization curve was measured by the disk electrode for reducing oxygen and the ring electrode for oxidizing the hydrogen peroxide produced on the disk electrode. The linear sweep voltammetry (LSV) curve was measured at room temperature in the potential range of 0.05–1.00 V_{RHE} in an O_2-saturated electrolyte solution at 10 mV/s and a rotating speed of 1600 rpm. The collection efficiency (N) was 25.6% and the ring current was kept constant at 1.20 V_{RHE} to oxidize the hydrogen peroxide. The accelerated durability test (ADT) was performed by cyclic voltammetry in the potential range of 0.05–1.00 V_{RHE} in an O_2-saturated 0.1 M $HClO_4$ solution for 1000 cycles.

The H_2O_2 yield and electron transfer number for all samples were calculated using the following equations:

$$n = 4\, I_D/(I_D + I_R/N), \quad (1)$$

$$H_2O_2 \text{ Selectivity} = 200 \times 2\, I_R/[N \times (I_D + I_R/N)], \quad (2)$$

where I_R is the ring current, I_D is the disk current, N is the electron collection efficiency (25.6%), and n is the electron transfer number.

3. Results and Discussion

We began with the synthesis of Pd cubic seeds enclosed by {100} facets by reducing Na_2PdCl_4 in an aqueous solution at 80 °C, with ascorbic acid (AA) serving as a reductant [18]. Poly(vinyl pyrrolidone) (PVP) was also added as a colloidal stabilizer to prevent the nanocrystals from aggregation, together with the Br^- ions from KBr to selectively cap the {100} facets [19]. The Pd cubic seeds had an average edge length of 9.5 ± 1.5 nm (see Supplementary Materials Figure S1A). A syringe pump was then used to titrate an aqueous $HAuCl_4$ solution into the reaction mixture containing the Pd cubic seeds, AA, PVP, and KBr to generate Pd@Au core-shell nanocubes. As shown in Supplementary Materials Figure S1B, the average edge length of the core-shell nanocubes was increased to 11.8±1.4 nm, corresponding to a Au shell of ca. 1 nm in thickness, or 4–5 atomic layers. Supplementary Materials

Figure S1C shows a typical high-angle annular dark-field scanning transmission electron microscopy (HAADF-STEM) image of the core-shell nanocubes, confirming a shell thickness of about 4 atomic layers. The lattice spacing in the shell was measured to be 0.208 nm, consistent with the lattice spacing, 0.204 nm of (200) planes of face-centered cubic Au.

Incorporation of Pt atoms into the Au shell was achieved by titrating an aqueous mixture of K_2PtCl_4 and $HAuCl_4$ into the growth solution (see Supplementary Materials for details). Since the precursors were added dropwise, the reduction of Pt(II) and Au(III) precursors should undergo a steady state during the deposition process [20]. Therefore, the Pt:Au atomic ratio in each layer of the shell should be similar. Supplementary Materials Figure S2 shows TEM images of the Pd@Pt_xAu_{1-x} nanocubes with different Pt to Au atomic ratios denoted by the feeding molar ratio between the two precursors. Figure 1A shows a transmission electron microscopy (TEM) image of the Pd@$Pt_{0.025}Au_{0.975}$ core-shell nanocubes. Figure 1B shows energy-dispersive X-ray (EDX) spectroscopy line scans of a single nanocube along the red arrow in the inset. The outer region (in yellow color) exhibited stronger Au signals when compared to the inner region (in blue color), indicating that the Au atoms were confined to the shell. The presence of Pt signals confirmed the successful incorporation of Pt. Since only a trace amount of Pt was incorporated into the shell of this sample, the Pt signals were extremely low in intensity.

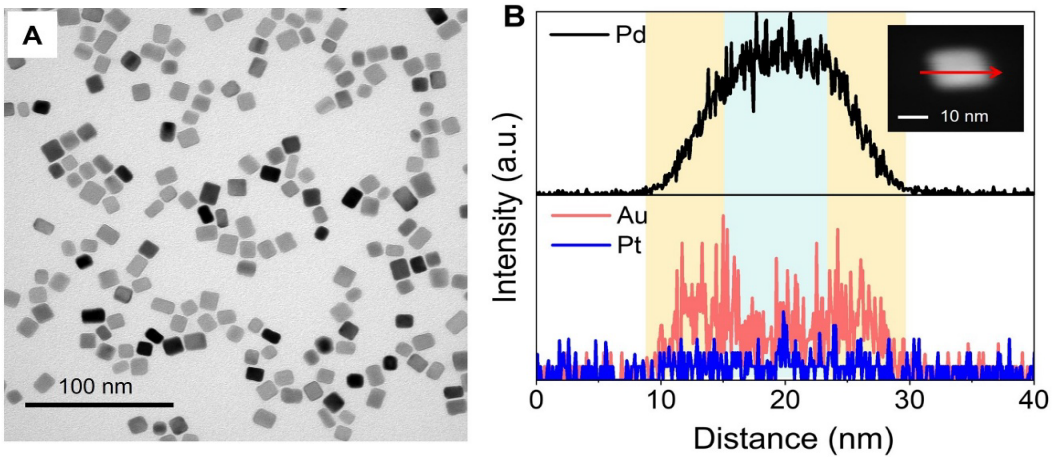

Figure 1. Characterizations of the Pd@$Pt_{0.025}Au_{0.975}$ core-shell nanocubes. (**A**) TEM image of the core-shell nanocubes and (**B**) EDX line scans along the red arrow on a STEM image shown in the inset.

To derive the average percentage of Pt in the shell, we conducted inductively-coupled plasma mass spectroscopy (ICP-MS) analysis of the sample and the data indicated that the Pt to Au atomic ratio in the shell was 0.001:0.999 (Supplementary Materials Table S1). The ICP-MS data also confirmed that with an increase in the feeding ratio between Pt(II) and Au(III) precursors from 0.025:0.975 to 0.1:0.9, the atomic ratio of Pt to Au in the shell also increased from 0.001:0.999 to 0.027:0.973. This trend implies that changing the feeding ratio of the precursors offers an effective means to tune the elemental composition of the shell. The difference between the feeding ratio and the exact atomic ratio determined by ICP-MS can be attributed to the variation in reduction rate between Pt(II) and Au(III) precursors during the synthesis. The X-ray photoelectron spectroscopy (XPS) data also confirmed the presence of Pt (Figure 2A). As expected, all the samples exhibited strong Pd 3d signals, together with Au 4f signals, as shown in Figure 2B,C, respectively. It should be noted that the position of the Au 4f peak was red-shifted due to the electron transfer between Au and Pt, and a detailed explanation will be given in the subsequent section. For the Pt 4f spectra (Figure 2D), the Pd@$Pt_{0.025}Au_{0.975}$ nanocubes did not show obvious Pt signals due to the extremely low amount of Pt in this sample. As the feeding ratio of Pt(II) to Au(III) precursors was increased, the Pt 4f peaks became more pronounced, consistent with the ICP-MS result. Notably, strong Br 3d peaks were observed (red dashed line), which could be attributed to the use of KBr in the synthesis and thus the chemisorption of Br^- ions on the {100} facets.

To prepare electrocatalysts, the core-shell nanocubes were loaded on carbon black by mixing in ethanol under ultrasonication. The particles maintained their cubic shape after ultrasonication, as shown by the TEM images in Supplementary Materials Figure S3B–D. We first obtained cyclic voltammetry (CV) curves of the different catalysts in an Ar-saturated 0.1 M $HClO_4$ solution after 20 cycles. As shown in Figure 3A, we observed the typical hydrogen adsorption/desorption peaks of Pt in the range of 0.10–0.30 V_{RHE}, as well as the negative Pt-O formation and removal peaks in the range of 0.50–0.80 V_{RHE} for all the samples [21]. We then evaluated the electrochemical performance of the different catalysts toward 2e^- ORR by measuring their polarization curves in the range of 0.05–1.00 V_{RHE}

in an O_2-saturated electrolyte solution using a rotation ring-disk electrode (RRDE). In this case, the disk electrode reduced oxygen while the ring electrode oxidized the H_2O_2 just formed on the disk electrode. We benchmarked the selectivity of the catalysts toward H_2O_2 against a commercial Pt/C catalyst. Figure 3B shows the polarization curves of different samples. The theoretical onset potential for $2e^-$ ORR is 0.70 V_{RHE} ($O_2+2H^++2e^- \rightarrow H_2O_2$ $E^\ominus$ = 0.70 V_{RHE}) [17]. For the commercial Pt/C catalyst, the onset potential was 0.94 V_{RHE}, indicating the dominance of the $4e^-$ ORR pathway. Compared to the other samples, the onset potentials of the Pd@$Pt_{0.05}Au_{0.95}$ and Pd@$Pt_{0.025}Au_{0.975}$ nanocubes were 0.60 V_{RHE} and 0.45 V_{RHE}, respectively, indicating the effective suppression of the $4e^-$ ORR pathway by alloying the Pt with Au. As shown by the results in Figure 3B, the catalytic performance of the Pd@Au nanocubes was relatively low compared to other samples containing Pt. This can be attributed to the involvement of different reaction intermediates. For the Pd@Au nanocubes, theoretical calculation has shown that the interaction between the Au{100} facets and O_2 molecules is weak and the rate-determining step (RDS) in ORR is the adsorption of the O_2 molecules [22,23], and the sluggish kinetics for the adsorption of O_2 molecules compromises the catalytic activity. Compared to Au, the interaction between Pt sites and O_2 molecules is much stronger, so the incorporation of Pt into the Au shell promotes the overall activity of ORR.

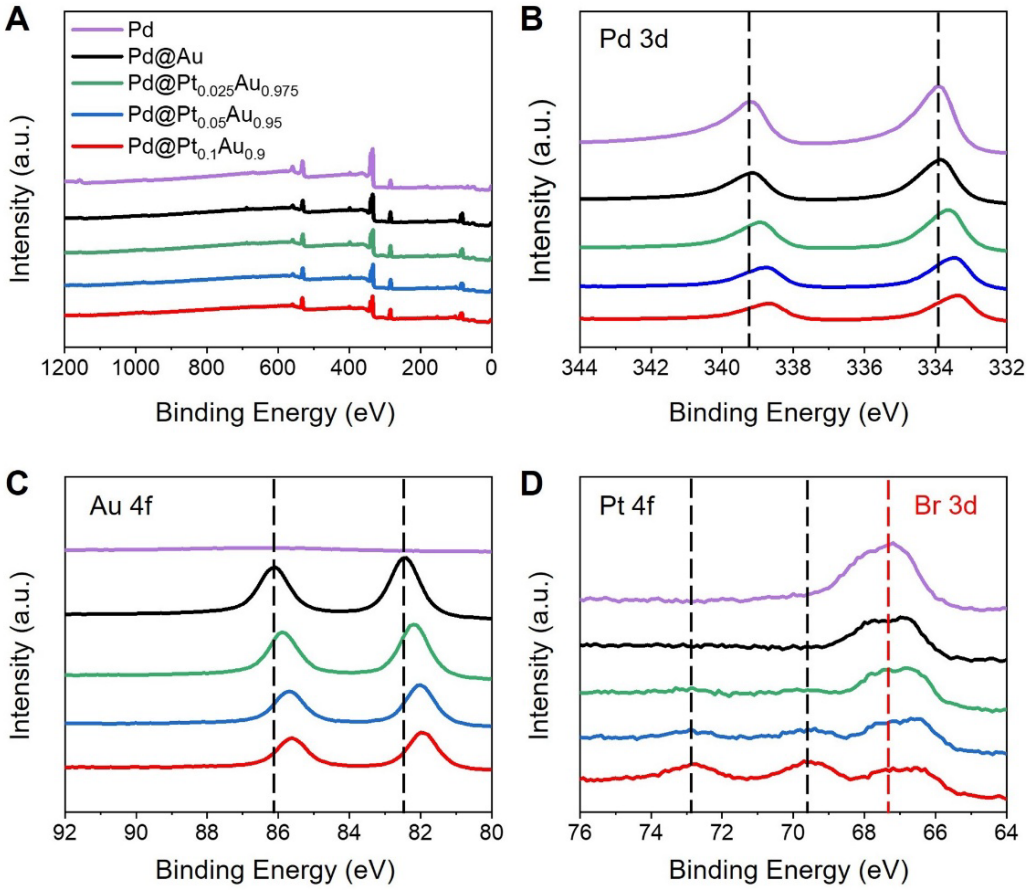

Figure 2. XPS spectra of the Pd cubic seeds and Pd@Pt_xAu_{1-x} core-shell nanocubes. (**A**) Survey spectra; (**B**) spectra of Pd 3d; (**C**) spectra of Au 4f; and (**D**) spectra of Pt 4f. The color scheme in (**A**) applies to all panels.

To further evaluate the catalytic performance, we calculated the selectivity toward H_2O_2 using Equation (1). As shown in Figure 3C, the selectivity toward $2e^-$ ORR for the commercial Pt/C catalyst (purple trace) was below 20%, primarily due to the preferential Yeager type adsorption of O_2 molecules on the surface of an extended Pt surface. In contrast, the selectivity of the Pd@$Pt_{0.1}Au_{0.9}$ nanocubes was increased to ca. 40%. The increase in selectivity relative to Pt/C confirmed that by decreasing the ratio of Pt to Au in the alloy shell, the adsorption mode of O_2 molecules could be switched from the Yeager to the Pauling type, promoting $2e^-$ ORR. Additionally, when the feeding ratio between Pt(II) and Au(III) precursors was reduced from 0.1:0.9 to 0.025:0.975, the selectivity was increased from 40% to 80% in the range of 0.20–0.45 V_{RHE}. Significantly, the selectivity of the Pd@$Pt_{0.025}Au_{0.975}$ nanocubes toward H_2O_2 production could be maintained over 77% in the range of 0.05–0.45 V_{RHE}, together with a maximum value of 91% at 0.45 V_{RHE}. This increase in selectivity could be ascribed to the favorable Pt ensembles state in the alloy shell. In general, the Au atoms in the alloy can lengthen the average Pt-Pt distance, boosting Pauling-type adsorption for the O_2 molecules and thus promoting the selectivity toward H_2O_2.

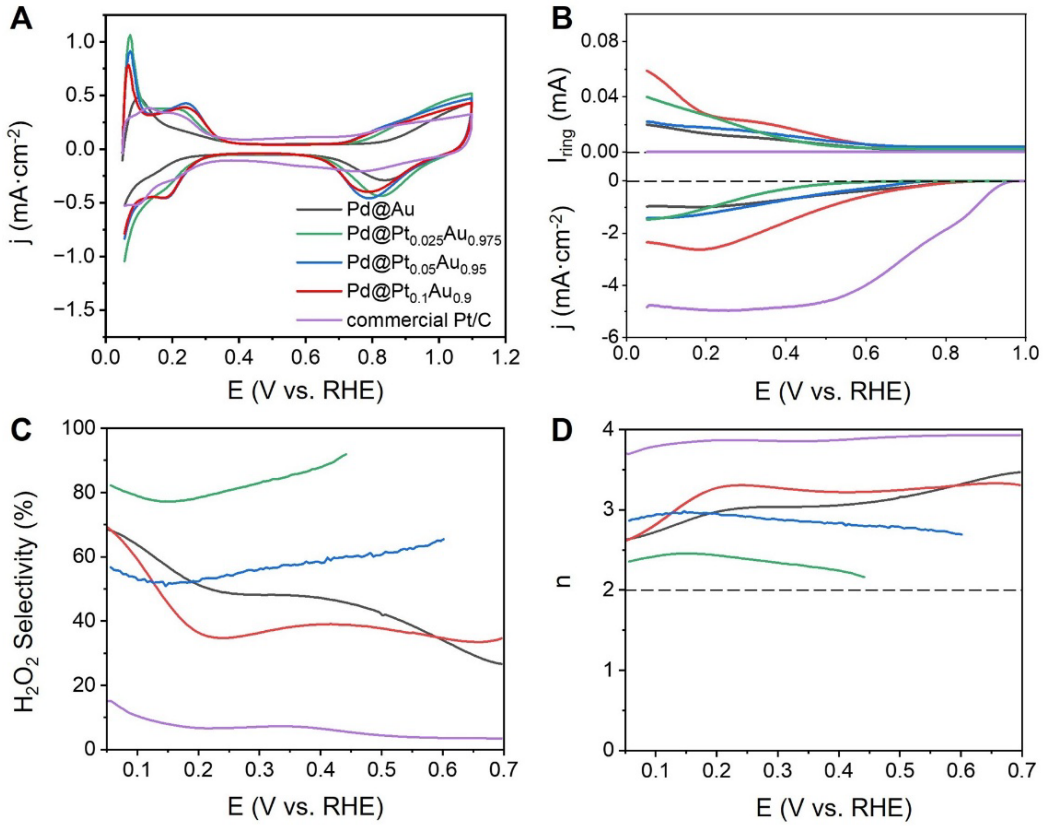

Figure 3. Electrocatalytic measurements of the Pd@Pt_xAu_{1-x} nanocubes and commercial Pt/C catalyst. (**A**) Cyclic voltammograms in an Ar-saturated 0.1 M $HClO_4$ solution; (**B**) polarization curves recorded using RRDE in an O_2-saturated 0.1 M $HClO_4$; (**C**) comparison of H_2O_2 selectivity; and (**D**) comparison of electron transfer number n. The color scheme in (**A**) applies to all panels.

We also calculated the electron transfer number (*n*) during ORR using Equation (2). As shown in Figure 3D, the electron transfer number of the commercial Pt/C catalyst was above 3.5 in the range of 0.05–0.70 V_{RHE}, implying the dominance of the $4e^-$ ORR pathway. In contrast, the value dropped to ca. 3 for Pd@$Pt_{0.05}Au_{0.95}$ and Pd@$Pt_{0.1}Au_{0.9}$ nanocubes, suggesting that there was a mixing in pathway between $2e^-$ and $4e^-$ ORR. For the Pd@$Pt_{0.025}Au_{0.975}$ nanocubes, the electron transfer number was close to 2, indicating the dominance of the $2e^-$ ORR pathway. Overall, the calculated electron transfer numbers were consistent with their selectivity toward H_2O_2.

The catalytic performance was found to be related to the electronic state of elements in the nanocrystals. To further understand the mechanism behind, a detailed analysis of XPS peaks of all the samples is summarized in Table S2. For the Pd@Au nanocubes, the Au 4f spectrum had peaks at 86.1 and 82.4 eV, corresponding to Au 4f5/2 and 4f7/2, respectively. Interestingly, increasing the amount of Pt in the Au shell to $Pt_{0.025}Au_{0.975}$ red-shifted the Au 4f peaks to 85.9 and 82.2 eV, respectively. The red shifts could be ascribed to an increase in electron density for Au. Since Au is more electronegative than Pt (electronegativity: Au/2.54 and Pt/2.28), there was a net charge transfer from Pt atoms to Au atoms. For $2e^-$ ORR, the direct binding between Pt and O_2 molecules was strong, making the desorption of *OOH to form H_2O_2 the rate-determining step. The charge transfer from Pt atoms to Au atoms leads to the decrease of electron density on Pt, thereby weakening the interaction between Pt and intermediate *OOH, as well as reducing the activation energy for the rate-determining step [24–26]. As a result, the $2e^-$ ORR pathway was preferred and hence the augmentation in selectivity toward H_2O_2.

We further evaluated the stability of the Pd@$Pt_{0.025}Au_{0.975}$ nanocubes through an accelerated durability test (ADT) by applying continuous cycling for up to 1000 cycles between 0.05–1.00 V_{RHE} in an O_2-saturated 0.1 M $HClO_4$ solution. Figure 4A,B, shows the selectivity toward H_2O_2 and the electron transfer number of the sample before and after ADT, respectively. After ADT, the selectivity toward H_2O_2 dropped to below 40% while the electron transfer number increased to ca. 4. This result indicates possible changes to surface composition and/or particle shape during the ADT process. Figure 4C,D, shows HAADF-STEM images of the Pd@$Pt_{0.025}Au_{0.975}$ nanocubes after 1000 cycles of ADT. The project profiles of the nanocubes became rounded, implying that their corners and edges were truncated during ADT. Such truncations could be attributed to the potential surface reconstruction of atoms, leading to the formation of Pd-Au-Pt alloy, which was supposed to be thermodynamically

more favorable [27]. This alloying effect would push the Pd atoms to the surface of the particle, promoting the Yeager type adsorption of O_2 molecules and thus compromising the selectivity toward $2e^-$ ORR.

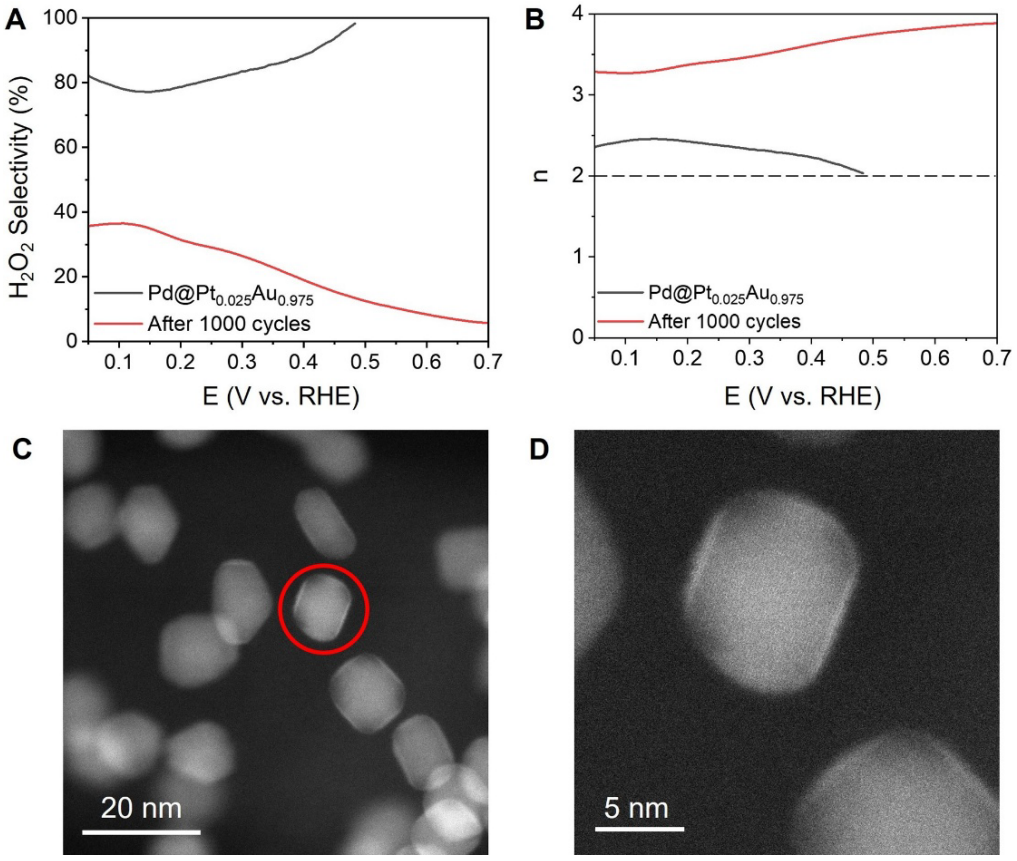

Figure 4. Stability test of the $Pd@Pt_{0.025}Au_{0.975}$ nanocubes. (**A**) Selectivity toward H_2O_2 in an O_2-saturated 0.1 M $HClO_4$ solution before and after 1000 cycles of ADT; (**B**) electron transfer number (n) before and after 1000 cycles of ADT; (**C**) HAADF-STEM image of the $Pd@Pt_{0.025}Au_{0.975}$ nanocubes after 1000 cycles of ADT; (**D**) enlarged image of a single $Pd@Pt_{0.025}Au_{0.975}$ nanocube marked by red circle in (**C**) with truncated corners. The color scheme in (**A**) also applies to panel (**B**).

5. Conclusions

In summary, controlling the ensemble state of Pt atoms in the surface of core-shell nanoparticles has been demonstrated as an effective means to regulate the reaction pathway in ORR and thereby boost the selectivity toward H_2O_2. The control could be readily achieved by changing the feeding ratio between the Pt(II) and Au(III) precursors during the synthesis. The synthesis has proven to be effective in producing a series of $Pd@Pt_xAu_{1-x}$ core-shell nanocubes with different Pt to Au atomic ratios in the shell, and thus different Pt ensemble states on the surface. The electrocatalytic measurements further confirmed that all the samples exhibited high selectivity toward H_2O_2 production in ORR when compared to the commercial Pt/C catalyst. The synthetic approach is potentially extendible to other types of nanomaterials sought for various applications [28–30].

Supplementary Materials: The following supporting information can be downloaded at: https://media.sciltp.com/articles/others/2511131438558612/MI-25100042-Supplementary-Materials-FC-done.pdf. Figure S1: Synthesis of Pd and Pd@Au core-shell nanocubes; Figure S2: Variation of the feeding molar ratio between the Pt and Au precursors. TEM image of $Pd@Pt_xAu_{1-x}$ core-shell nanocubes obtained with the different Pt:Au precursor molar ratio; Figure S3: TEM image of catalyst inks; Table S1: The Pt:Au atomic ratio in $Pd@Pt_xAu_{1-x}$ nanocubes as derived from ICP-MS data; Table S2: Summary of the XPS peak position (unit: eV) of Pd and core-shell nanocubes.

Author Contributions: Y.X.: conceived the concept; Z.W.: conducted experiments on materials preparation, electrochemical measurements and analyzed the data; Y.D.: contributed to materials characterization; K.K.L.: conducted experiments on ICP measurements; Z.W. and K.K.L.: prepared the manuscript and Y.X.: revised the writing. All authors have read and agreed to the published version of the manuscript.

Funding: This work was supported in part by a grant from NSF (DMR-2333595) and start-up funds from the Georgia Institute of Technology.

Data Availability Statement: The dataset generated and/or analyzed during the current study are available from the corresponding author on reasonable request.

Conflicts of Interest: The authors declare no conflict of interest. Given the role as Editor-in-Chief, Younan Xia was not involved in the peer review of this paper and had no access to information regarding its peer-review process. Full responsibility for the editorial process of this paper was delegated to another editor of the journal.

Use of AI and AI-Assisted Technologies: No AI tools were utilized for this paper.

References

1. Luna, P.D.; Hahn, C.; Higgins, D.; Jaffer, S.A.; Jaramillo, T.F.; Sargent, E.H. What would it take for renewably powered electrosynthesis to displace petrochemical processes? *Science* **2019**, *364*, eaav3506.
2. Lewis, R.J.; Hutchings, G.J. Recent advances in the direct synthesis of H_2O_2. *ChemCatChem* **2019**, *11*, 298–308.
3. Siahrostami, S. H_2O_2 electrosynthesis and emerging applications challenges and opportunities: A computational perspective. *Chem Catal.* **2023**, *3*, 100568.
4. Shin, H.; Lee, S.; Sung, Y.-E. Industrial-scale H_2O_2 electrosynthesis in practical electrochemical cell systems. *Curr. Opin. Electrochem.* **2023**, *38*, 101224.
5. Wroblowa, H.S.; Pan, Y.-C.; Razumney, G. Electroreduction of oxygen: A new mechanistic criterion. *J. Electroanal. Chem*. **1976**, *69*, 195–201.
6. Shen, R.; Chen, W.; Peng, Q.; Lu, S.; Zheng, L.; Cao, X.; Wang, Y.; Zhu, W.; Zhang, J.; Zhuang, Z.; et al. High-concentration single atomic Pt sites on hollow CuS_x for selective O_2 reduction to H_2O_2 in acid solution. *Chem* **2019**, *5*, 2099–2110.
7. Zhang, J.; Ma, J.; Choksi, T.S.; Zhou, D.; Han, S.; Liao, Y.-F.; Yang, H.B.; Liu, D.; Zeng, Z.; Liu, W.; et al. Strong metal-support interaction boosts activity, selectivity and stability in electrosynthesis of H_2O_2. *J. Am. Chem. Soc*. **2022**, *144*, 2255–2263.
8. Shen, H.; Janes, A.N.; Ross, R.D.; Kaiman, D.; Huang, J.; Song, B.; Schmidt, J.R.; Jin, S. Stable and selective electrosynthesis of hydrogen peroxide and the electro-Fenton process on $CoSe_2$ polymorph catalysts. *Energy Environ. Sci*. **2020**, *13*, 4189–4203.
9. Zhang, Y.; Lyu, Z.; Chen, Z.; Zhu, S.; Shi, Y.; Chen, R.; Xie, M.; Yao, Y.; Chi, M.; Shao, M.; et al. Maximizing the catalytic performance of $Pd@Au_xPd_{1-x}$ nanocubes in H_2O_2 production by reducing shell thickness to increase compositional stability. *Angew. Chem. Int. Ed*. **2021**, *60*, 19643–19647.
10. Liu, M.; Zhao, Z.; Duan, X.; Huang, Y. Nanoscale structure design for high-performance Pt-based ORR catalysts. *Adv. Mater*. **2019**, *31*, 1802234.
11. Zhang, G.; Wei, Q.; Yang, X.; Tavares, A.C.; Sun, S. RRDE experiments on noble-metal and noble-metal-free catalysts: Impact of loading on the activity and selectivity of oxygen reduction reaction in alkaline solution. *Appl. Catal. B Environ*. **2017**, *206*, 115–126.
12. Gao, J.; Liu, B. Progress of electrochemical hydrogen peroxide synthesis over single atom catalysts. *ACS Mater. Lett*. **2020**, *2*, 1008–1024.
13. Siahrostami, S.; Verdaguer-Casadevall, A.; Karamad, M.; Deiana, D.; Malacrida, P.; Wickman, B.; Escudero-Escribano, M.; Paoli, E.A.; Frydendal, R.; Hansen, T.W.; et al. Enabling direct H_2O_2 production through rational electrocatalyst design. *Nat. Mater*. **2013**, *12*, 1137–1143.
14. Duan, Z.; Wang, G. Comparison of reaction energetics for oxygen reduction reactions on Pt(100), Pt(111), Pt/Ni(100) and Pt/Ni(111) surfaces: A first-principles study. *J. Phys. Chem. C* **2013**, *117*, 6284–6292.
15. Choi, C.H.; Kwon, H.C.; Yook, S.; Shin, H.; Kim, H.; Choi, M. Hydrogen peroxide synthesis via enhanced two-electron oxygen reduction pathway on carbon-coated Pt surface. *J. Phys. Chem. C* **2014**, *118*, 30063–30070.
16. Jiang, K.; Zhao, J.; Wang, H. Catalyst design for electrochemical oxygen reduction toward hydrogen peroxide. *Adv. Funct. Mater*. **2020**, *30*, 2003321.
17. Brimaud, S.; Engstfeld, A.K.; Alves, O.B.; Behm, R. Structure-reactivity correlation in the oxygen reduction reaction: Activity of structurally well-defined Au_xPt_{1-x}/Pt(111) monolayer surface alloys. *J. Electroanal. Chem*. **2014**, *716*, 71–79.
18. Jin, M.; Liu, H.; Zhang, H.; Xie, Z.; Liu, J.; Xia, Y. Synthesis of Pd nanocrystals enclosed by {100} facets and with sizes <10 nm for application in CO oxidation. *Nano Res*. **2011**, *4*, 83–91.
19. Peng, H.-C.; Xie, S.; Park, J.; Xia, X.; Xia, Y. Quantitative analysis of the coverage density of Br^- ions on Pd{100} facets and its role in controlling the shape of Pd nanocrystals. *J. Am. Chem. Soc*. **2013**, *135*, 3780–3783.
20. He, J.; Yu, H.; Xia, Y. Steady-state synthesis of colloidal metal nanocrystals. *Mater. Interfaces* **2025**, *2*, 213–225.
21. Duchesne, P.N.; Li, Z.Y.; Deming, C.P.; Fung, V.; Zhao, X.; Yuan, J.; Regier, T.; Aldalbahi, A.; Almarhoon, Z.; Chen, S.; et al. Golden single-atom-site platinum electrocatalysts. *Nat. Mater*. **2018**, *17*, 1033–1039.

22. Siahrostami, S.; Villegas, S.J.; Mostaghimi, A.H.B.; Back, S.; Farimani, A.B.; Wang, H.; Persson, K.A.; Montoya, J. A review on challenges and successes in atomic-scale design of catalysts for electrochemical synthesis of hydrogen peroxide. *ACS Catal*. **2020**, *10*, 7495–7511.
23. Mei, D.; He, Z.D.; Zheng, Y.L.; Jiang, D.C.; Chen, Y.-X. Mechanistic and kinetic implications on the ORR on a Au(100) electrode: pH, temperature and H-D kinetic isotope effects. *Phys. Chem. Chem. Phys.* **2014**, *16*, 13762–13773.
24. Ma, Z.; Cano, Z.P.; Yu, A.; Chen, Z.; Jiang, G.; Fu, X.; Yang, L.; Wu, T.; Bai, Z.; Lu, J. Enhancing oxygen reduction activity of Pt-based electrocatalysts: From theoretical mechanisms to practical methods. *Angew. Chem. Int. Ed*. **2020**, *59*, 18334–18348.
25. Kulkarni, A.; Siahrostami, S.; Patel, A.; Nørskov, J.K. Understanding catalytic activity trends in the oxygen reduction reaction. *Chem. Rev*. **2018**, *118*, 2302–2312.
26. Nørskov, J.K.; Rossmeisl, J.; Logadottir, A.; Lindqvist, L.; Kitchin, J.R.; Bligaard, T.; Josson, H. Origin of the overpotential for oxygen reduction at a fuel-cell cathode. *J. Phys. Chem. B* **2004**, *108*, 17886–17892.
27. Li, J.; Yin, H.-M.; Li, X.-B.; Okunishi, E.; Shen, Y.-L.; He, J.; Tang, Z.-K.; Wang, W.-X.; Yücelen, E.; Li, C.; et al. Surface evolution of a Pd-Pt-Au electrocatalyst for stable oxygen reduction. *Nat. Energy* **2017**, *2*, 17111–17116.
28. Yu, S.; Yang, H. One the surface composition of molybdenum carbide nanoparticles for electrocatalytic applications. *Mater. Interfaces* **2024**, *1*, 3–12.
29. Sun, W.; Min, B.; Wang, M.; Han, X.; Gao, Q.; Hwang, S.; Zhou, H.; Zhu, H. Catholic corrosion-induced structural evolution of CuNi electrocatalysts for enhanced CO_2 reduction. *Mater. Interfaces* **2024**, *1*, 79–88.
30. Zhou, J.; Shao, S.; Wei, Z.; Xia, X. Silver-platinum hollow nanoparticles for colorimetric lateral flow assay. *Mater. Interfaces* **2024**, *1*, 58–67.

Article

Chemically Interpretable Machine Learning for Predicting HER Activity in Au-Based Alloys

Maja Kubik, Shiqi Wang *, and Pedro H. C. Camargo *

Department of Chemistry, University of Helsinki, A.I. Virtasen aukio 1, FIN-0014 Helsinki, Finland
* Correspondence: shiqi.z.wang@helsinki.fi (S.W.); pedro.camargo@helsinki.fi (P.H.C.C.)
Received: 10 October 2025; Revised: 13 November 2025; Accepted: 17 November 2025; Published: 24 November 2025

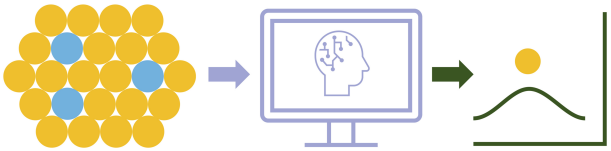

Abstract: Hydrogen evolution reaction (HER) catalysts are essential for renewable hydrogen production, but conventional screening through density functional theory (DFT) remains computationally demanding. Here, we present a proof-of-concept machine learning (ML) framework that predicts hydrogen adsorption energies on Au-based alloys using a curated dataset and nine chemically interpretable descriptors. Tree-based ensemble models achieve quantitative accuracy (mean absolute error ≈ 0.13 eV), sufficient to resolve weak, optimal, and strong adsorption regimes. Feature attribution highlights generalized coordination number and site-specific electronic descriptors as dominant factors, consistent with established chemisorption principles. Guided by these insights, the trained model was applied to a library of Au–M alloys, with targeted DFT validation identifying Au–Mo, Au–W, Au–Ta, Au–Hf, and Au–Tc as promising candidates that couple favorable adsorption with alloy stability. Beyond specific predictions, this work introduces an accessible, reproducible workflow that connects ML predictions to catalytic intuition. The framework serves as a reference for experimental chemists, lowering the barrier for integrating data-driven approaches into catalyst discovery.

Keywords: hydrogen evolution reaction (HER); machine learning in catalysis; Au-based alloys; adsorption energy prediction; interpretable descriptors

1. Introduction

The discovery of efficient catalysts is central to advancing sustainable energy technologies, particularly in the context of green hydrogen production from water electrolysis [1–3]. The hydrogen evolution reaction (HER) plays an important role in this process, as its activity depends sensitively on the adsorption energy of hydrogen intermediates [4,5]. Conventional catalyst discovery has relied on experimental trial-and-error or density functional theory (DFT) calculations, but both approaches are resource-intensive and scale poorly to large chemical spaces [6]. Machine learning (ML) offers a promising alternative by recognizing patterns in large datasets and predicting catalytic descriptors with far lower cost, thereby accelerating the design of new materials [7–10].

Despite this potential, ML has not been widely adopted in experimental catalysis laboratories. A major reason is that many existing studies focus on technical aspects of model development rather than on providing workflows that are accessible to chemists without a background in data science [11,12]. Data representations such as one-hot encodings or high-dimensional fingerprints often lack direct chemical interpretability [13,14]. For example, they encode 'which element' without reflecting chemical similarity or catalytic trends, which can make it difficult for experimentalists to connect model outputs to catalytic principles [15]. In addition, the implementation of ML pipelines typically requires extensive computational expertise, further limiting their uptake by the broader catalysis community [16–18]. These barriers have created a gap between the capabilities of ML and its practical use in guiding experimental catalyst discovery.

In this work, we present an ML workflow for predicting hydrogen adsorption on Au-based alloy surfaces. By combining a publicly available DFT dataset with a set of curated, physically meaningful descriptors, such as generalized coordination number, weighted electronegativity, and site-specific electronic parameter, we demonstrate an interpretable workflow that can be readily understood and reproduced by chemists. Using tree-

Copyright: © 2025 by the authors. This is an open access article under the terms and conditions of the Creative Commons Attribution (CC BY) license (https://creativecommons.org/licenses/by/4.0/).
Publisher's Note: Scilight stays neutral with regard to jurisdictional claims in published maps and institutional affiliations.

based regression models, we achieve reliable prediction accuracy (mean absolute error ~0.13 eV for Au-containing systems) while also providing feature-importance analyses that connect directly to catalytic intuition. The aim of this study is not to introduce a new machine learning methodology, but rather to illustrate how chemists can integrate accessible ML tools into their research. The same descriptor set and ML workflow can be applied to Pt-M and Pd-M alloys once suitable training data are available, making the approach transferable to other HER catalyst families. By presenting a transparent and reproducible workflow, we seek to lower the barrier to entry for ML in catalysis and to provide a reference framework for future studies of HER and beyond.

2. Methodology

2.1. Machine Learning Workflow

Our machine learning framework follows a structured pipeline from dataset curation to catalyst screening (Figure 1). Adsorption data were first extracted and preprocessed, then transformed into chemically interpretable descriptors capturing both geometric and electronic factors that govern hydrogen binding. Tree-based ensemble algorithms were trained on these features, with iterative feedback guiding hyperparameter tuning and feature selection. The optimized model was then applied to screen Au–M alloy candidates, translating predictive insights into experimental guidance. This workflow explicitly links catalytic intuition with data-driven predictions, ensuring that each stage remains transparent and interpretable for chemists.

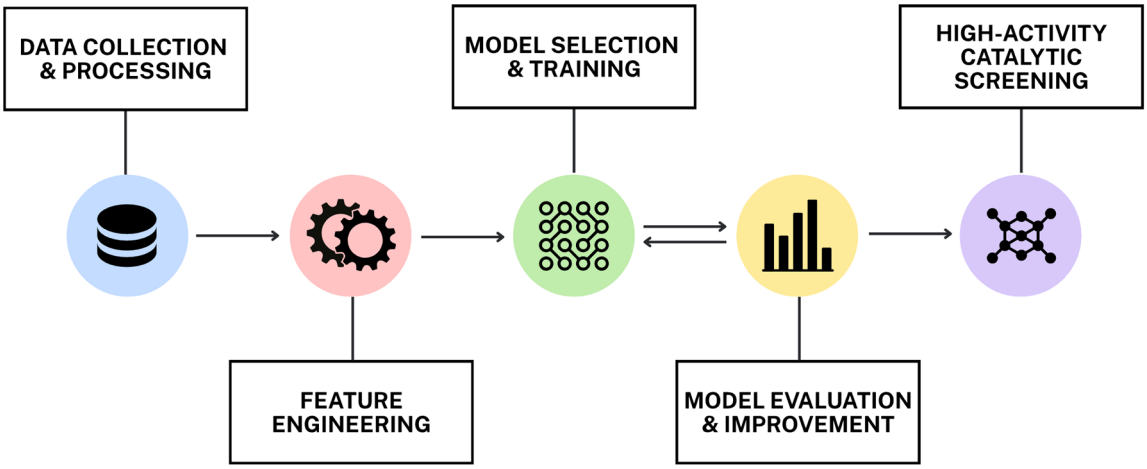

Figure 1. The machine learning workflow begins with data collection and preprocessing, followed by feature engineering to derive chemically interpretable descriptors. Models are then trained and optimized, evaluated for accuracy and interpretability, and finally applied to high-throughput screening of candidate catalytic compositions.

2.2. Data Extraction and Processing

Robust machine learning predictions require reliable and well-curated input data. For this purpose, we employed the dataset of Mamun et al. [19], which reports approximately 90,000 DFT adsorption and reaction energies across 2035 alloy surfaces for diverse adsorbates. Here, the dataset was restricted to dilute hydrogen adsorption, ensuring that the target variable corresponds directly to the HER. Only entries with a single H atom per surface unit cell were retained, while fourfold sites were discarded due to their scarcity and limited relevance under realistic catalytic conditions.

The hydrogen adsorption geometries used for model training were obtained directly from this dataset [19], in which all unique high-symmetry adsorption sites (ontop, bridge, *fcc* hollow, and *hcp* hollow) were systematically enumerated using CatKit. The slab models used in the ML part were obtained directly from the same dataset [19]. Alloy surfaces were constructed as three-layer 2 × 2 *fcc*-based slabs (A1, $L1_2$, $L1_0$), cleaved along the (111) facet for A1/$L1_2$ and the equivalent (101)/(111) facet for $L1_0$. Slabs were generated with CatKit, with the bottom two layers fixed during relaxation and only non-reconstructed surfaces retained. These structures form the basis for the adsorption data used in this study. The optimized slab geometries are publicly available through Catalysis-Hub.org and Materials Cloud.

Feature construction considered only the identity and arrangement of first-layer atoms surrounding the adsorption site. The Mamun dataset often reports multiple rows that differ only in second-layer composition, particularly for bridge motifs. Because hydrogen binding is primarily governed by the first coordination shell

[20,21], these variants were treated as replicate measurements and replaced by their mean adsorption energy. This consolidation reduced label noise and prevented over-representation of near-duplicate records. After filtering and averaging, the HER subset was reduced from 8856 to 6749 unique entries, which formed the foundation for model training and validation. This curated dataset provides a reliable platform for developing compact yet accurate ML models for catalyst discovery.

2.3. Feature Engineering

Our chosen descriptor set of nine features was designed to encode both composition and local structure at the adsorption site. Two descriptors captured the valence electron counts of the constituent elements A (S_A) and B (S_B) [22]. Three geometric descriptors were included: generalized coordination number (GCN, Equation (S1)) [23], surface facet, and volume per atom (Å^3, Equation (S2)) [24]. Three additional descriptors quantified composition-weighted elemental properties: average ionization energy (WIE, Equation (S3)) [25], average electronegativity (WEN, Equation (S4)) [26], and average atomic radius (WAR, Equation (S5)) [27]. The final input was a site-specific electronic descriptor (ψ, Equation (S6)) [28], which integrates local electronegativity with the valence environment of nearest neighbors. All inputs were obtained from the Mamun dataset or from standard elemental property databases. In this design, elemental type and proportion are captured numerically, in contrast to one-hot representations that only indicate the presence or absence of an element [29], providing only categorical identity but no chemical information.

The geometric descriptors establish the structural context for adsorption [30]. GCN provides a continuous measure of local coordination and serves as a compact identifier of adsorption motif [31]. Within the HER subset, which is derived from 3-layer 2 × 2 *fcc*-based slabs including single *fcc* metals (A_1), A_3B *fcc* alloys ($L1_2$, Cu_3Au type), and ordered AB *fcc* alloys ($L1_0$, CuAu type) cleaved along (111) or (101), this mapping yields four characteristic values corresponding to ontop, bridge, and hollow sites (*fcc* and *hcp*). All the geometries of hydrogen adsorption on various models are fully relaxed with the top layer and adsorbate. The facet descriptor, given by the Miller index, accounts for crystallographic orientation, while the atomic volume provides a proxy for bond length trends. Since many alloy compositions in the Mamun dataset are not tabulated in standard repositories, volumes were estimated by Vegard-type mixing of pure elements.

Electronic descriptors capture how alloy composition modulates charge donation and withdrawal at the adsorption site. S_A and S_B summarize shell occupancy near the Fermi level, linking directly to the familiar d-band filling picture. WEN reflects the ability of a site to attract charge, WIE describes how tightly valence electrons are bound, and WAR provides a coarse measure of size that correlates with orbital overlap. The site-specific ψ descriptor combines local electronegativity with valence counts of nearest neighbors, providing a compact representation of the immediate electronic environment and a strong predictor of hydrogen binding energy [32].

Together, our descriptor set provide a minimal yet transparent representation of adsorption environments, built entirely from basic quantities available a priori. They capture both elemental identity and local arrangement without heavy featurization or system-specific metrics, ensuring transferability across compositions, surfaces, and motifs. Importantly, each input can be directly rationalized in terms of chemisorption principles and ensemble effects in alloys, thereby enabling mechanistic interpretation alongside predictive accuracy.

3. Results and Discussion

3.1. Exploratory Data Analysis

After constructing the HER subset and defining the descriptor set, an exploratory data analysis was performed prior to model training. Elemental coverage, adsorption site labels, and the ranges of key descriptors (WAR, WEN, WIE, GCN, and Ψ) were examined to establish baseline expectations for model uncertainty and to guide data partitioning (Table S1). This ensured that subsequent learning was based on a consistently structured dataset.

The elemental distribution is shown in Figure 2A, with Au-containing entries highlighted. Broad coverage across late transition metals is evident, and the Au subset contributes with ~405 entries, sufficient for assessing Au-based systems independently. The distribution of adsorption site types is summarized in Figure 2B, where hollow motifs (*fcc* and *hcp*) dominate, while bridge and ontop sites are comparatively underrepresented. The imbalance suggests higher predictive confidence for hollow sites and motivates the use of site-resolved diagnostics in subsequent model evaluation. A schematic representation of the four characteristic adsorption site types (*fcc*, *hcp*, bridge, and ontop) considered in this study is provided in Figure S1.

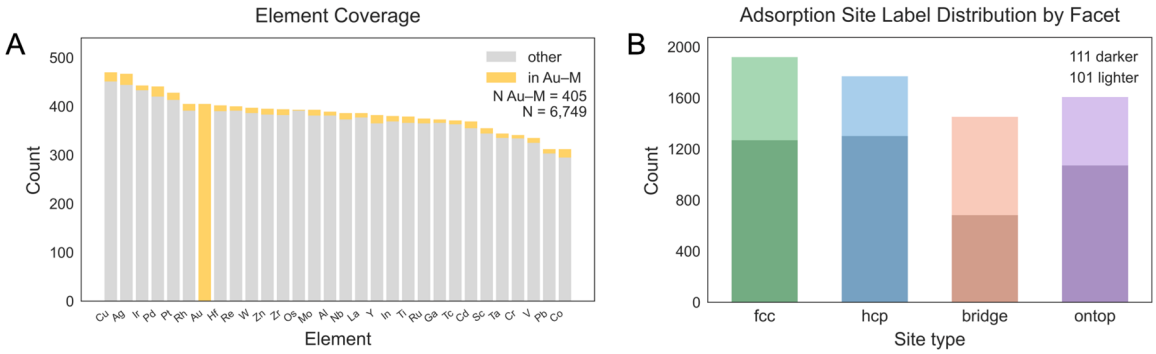

Figure 2. (**A**) Elemental distribution across the dataset [19] with Au-containing entries highlighted in yellow (405 rows). (**B**) Frequency of adsorption motifs (ontop, bridge, *fcc* hollow, and *hcp* hollow), showing dominance of close-packed hollow sites relative to bridge and ontop motifs. These distributions illustrate the chemical diversity of the dataset and the relative scarcity of undercoordinated sites, which might contribute to site-dependent variability in model performance.

Descriptor distributions were further analyzed to confirm that the feature set captures distinct structural and electronic environments. Histograms of the engineered descriptors reveal broad variation across WAR, WEN, WIE, Ψ, and GCN values, reflecting the chemical diversity of the curated dataset (Figure S2). These checks confirmed that the dataset is chemically rich and well balanced for Au systems, while also highlighting motif-dependent sampling biases that influence predictive uncertainty.

The distribution of hydrogen adsorption energies (E_{ads}) in the processed HER subset is shown in Figure 3A. Adsorption values span from approximately −2.0 to +3.0 eV, reflecting the diversity of local atomic environments sampled in the dataset. The histogram is skewed toward negative energies, with a broad maximum near the practical target of −0.24 eV. This skewness arises primarily from relaxation behavior during DFT optimization, where unstable high-energy configurations frequently relax into more stable hollow sites. In addition, the prevalence of threefold hollow motifs on *fcc*-derived surfaces contributes to the overrepresentation of strongly binding configurations in the dataset.

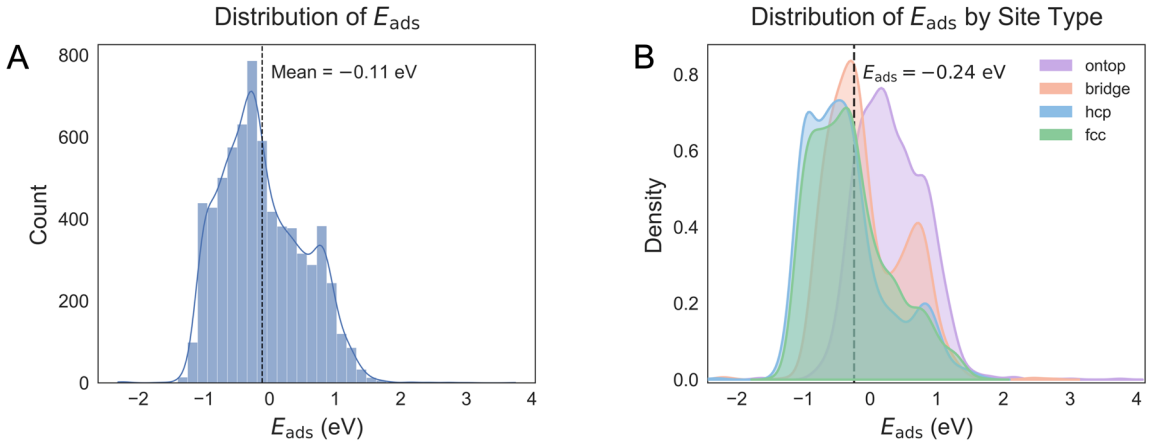

Figure 3. (**A**) Distribution of hydrogen adsorption energies (E_{ads}) in the curated HER dataset, spanning from approximately −2.0 to +3.0 eV with a peak density near the Sabatier optimum (−0.24 eV). (**B**) Site-resolved distributions, showing that hollow motifs (*fcc* and *hcp*) cluster near optimal binding, while ontop sites are shifted toward weaker binding with broader positive tails. These trends highlight the strong dependence of adsorption energetics on local coordination environment.

Site dependence of adsorption energetics is further illustrated in Figure 3B, which separates the distributions by adsorption motif. *fcc* and *hcp* hollow sites cluster on the negative side of the distribution and display the narrowest spreads, consistent with their thermodynamic stability [33]. Bridge sites shift toward weaker binding and exhibit a secondary lobe at positive energies, while ontop sites extend even further into positive values with the broadest tails. These long positive tails reflect the reduced stability of undercoordinated motifs and their high sensitivity to subtle changes in the local atomic environment. The magnitude of these site-dependent shifts, reaching up to ~1 eV between motifs, is consistent with prior reports and underscores the need for encoding of site

identity in the feature set (Table S1) [33,34]. Together, these observations justify the inclusion of coordination-sensitive descriptors and stratified model validation to ensure that predictive accuracy is assessed separately for each adsorption motif rather than in aggregate.

3.2. Correlation Analysis

After defining the feature set, relationships among descriptors were examined prior to model training. Pairwise Pearson correlation coefficients were calculated for all descriptors and for the target variable, as summarized in Figure 4. Strong positive correlations were observed among WIE, WEN, and S_A, reflecting their shared origin in periodic trends. Similarly, the unit cell volume per atom (Å^3) tracked closely with the WAR, with a correlation coefficient of 0.80, as expected for two descriptors that encode atomic size. By contrast, the GCN and facet label exhibited negligible correlation with other descriptors (Table S2), indicating that geometric terms provide largely independent information relative to element-based quantities. Adsorption energy itself showed only weak linear correlations with any single descriptor, reinforcing the need for a multivariate ML model rather than a screening approach based on individual variables.

This correlation analysis served two main purposes. It first confirmed that geometric and electronic descriptors provide complementary information for modeling adsorption behavior. It also revealed pairs of features whose collinearity could undermine the reliability of importance estimates, as correlated variables may share or distort their relative contributions. These findings informed our modeling strategy, where we represented site geometry through the GCN and explicitly retained the facet label to preserve essential structural distinctions while avoiding one-hot encoding. This approach follows recent HER-focused ML studies in which compact descriptor sets are systematically analyzed for collinearity, and tree ensemble methods are favored for their ability to capture non-linear interactions while remaining robust to between-feature correlation. Complete distributions of all descriptors and additional statistics are provided in Figure S2. Together, these checks ensured that the final feature set is compact, interpretable, and physically meaningful, thereby establishing a robust foundation for predictive modeling.

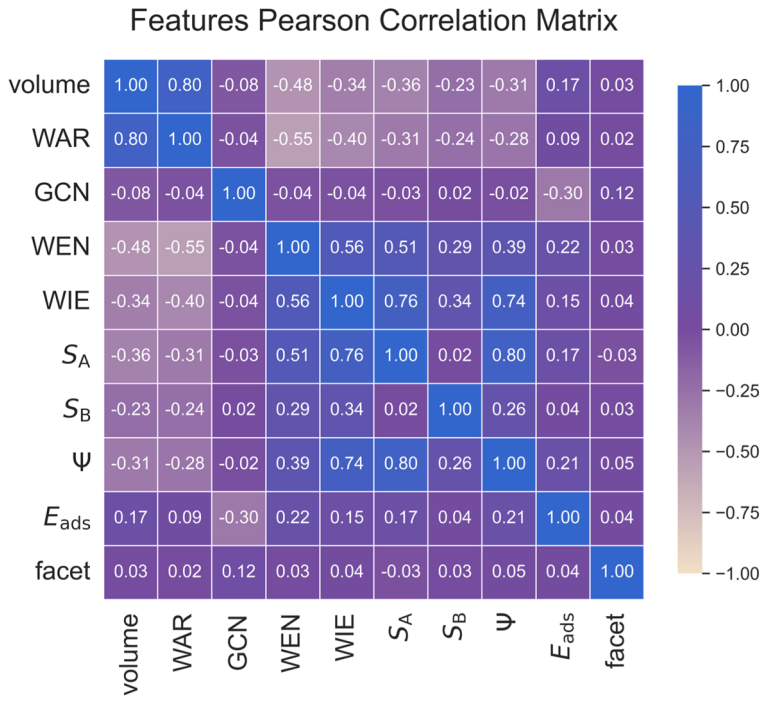

Figure 4. Pearson correlation matrix of the engineered descriptors and hydrogen adsorption energy (E_{ads}). Strong correlations are observed between weighted electronegativity (WEN), weighted ionization energy (WIE), and valence electron count (S_A), while geometric descriptors such as generalized coordination number (GCN) and facet remain largely independent. The weak correlation between any single descriptor and E_{ads} emphasizes the need for multivariate ML models to capture adsorption trends.

3.3. Model Development

The prediction of hydrogen adsorption energies was framed as a supervised regression problem [35]. To avoid data leakage, data were partitioned using a group-aware strategy in which surface composition–facet–site identifiers served as grouping keys. This ensured that chemically identical motifs did not appear in both training

and test sets. An 80/20 data split was used for model evaluation, and StratifiedGroupKFold cross-validation was applied within the training set to ensure both balanced representation of Au-containing entries and group integrity. As summarized in Table S3, the mean absolute error (MAE) across folds remains consistent, indicating stable model behavior and confirming the effectiveness of the grouping strategy in preventing data leakage.

Three tree-based ensemble algorithms were evaluated: Random Forest (RF) [36], Extra Trees (ET) [37], and Extreme Gradient Boosting (XGBoost) [38]. The chosen models all rely on ensembles of decision trees, with RF and ET using randomized averaging strategies to reduce variance, while XGBoost builds trees sequentially via gradient boosting to minimize prediction error. These methods were selected for their ability to capture non-linear relationships among features while providing interpretable measures of feature importance. Hyperparameters for each model were optimized using grid search with cross-validation, and the final settings are listed in Table S4. Model performance was primarily assessed MAE, with root-mean-square error (RMSE) and coefficient of determination (R^2) reported as secondary metrics.

Training on the full alloy dataset yielded quantitative accuracy sufficient to resolve motif-dependent differences in adsorption behavior. The Extra Trees algorithm exhibited the best overall performance, achieving a mean average error of 0.131 eV ($R^2 = 0.86$) on the full test set and 0.136 eV ($R^2 = 0.82$) for the Au subset. This level of accuracy is sufficient to distinguish between weak, optimal, and strong hydrogen binding regimes, which is the relevant resolution for catalytic screening. RF and XGBoost showed slightly higher errors, with ~0.146 and ~0.149 eV, respectively. Site-resolved diagnostics revealed strong heterogeneity in predictive accuracy (Table S5): hollow sites (*fcc*, *hcp*) displayed the lowest errors (0.07 eV), while ontop sites exhibited errors exceeding 0.25 eV. Attempts to improve performance using site-specific ET submodels, each trained and tuned separately while retaining the same descriptor set, did not outperform the unified model (Table S6). This confirms that a global framework incorporating site descriptors remains preferable for high-throughput screening.

These results demonstrate that a compact set of physically interpretable descriptors, when combined with tree-based ensemble models, can achieve prediction errors on the order of 0.1 eV for stable adsorption motifs. The higher errors observed for ontop sites likely arise from their intrinsic instability in the underlying DFT dataset. As shown by the plateau of the learning curves around 3500 training points (Figure S3), the limited sampling of undercoordinated motifs appears to have only a minor impact on overall accuracy. Instead, the model performance seems constrained by the informational capacity of the current descriptor set, highlighting the need for coordination-sensitive features to better capture adsorption trends.

3.4. Model Evaluation

The performance of the Extra Trees (ET) model was examined in detail through residual and feature attribution analyses. Residual plots (Figure 5A) show that errors are symmetrically distributed around zero with no significant systematic bias. A modest widening of the residual spread at higher adsorption energies reflects heteroscedasticity in the underlying dataset. Site-resolved residuals (Figure 5B) confirm the motif-dependent accuracy: *fcc* and *hcp* hollow sites exhibit narrow, centered distributions, while ontop sites display the largest variance, consistent with their intrinsic instability and sparse representation in the training data.

Feature attribution was investigated using both Gini importance and SHAP (SHapley Additive exPlanations) values (Figure 6). Gini importance captures the average decrease in model error from splits on each feature, while SHAP values estimate the marginal contribution of each feature to individual predictions. These methods exhibit which chemical descriptors the model relies on most, and in which direction they influence adsorption strength. The Gini ranking identified the ψ as the most influential input, followed by GCN, WEN, and S_A. Secondary contributions were observed from WAR, volume per atom, and WIE, while facets contributed modestly. Collinearity among certain descriptors tends to redistribute feature importance within correlated groups, which can mask the apparent contribution of secondary variables. Nevertheless, the overall ranking of descriptors and the chemical interpretability of the model remain largely unaffected. SHAP analysis provided additional mechanistic insight: higher GCN and WEN values shifted predictions toward stronger binding (more negative E_{ads}), whereas larger S_A and volume per atom were associated with weaker binding. Notably, ψ exhibited a broad SHAP distribution with both positive and negative contributions, highlighting its ability to capture non-linear interactions between local electronic environment and coordination.

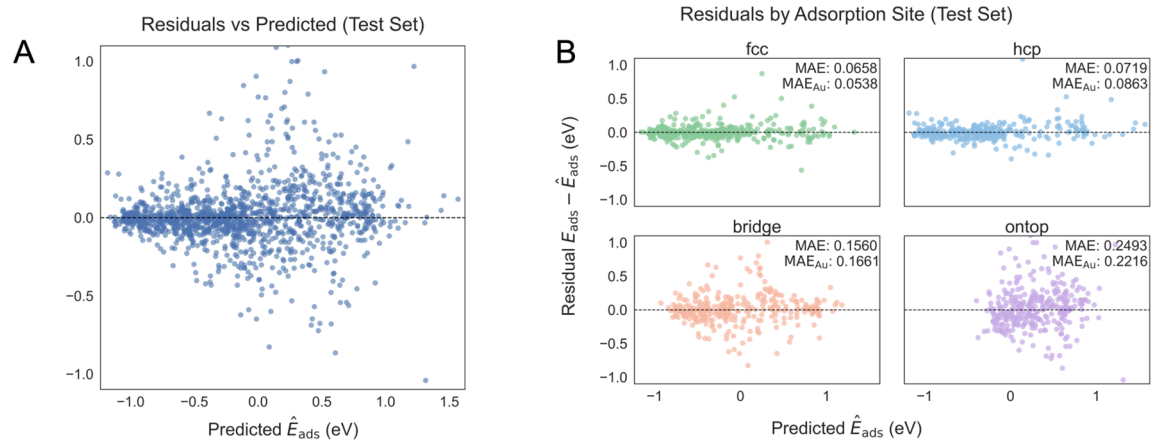

Figure 5. (**A**) Residuals of the Extra Trees (ET) model plotted against predicted adsorption energies ($\hat{E}_{ads}$), showing symmetric distribution around zero and modest heteroscedasticity at higher energies. (**B**) Site-resolved residuals for *fcc*, *hcp*, bridge, and ontop motifs. Narrow, centered distributions for *fcc* and *hcp* sites indicate reliable predictions, while ontop sites display the largest variance, reflecting their intrinsic instability.

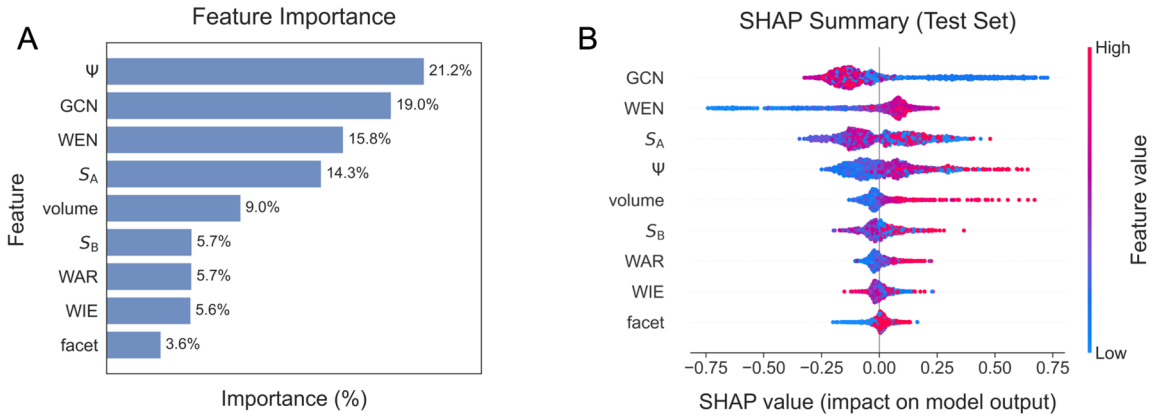

Figure 6. Feature attribution analysis of the Extra Trees (ET) model. (**A**) Gini importance ranking, highlighting ψ, generalized coordination number (GCN), and weighted electronegativity (WEN) as dominant descriptors. (**B**) SHAP summary plot, which provides directional insight: higher GCN and WEN values drive predictions toward stronger binding (more negative E_{ads}), while larger S_A and volume per atom shift predictions toward weaker binding. The broad distribution of ψ underscores its role in capturing non-linear site–composition interactions. Agreement between the two approaches confirms that physically motivated descriptors govern model predictions.

The strong agreement between Gini and SHAP analyses underscores that the model relies on chemically interpretable features to reproduce adsorption trends [39]. In particular, the prominence of ψ and GCN is consistent with established catalytic intuition, as adsorption strength is governed jointly by coordination environment and electronic character. These findings confirm that the ML framework not only achieves quantitative accuracy but also produces insights that can be rationalized within well-known chemisorption principles.

3.5. Discussion and Implications

The results demonstrate that hydrogen adsorption on Au-based alloys can be predicted with quantitative accuracy using compact, chemical interpretable descriptors combined with tree-based ensemble models. The achieved mean absolute error of ~0.1 eV is sufficient to differentiate weak, optimal, and strong binding regimes, providing a practical level of resolution for catalytic prescreening. Site-resolved diagnostics confirm that the most stable motifs (*fcc* and *hcp* hollow sites) are predicted with highest fidelity, while undercoordinated ontop sites remain a source of uncertainty. This performance profile mirrors the intrinsic thermodynamic variability of adsorption motifs in the underlying DFT dataset, highlighting both the strengths and the limitations of data-driven modeling in catalysis.

A key outcome of this work is the demonstration that predictive accuracy does not require large descriptor sets or complex neural architectures. Instead, the most influential features, coordination number and site-specific electronic descriptors, are directly tied to well-established chemisorption principles. This interpretability allows

experimental chemists to rationalize predictions within familiar frameworks, thereby lowering the barrier to adopting ML tools in catalyst discovery. Such predictions can help experimentalists prioritize alloy families before investing in DFT validation or synthesis. The workflow presented here thus complements intuition and conventional high-throughput screening by offering rapid, reproducible insights into alloy composition–structure–property relationships.

At the same time, limitations must be acknowledged. The training data originate from static DFT calculations and do not capture solvation, applied potential, or long-term surface restructuring under operating conditions [40]. The reduced accuracy for ontop sites reflects both their intrinsic instability and their underrepresentation in the dataset, suggesting that further improvements will require expanded sampling of undercoordinated environments. Broader validation beyond Au-based alloys will also be necessary to establish the generality of this approach.

Despite these caveats, the present study provides a proof of concept for integrating ML into catalytic discovery pipelines in a manner that is accessible to chemists. By focusing on chemically meaningful features and transparent workflows, the approach serves as a reference model for bridging computational screening and experimental exploration of electrocatalysts for the HER and related transformations.

Although the present study focuses on Au-based alloys as a proof of concept, the proposed ML framework is composition-agnostic and readily transferable to other metallic systems. The nine engineered descriptors capture general geometric and electronic factors, such as coordination environment, electronegativity, valence electron count, and local site potential, that are not specific to Au chemistry. Consequently, the same workflow can be directly retrained on DFT datasets for Pt-, Pd-, or other transition-metal catalysts without modification of the feature set or model architecture. Because these descriptors encode fundamental chemisorption principles, their physical interpretability ensures consistent predictive trends across different catalyst families. In this sense, the present work provides a transferable template for integrating interpretable machine learning into the discovery of diverse HER catalysts beyond Au-based systems.

While the present framework is trained on DFT-calculated adsorption energies, its purpose is to decouple predictive screening from the need for additional first-principles calculations. Once trained, the model can rapidly estimate adsorption trends across uncalculated alloy compositions at negligible computational cost, providing scalability that would be unattainable through DFT alone. The use of descriptors restricted to the first coordination shell intentionally balances accuracy and generalizability: local atomic and electronic environments dominate hydrogen binding, as reflected by the quantitative accuracy achieved here (MAE ≈ 0.13 eV). This design allows the framework to retain physical interpretability while remaining computationally lightweight and transferable to broader catalyst discovery tasks.

Although the training data comprise ordered *fcc*-based alloys, the feature design is inherently local and therefore independent of long-range periodicity. Each descriptor is constructed from first-shell coordination and elemental properties, quantities that can be equally obtained for amorphous or defect-rich structures from atomic coordinates or short-range order parameters. As such, the same ML workflow can, in principle, be applied to amorphous catalysts without modification, offering a generalizable route for modeling hydrogen adsorption in both crystalline and non-crystalline materials.

3.6. Catalyst Screening

Guided by the feature attribution analyses and the site-resolved error diagnostics, the final stage applied the trained Extra Trees model to a targeted library of Au–M alloys. Partner elements were drawn from the 3d, 4d, and 5d transition series, together with representative p-block and rare-earth elements, to ensure broad chemical coverage while remaining within the interpolation regime of the training set. The chosen set included Sc, Ti, V, Cr, Mn, Fe, Co, Ni, Cu, Zn, Y, Zr, Nb, Mo, Tc, Ru, Rh, Pd, Ag, Cd, Hf, Ta, W, Re, Os, Ir, Pt, Hg, Al, Bi, Ga, In, La, Pb, Sn, and Tl. For each Au–M pair, compositions in AB, AB_3, and A_3B stoichiometries were generated, preserving local coordination environments consistent with those in the curated dataset. Adsorption motifs were expanded to include ontop, bridge, *fcc* hollow, and *hcp* hollow sites, with further enumeration into first-layer variants (e.g., fccAAA, fccAAB, fccABB, fccBBB), as summarized in Table S7. In total, 1404 candidate rows were constructed, of which 1003 were absent from the training data and thus represent a genuine screening space.

To evaluate thermodynamic feasibility, DFT calculations were performed on representative screened alloys. Formation energies are presented in Figure 7A, where early 4d and 5d partners (Zr, Nb, Mo, Tc, Hf, Ta, W) yield strongly negative values (as low as −0.45 eV), consistent with robust heteronuclear bonding and a high likelihood of forming ordered intermetallics [41]. Chromium also exhibits negative formation energies near equiatomic compositions. In contrast, late transition partners (Rh, Pd, Ag) and light elements (Ti, V) display near-zero or slightly positive formation energies, reflecting reduced alloy stability. A clear compositional trend is observed:

many systems show maximum stability near 50% M (AB-type ordering), with only mild destabilization at Au-rich or M-rich extremes.

Cohesive energies, shown in Figure 7B, further reinforce these trends. Early transition partners (Mo, W, Ta, Hf, Tc) exhibit strong cohesion (−6 to −7 eV), suggesting resistance to dealloying and long-term structural integrity. In contrast, Au–Pd and Au–Ag exhibit weaker cohesion (−4 to −5 eV), indicating reduced stability under corrosive conditions [42]. Integrating adsorption and stability maps identifies Au–Mo, Au–W, Au–Ta, Au–Hf, and Au–Tc as particularly promising candidates that combine near-optimal hydrogen adsorption with robust alloy stability.

Together, these results provide a chemically grounded roadmap for Au-based HER catalyst design. Au-rich stoichiometries (A_3B, AB_3) yield surfaces resistant to corrosion while maintaining favorable adsorption energies at hollow sites, while equiatomic AB systems provide bulk stabilization. Reference alloys such as Au–Pd and Au–Ag remain useful benchmarking systems but are less likely to withstand aggressive electrochemical environments. This integrated ML–DFT workflow demonstrates how interpretable machine learning, coupled with targeted validation, can accelerate the identification of practical electrocatalyst candidates.

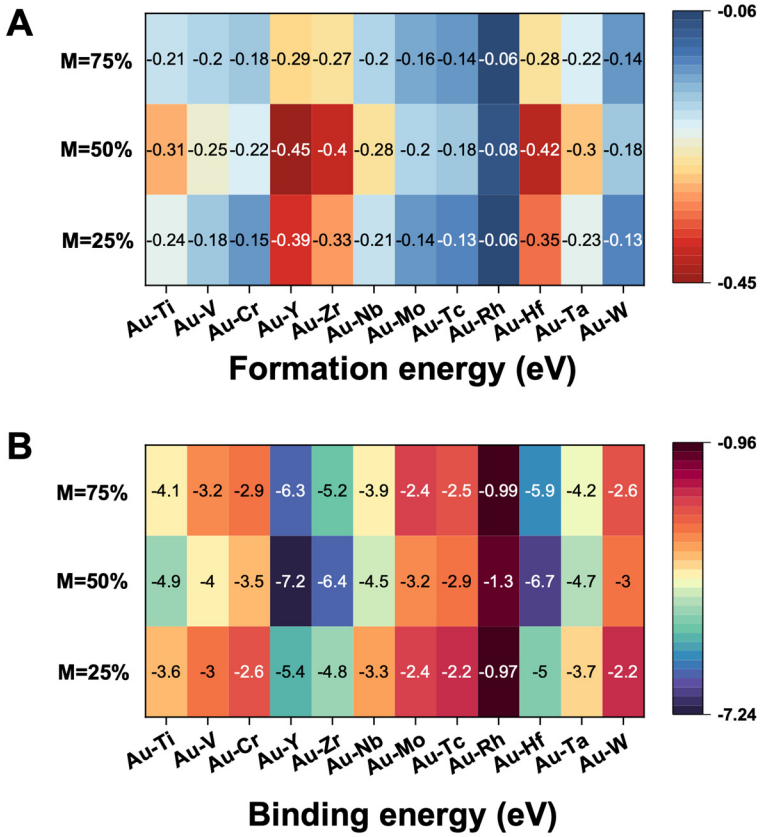

Figure 7. Thermodynamic stability of Au–M alloys across three stoichiometries (A_3B, AB, AB_3). (**A**) Formation energies, showing negative values for early 4d and 5d partners (e.g., Mo, W, Ta, Hf, Tc, Nb), consistent with strong heteronuclear bonding and ordered intermetallic formation. Late transition partners (Pd, Ag, Rh) and light elements (Ti, V) yield values near zero or positive, reflecting reduced alloy stability. (**B**) Cohesive energies, which strengthen progressively from late to early transition series. Au–Mo, Au–W, Au–Ta, and Au–Hf exhibit high cohesive energies (−6 to −7 eV), while Au–Pd and Au–Ag fall closer to −4 to −5 eV. Combined, the formation and cohesive energy maps identify Au–Mo, Au–W, Au–Ta, Au–Hf, and Au–Tc as promising candidates that couple robust alloy stability with favorable hydrogen adsorption.

4. Conclusions

This study presents a proof-of-concept machine learning framework for predicting hydrogen adsorption energies on Au-based alloys, built on a curated dataset and nine chemically interpretable descriptors. Using tree-based models, we show that catalytic trends across different compositions and adsorption motifs can be captured in a transparent and reproducible manner. Feature attribution highlights coordination environment and local electronic structure as the dominant factors, in agreement with established chemisorption principles. Applying the trained model to a targeted Au–M alloy library, followed by DFT-based stability validation, identified promising candidates such as Au–Mo, Au–W, Au–Ta, Au–Hf, and Au–Tc. Beyond these specific predictions, the workflow

provides an accessible reference for experimental chemists, offering a practical way to prioritize alloy families for further DFT calculations or synthesis. More broadly, this work illustrates how interpretable ML can accelerate the discovery of HER catalysts and related materials.

Supplementary Materials: The following supporting information can be downloaded at: https://media.sciltp.com/articles/others/2511241531482990/MI-25100039-SI.pdf, Figure S1: Schematic illustration of the four characteristic adsorption site types, ontop, bridge, *fcc* hollow, and *hcp* hollow, on an *fcc* (111) surface; Figure S2: Histograms of engineered descriptors in the HER-only training set (N =1394); Figure S3: Learning curve analysis for Extra Trees, Random Forest, and XGBoost models; Table S1: Mapping of coefficients used to calculate the site-specific electronic descriptor (Ψ); Table S2: Values of generalized coordination number (GCN) for canonical adsorption sites (*fcc*, *hcp*, bridge, ontop) on *fcc*(111) and *fcc*(101) surfaces, adapted from Martínez-Alonso et al. (2024); Table S3: Per-fold mean absolute error (MAE, eV) for Extra Trees (ET), Random Forest (RF), and XGBoost models under the 5-fold StratifiedGroupKFold split; Table S4: Optimized hyperparameters for Extra Trees, Random Forest, and XGBoost models, together with the ranges explored during grid search; Table S5: Site-resolved test metrics for the unified Extra Trees model; Table S6: Performance of site-specific models trained separately on ontop, bridge, *fcc*, and *hcp* subsets; Table S7: Canonical adsorption site types used in this study (ontop, bridge, *fcc*, *hcp*) and the corresponding normalized site-label variants grouped under each type. Reference [43] is cited in Supplementary Materials.

Author Contributions: M.K. and S.W.: conceptualization, methodology, visualization, software, data curation, writing—original draft preparation; P.H.C.C.: supervision; conceptualization, writing—reviewing and editing. All authors have read and agreed to the published version of the manuscript.

Funding: This work was supported by the Jane and Aatos Erkko Foundation (grant no. 240052), and the Academy of Finland (decision no. 334826).

Data Availability Statement: All scripts and notebooks used for data preprocessing, feature engineering, model training, and alloy screening are openly available at https://github.com/majakubik/her-au-ml-code (accessed on 10 November 2025). The repository contains step-by-step Jupyter notebooks reproducing the main results and figures of this study, together with example input data and trained models. This ensures full reproducibility of our workflow and provides an accessible reference for researchers seeking to apply chemically interpretable machine-learning frameworks in catalysis.

Conflicts of Interest: The authors declare no conflict of interest.

Use of AI and AI-Assisted Technologies: AI tools were employed for text editing. After using this, the authors reviewed and edited the content as needed and take full responsibility for the content of the published article.

References

1. Gao, Y.; Xu, Y.; Guo, H.; Li, J.; Ding, L.; Wang, T.; He, J.; Chang, K.; Wu, Z. A 17.73% Solar-To-Hydrogen Efficiency with Durably Active Catalyst in Stable Photovoltaic-Electrolysis Seawater System. *Angew. Chem. Int. Ed.* **2025**, *64*, e202420814. https://doi.org/10.1002/anie.202420814.
2. Nsanzimana, J.M.V.; Cai, L.; Djire, A.; Pagot, G.; Mattana, P.; Vezzù, K.; Negro, E.; Xia, B.Y.; Di Noto, V. Tailoring Chemical Microenvironment of Iron-Triad Electrocatalysts for Hydrogen Production by Water Electrolysis. *Adv. Energy Mater.* **2025**, *15*, 2501686. https://doi.org/10.1002/aenm.202501686.
3. Tang, J.; Guo, K.; Guan, D.; Hao, Y.; Shao, Z. A Semi-Vapor Electrolysis Technology for Hydrogen Generation from Wide Water Resources. *Energy Environ. Sci.* **2024**, *17*, 7394–7402. https://doi.org/10.1039/D4EE02722A.
4. Zhang, X.; Cao, C.; Ling, T.; Ye, C.; Lu, J.; Shan, J. Developing Practical Catalysts for High-Current-Density Water Electrolysis. *Adv. Energy Mater.* **2024**, *14*, 2402633. https://doi.org/10.1002/aenm.202402633.
5. Liu, Z.; Zhang, L.; Zheng, C.J.; Zhang, Y.; Chen, B.; Shao, Z.; Ge, J. Advanced Electrode Materials for Efficient Hydrogen Production in Protonic Ceramic Electrolysis Cells. *Adv. Mater.* **2025**, 2503609. https://doi.org/10.1002/adma.202503609.
6. Brunin, G.; Ricci, F.; Ha, V.-A.; Rignanese, G.-M.; Hautier, G. Transparent Conducting Materials Discovery Using High-Throughput Computing. *NPJ Comput. Mater.* **2019**, *5*, 63. https://doi.org/10.1038/s41524-019-0200-5.
7. Wang, C.; Wang, B.; Wang, C.; Chang, Z.; Yang, M.; Wang, R. Efficient Machine Learning Model Focusing on Active Sites for the Discovery of Bifunctional Oxygen Electrocatalysts in Binary Alloys. *ACS Appl. Mater. Interfaces* **2024**, *16*, 16050–16061. https://doi.org/10.1021/acsami.3c17377.
8. Mai, H.; Le, T.C.; Chen, D.; Winkler, D.A.; Caruso, R.A. Machine Learning for Electrocatalyst and Photocatalyst Design and Discovery. *Chem. Rev.* **2022**, *122*, 13478–13515. https://doi.org/10.1021/acs.chemrev.2c00061.
9. Jeong, I.; Shim, Y.; Oh, S.; Yuk, J.M.; Roh, K.; Lee, C.; Lee, K.T. A Machine Learning-Enhanced Framework for the Accelerated Development of Spinel Oxide Electrocatalysts. *Adv. Energy Mater.* **2024**, *14*, 2402342. https://doi.org/10.1002/aenm.202402342.
10. Chen, L.; Tian, Y.; Hu, X.; Yao, S.; Lu, Z.; Chen, S.; Zhang, X.; Zhou, Z. A Universal Machine Learning Framework for Electrocatalyst Innovation: A Case Study of Discovering Alloys for Hydrogen Evolution Reaction. *Adv. Funct. Mater.* **2022**, *32*, 2208418. https://doi.org/10.1002/adfm.202208418.
11. Liu, J.; Luo, W.; Wang, L.; Zhang, J.; Fu, X.; Luo, J. Toward Excellence of Electrocatalyst Design by Emerging Descriptor-Oriented Machine Learning. *Adv. Funct. Mater.* **2022**, *32*, 2110748. https://doi.org/10.1002/adfm.202110748.

12. Jung, W.; Choi, J.; An, S.; Yun, S.; Chung, D.S.; Cha, H.; Lim, J.; Park, T. Photocatalytic Hydrogen Evolution with Conjugated Polymers: Structure–Property Insights and Design Strategies. *Adv. Energy Mater.* **2025**, *15*, 2501600. https://doi.org/10.1002/aenm.202501600.
13. Lee, W.J.; Kwak, H.S.; Lee, D.; Oh, C.; Yum, E.K.; An, Y.; Halls, M.D.; Lee, C.-W. Design and Synthesis of Novel Oxime Ester Photoinitiators Augmented by Automated Machine Learning. *Chem. Mater.* **2022**, *34*, 116–127. https://doi.org/10.1021/acs.chemmater.1c02871.
14. Nuñez, M. Exploring Materials Band Structure Space with Unsupervised Machine Learning. *Comput. Mater. Sci.* **2019**, *158*, 117–123. https://doi.org/10.1016/j.commatsci.2018.11.002.
15. Wang, C.; Wang, B.; Wang, C.; Li, A.; Chang, Z.; Wang, R. A Machine Learning Model with Minimize Feature Parameters for Multi-Type Hydrogen Evolution Catalyst Prediction. *NPJ Comput. Mater.* **2025**, *11*, 111. https://doi.org/10.1038/s41524-025-01607-4.
16. Wang, Z.; Yang, M.; Xie, X.; Yu, C.; Jiang, Q.; Huang, M.; Algadi, H.; Guo, Z.; Zhang, H. Applications of Machine Learning in Perovskite Materials. *Adv. Compos. Hybrid. Mater.* **2022**, *5*, 2700–2720. https://doi.org/10.1007/s42114-022-00560-w.
17. Mou, L.; Han, T.; Smith, P.E.S.; Sharman, E.; Jiang, J. Machine Learning Descriptors for Data-Driven Catalysis Study. *Adv. Sci.* **2023**, *10*, 2301020. https://doi.org/10.1002/advs.202301020.
18. Zhang, N.; Yang, B.; Liu, K.; Li, H.; Chen, G.; Qiu, X.; Li, W.; Hu, J.; Fu, J.; Jiang, Y.; et al.Machine Learning in Screening High Performance Electrocatalysts for CO_2 Reduction. *Small Methods* **2021**, *5*, 2100987. https://doi.org/10.1002/smtd.202100987.
19. Mamun, O.; Winther, K.T.; Boes, J.R.; Bligaard, T. High-Throughput Calculations of Catalytic Properties of Bimetallic Alloy Surfaces. *Sci. Data* **2019**, *6*, 76. https://doi.org/10.1038/s41597-019-0080-z.
20. Chen, X.; Zhou, T.; He, T.; Liu, Q. Vacancy Engineering in the First Coordination Shell of Single-Atom Catalysts for Enhanced Hydrogen and Oxygen Evolution Reactions. *Small* **2025**, *21*, 2412000. https://doi.org/10.1002/smll.202412000.
21. Li, Y.; Zheng, S.; He, Y.; Yang, S.; Huang, W.-H.; Pao, C.-W.; Hu, Z.; Huang, X. Masked Second-Shell Sulfur Coordinating Atomically Dispersed Pd on Tin Oxide Boosts the Direct Synthesis of Hydrogen Peroxide. *Chem. Eng. J.* **2024**, *500*, 157297. https://doi.org/10.1016/j.cej.2024.157297.
22. Lv, Y.; Sun, W.; Luo, Q.; Gao, J.; Gu, G.; Ma, F. Fast Screening of High Anti-Corrosion Ta Ternary Alloys by Machine Learning and Electron-Level Descriptors. *Mater. Chem. Phys.* **2025**, *339*, 130820. https://doi.org/10.1016/j.matchemphys.2025.130820.
23. Tereshchenko, A.; Pashkov, D.; Guda, A.; Guda, S.; Rusalev, Y.; Soldatov, A. Adsorption Sites on Pd Nanoparticles Unraveled by Machine-Learning Potential with Adaptive Sampling. *Molecules* **2022**, *27*, 357. https://doi.org/10.3390/molecules27020357.
24. Shapera, E.P.; Bučar, D.-K.; Prasankumar, R.P.; Heil, C. Machine Learning Assisted Prediction of Organic Salt Structure Properties. *NPJ Comput. Mater.* **2024**, *10*, 176. https://doi.org/10.1038/s41524-024-01355-x.
25. Chen, K.; Kunkel, C.; Cheng, B.; Reuter, K.; Margraf, J.T. Physics-Inspired Machine Learning of Localized Intensive Properties. *Chem. Sci.* **2023**, *14*, 4913–4922. https://doi.org/10.1039/D3SC00841J.
26. Zou, Y.; Qian, J.; Wang, X.; Li, S.; Li, Y. Machine Learning-Assisted Prediction and Interpretation of Electrochemical Corrosion Behavior in High-Entropy Alloys. *Comput. Mater. Sci.* **2024**, *244*, 113259. https://doi.org/10.1016/j.commatsci.2024.113259.
27. Mishra, A.; Kompella, L.; Sanagavarapu, L.M.; Varam, S. Ensemble-Based Machine Learning Models for Phase Prediction in High Entropy Alloys. *Comput. Mater. Sci.* **2022**, *210*, 111025. https://doi.org/10.1016/j.commatsci.2021.111025.
28. Kapse, S.; Janwari, S.; Waghmare, U.V.; Thapa, R. Energy Parameter and Electronic Descriptor for Carbon Based Catalyst Predicted Using QM/ML. *Appl. Catal. B: Environ.* **2021**, *286*, 119866. https://doi.org/10.1016/j.apcatb.2020.119866.
29. Cerda, P.; Varoquaux, G.; Kégl, B. Similarity Encoding for Learning with Dirty Categorical Variables. *Mach. Learn.* **2018**, *107*, 1477–1494. https://doi.org/10.1007/s10994-018-5724-2.
30. Esterhuizen, J.A.; Goldsmith, B.R.; Linic, S. Uncovering Electronic and Geometric Descriptors of Chemical Activity for Metal Alloys and Oxides Using Unsupervised Machine Learning. *Chem. Catal.* **2021**, *1*, 923–940. https://doi.org/10.1016/j.checat.2021.07.014.
31. Lansford, J.L.; Vlachos, D.G. Spectroscopic Probe Molecule Selection Using Quantum Theory, First-Principles Calculations, and Machine Learning. *ACS Nano* **2020**, *14*, 17295–17307. https://doi.org/10.1021/acsnano.0c07408.
32. Chen, M.S.; Zuehlsdorff, T.J.; Morawietz, T.; Isborn, C.M.; Markland, T.E. Exploiting Machine Learning to Efficiently Predict Multidimensional Optical Spectra in Complex Environments. *J. Phys. Chem. Lett.* **2020**, *11*, 7559–7568. https://doi.org/10.1021/acs.jpclett.0c02168.
33. Wexler, R.B.; Martirez, J.M.P.; Rappe, A.M. Chemical Pressure-Driven Enhancement of the Hydrogen Evolving Activity of Ni_2 P from Nonmetal Surface Doping Interpreted via Machine Learning. *J. Am. Chem. Soc.* **2018**, *140*, 4678–4683. https://doi.org/10.1021/jacs.8b00947.

34. Padama, A.A.B.; Palmero, M.A.; Shimizu, K.; Chookajorn, T.; Watanabe, S. Machine Learning and Density Functional Theory-Based Analysis of the Surface Reactivity of High Entropy Alloys: The Case of H Atom Adsorption on CoCuFeMnNi. *Comput. Mater. Sci.* **2025**, *247*, 113480. https://doi.org/10.1016/j.commatsci.2024.113480.
35. Pandit, N.K.; Roy, D.; Mandal, S.C.; Pathak, B. Rational Designing of Bimetallic/Trimetallic Hydrogen Evolution Reaction Catalysts Using Supervised Machine Learning. *J. Phys. Chem. Lett.* **2022**, *13*, 7583–7593. https://doi.org/10.1021/acs.jpclett.2c01401.
36. Dong, C.; Zhu, Y.; Qu, C.; Chen, Y.; Ma, Y.; Yu, Y.; Li, C. Coordination Chemistry-Driven Oxygen Vacancy Strategy for Rational Design of High-Performance Catalysts in BTX Oxidation. *Coord. Chem. Rev.* **2025**, *545*, 217007. https://doi.org/10.1016/j.ccr.2025.217007.
37. Chen, R.; Yang, J.; Yu, Y.; Liu, Z.; Wang, C.; Wen, Y.; Gao, Y.; Zhao, Y.; Sampara, C.S.; Li, W.; et al. Extra Trees Regression Assisted 1D Monolith Reactor Simulations Based on Microkinetic Analysis and Rate Transformation. *Chem. Eng. Sci.* **2025**, *302*, 120721. https://doi.org/10.1016/j.ces.2024.120721.
38. Da Costa, M.L.; Oviedo, L.R.; Franco, D.S.P.; Da Silva, W.L.; De Oliveira, J.S. Catalytic Ozonation for the Efficient Degradation of Tetracycline Using CoFe2O4@TiO2 Ceramic Nanocomposite: Kinetic, Thermodynamic and Machine Learning Study. *Ceram. Int.* **2025**, *51*, 7143–7158. https://doi.org/10.1016/j.ceramint.2024.12.149.
39. Naqvi, S.K.H.; Chong, K.T.; Tayara, H. Machine Learning-Enhanced Analysis of Catalyst Particle Size Effects and Performance Prediction of Platinum on Carbon Electrocatalysts. *Comput. Mater. Sci.* **2025**, *259*, 114105. https://doi.org/10.1016/j.commatsci.2025.114105.
40. Panapitiya, G.; Avendaño-Franco, G.; Ren, P.; Wen, X.; Li, Y.; Lewis, J.P. Machine-Learning Prediction of CO Adsorption in Thiolated, Ag-Alloyed Au Nanoclusters. *J. Am. Chem. Soc.* **2018**, *140*, 17508–17514. https://doi.org/10.1021/jacs.8b08800.
41. He, X.; Liu, J.; Yang, C.; Jiang, G. Predicting Thermodynamic Stability of Magnesium Alloys in Machine Learning. *Comput. Mater. Sci.* **2023**, *223*, 112111. https://doi.org/10.1016/j.commatsci.2023.112111.
42. Cheng, G.; Gong, X.-G.; Yin, W.-J. An Approach for Full Space Inverse Materials Design by Combining Universal Machine Learning Potential, Universal Property Model, and Optimization Algorithm. *Sci. Bull.* **2024**, *69*, 3066–3074. https://doi.org/10.1016/j.scib.2024.07.015.
43. Martínez-Alonso, C.; Vassilev-Galindo, V.; Comer, B.M.; Abild-Pedersen, F.; Winther, K.T.; LLorca, J. Application of machine learning to discover new intermetallic catalysts for the hydrogen evolution and the oxygen reduction reactions. *Catal. Sci. Technol.* **2024**, *14*, 3784–3799.

Article

Redox Behavior and Electrochromism of a Viologen-Based Molten Poly(ionic liquid)

Hironobu Tahara [1,2,*], Saki Takuma [2], Suguru Motokucho [1,2], and Hiroto Murakami [1,2,*]

[1] Graduate School of Integrated Science and Technology, Nagasaki University 1-14 Bunkyo, Nagasaki 852-8521, Japan
[2] Graduate School of Engineering, Nagasaki University 1-14 Bunkyo, Nagasaki 852-8521, Japan
* Correspondence: h-tahara@nagasaki-u.ac.jp (H.T.); hiroto@nagasaki-u.ac.jp (H.M.)
Received: 30 August 2025; Revised: 8 December 2025; Accepted: 14 December 2025; Published: 16 December 2025

Abstract: We present the synthesis and characterization of a viologen-based molten poly(ionic liquid), VPIL(TFSI), and its application to electrochromic (EC) devices. VPIL(TFSI) was obtained as a highly viscous liquid with a glass transition temperature of −23 °C, enabling its use in a molten state without additional solvent. Electrochemical analysis by cyclic voltammetry (CV) and electrochemical impedance spectroscopy (EIS) of neat VPIL(TFSI) revealed a unique conduction mechanism: while ionic conductivity is dominated by the counter-anion (TFSI) migration, charge transport during redox cycling involves electron hopping between viologen units. Diffusion coefficient analysis indicated that electron hopping is slower than counter-anion migration, suggesting that the reorientation of viologen moieties, rather than ion migration, determines the transport kinetics. An EC device was fabricated using an equimolar mixture of VPIL(TFSI) and a ferrocene-based RAIL as cathodic and anodic components, respectively, without any supporting electrolyte. The device exhibited distinct coloration with strong absorption bands at 530 and 890 nm, attributed to π-dimerization of reduced viologen species, along with high contrast and coloration efficiency comparable to theoretical values. These findings demonstrate the potential of molten poly(ionic liquids) as promising redox-active media for solvent-free and durable electrochromic devices.

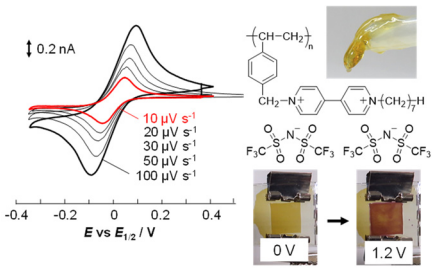

Keywords: redox-active ionic liquid; poly(ionic liquid); conducting polymer; electrochromism

1. Introduction

Ionic liquids (ILs) are often described as designer solvents [1] because their physicochemical properties, such as viscosity, ionic conductivity, melting point, and solubility, can be widely tuned. Redox-active ionic liquids (RAILs), a functional subclass of ILs, have attracted considerable attention as a new class of materials for electrochemical devices [2,3], since they can simultaneously serve as redox-active species, solvent, and supporting electrolyte. Compared with all-solid-state electrolytes, ILs generally offer higher ionic conductivity, better flexibility, and greater tunability. Consequently, RAILs have been applied to supercapacitors [4,5], redox flow batteries [6], and electrochromic (EC) devices [7,8], demonstrating new design concepts and good performance.

Organic-material-based EC devices have also been extensively developed owing to their flexibility, compatibility with solution processing, and tunable physicochemical and electronic properties through molecular design. Among them, diquaternary salts of 4,4′-bipyridinium, commonly known as viologens, are well-established organic EC materials. Several viologen-based RAILs have been reported and investigated with respect to their electron transport properties and pronounced EC response [9–12]. EC devices employing viologen-based RAILs can operate without additional solvent and supporting electrolyte, thereby achieving improved durability by avoiding solvent evaporation, solution leakage, phase segregation, and component decomposition [8]. Nevertheless, demonstrations of such solvent- and electrolyte-free devices remain rare, because ionic redox-active species typically possess high melting points that are difficult to be lowered.

To expand the RAIL family, we have focused on poly(ionic liquid)s (PILs). PILs have received increasing attention due to their unique characteristics arising not only from their IL monomers but also from polymeric structural features rarely observed in conventional ILs [13–15]. Pioneering studies on the electrochemistry of redox-

Copyright: © 2025 by the authors. This is an open access article under the terms and conditions of the Creative Commons Attribution (CC BY) license (https://creativecommons.org/licenses/by/4.0/).
Publisher's Note: Scilight stays neutral with regard to jurisdictional claims in published maps and institutional affiliations.

active viologen-based PILs were reported by Ohno and co-workers [16], who elucidated their fundamental redox and conductive properties. Although several viologen-based polymers have been synthesized and studied [17–20], they have not been applied in the molten state. Thus, electrochromic devices incorporating viologen-based PILs without solvent or additional supporting electrolyte remain unexplored.

In this study, we describe the synthesis of a viologen-based PIL, investigate its charge transport properties, and demonstrate its application in a two-electrode EC device. The device employs a mixed RAIL system comprising a viologen-based PIL as the electrochromic cathodic component and a ferrocene-based RAIL as the anodic redox component, without solvent and supporting electrolyte. Even with VPIL(TFSI), high contrast and large absorbance were achieved, comparable to those of EC devices employing viologen-based ionic liquids reported in our previous work [7,8].

2. Materials

The ferrocene-based RAIL ([FcC_6ImC_1][TFSI], Figure 1a), used as a charge-compensating material for the reduction of VPIL, was synthesized according to a reported procedure [21]. The viologen-based PIL (VPIL(TFSI)) was prepared as outlined in Figure 1, with detailed procedures provided in the Supporting Information (SI). A viologen monomer bearing a styrene group at the terminal of the bipyridinium unit was first synthesized stepwise from 4,4′-bipyridyl. The viologen polymer, VPIL(X), was obtained by radical polymerization using potassium peroxodisulfate as the initiator. The water-soluble crude polymer was purified by dialysis (molecular weight cut-off 1.4×10^4) to remove low-molecular-weight components. No residual monomer (StC_1VC_7) was detected in the purified product, as confirmed by ^{1}H NMR. Ion exchange of VPIL(X) to VPIL(TFSI) was achieved by treatment with LiTFSI in water. To eliminate residual halides, repeated liquid-liquid extraction with water and ethyl acetate was carried out until the aqueous layer no longer turned cloudy upon $AgNO_3$ testing. After evaporation of the ethyl acetate layer and careful drying under vacuum, a faint brown viscous liquid was obtained as VPIL(TFSI). The final product was characterized by ^{1}H NMR and energy-dispersive X-ray fluorescence spectroscopy to confirm the absence of residual monomer and halides, and the presence of the TFSI anion. The glass transition temperature was determined to be −23 °C by differential scanning calorimetry (DSC) (Figure S1).

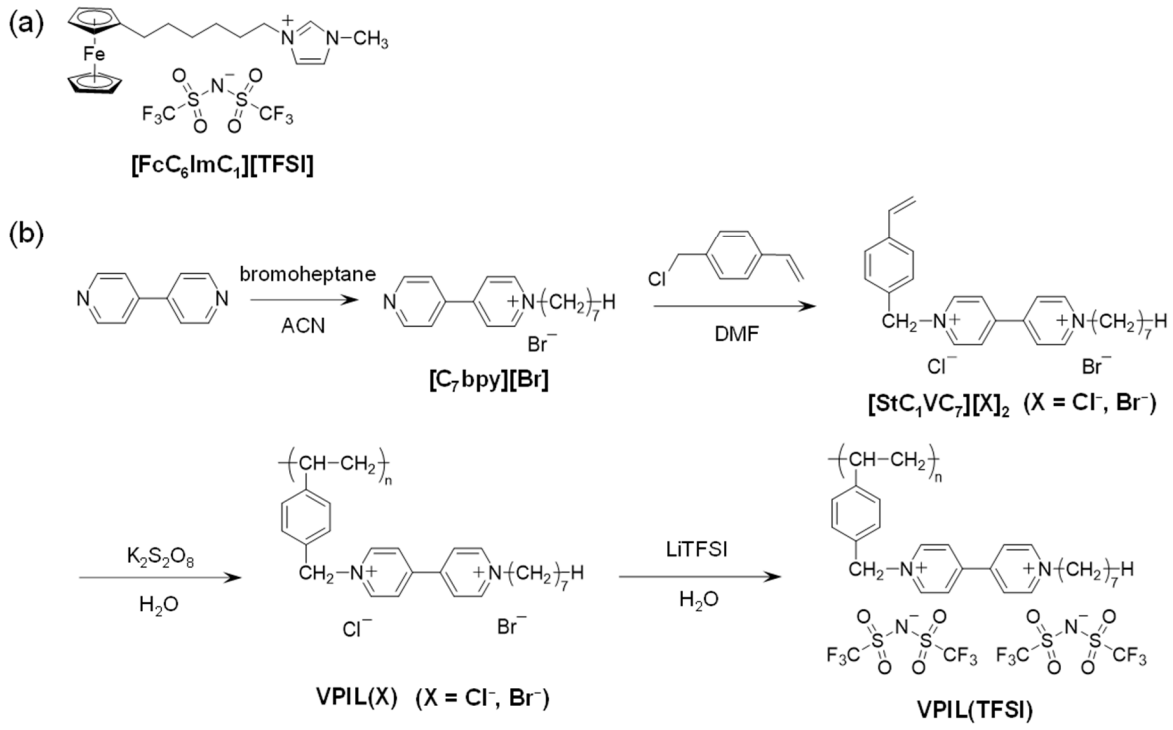

Figure 1. (**a**) Structure of [FcC_6ImC_1][TFSI]. (**b**) Synthetic scheme of VPIL(TFSI).

3. Measurement and Equipment

To evaluate the redox properties and charge transport characteristics of VPIL(TFSI), cyclic voltammetry and electrochemical impedance spectroscopy (EIS) were employed. The cell configuration for the cyclic voltammetry was the same as that reported in our previous study [22] (Figure 2a). A gold micro disk electrode with a diameter

of 100 μm was used as a working electrode and platinum plate electrode was used as a counter electrode. The micro disk electrode experiment was carried out with a potentiostat (Huso (Kawasaki, Kanagawa, Japan), HECS 9094), a function generator (TEXIO Technology Corporation (Yokohama, Kanagawa, Japan), FGX-295), and a recorder (Yokogawa Test & Measurement Corporation (Hachioji, Tokyo, Japan), DL750). For the EIS measurements, a cell was constructed by sandwiching VPIL(TFSI) between two platinum plates, using a PTFE sheet (0.50 mm thick) with a 0.61 cm^2 hole as a separator. The sample was degassed under reduced pressure (15 Pa) at 90 °C to remove bubbles. For the evaluation of ionic conductivity, the cell constant was K_{cell} = 0.11 cm^{-1}. EIS measurements were conducted using a lock-in amplifier (Edgerton, Germeshausen, and Grier, Inc. (Bedford, MA, USA), EG&G 7265) and a home-made potentiostat.

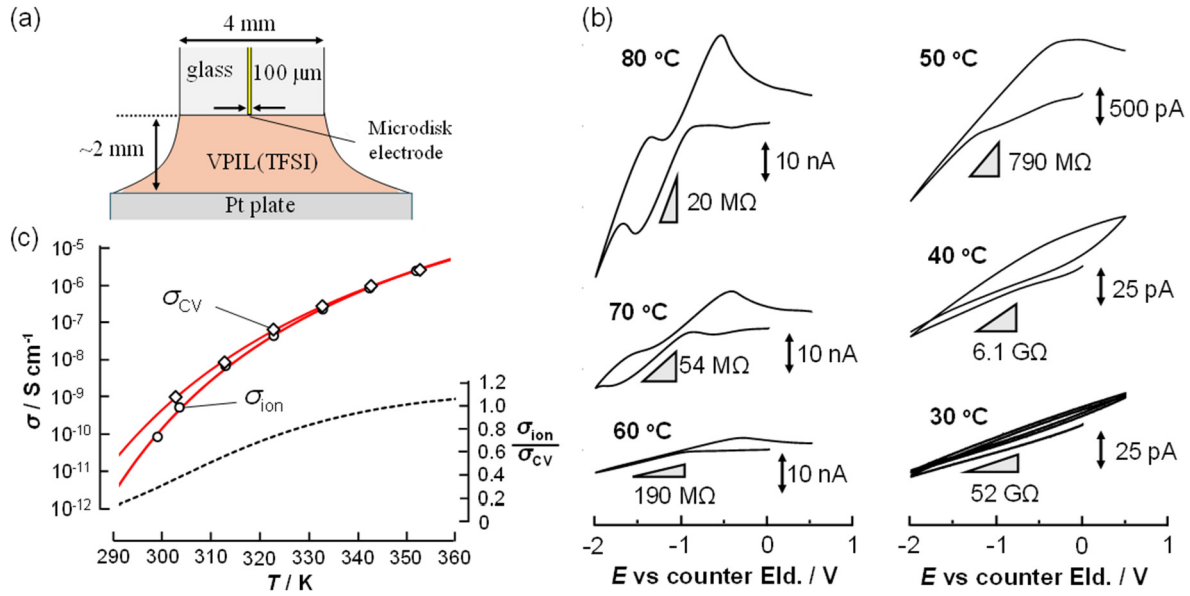

Figure 2. (**a**) Configuration of the CV experiment. The working electrode was Au microdisk electrode (diameter 100 μm) and the counter electrode was Pt plate. The overall setup was the same as our previous report [22]. (**b**) CVs (v = 100 mV·s^{-1}) of VPIL(TFSI) at various temperatures (30–80 °C). The triangles in the charts were the slope of the CVs in the straight-line region. The resistance values were the corresponding R_s values. (**c**) Conductivity of VPIL(TFSI) evaluated by AC impedance (σ_{ion}, ○) and CV (σ_{CV}, ◇) at various temperatures and the ratio of σ_{ion} and σ_{CV} (dashed line). Corresponding red lines were drawn using the VTF parameters in Table 1. The temperature dependence of σ_{ion}/σ_{CV} was plotted using the VFT parameters.

The EC device was fabricated following a procedure similar to that reported in our previous studies [7,8]. VPIL(TFSI) and [FcC_6ImC_1][TFSI] (Figure 1b) were mixed in a 1:1 molar ratio, calculated for VPIL(TFSI) on the basis of its viologen monomer units. A cleaned indium-tin-oxide (ITO) transparent electrode (GEOMATEC Co., Ltd. (Yokohama, Kanagawa, Japan), sheet resistance 10 Ω/sq, ITO thickness 200 nm) was laminated with a Himilan® ionomer film (25 μm thick) containing a 1 cm × 1 cm square aperture. The mixture of VPIL(TFSI) and [FcC_6ImC_1][TFSI] was then cast into the aperture, and the assembly was sealed by sandwiching with another bare ITO electrode to construct the EC device.

The EC experiment was carried out with a potentiostat (Huso (Kawasaki, Kanagawa, Japan), HECS 1110), a function generator (ToHo-TeCh (Yokohama, Kanagawa, Japan), FG-02), and a recorder (CONTEC (Osaka, Japan), AI-1664LAX-USB). Transmission absorption spectra were recorded by a multichannel spectrophotometer (Ocean Optics (Orlando, Florida, USA), HR4000CG-UV-NIR) with a Xe lamp (Ritu Oyo Kougaku Co., Ltd., (Niiza, Saitama, Japan)).

4. Results and Discussion

4.1. Conducting Properties of VPIL(TFSI)

Cyclic voltammograms (CVs) of VPIL(TFSI) were recorded at various temperatures using a two-electrode cell (Figure 2a). At 70 °C and 80 °C, the CVs obtained at 100 mV·s^{-1} exhibited peak-shaped waves (Figure 2b), characteristic of diffusion-controlled redox processes. At 60 °C and lower, however, the voltammograms became linear waveform, indicative of Ohmic behavior, in which the migration (drift) of redox-active ions is driven by the

potential gradient at the electrode surface. In this region, the current is dominated by migration and is independent of scan rate. The conductivity can be evaluated from the slope of the linear region according to Ohm's law:

$$R_s = \Delta E/\Delta I_{mig} \quad (1)$$

where R_s is the solution static resistance, ΔI_{mig} is the change in migration current, and ΔE is the electrode potential difference. The slopes of the CVs in the straight-line region directly correspond to the inverse number of $\Delta E/\Delta I_{mig}$. When the counter electrode is sufficiently large and placed far enough to surround the working electrode, the conductivity (σ_{CV}) can be obtained from the electrode radius (r_e) of the working electrode by the Newman equation [23]:

$$\sigma_{CV} = 1/(4r_e R_s) \quad (2)$$

The σ_{CV} values were compared with the ionic conductivity (σ_{ion}) obtained by AC impedance spectroscopy (Figure S2). Figure 2c shows the temperature dependence of σ_{CV}, σ_{ion}, and σ_{ion}/σ_{CV} values. Both conductivities exhibited similar temperature dependence. Since σ_{CV} is measured during the redox process of viologen units at the electrode surface, it could reflect not only electron transfer at the electrode/VPIL(TFSI) interface but also electron hopping transport into the bulk coupled with counter-ion migration. Moreover, ionic conductivity is mainly attributed to TFSI migration ($\sigma_{ion} \approx \sigma_{TFSI}$), because the viologen dication units are immobilized on the polymer backbone. In 60–80 °C range, the ratio σ_{ion}/σ_{CV} was approximately unity. Therefore, the electron hopping transport was limited solely by counter-ion migration at the temperature range. However, the observed ratio σ_{ion}/σ_{CV} was less than unity at lower temperatures and decreased further with decreasing temperature. This discrepancy likely reflects differences in phase constitution (formation of reduced phases) and transport mode (mixed-valence conduction), resulting in higher conductivity in the CV experiment than the ionic conductivity of TFSI species. That is, at low temperatures, the macroscopic motion of counter ions is significantly restricted, whereas electron hopping, which involves short-range electron transfer driven by microscopic reorientation, can remain effective. Furthermore, a reduced phase composed of oxidized and reduced viologen species, i.e., a mixed-valence phase, may be stabilized at lower temperatures. The pronounced difference observed for VPIL(TFSI) suggests a distinctive charge-transport mechanism arising from the immobilization of the redox-active viologen units on the polymer backbone.

The Arrhenius plots of conductivity were nonlinear (Figure S3) and could be fitted by the Vogel-Fulcher-Tammann (VFT) equation:

$$\sigma(T) = \sigma_0 \exp\left(\frac{B}{T - T_0}\right) \quad (3)$$

The fitted parameters are summarized in Table 1. The T_0 values obtained from σ_{ion} and σ_{CV} were close to each other and slightly lower than the glass transition temperature of VPIL(TFSI) (−23 °C, 250 K), consistent with their origin from the same T_g. At lower temperatures, the enhanced contribution from mixed-valence conduction could be attributed to the prolonged lifetime of reduced states formed near the electrode surface under higher viscosity.

Table 1. VFT parameters of σ_{CV} and σ_{ion}.

	σ_{CV}	σ_{ion}
$\ln(\sigma_0/S\cdot cm^{-1})$	−0.3839	−1.080
B/K	1601	1453
T_0/K	224.6	211.5

The apparent diffusion coefficient (D_{app}), which includes contributions from both physical diffusion and electron hopping diffusion, is a key electrochemical parameter for concentrated redox systems. Murray and co-workers reported extremely low diffusion coefficients for undiluted redox melts without solvent and supporting electrolyte, obtaining reversible CVs only at very slow scan rates (50 $\mu V\cdot s^{-1}$) [24]. Similarly, we observed quasi-reversible CVs for VPIL(TFSI) when the scan rate was decreased stepwise (Figure 3a,b). The peak-to-peak separation (ΔE_p) decreased with decreasing scan rate, reaching 91 mV at 10 $\mu V\cdot s^{-1}$ at 70 °C (Figure 3c). The linear dependence of peak current (i_p) on the square root of scan rate ($v^{1/2}$) indicated planar diffusion behavior. Incidentally, the measurement time was too long to collect the temperature dependence data. The diffusion coefficient was evaluated from the Randles–Ševčík equation:

$$i_p = 0.4463\, nFAc\sqrt{\frac{nFDv}{RT}} \quad (4)$$

where n, F, A, c, D, v, R, and T are the number of electrons, the Faraday constant, electrode area, concentration of redox species in the bulk, diffusion coefficient, scan rate, gas constant, and absolute temperature, respectively. In general, Equation (4) is applicable under purely diffusional conditions, i.e., in supporting electrolyte-containing solutions where migration currents are suppressed. In the case of the VPIL(TFSI) system, although no supporting electrolyte was added, Equation (4) was applied to estimate D_{app} value, because i_p and $v^{1/2}$ exhibited a good linear relationship at lower scan rates. As the result, D_{app} was calculated to be 2.2×10^{-11} cm^2·s^{-1} (2.4×10^{-11} cm^2·s^{-1} for the anodic process and 2.0×10^{-11} cm^2·s^{-1} for the cathodic process), assuming a redox-site concentration of $c_V = 1.0$ mol·L^{-1} at 70 °C.

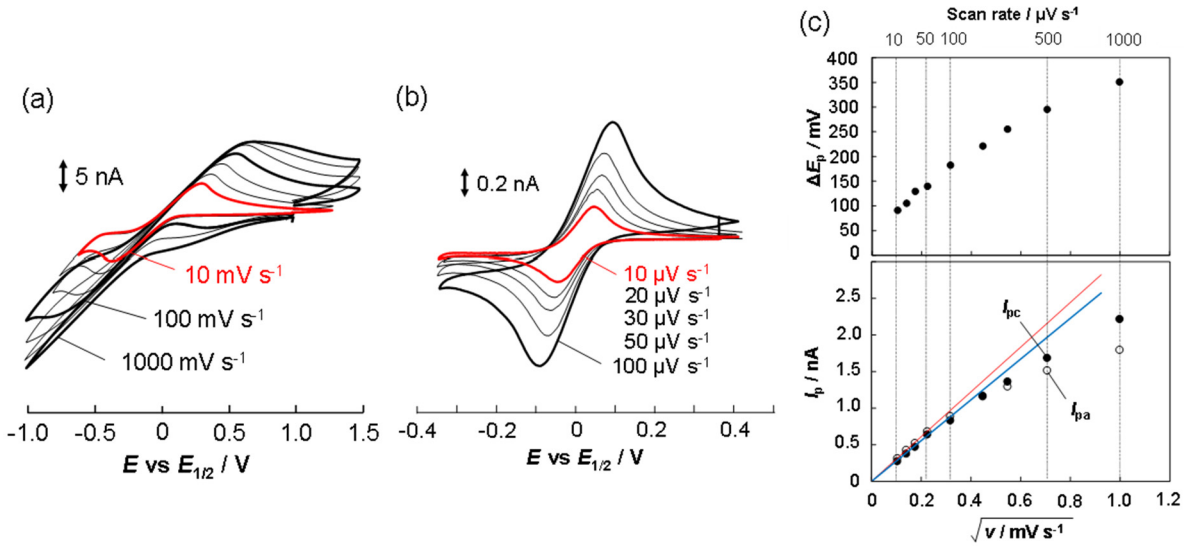

Figure 3. CVs and peak current analysis of VPIL(TFSI) at 70 °C with various scan rates. (**a**) CVs at the higher scan rates region. (**b**) CVs at the slower scan rate region. (**c**) Scan rate dependence of the peak separation (ΔE) and the peak currents (I_p) at 70 °C. The red and blue lines are the slopes in cathodic and anodic peak currents, respectively.

According to the Dahms-Ruff model [25–27], D_{app} is the sum of physical diffusion coefficient (D_{phys}) and electron hopping diffusion coefficient (D_{hop}). Because the viologen redox sites are covalently bound to the polymer backbone, D_{phys} is negligible, and $D_{app} \approx D_{hop}$. However, since migration effects (the enhancement of electron hopping by potential gradients) were not considered, the obtained D_{hop} is expected to be overestimated. The extent of this overestimation can be estimated from the ionic conductivity of the counter ion, as expressed by the Nernst-Einstein relation:

$$\sigma = \frac{F^2}{RT}\sum_i z_i^2 c_i D_i \quad (4)$$

where z_i, c_i, and D_i are the charge, concentration, and diffusion coefficient of species i, respectively. As previously mentioned, ionic conductivity is effectively governed by TFSI transport ($\sigma_{ion} \approx \sigma_{TFSI}$). At 70 °C, D_{TFSI} was 7.7×10^{-11} cm^2·s^{-1} with $c_{TFSI} = 2.0$ M. Since D_{TFSI} was 3.5 times larger than the measured D_{hop}, even when migration contributions were included, D_{hop} is presumed to be overestimated by several tens of percent. It is very difficult to quantitatively estimate migration contribution. However, according to steady-state theory of Hyk and Stojek [22,28], D_{hop} is overestimated by approximately 27% in the absence of supporting electrolyte and one-electron reduction of a dicationic redox species. This theory can also be applied to quasi-steady-state conditions, such as cyclic voltammetry at slow scan rates [22]. In addition, as reported by Savéant and co-workers, this estimation is considered to be valid [29]. Therefore, since D_{TFSI} is approximately five times greater than true D_{hop}, the apparent value of D_{hop} obtained experimentally is overestimated due to the migration effect. The electron-hopping scheme between reduced viologen (V^+) and oxidized viologen (V^{2+}), accompanied by counter anion A^- movement under charge-neutrality condition described as follows:

$$[A^-\ldots V^+] + [A^-\ldots V^{2+}\ldots A^-] \rightarrow [A^-\ldots V^+\ldots A^-\ldots V^{2+}\ldots A^-] \rightarrow [A^-\ldots V^{2+}\ldots A^-] + [V^+\ldots A^-]$$

When counter anion movement is sufficiently fast, it efficiently neutralizes the charge of the viologen species, allowing electron hopping to proceed smoothly. Thus, the rate-determining step for electron hopping reaction in VPIL(TFSI) is more likely the reorientation of viologen units, rather than counter-ion migration.

4.2. Application to EC Device

VPIL(TFSI) was employed as the active material in an EC device. The single liquid layer consisted of an equimolar mixture of VPIL(TFSI) (calculated on a viologen unit basis) and [FcC_6ImC_1][TFSI]. CV of the EC device is shown in Figure 4a. A driving voltage of 1.2 V was selected, which corresponds to the potential range of the one-electron oxidation of ferrocene and the one-electron reduction of viologen [7,8]. Figure 4b presents the difference absorbance spectra, defined as $\Delta Abs(1.2\ V) = -\log(I(1.2\ V)/I(0\ V))$, where $I(E)$ is the transmitted light intensity at voltage E. Two characteristic absorption bands appeared at 530 and 890 nm, indicative of the formation of π-dimerized reduced viologen units. In contrast to our previous reports [7,8], no band was observed at 600 nm, confirming the absence of monomeric viologen radical species. Initially, the EC device appeared light yellow due to the ferrocene, but upon applying 1.2 V it turned reddish purple, originating from the reduced viologen (Figure 4c).

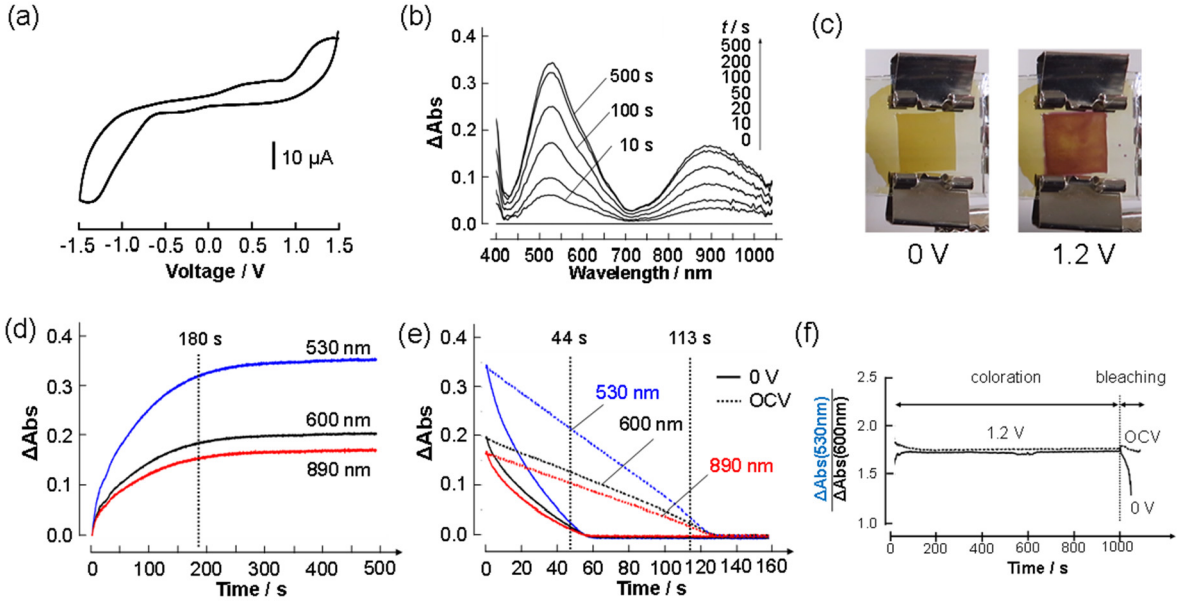

Figure 4. Electrochemical and spectro-electrochemical response of the EC device using VPIL(TFSI) and [FcC_6ImC_1][TFSI] at 298 K. (**a**) Cyclic voltammogram at 20 $mV \cdot s^{-1}$. (**b**) Absorption spectrum changes under electrolysis at 1.2 V. (**c**) Photo images of the EC device at 0 V and 1.2V. (**d**,**e**) Time course of absorbance changes at characteristic wavelengths in coloring process at 1.2 V and bleaching process at 0 V and OCV. (**f**) Time course of the absorbance ratio at 530 nm and 600nm in coloring (0 V to 1.2 V) and bleaching (1.2 V to 0 V and OCV) process.

Figure 4d,e show the time-dependent optical response during potential steps from 0 to 1.2 V (coloration) and back to 0 V and open circuit condition (bleaching). The coloration reached a steady state around 180 s (time to reach 90% absorbance change of steady state) at 1.2 V and proceeded under diffusion-controlled kinetics, as evidenced by the proportionality of absorbance to the square root of time (Figure S4a). Because of the greater IR drop in this system, a higher driving voltage (1.2 V) was required compared with our previous study (1.0 V) [7,8]. Bleaching required 44 s at 0 V and 113 s under open-circuit conditions, defined as the time needed to recover 90% of the initial state (see the supporting information video). In contrast, in our previous EC device based on a mixture of viologen-based and ferrocene-based RAILs [8], coloration reached a steady state within 26 s at 1.0 V, and bleaching required 12 s at 0 V and 45 s under open-circuit conditions. These can be attributed to the extremely high viscosity of the VPIL(TFSI)/[FcC_6ImC_1][TFSI] mixture, retarding the transport of redox species. This slow bleaching rate contributes to the memory effect of coloration, namely the persistence of the colored state even in the absence of an applied voltage. Increasing the viscosity of the solution and controlling the deposition behavior of the EC species on the electrode surface are considered effective strategies for enhancing the memory effect. However, careful design is required, as excessive deposition can also diminish the reversibility of the EC device. The absorbance ratio ΔAbs(530 nm)/ΔAbs(600 nm) remained constant during both coloring and bleaching (Figure 4f), suggesting that π-dimerization occurs much faster than the electrode reaction. This can be rationalized by the fact that the viologen units in VPIL(TFSI) are fixed to the polymer backbone, enabling reduced viologens to aggregate rapidly and efficiently. However, this aggregation behavior does not always have a positive effect on the EC device. The coloration and bleaching response during voltage cycling between 0 and 1.2 V gradually deteriorated, and noticeable color non-uniformity appeared after approximately 700 cycles (Figure S6). This degradation is

likely associated with the aggregation behavior of VPIL. The observed color non-uniformity suggests that the reduced viologen species are distributed unevenly in the solution, resulting in non-uniform conductivity. In fact, such non-uniform coloration was not observed in the system using a mixture of viologen-based RAIL and [FcC_6ImC_1][TFSI]. PILs can form various structures, which can be tuned by solvents or coexisting components [13–15]. In this study, we did not focus on optimizing the solvent or coexisting materials for VPIL(TFSI) to control its solubility and structural organization in the solution. Therefore, it will be necessary to develop a suitable coexisting component (e.g., a counter-electrode reactant or a solvent—only [FcC_6ImC_1][TFSI] was used in this study) that can dissolve the reduced form of VPIL(TFSI) uniformly in order to maintain high conductivity in the PIL-based system.

The coloration efficiency, defined as $\eta(\lambda) = \Delta Abs(\lambda)/Q$, was evaluated to be 118 $cm^2 \cdot C^{-1}$ from the slope of the charge-ΔAbs relationship at the initial stage of redox process (Figure S4c). The maximum coloration efficiency of the EC device can be described with molar absorption coefficient of the EC species according to the following equation [30]:

$$\eta_{\max} = 1000 \frac{\Delta\varepsilon(\lambda)}{F} \quad (5)$$

where $\Delta\varepsilon(\lambda)$ is molar absorption coefficient changes of electrochromic species both on anode and cathode and F is Faraday constant. The typical molar absorption coefficients of ferrocene are 100 $M^{-1} \cdot cm^{-1}$ at 440 nm in reduced form (Fc^0) and 425 $M^{-1} \cdot cm^{-1}$ around 620 nm in oxidized form (Fc^+) [31], and those of viologen are zero around visible region in oxidized form (V^{2+}), 1.0–1.4 × 10^4 $M^{-1} \cdot cm^{-1}$ around 600 nm in reduced monomer form (V^+), and 0.85–3.2 × 10^4 $M^{-1} \cdot cm^{-1}$ around 550 nm in the reduced π-dimer form (V^+) [32]. Those values give a practical approximation of $\Delta\varepsilon(\lambda) = (\varepsilon_{V+}(\lambda) - \varepsilon_{V2+}(\lambda)) - (\varepsilon_{Fc+}(\lambda) - \varepsilon_{Fc0}(\lambda)) \approx \varepsilon_{V+}(\lambda)$, resulting in η_{max} = 140 $cm^2 \cdot C^{-1}$ around 600 nm in the monomer form and 160 $cm^2 \cdot C^{-1}$ around 550 nm in the π-dimer form. The experimental coloration efficiencies were 118 $cm^2 \cdot C^{-1}$ at 530 nm, 73 $cm^2 \cdot C^{-1}$ at 600 nm, and 55 $cm^2 \cdot C^{-1}$ at 890 nm comparable to the theoretical value. By comparison with the EC devices based on viologen polymers and ferrocenes [33,34], coloration efficiency in this study was comparable. Thus, by utilizing VPIL(TFSI), we successfully fabricated an EC device exhibiting sharp contrast and high coloration efficiency. Again, EC device using VPIL(TFSI)

5. Conclusions

In this study, we demonstrated that a viologen-based molten poly(ionic liquid), VPIL(TFSI), can serve as a redox-active medium with distinctive charge transport properties and practical applicability in an EC device. Electrochemical analyses revealed that the conductivity of VPIL(TFSI) originates from electron hopping coupled with counter-ion migration, while diffusion coefficient evaluation suggested that the rate-determining step is the reorientation of viologen sites rather than ion transport. The combination of VPIL(TFSI) with a ferrocene-based RAIL enabled the fabrication of an EC device that operates without solvent and supporting electrolyte. The device exhibited reversible coloration with strong absorption associated with π-dimerized viologen species and delivered coloration efficiencies comparable to theoretical expectations. The use of VPIL(TFSI) in EC devices offers significant advantages. While the electronic conductivity of VPIL(TFSI) contributes positively to device performance, the tendency of viologen units to aggregate can adversely affect color uniformity. Therefore, the development of suitable cosolvents or counter-electrode coexistence materials that suppress aggregation is highly desirable. These findings highlight the potential of molten poly(ionic liquids) as a new platform for solvent-free, durable, and efficient redox-active systems, offering a promising design strategy for next-generation electrochromic and related electrochemical devices.

Supplementary Materials: The following supporting information can be downloaded at: https://media.sciltp.com/articles/others/2512161608182500/MI-25080353-SI.zip. Materials and Synthesis of VPIL(TFSI); Figure S1: DSC thermogram of VPIL(TFSI); Figure S2: EIS experiment; Figure S3: Arrhenius plot of σ_{CV} and σ_{imp}; Figure S4: Coloration kinetics and coloration efficiency of the EC device; Figure S5: Potential step durability test; Figure S6: Photo image of the EC device after 700th voltage cycling. Video S1: Coloration of EC device by the voltage of 1.2 V.

Author Contributions: H.T.: conceptuation, methodology, data curation, funding acquisition, writing—original draft preparation, investigation; S.T.: synthesis; S.M.: methodology; H.M.: investigation, data curation, funding acquisition, writing—reviewing and editing. All authors have read and agreed to the published version of the manuscript.

Funding: This work was supported by a Japan Society for the Promotion of Science (JSPS) Grant-in-Aid for Young Scientists (B) No. 26810052 (H.T.), Grant-in-Aid for Scientific Research (C) No. 20K05649 (H.T.), and 22K05258 (H.M.).

Data Availability Statement: Not applicable.

Acknowledgments: This work was the result of using research equipment (^{1}H NMR, elemental analysis, mass spectroscopy) shared in MEXT Project for promoting public utilization of advanced research infrastructure (Program for supporting introduction of the new sharing system) Grant Number JPMXS0422500320.

Conflicts of Interest: The authors declare no conflict of interest.

Use of AI and AI-Assisted Technologies: No AI tools were utilized for this paper.

References

1. Freemantle, M. Designer Solvents. *Chem. Eng. News* **1998**, *76*, 32–37.
2. Doherty, A.P. Redox-active ionic liquids for energy harvesting and storage applications. *Curr. Opin. Electrochem.* **2018**, *7*, 61–65.
3. Rochefort, D. Enabling new electrochemical methods with redox-active ionic liquids. *Curr. Opin. Electrochem.* **2019**, *15*, 125–132.
4. Xie, H.J.; Gelinas, B.; Rochefort, D. Redox-active electrolyte supercapacitors using electroactive ionic liquids. *Electrochrm. Commun.* **2016**, *66*, 42–45.
5. Mourad, E.; Coustan, L.; Lannelongue, P.; Zigah, D.; Medhdi, A.; Vioux, A.; Freunberger, S.A.; Favier, F.; Fontaine, O. Biredox ionic liquids with solid-like redox density in the liquid state for high-energy supercapacitors. *Nature Mater.* **2017**, *16*, 446.
6. Takechi, K.; Kato, Y.; Hase, Y. A Highly Concentrated Catholyte Based on a Solvate Ionic Liquid for Rechargeable Flow Batteries. *Adv. Mater.* **2015**, *27*, 2501–2506.
7. Tahara, H.; Baba, R.; Iwanaga, K.; Sagara, T.; Murakami, H. Electrochromism of a bipolar reversible redox-active ferrocene–viologen linked ionic liquid. *Chem. Commun.* **2017**, *53*, 2455–2458.
8. Tahara, H.; Uranaka, K.; Hirano, M.; Ikeda, T.; Sagara, T.; Murakami, H. Electrochromism of Ferrocene- and Viologen-Based Redox-Active Ionic Liquids Composite. *ACS Appl. Mater. Interfaces* **2019**, *11*, 1–6.
9. Hatazawa, T.; Terrill, R.H.; Murray, R.W. Microelectrode Voltammetry and Electron Transport in an Undiluted Room Temperature Melt of an Oligo(ethylene glycol)-Tailed Viologen. *Anal. Chem.* **1996**, *68*, 507–603.
10. Causin, V.; Saielli, G. Effect of asymmetric substitution on the mesomorphic behaviour of low-1melting viologen salts of bis(trifluoromethanesulfonyl)amide. *J. Mater. Chem.* **2009**, *19*, 9153–9162.
11. Jordao, N.; Cabrita, L.; Pina, F.; Branco, L. Novel Bipyridinium Ionic Liquids as Liquid Electrochromic Devices. *Chem. Eur. J.* **2014**, *20*, 3982–3988.
12. Bodappa, N.; Broekmann, P.; Fu, Y.-C.; Furrer, J.; Furue, Y.; Sagara, T.; Siegenthaler, H.; Tahara, H.; Vesztergom, S.; Zick, K.; et al. Temperature-Dependent Transport Properties of a Redox-Active Ionic Liquid with a Viologen Group. *J. Phys. Chem. C* **2015**, *119*, 1067–1077.
13. Yuan, J.; Mecerreyes, D.; Antonietti, M. Poly(ionic liquid)s: An update. *Progress in Polym. Sci.* **2013**, *38*, 1009–1036.
14. Qian, W.; Texter, J.; Yan, F. Frontiers in poly(ionic liquid)s: Syntheses and applications *Chem. Soc. Rev.* **2017**, *46*, 1124–1159.
15. Zhang, S.-Y.; Zhuang, Q.; Zhang, M.; Wang, H.; Gao, Z.; Yuan, J. Poly(ionic liquid) composites. *Chem. Soc. Rev.* **2020**, *49*, 1726–1755.
16. Ito, K.; Ohno, H. Polyether/salt hybrid: 5. Phase and bulk electrochemical response of viologens having poly(ethylene oxide) chain. *Polymer* **1997**, *38*, 921–926.
17. Chen, F.; Ren, Y.; Guo, J.; Yan, F. Thermo- and Electro-Dual Responsive Poly(ionic liquid) Electrolyte Based Smart Windows. *Chem. Commun.* **2017**, *53*, 1595–1598.
18. Burgess, M.; Chénard, E.; Hernández-Burgos, K.; Nagarjuna, G.; Assary, R.S.; Hui, J.; Moore, J.S.; Rodríguez-López, J. Impact of Backbone Tether Length and Structure on the Electrochemical Performance of Viologen Redox Active Polymers. *Chem. Mater.* **2016**, *28*, 7362–7374.
19. Greene, A.F.; Danielson, M.K.; Delawder, A.O.; Liles, K.P.; Li, X.; Natraj, A.; Wellen, A.; Barnes, J.C. Redox-Responsive Artificial Molecular Muscles: Reversible Radical-Based Self-Assembly for Actuating Hydrogels. *Chem. Mater.* **2017**, *29*, 9498–9508.
20. In, Y.; Park, H.; Kwon, J.; Kim, Y.; Kim, K.-W.; Pathak, D.; Kim, S.; Lee, S.; Moon, H. Isomeric effects of poly-viologens on electrochromic performance and applications in low-power electrochemical devices. *Sol. Energy Mater. Sol. Cells* **2022**, *240*, 111734.
21. Gharib, B.; Hirsch, A. Synthesis and Characterization of New Ferrocene-Containing Ionic Liquids. *J. Org. Chem.* **2014**, *2014*, 4123–4136.
22. Tahara, H.; Miyaji, M.; Murakami, H.; Sagara, T. Determination Method of Diffusion Coefficient in a Neat Redox-Active Ionic Liquid at a Microdisk Electrode in the Domains Ranging from the Steady-State to Potentiodynamic Near-Steady-State. *Anal. Chem.* **2023**, *95*, 9822–9830.
23. Newman, J. Resistance for Flow of Current to a Disk. *J. Electrochem. Soc.* **1966**, *113*, 501–502.
24. Vellzquez, C.S.; Hutchison, J.E.; Murray, R.W. Electrochemical Reactions and Charge Transport in Undiluted Room-Temperature Melts of Oligo(ethy1ene glycol)-Based Electron Carriers. *J. Am. Chem. Soc.* **1993**, *115*, 7896–7897.
25. Dahms, H. Electronic conduction in aqueous solution. *J. Phys. Chem.* **1968**, *72*, 362–364.

26. Ruff, I.; Friedrich, V.J. Transfer diffusion. I. Theoretical. *J. Phys. Chem.* **1971**, *75*, 3297–3302.
27. Lyons, M.E. Transport and kinetics in electroactive polymers. In *Advances in Chemical Physics*; Prigogine, I., Rice, S.A., Eds.; Wiley: New York, NY, USA, 1996.
28. Hyk, W.; Stojek, Z. Generalized Theory of Steady-State Voltammetry without a Supporting Electrolyte. Effect of Product and Substrate Diffusion Coefficient Diversity. *Anal. Chem.* **2002**, *74*, 4805–4813.
29. Andrieux, C.P.; Savéant, J.M. Electroneutrality coupling of electron hopping between localized sites with electroinactive counterion displacement. 1. Potential-step plateau currents. *J. Phys. Chem.* **1988**, *92*, 6761–6767.
30. Sagara, T.; Tahara, H. Redox of Viologen for Powering and Coloring. *Chem. Rec.* **2021**, *21*, 2375–2388.
31. Luong, J.H.T.; Male, K.B.; Zhao, S. Electrochemical Preparation of 1,1′-Dimethylferricinium from a Water-Soluble 1,1′-Dimethylferrocene-2-Hydroxypropyl-{3-cyclodextrinComplex and Its Applications in Enzyme Assay. *Anal. Biochem.* **1993**, *212*, 269–276.
32. Nchimi-Nono, K.; Dalvand, P.; Wadhwa, K.; Nuryyeva, S.; Alneyadi, S.; Prakasam, T.; Fahrenbach, A.C.; Olsen, J.-C.; Asfari, Z.; Platas-Iglesias, C.; et al. Radical-Cation Dimerization Overwhelms Inclusion in [*n*]Pseudorotaxanes. *Chem. Eur. J.* **2014**, *20*, 7334–7344.
33. Wang, X.; Guo, L.; Cao, S.; Zhao, W. Highly stable viologens-based electrochromic devices with low operational voltages utilizing polymeric ionic liquids. *Chem. Phys. Lett.* **2020**, *749*, 137434.
34. Correa, C.; Cordoba de Torresi, S.I.; Benedetti, T.M.; Torresi, R.M.; Correa, C.; Cordoba de Torresi, S.I.; Benedetti, T.M.; Torresi, R.M.J. Viologen-functionalized poly (ionic liquids): Spectroelectrochemical and QCM-D studies. *Electroanal. Chem.* **2018**, *819*, 365–373.

Commentary

Attaching Nanomaterials to the Cell Surface for Better Performance

Min Hao

The Wallace H. Coulter Department of Biomedical Engineering, Georgia Institute of Technology and Emory University, Atlanta, GA 30332, USA; mhao36@gatech.edu

Received: 6 December 2025; Accepted: 15 December 2025; Published:17 December 2025

Abstract: Piezoelectric nanostickers offer a promising strategy for neuronal repair by shifting stimulation from inside the cell to the cell surface and thereby overcoming lysosomal sequestration and potential cytotoxicity. This article highlights the mechanism, therapeutic potential, and key challenges toward clinical translation of this extracellular approach.

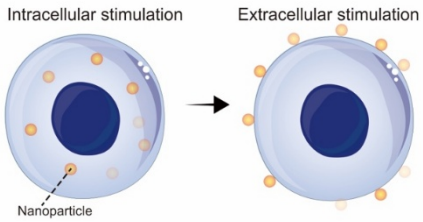

Keywords: nanomaterials, cellular internalization, cell surface

It is a major clinical challenge to repair traumatic brain injury (TBI), which is characterized by rapid neurological decay and long-term functional deficits [1]. The inherent difficulty stems from the limited regenerative potential of the central nervous system in adults. Neural stem cells (NSCs) offer a potential solution owing to their ability to differentiate into neurons or glial cells, but, in the absence of instructive cues, their spontaneous differentiation remains slow, inefficient, and often diverted from the neuronal lineage [2]. To this end, it is of paramount importance to develop effective strategies capable of regulating the fate of NSCs and accelerating neuronal differentiation. Recent years have witnessed the successful development of functional nanomaterials with well-controlled properties to guide the differentiation of NSCs toward neuronal lineages. In general, these nanomaterials exert their roles by interacting with the cells through either intracellular or extracellular stimulation.

In the case of intracellular stimulation, the nanomaterials are internalized by the cells prior to exerting their roles in the cytoplasm or specific organelles. Although this strategy may appear to be straightforward, its practical use is hampered by major biocompatibility issues, particularly for piezoelectric nanomaterials that have been shown with high cytotoxicity upon internalization. A notable example involves the use of barium titanate (BTO) nanoparticles [3]. Although BTO nanoparticles exhibit piezoelectric properties suitable for promoting neuronal differentiation, their internalization by cells paradoxically induces cytotoxic effects and compromises cell viability. The key issue lies in how BTO nanoparticles are processed inside the cell: once internalized, they are typically sequestered in the acidic environment of lysosomes. When subjected to ultrasound (US) irradiation to produce piezoelectric stimulation, this acidic sequestration can trigger a deleterious oxygen-evolution reaction, leading to the uncontrolled generation of highly reactive oxygen species. As a result, intracellular delivery is a detrimental strategy for this class of piezoelectric nanomaterials.

The extracellular route, in contrast, relies on nanomaterials capable of anchoring to the cell membrane for the delivery of factors directly to surface receptors or ion channels. Writing in *Nature Materials*, Qiu and coworkers report an elegant solution that moves the focus of stimulation from inside the cell to the cell surface [4]. The authors developed piezoelectric nanostickers comprised of BTO nanoparticles immobilized on flexible, conductive reduced graphene oxide (rGO) nanosheets (Figure 1A). The rGO nanoshet is instrumental in achieving stable adhesion to the cell membrane while preventing the nanoparticles from internalization. The BTO nanoparticles can generate piezoelectric stimulation under US, accelerating neuronal differentiation (Figure 1B,C). When NSCs equipped with these piezoelectric nanostickers were transplanted into the TBI site and exposed to 5-min US sessions every two days for 28 days, the treated tissue showed significant neuronal functional recovery and substantial structural repair (Figure 1D). Taken together, by shifting the location of BTO nanoparticles from the cytoplasm to the cell surface, this work demonstrates an effective method to overcome the critical barrier of

Copyright: © 2025 by the authors. This is an open access article under the terms and conditions of the Creative Commons Attribution (CC BY) license (https://creativecommons.org/licenses/by/4.0/).
Publisher's Note: Scilight stays neutral with regard to jurisdictional claims in published maps and institutional affiliations.

lysosomal sequestration and the subsequent toxicity from highly reactive oxygen species. In addition to BTO-based piezoelectric nanoparticles, other membrane-anchoring strategies have also been developed in the fields of drug delivery and immunotherapy, including Janus particles and microdisks with high biocompatibility [5,6]. These versatile platforms could, in principle, be adapted to anchor to the membrane of NSCs, activating specific surface receptors to promote neuronal differentiation and thereby offering alternative or complementary routes to neuronal regeneration.

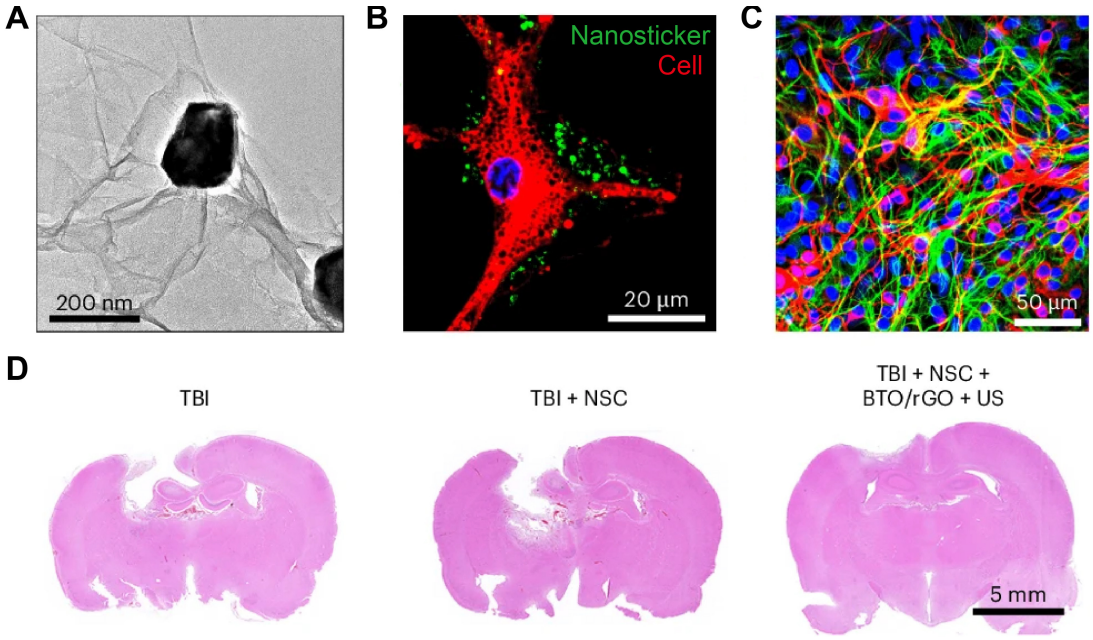

Figure 1. Characterizations and functionality of nanostickers. (**A**) Transmission electron microscopy image of a BTO/rGO nanosticker. (**B**) Fluorescence images showing the spatial distribution of nanostickers (green) on the membrane of NSC (red). (**C**) Fluorescence micrograph showing neurons (red) differentiated from NSCs upon piezoelectric stimulation with US for 15 days. (**D**) Hematoxylin and eosin staining images illustrating enhanced brain tissue regeneration at the TBI site following transplantation of NSCs with BTO/rGO piezoelectric nanostickers and subsequent US irradiation. Modified from Ref. [4] with permission. Copyright 2025, The Author(s).

Moving forward, translating this nanosticker technology from the laboratory to clinical use requires the addressing of several key challenges: (i) Are nanostickers safe and degradable in the brain? While the technology successfully avoids intracellular BTO toxicity, the long-term safety index (e.g., inflammatory response and biodegradability) in the sensitive brain microenvironment remains to be determined. (ii) How to appropriately administer the US stimulation to a patient? Since the therapeutic efficacy of the nanostickers depends on sustained US activation, establishing clinically safe and effective US delivery protocols becomes critical. Key parameters, including the application mode, treatment duration, frequency, and distance to the injury site, all need to be systematically optimized to achieve reproducible piezoelectric stimulation in the patient. (iii) How to achieve standardization and scalability? Transitioning toward large-scale clinical trials requires not only cost-effective and reproducible fabrication of nanostickers but also the establishment of standardized protocols for quality control, safety testing, and performance validation. Such efforts are critical to ensure inter-batch consistency and regulatory compliance during clinical manufacturing. (iv) Can precise control over neuronal lineage be achieved? Different injury models, such as TBI versus spinal cord injury, require distinct neuronal subtypes (e.g., glutamatergic or GABAergic neurons) for proper circuit repair. Achieving such lineage-specific control remains a major challenge in neural tissue engineering. Although the nanosticker can promote neuronal differentiation, further advances are needed to program the fate of NSCs with single-lineage precision, enabling the production of defined neuronal subtypes and supportive glial populations. Overcoming these barriers will be key to translating this nanosticker technology from a proof-of-concept to a clinically viable therapeutic platform.

Funding: This research received no external funding.

Data Availability Statement: Not applicable.

Conflicts of Interest: The author declares no conflict of interest.

Use of AI and AI-assisted Technologies: No AI tools were utilized for this paper.

References

1. Empl, L.; Chovsepian, A.; Chahin, M.; Kan, W.Y.V.; Fourneau, J.; Van Steenbergen, V.; Weidinger, S.; Marcantoni, M.; Ghanem, A.; Bradley, P.; et al. Selective Plasticity of Callosal Neurons in the Adult Contralesional Cortex Following Murine Traumatic Brain Injury. *Nat. Commun.* **2022**, *13*, 2659.
2. Hao, M.; Zhang, Z.; Liu, C.; Tian, Y.; Duan, J.; He, J.; Sun, Z.; Xia, H.; Zhang, S.; Wang, S.; et al. Hydroxyapatite Nanorods Function as Safe and Effective Growth Factors Regulating Neural Differentiation and Neuron Development. *Adv. Mater.* **2021**, *33*, 2100895.
3. Zhu, P.; Chen, Y.; Shi, J. Piezocatalytic Tumor Therapy by Ultrasound-Triggered and $BaTiO_3$-Mediated Piezoelectricity. *Adv. Mater.* **2020**, *32*, 2001976.
4. Wang, W.; Li, K.; Ma, W.; Li, Y.; Liu, F.; Kong, Y.; Wang, L.; Yi, F.; Sang, Y.; Li, G.; et al. Ultrasound-Activated Piezoelectric Nanostickers for Neural Stem Cell Therapy of Traumatic Brain Injury. *Nat. Mater.* **2025**, *24*, 1137–1150.
5. Hao, M.; Chen, Y.; Leisen, J.; Whitworth, T.J.; Xia, Y. Multifunctional Janus Nanoparticles Capable of Anchoring to the Cell Membrane and Serving as "Cellular Backpacks" for Advanced Theranostics. *J. Am. Chem. Soc.* **2025**, *147*, 12973–12981.
6. Shields, C.W.; Evans, M.A.; Wang, L.L.-W.; Baugh, N.; Iyer, S.; Wu, D.; Zhao, Z.; Pusuluri, A.; Ukidve, A.; Pan, D.C.; et al. Cellular Backpacks for Macrophage Immunotherapy. *Sci. Adv.* **2020**, *6*, eaaz6579.

Review

CO-Resistant Surface Dopant Engineering of Pt/Pd Catalysts for High-Performance Liquid Fuel Oxidation Reactions

Mrinal Kanti Kabiraz †, Joyjit Kundu †, Shajahan Shaik, and Sang-Il Choi *

Department of Chemistry and Green-Nano Materials Research Center, Kyungpook National University, Daegu 41566, Republic of Korea
* Correspondence: sichoi@knu.ac.kr
† These authors contributed equally to this work.
Received: 10 October 2025; Revised: 20 November 2025; Accepted: 25 November 2025; Published: 23 December 2025

Abstract: Surface dopant engineering has emerged as a powerful approach to enhance the catalytic properties of Pt and Pd nanomaterials by introducing site-specific modifications at the atomic scale. In liquid fuel oxidation reactions (LFORs), surface-decorated Pt/Pd catalysts demonstrate remarkable activity and durability by providing engineered sites that mitigate the long-standing challenge of carbon monoxide (CO) poisoning. Transition metal atoms and their oxides anchored on Pt/Pd surfaces act as anti-CO centers, facilitating more efficient fuel oxidation pathways while preserving catalytic stability. This review highlights recent advances in surface-decorated Pt/Pd catalysts, emphasizing the underlying mechanisms of CO resistance, synthetic strategies for dopant incorporation, and the structure-performance correlations that define their electrocatalytic behavior. We also summarize the performances achieved in methanol, ethanol, and other liquid fuel oxidation systems using dopant-engineered catalysts. Finally, we discuss the remaining challenges and future opportunities in rationally designing CO-tolerant catalytic surfaces for next-generation energy conversion devices.

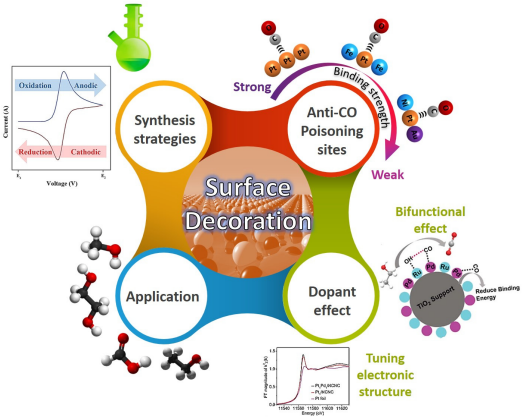

Keywords: surface dopant engineering; platinum; CO poisoning; fuel cell; electrocatalysis

1. Introduction

Renewable energy technology can tackle the current global energy crisis while minimizing environmental pollution. As a renewable energy technology, a direct liquid fuel cell (DLFC) has been regarded as one of the promising energy conversion devices that can convert the chemical energy of liquid fuels such as methanol, ethanol, and formic acid into electrical energy [1–4]. This DLFC system has certain advantages compared to hydrogen (H_2)-based fuel cells: low cost, plentiful, easy to transport, and safe to store. However, practical applications of DLFCs are limited mainly due to the poisoning effect of a reaction intermediate, such as carbon monoxide (CO), on the surface of catalysts, resulting in sluggish kinetics of anodic liquid fuel oxidation reaction (LFOR) and thus deteriorating the cell performances [5–7]. For example, platinum (Pt) and palladium (Pd) have been utilized as excellent LFOR catalysts, but their LFOR performances rapidly decrease owing to the CO adsorption (CO_{ads}) on their surfaces [8–12]. Therefore, from the viewpoint of catalyst poisoning, one way to improve LFOR is to develop state-of-the-art catalysts with anti-CO-poisoning sites [13–17]. Interestingly, decorating the surface of Pt/Pd catalysts with transition metal dopants, including Ru, Sn, Pd, Ni, and Cu, has been reported to create favorable surface-active sites toward LFOR. It is well-known that these dopants could increase the catalytic surface roughness, resulting in the non-continuous distribution of CO and thus the tolerance of the strong CO_{ads} behavior [18–20]. In addition, metal dopants on the surface of Pt/Pd promote the water dissociation at a lower potential, and the adsorbed OH (OH_{ads}) facilitates the oxidation of CO_{ads} to CO_2 [21–24]. These attractive

Copyright: © 2025 by the authors. This is an open access article under the terms and conditions of the Creative Commons Attribution (CC BY) license (https://creativecommons.org/licenses/by/4.0/).
Publisher's Note: Scilight stays neutral with regard to jurisdictional claims in published maps and institutional affiliations.

features of surface metal dopants have drawn much attention from the research community. Although there have been numerous articles related to the metal dopant strategy, to the best of our knowledge, there is an absence of a comprehensive overview of decorating anti-CO poisoning metal dopants on the surface of Pt/Pd nanocrystals for LFOR. Therefore, in this review, we discuss the underlying LFOR mechanisms in pristine and decorated catalyst surfaces, the metal doping synthesis strategies, advanced techniques to analyze LFOR, and the electrocatalytic performances of various LFOR. The liquid fuels discussed in this review are limited to ethanol, methanol, formic acid, and ethylene glycol (EG), considering their close feasibility in the practical DLFC systems regarding chemical energy density per volume and efficiency (Table 1). It is evident that liquid fuels, despite their higher theoretical chemical energy density per unit volume compared to H_2, still encounter significant challenges in DLFCs. The primary concern with DLFCs is the catalyst poisoning caused by CO. As such, in this review, we place emphasis on dopant metals as bifunctional catalytic sites and attribute them as anti-CO poisoning agents to tackle this issue. Finally, we outline the future designs of selective and highly stable electrocatalysts toward LFOR and provide practical insights for the DLFC applications.

Table 1. The number of electrons transferred, theoretical energy density normalized with fuel weight (W_s) and volume (W_e), standard redox potential, and theoretical energy conversion efficiency for various liquid fuels [25–27].

Liquid Fuel	Number of Electrons Transferred	W_s (kWh·kg^{-1})	W_e (kWh·l^{-1})	Standard Redox Potential (V)	Efficiency (%)
Hydrogen	1	32.80	1800	1.23	83
Formic acid	2	2.08	2086	1.40	99
Methanol	6	4.69	4820	1.21	97
Ethanol	12	8.99	6280	1.15	63
Ethylene glycol	10	5.27	5800	1.22	99

2. Understanding of LFOR Mechanisms

A typical working process of a DLFC is illustrated in Figure 1a. Liquid fuel is fed directly to the anode of the DLFC, and air/oxygen gas is provided to the cathode for the oxygen reduction reaction (ORR). During the fuel cell operation, charged ions pass through the membrane, and the electrons travel via an external circuit, generating electricity. To boost the DLFC performance, understanding of CO_{ads} configuration on the catalyst surface at the anode is essential. At the anode, electrocatalytic reactions using Pt-/Pd-based catalysts are generally hampered by the presence of CO_{ads}, as illustrated in Figure 1b. CO_{ads} can exist in two distinct configurations, namely top-type and bridge-type. The CO_{ads} configuration can be determined by IR analysis, which reveals a decrease in vibrational frequencies, indicating a stronger interaction of CO [28]. It has been observed that removing bridge-type CO_{ads} from the catalytic surface is more difficult compared to top-type CO_{ads}, as evidenced by the decreased vibrational frequencies in Figure 1c. Therefore, oxidizing bridge-type CO_{ads} to CO_2 requires more energy, as depicted in Figure 1c. Additionally, bridge-type CO_{ads} tend to be more prevalent on continuous Pt/Pd atom arrangements. Therefore, increasing the surface roughness of the catalyst by adding transition metal dopants can generate catalytic sites favoring a top-type CO_{ads} and disrupt the formation of bridge-type CO_{ads} [29,30]. In addition, decorating transition metal dopants (M) on the surface of Pt/Pd assists the dissociation of water molecules at a lower overpotential compared to the pristine Pt/Pd surface, and the produced OH_{ads} adsorbs preferentially on the dopants (M–OH_{ads}) [31,32]. Then, the M–OH_{ads} facilitates the oxidation of CO_{ads} to CO_2 on the neighboring Pt sites (Pt–CO_{ads} + M–OH_{ads} → CO_2 + H^+ + e^- + Pt + M) [33,34]. Therefore, a proper understanding of the reaction mechanism at a molecular level on the catalyst surface containing metal-dopants is important to enhance the performance of LFOR.

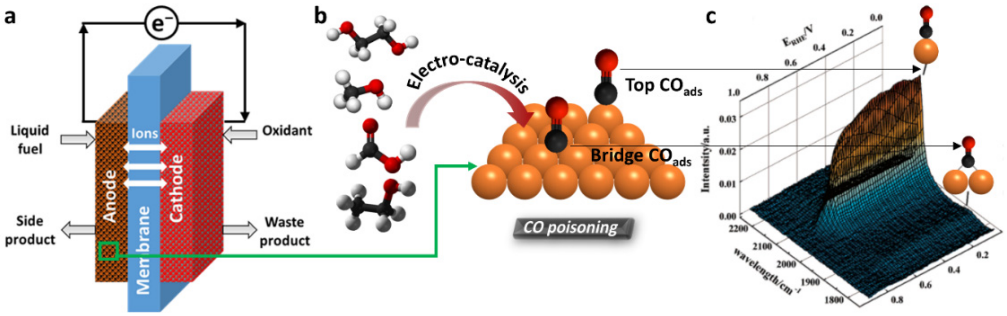

Figure 1. (**a**) A schematic illustration of a DLFC. (**b**) Indirect pathway during LFOR leading to catalyst poisoning by produced CO_{ads}. (**c**) Top and bridged CO_{ads} showing different IR spectra at different potentials. Reproduced with permission [28]. Copyright 2005, American Chemical Society.

2.1. Mechanism for Ethanol Oxidation Reaction (EOR)

Ethanol oxidation on Pt-/Pd-based catalysts generally proceeds through two competing pathways (Figure 2a) [35–37]. The direct pathway involves the complete oxidation of ethanol to CO_2, while the indirect pathway leads to incomplete oxidation to acetate anion. Both routes begin with the initial dehydrogenation of ethanol by breaking the C_α–H and O–H bonds [38], forming the stable *CH_3CO intermediate (Figure 2a) [39]. In the direct pathway, the C_β-dehydrogenation of *CH_3CO on pure Pt is the rate-determining step (RDS), producing intermediates such as *CH_2CO and *CHCO. These are ultimately oxidized to *CO_{ads}, which must be removed by OH-assisted oxidation to generate CO_2 [38]. However, the strong binding of *CO on Pt/Pd surfaces often leads to poisoning, limiting the C_1 route. As a result, the reaction frequently diverts toward the C_2 pathway, where *CH_3CO is oxidized to acetate without C–C bond cleavage [40].

For example, the DFT calculation of Pt(100) and Rh–O decorated Pt(100) surfaces provides direct evidence of their mechanistic differences during ethanol oxidation [41]. The calculated free energy profiles (Figure 2b,c) highlight the contrast clearly. On pure Pt(100) (Figure 2b), ethanol sequentially dehydrogenates to *CH_3CO, but the strong *CO adsorption and high barriers for its removal ($E_a \approx 0.92$–0.94 eV) restrict the direct pathway, causing poisoning and favoring C_2 product formation. By contrast, Rh–O decorated Pt(100) (Figure 2c) not only lowers the energy barrier for the potential-limiting step (*$CH_3CH_2OH \rightarrow$ *CH_3CHOH, $\Delta G \approx 0.27$ eV) but also facilitates C–C scission of *CH_3CO. Importantly, Rh–O sites weaken *CO binding and accelerate its OH-assisted oxidation (E_a = 0.72 and 0.24 eV), ensuring rapid *CO turnover and enabling near-complete ethanol oxidation to CO_2 at relatively low potentials.

Beyond single-site decoration, additional metal dopants can further promote full ethanol oxidation (Figure 2d,e). Transition metals (M) incorporated into the Pt/Pd surface enhance water dissociation, generating M–OH_{ads} that accelerate *CO oxidation on adjacent Pt/Pd sites (Figure 2d) [42,43]. This bifunctional effect alleviates poisoning and sustains the direct C_1 route. Moreover, introducing a second dopant creates a synergistic trimetallic environment that stabilizes intermediates in favorable adsorption geometries. For instance, on a Pt–Rh–M surface, *CH_3CO can adopt a chair-like configuration in which the C_α atom binds to Pt, the C_β atom strongly interacts with Rh, and the O atom coordinates with M (Figure 2e) [38]. This geometry lowers the barrier for C–C bond cleavage, making the pathway to CO_2 more accessible. Thus, multi-metallic decoration integrates bifunctional OH supply with geometric stabilization of intermediates, offering a powerful strategy to overcome CO poisoning and achieve complete EOR.

2.2. Mechanism for Methanol Oxidation Reaction (MOR)

Pt-/Pd-based catalysts have been reported to possess good activity and stability toward the MOR in acidic and alkaline media [44]. Previous studies indicated that electrocatalytic MOR performance is better in alkaline than in acidic media. In alkaline media, methanol and OH^- are initially adsorbed on the catalyst surface (Figure 3a). Subsequently, methanol dissociates into various CH_XO species and is continuously oxidized by OH_{ads}. The continuous supply of OH_{ads} comes from the water dissociation. In the final step, CO_{ads} react with OH_{ads} to generate CO_2 [45]. The MOR mechanism in acidic media differs from the alkaline one (Figure 3b). When the methanol is adsorbed on the Pt/Pd surface, the C–H bonds dissociate, leading to the formation of CO_{ads} intermediates and finally generation of CO_2 by reacting with OH_{ads}.

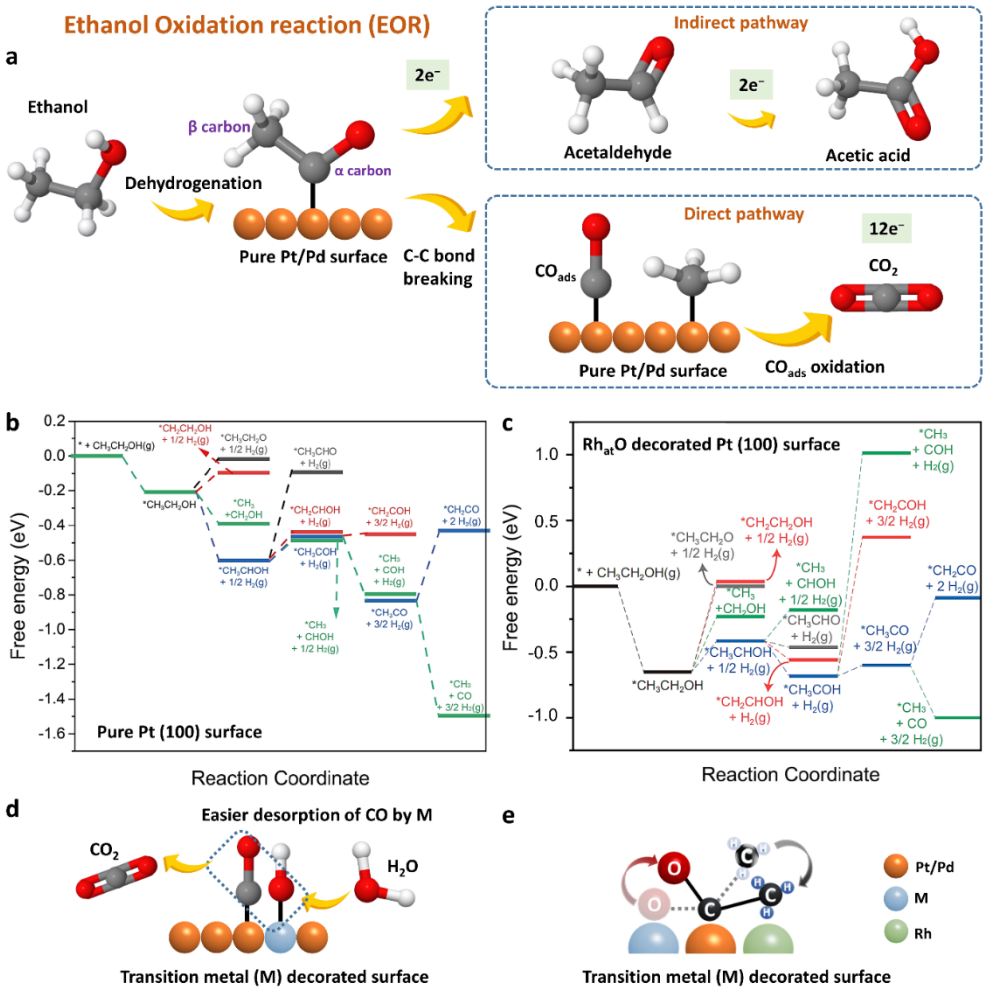

Figure 2. (**a**) Reaction pathways for the EOR mechanism on the pure Pt/Pd surface. (**b**) Free energy profile on Pt(100), where strong *CO adsorption limits C–C cleavage and favors C_2 products. (**c**) Free energy profile on Rh–O decorated Pt(100), where weakened *CO binding and faster CO oxidation promote complete oxidation to CO_2. Reproduced with permission [41]. Copyright 2022, National Academy of Sciences. (**d**) Bifunctional role of dopant atoms (M) in generating M–OH_{ads} that oxidize *CO_{ads} on neighboring Pt/Pd sites. (**e**) Chair-like adsorption of *CH_3CO on a trimetallic Pt–Rh–M surface, lowering the C–C cleavage barrier and driving full EOR.

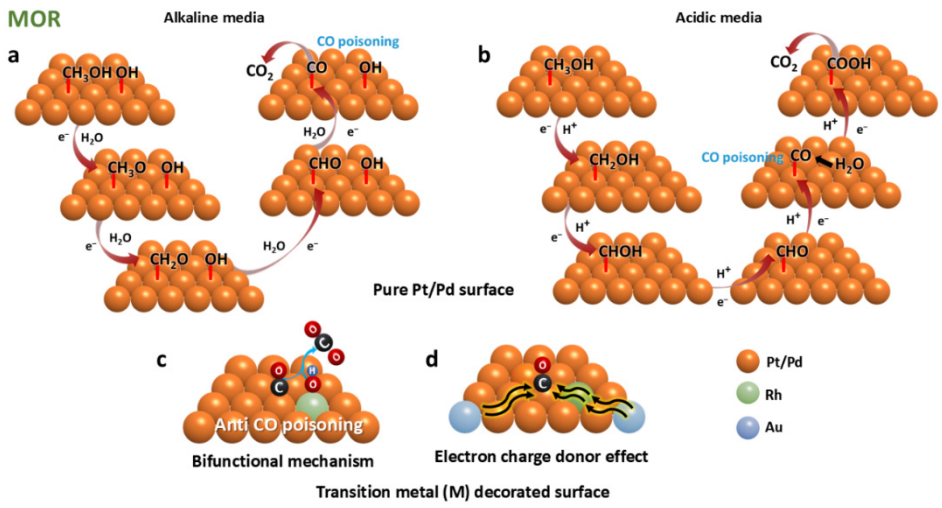

Figure 3. Reaction pathways for MOR in (**a**) alkaline and (**b**) acidic media on pure Pt/Pd surface. (**c**) Bifunctional mechanism of transition metal M decorated surface. (**d**) Stable adsorption configurations of CH_3CO* on M–Pt–Rh sites.

However, these MOR mechanisms are inhibited by strong CO_{ads} on the Pt/Pd surface, reducing the reaction between CO_{ads} and OH_{ads}. Therefore, introducing metal dopants that prefer OH_{ads} on the Pt/Pd surface can alleviate CO poisoning and increase the surface density of OH_{ads}, facilitating the oxidation of CO_{ads} to CO_2 (Figure 3c) [46–48]. In addition, selective dopants such as Sn, Ru, and Mo on the Pt/Pd surface can mitigate the bond strength of Pt–/Pd–CO_{ads} by donating charge to Pt/Pd and thus increasing their surface electron density. This electron donor effect enhances the bifunctional mode, which can dramatically improve the MOR performance (Figure 3d) [49].

2.3. Mechanism for Formic Acid Oxidation Reaction (FAOR)

Depending on the catalytic surface, the FAOR can follow two distinct reaction pathways, termed direct and indirect pathways (Figure 4a) [50]. A direct pathway is the direct conversion of HCOOH to CO_2 via dehydrogenation. However, the indirect or dehydration pathway is dominant since Pt–/Pd–COOH, and sequential Pt–/Pd–CO_{ads} are readily formed due to the difficulty of C-O bond cleavage during FAOR. The poisoning of CO_{ads} can be minimized by decorating the catalyst surface with another metal. Dinesh et al. showed the FAOR mechanism on a trimetallic PdRuPt catalyst [51]. Due to the substantial relocation of electrons from Pd and Ru to Pt, the binding energy of Pt–CO_{ads} is suppressed (Figure 4b). Additionally, Ru dopant preferring OH_{ads} can affect the oxidation of Pt–CO_{ads} to CO_2 formation. Thus, the bifunctional mechanism enables the suppression of CO poisoning and hence enhances the FAOR.

2.4. Mechanism for Ethylene Glycol Oxidation Reaction (EGOR)

EGOR is promising for direct alcohol fuel cells due to its high theoretical energy density (10 e^- per molecule) and safer handling compared to methanol. In addition to electricity generation, EGOR can yield value-added C_2 products (e.g., glycolic and oxalic acids), while also serving as a platform to design CO-tolerant catalysts relevant for broader electrocatalysis. Mechanistically, complete oxidation to CO_2 is rarely achieved because O–H bond cleavage is less favorable than C–O cleavage (Figure 4c). In addition, owing to the high activation for C–C bond cleavage, the oxidative products of EG are dominantly C_2 species (glycolaldehyde, glyoxal, glycolic acid, glyoxylic acid, oxalic acid) [42,43,52,53]. Only a tiny amount of EG is oxidized to C_1 species, which are further oxidized to CO and finally to CO_2. The sluggish EGOR can be enhanced by adding metal dopants on Pt or Pd surface. The electron charge donor effect of the metal dopant to Pt/Pd facilitates the breaking of the C–C bond and increases CO tolerance capacity (Figure 4d). Moreover, the bifunctional effect is also observed on metal dopant-containing surfaces to boost EGOR.

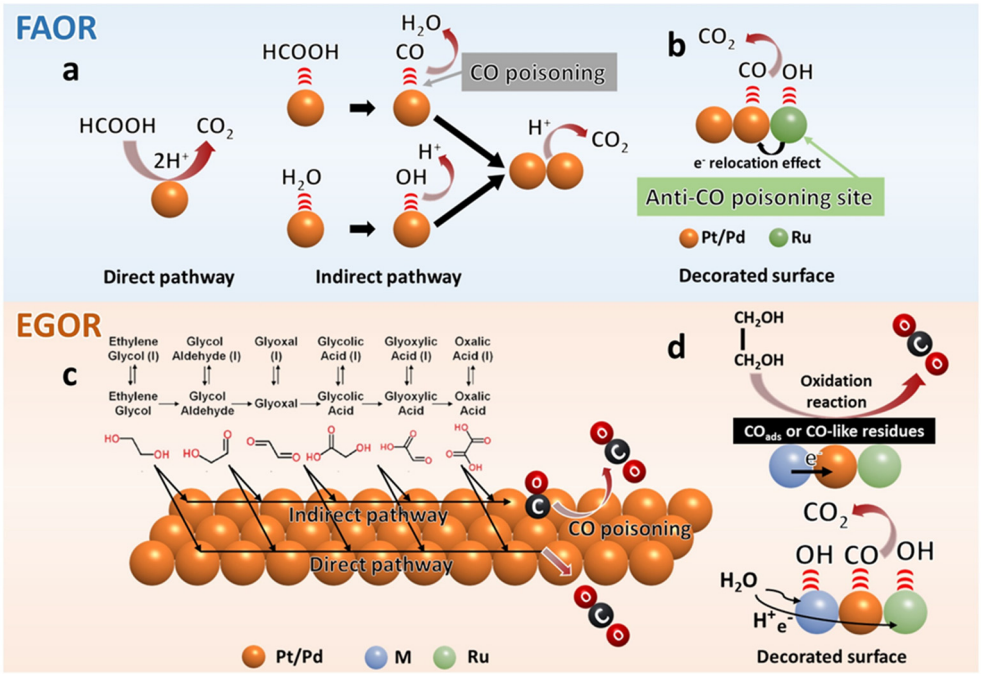

Figure 4. (**a**) Direct and indirect mechanisms of the FAOR on Pd/Pt surface and (**b**) FAOR on dopant-containing surface. Mechanism for EGOR (**c**) on Pt or Pd surface and (**d**) metal dopant-containing surface. Reproduced with permission [54]. Copyright 2009 Elsevier.

3. Protocols for Elemental Doping on Nanosurfaces

Surface doping with metals and metal oxides has become a central strategy for enhancing the electrocatalytic activity of Pt- and Pd-based nanocatalysts in liquid fuel oxidation reactions (LFOR). By tuning surface composition and introducing new active sites, these modifications alleviate CO poisoning and improve reaction pathways. Among the available synthetic approaches, wet-chemical routes are particularly attractive due to their scalability, reproducibility, and precise control over morphology and composition.

Choi et al. demonstrated this strategy by decorating Pt nanocubes with Rh using a two-step wet-chemical process [41]. At low Rh precursor loading, atomically dispersed single Rh sites were formed ($Rh_{at}O$–Pt NCs), whereas higher Rh input led to clustered Rh species ($Rh_{cl}O$–Pt NCs). HAADF-STEM and elemental mapping confirmed the uniform cubic morphology with distinct distributions of Pt, Rh, and O (Figure 5a,b). In-situ EXAFS at the Rh K-edge further revealed Rh–O coordination for the atomically dispersed case, while additional Rh–Rh peaks appeared in the clustered sample (Figure 5c,d). Structural models clearly distinguish isolated Rh–O sites from Rh–O clusters on Pt surfaces (Figure 5e,f).

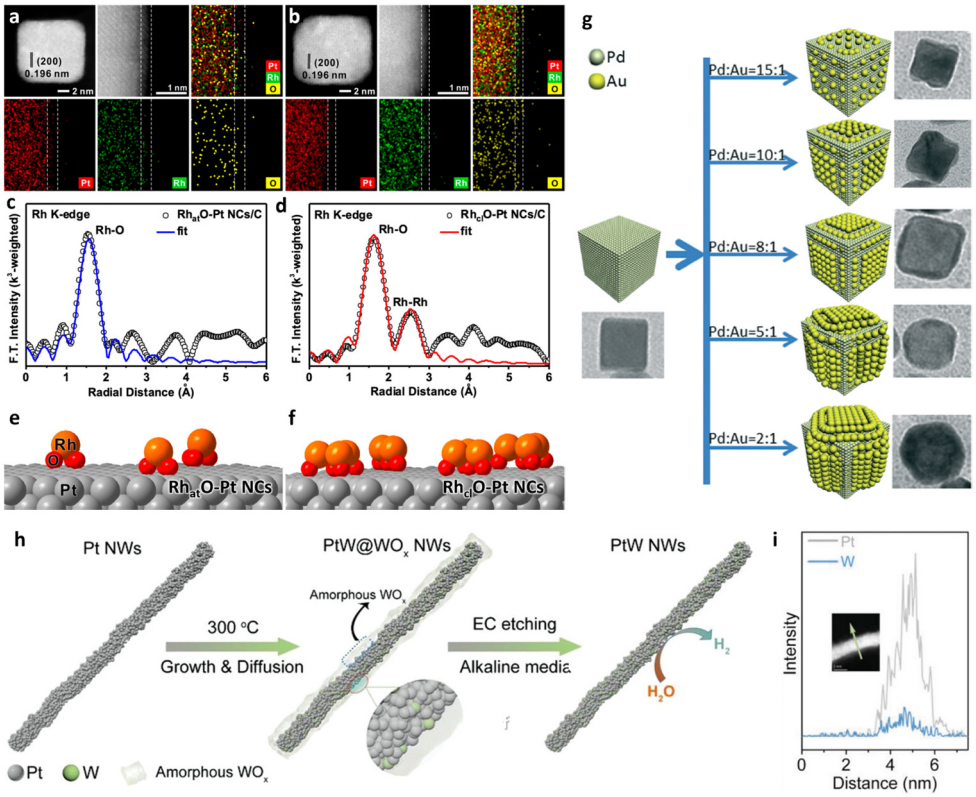

Figure 5. HAADF-STEM images and EDS mapping of (**a**) $Rh_{at}O$-Pt NCs and (**b**) $Rh_{cl}O$-Pt NCs. k^3-weighted Rh K-edge EXAFS spectra of (**c**) $Rh_{at}O$-Pt NCs/C and (**d**) $Rh_{cl}O$-Pt NCs/C. Schematic of (**e**) $Rh_{at}O$-Pt NCs and (**f**) $Rh_{cl}O$-Pt NCs decorated Pt surface obtained from wet-chemical synthesis. Reproduced with permission [41]. Copyright 2022, The National Academy of Sciences. (**g**) Schematic of Au-decorated Pd nanocubes showing the different surface composition. Reproduced with permission [55]. Copyright 2016, The Royal Society of Chemistry. (**h**) Schematic illustration for the decoration on the PtW NWs using electrochemical etching process. (**i**) EDS line mapping profile for W-doped Pt NWs. Reproduced with permission [57]. Copyright 2022, John Wiley & Sons.

Du et al. extended the concept to Pd nanocubes by introducing Au decoration via a seed-mediated method [55]. Pd nanocubes were first synthesized by ascorbic acid reduction and subsequently coated with Au at controlled Pd/Au ratios. The degree of Au coverage strongly influenced morphology: discrete decoration was obtained at 15:1 and 10:1 ratios, more uniform layers at 8:1 and 5:1, and complete surface encapsulation at 2:1. The progressive evolution from sharp cubes to irregular morphologies was clearly observed in TEM and schematic models (Figure 5g). EDS mapping further confirmed Au enrichment on Pd surfaces, and the decorated catalysts showed enhanced ethanol oxidation activity.

Beyond chemical synthesis, electrochemical methods offer dynamic restructuring of catalytic surfaces. Yin et al. produced PdBi–$Bi(OH)_3$ nanochains by solvothermal synthesis followed by electrochemical cycling in alkaline

electrolyte [56]. The surface oxidation of Bi introduced abundant OH_{ad} species that promoted CO removal, thereby boosting EOR performance.

Electrochemical etching provides yet another doping route. Electrochemical etching is a process that removes a metal component from the catalyst surface via electrochemical treatment. For example, Huang et al. utilized EC on amorphous WO_x-coated ultrathin PtW nanowires (PtW@AWO$_x$ NWs) to form W-doped PtW NWs [57]. For the synthesis, Pt NWs in OAm solution containing W species were heated at 300 °C to obtain the PtW@AWO$_x$ NWs (Figure 5h). Then, etching was performed on PtW@AWO$_x$ NWs using linear sweep voltammetry in 1.0 M KOH solution for 7 cycles. EDS line scanning revealed that the W was doped on the PtW NWs after EC etching (Figure 5i). Despite the negative reduction potential of W^{6+}/W^0 (E_0 = −1.1 V vs. RHE), the WO_x species was reduced to W^0 and doped into Pt NWs. The preformed Pt NWs created strongly reductive species of Pt–H by an autocatalytic surface reduction process, which led to the reduction of W^{6+} to W^0 and finally doped on the surface of Pt NWs.

Together, these studies demonstrate how surface doping through noble metals, oxides, or electrochemical modification enables precise control over catalytic interfaces and enhances resistance to CO poisoning. While electrochemical treatments provide mechanistic insights and dynamic modification, wet-chemical synthesis remains dominant due to its reproducibility and scalability. Integrating both strategies, supported by advanced characterization tools, will be crucial for designing next-generation nanocatalysts with optimized activity and durability for LFOR.

4. Surface Decorated Pt/Pd Catalysts Toward LFOR

The decorated nanocatalysts with anti-CO poisoning sites demonstrated their superior electrocatalytic performance toward LFOR over pure Pt/Pd surfaces. This section discusses the activity, stability, and *in-operando* techniques to electrochemically characterize the catalytic performance of the decorated surfaces toward LFOR. The extensively studied liquid fuels discussed in this paper include methanol, ethanol, formic acid, and ethylene glycol.

4.1. MOR Performance

In direct methanol fuel cell (DMFC), the hydrogen oxidation reaction (HOR) at the anode of proton exchange membrane fuel cells (PEMFCs) is replaced by the MOR. DMFCs are suitable for small portable electronic devices due to their easily exchangeable fuel cartridges, high energy density, and fast charging rate [58–60]. Despite the advantages described above, the practical use of the DMFC is laden with several challenges. One of the major problems is the partial oxidation of the methanol, leading to sluggish oxidation reaction kinetics that reduce the number of transferred electrons [59–61]. Moreover, the partial oxidation of methanol produces CO, which deteriorates the cell performance [62,63].

Nanocatalysts containing anti-CO sites on the surface have been proven to be an effective strategy to address the problem and improve the MOR performance significantly [64,65]. For instance, Lin et al. reported a facile synthesis of Ru-decorated Pt icosahedra and cubes as highly active electrocatalysts for MOR [66]. Ru-decorated Pt catalysts have been identified as a promising candidate for MOR due to their excellent catalytic activity and improved CO tolerance arising from the bifunctional and ligand effects between the two metal elements [67–69]. Figure 6a,b show HAADF-STEM images with atomic resolution and EDX mapping images of the PtRu icosahedron and cube enclosed by (100) and (111) facets, respectively. From the EDX mapping of the icosahedron and cube, Ru (red color) was found to be decorated on the Pt surface (green color), suggesting a Ru-decorated Pt structure. Figure 6c compares the CVs of the catalysts for MOR performed in a solution containing 0.5 M H_2SO_4 and 0.5 M CH_3OH. The higher I_f/I_r value of 1.50 and 2.02 for PtRu icosahedra and cubes than that of a typical PtRu alloy catalyst (Pt_7Ru/C) indicates that the decoration of Ru on the surface of Pt can improve CO tolerance during MOR. Accordingly, the Ru-decorated Pt icosahedra exhibited enhanced specific (0.76 mA·cm^{-2}) and mass (74.4 mA·mg$_{Pt}^{-1}$) activities toward MOR, which were about ~6.7 and ~2.2 times higher than those of the Pt_7Ru/C, respectively (Figure 6d). The enhanced performance of the Ru-decorated Pt nanocrystals can be explained by the bifunctional mechanism discussed in Section 2.2 [70,71]. In terms of stability, the Ru-decorated Pt icosahedra showed ~10% current retention (0.05 mA·cm^{-2}) and the Pt cubes showed ~5% retention (0.01 mA·cm^{-2}) after 2000 s of continuous operation, confirming improved but still limited stability. Although PtRu alloys also exhibit bifunctional behavior, surface Ru decoration provides a greater improvement. This is because Ru atoms in alloys may be buried in the bulk lattice and thus unavailable for catalysis, while surface-decorated Ru remains fully accessible at the reaction interface. Generally, the presence of Ru on the Pt surface can activate the water to form oxygenated species such as OH_{ads} [72]. The OH_{ads} species on Ru sites further oxidize and finally remove the CO_{ads} intermediates on Pt sites, which enhances the electrocatalytic properties of Ru-decorated Pt catalysts towards

MOR. Moreover, Pellicione et al. showed that on a Ru-decorated Pt surface, the removal of CO species on Pt sites is limited, and CO can co-adsorb on Ru sites with OH species through the migration from Pt sites [73]. Oxidation of CO species with co-adsorbed OH species on Ru sites is also a critical step for the enhanced activity towards MOR. This analysis also supports the bifunctional mechanism towards MOR for such Ru-decorated Pt bimetallic catalysts, where surface decoration ensures a higher density of exposed Ru–OH sites compared to alloyed PtRu, thereby enabling more effective CO oxidation.

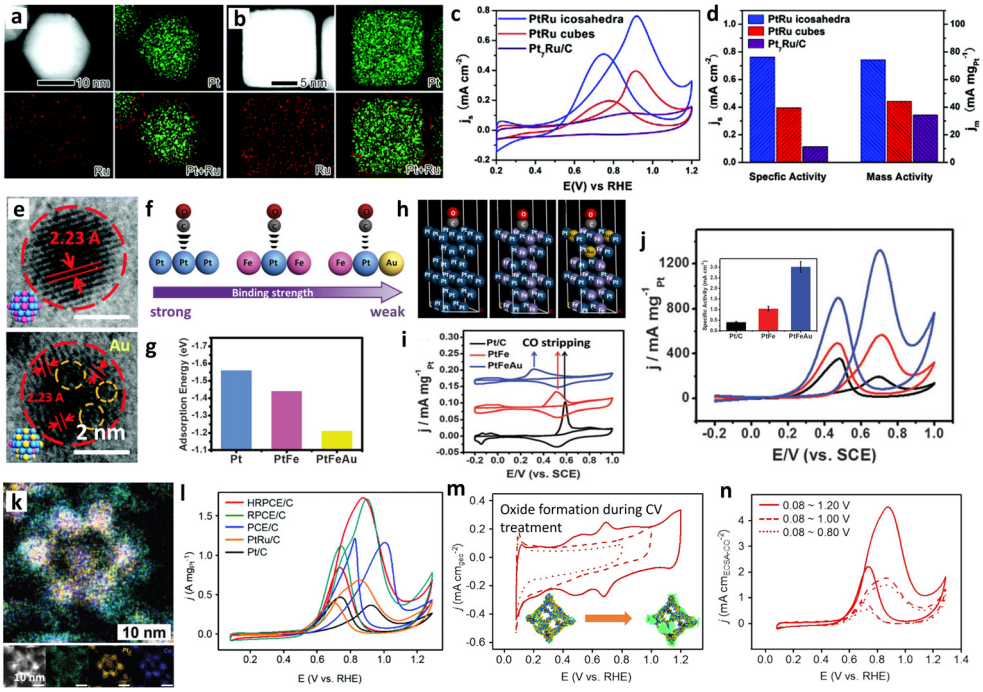

Figure 6. EDX mapping images of (**a**) Ru decorated Pt bimetallic icosahedra and (**b**) Ru decorated Pt bimetallic cubes. (**c**) CV of three different catalysts, including Ru-decorated Pt icosahedra, Ru-decorated Pt cubes, and Pt_7Ru/C for MOR. (**d**) MOR specific and mass activity at the peak position of forward curve. Reproduced with permission [66]. Copyright 2016, The Royal Society of Chemistry. (**e**) HRTEM images of PtFe and PtFeAu nanocrystals, the discontinuous lattice circles of PtFeAu (yellow circles) indicate the decoration of Au atoms. (**f**) Schematic illustration of the binding strength between CO molecule and the Pt centers of Pt, PtFe, and PtFeAu catalysts. (**g**) The model of adsorption of CO on top-site of Pt (111), PtFe (111), and PtFeAu (111). (**h**) Simulation of adsorption energy (E_{ads}) of CO on these three catalysts. (**i**) CO stripping curves of PtFeAu, PtFe, and Pt/C nanocrystals. (**j**) MOR curves of the catalysts in an electrolyte containing 0.5 M H_2SO_4 and 1.0 M CH_3OH. Inset shows the specific activities for MOR. Reproduced with permission [74]. Copyright 2016, The Royal Society of Chemistry. (**k**) HAADF-STEM with EDX mapping images of RuO_x-decorated RuPtCu nanocages. (**l**) CVs of RuO_x-decorated RuPtCu nanocages, state-of-the-art PtRu/C and Pt/C normalized by $ECSA_{CO}$ in solutions containing 0.1 M $HClO_4$ and 1.0 M CH_3OH with a scan rate of 50 $mV \cdot s^{-1}$. (**m**) CVs of RuO_x-decorated RuPtCu nanocages at different potential range in a solution containing 0.1 M $HClO_4$ and (**n**) their corresponding MOR performance [78]. Copyright 2018, The Royal Society of Chemistry.

Surface decoration of a bimetallic alloy with a third metal, forming a trimetallic surface, can also enhance MOR performance. For instance, Cai et al. reported that Au-decorated PtFe nanocatalysts show high resistance to CO poisoning owing to the role of Au as the anti-CO poisoning site [74]. HRTEM images showed the highly crystalline nature of PtFe nanocubes (NCs), whereas the Au-decorated PtFe NCs showed a discontinuous structure (indicated by yellow circles) (Figure 6e). The adsorption energy (E_{ads}) of CO on the (111) plane of bare Pt, Pt_1Fe_1, and $Pt_5Fe_4Au_1$ was calculated (Figure 6f–h), showing that Pt(111) exhibited the highest E_{ads} of −1.56 eV, while the Pt_1Fe_1(111) offered a lower E_{ads} (−1.44 eV). Interestingly, $Pt_5Fe_4Au_1$ reported the reduced E_{ads} of −1.21 eV. The electron charge transfer between the Pt atoms surrounded by Fe and Au atoms resulted in a weaker binding interaction between the CO and the Pt surface [75,76]. The authors proved their claims by conducting CO stripping analysis, showing that the peak potential of ternary PtFeAu (312 mV vs. SCE) is lower by 274 and 201 mV compared to Pt/C and PtFe, respectively. This significant negative shift of Au-decorated PtFe reveals the weakest CO-binding on Pt centers [74,77]. The anti-CO poisoning capacity of Au-decorated PtFe showed a mass activity of 1324 $mA \cdot mg_{Pt}^{-1}$, which was 2.3 and 6.6 times that of PtFe and commercial Pt/C catalysts, respectively (Figure 6j).

Moreover, these Au-decorated PtFe catalysts retained ~35% of their activity (~1.0 mA·cm^{-2}) even after 5000 s of operation, indicating superior long-term stability compared to PtFe and Pt/C.

Metal oxides can also improve the CO tolerance capability when utilized as a dopant on the Pt surface. For instance, Park et al. reported the CO-tolerant RuO_x decorated RuPtCu trimetallic nanocages (HRPCE/C) with highly improved MOR performance [78]. Representative HAADF- STEM with EDX mapping images of RuO_x decorated ternary nanocages are shown in Figure 6k. Since the OH (OH_{ad}) adsorbed on RuO_2 sites adjacent to Pt could promote the CO tolerance, MOR activity was expected to be enhanced [79–81]. For this, MOR activities of HRPCE/C, state-of-the-art PtRu/C, and Pt/C were recorded in solutions containing 0.1 M $HClO_4$ and 1.0 M CH_3OH with a scan rate of 50 mV·s^{-1} from 0.08 to 1.29 V (vs. RHE) (Figure 6l). The MOR mass activity of HRPCE/C (1.73 A·mg^{-1}) was about 2.5 and 5 times that of PtRu/C (0.69 A·mg^{-1}) and Pt/C (0.37 A·mg^{-1}), respectively. In order to understand the role of RuO_2, the authors controlled the amount of RuO_2 formed on the surface of the catalyst by conducting CV cycling at different potential ranges (Figure 6m). When the HRPCE/C was pre-cycled at a vertex potential of 1.20 V (vs. RHE), a larger amount of RuO_2 was formed, resulting in the specific activity of 4.52 mA cm^{-2}, which was 2.6 and 3.1 times higher than the catalysts pre-cycled at 0.80 V (1.76 mA·cm^{-2}) and at 1.00 V (1.48 mA·cm^{-2}) (Figure 6n), respectively. Importantly, these RuO_x-decorated RuPtCu nanocages maintained ~19% activity (~0.8 mA·cm^{-2}) even after 4000 s of testing, highlighting their stable long-term performance. The authors concluded that the enhanced MOR performances of HRPCE/C are linked to the synergy between the decorated RuO_2 and Pt sites [78]. A comparison of the MOR performance of the catalysts, including stability, is listed in Table 2. These results demonstrate that the MOR performance can be significantly improved by enhancing the anti-CO poisoning capability by decorating a suitable third metal atom on the surface.

Table 2. Comparison of MOR performance of various decorated nanocatalysts.

Catalyst	MA [a] (A·mg$_{Pt/Pd}^{-1}$)	MA Enhancement vs. Pt/C	SA [b] (mA·cm^{-2})	SA Enhancement vs. Pt/C	CA Stability [c]	Electrolyte	Ref.
Ru-decorated Pt cubes	0.41	~3	0.42	~2	~5% (0.01 mA·cm^{-2}) activity retention after 2000 s	0.5 M CH_3OH + 0.5 M H_2SO_4	[66]
Ru-decorated Pt icosahedra	0.75	~5	0.76	~4	~10% (0.05 mA·cm^{-2}) activity retention after 2000 s	0.5 M CH_3OH + 0.5 M H_2SO_4	[66]
Pt decorated Ru NWs	0.36	4	0.36	3	N/A	0.5 M CH_3OH + 0.1 M $HClO_4$	[82]
Au-decorated PtFe	1.32	6.6	3.01	7.34	~35% (~1.0 mA·cm^{-2}) activity retention after 5000 s	0.5 M CH_3OH + 0.5 M H_2SO_4	[74]
Au decorated PtNi	1.48	5	3.84	2	~10% activity retention after 4000 s	1.0 M CH_3OH + 0.5 M H_2SO_4	[49]
RuO_x-decorated RuPtCu nanocages	1.73	5	4.52	8	~19% (~0.8 mA·cm^{-2}) activity retention after 4000 s	1.0 M CH_3OH + 0.1 M $HClO_4$	[78]

[a] Mass activity, [b] Specific activity, [c] Chronoamperometry.

The recent progress in decorated Pt/Pd catalysts clearly shows that surface dopant engineering is a powerful strategy for enhancing MOR activity and CO tolerance. In particular, surface-exposed dopants, compared to alloyed or buried atoms play a significant role by supplying abundant OH_{ad} species and weakening CO adsorption. However, long-term stability remains a major limitation, as most catalysts still show decreased activity under continuous operation. In this view, future MOR catalysts should prioritize stabilizing the dopant-Pt interface, preventing dissolution, and maintaining accessible bifunctional sites.

4.2. EOR Performance

Ethanol is often discussed as a promising fuel candidate for the large-scale applications of fuel cells due to its high energy density (Table 1), low toxicity, and easy storage and transportation for practical uses compared to H_2 gas; however, its practical feasibility is still under active investigation [83,84]. Though pure Pt/Pd nanocatalysts are usually utilized for EOR, CO poisoning during EOR severely affects their durability performance. Therefore, a series of modifications to pure Pt/Pd surface by adding transition metals as co-catalysts in various structures and

compositions, including adatoms, adlayers and intermetallic Pt–M assemblies, bimetallic alloys, metal oxides, and core-shell nanostructures were introduced to improve EOR performance [9,78,85–89]. However, those Pt-/Pd-based catalysts could not perform the total oxidation of ethanol to CO_2 at moderate positive potentials and were poisoned by CO species over time [90–92]. These led to the investigation of decorating pure Pt or Pd surface with metal dopants as anti-CO sites. For example, Zhong et al. demonstrated that the EOR activity of Au-decorated Pd heterogeneous nanocubes strongly depends on Pd/Au molar ratios ranging from 15:1 to 8:1 (Figure 7a,b) [55]. Their results indicated that Pd_5Au_1 exhibited the highest EOR mass activity which is around 2.2 times higher than that of monometallic Pd. The possible EOR enhancement was due to the addition of Au to Pd nanocubes, resulting in a tensile strain in the structure of the surface of Pd and an upper shift in the d-band center of Pd [93,94]. It was also reported that the improved OH^- adsorption onto the surface of the catalyst promoted the elimination of ethoxy intermediates from the catalyst surface and enhanced EOR performance [95]. They also suggested that the optimal ratio of Pd_5Au_1 showed a higher ECSA value due to the presence of more active sites, which might significantly affect EOR. Therefore, it is expected that maximum EOR can be achieved by decoration and optimal surface composition. However, Pd–Au catalysts still showed limited durability, with only ~5% activity retained after 2000 s.

Occasionally, a stable surface is projected to behave as an excellent catalytic site for EOR. The surface decoration strategy, including heterogeneous atomic doping, can stabilize the initial morphology and prevent the loss of transition metals during electrocatalysis. In particular, morphology such as one-dimensional (1D) nanowires (NWs) can benefit from surface decoration due to its exceptional surface area and intrinsic activity to improve catalytic performance. For example, Li et al. investigated lavender-like Ga-doped Pt_3Co NWs on EOR, where optimized surface energy derived from the doping of Ga atoms improved EOR activity [96]. The surface energy of the Ga-doped Pt_3Co (111) surface was measured and further compared to the Pt_3Co (111) and pure Pt surfaces (Figure 7c). Surface energy indicates an approximate measure of energetic surface stability and the lower the surface energy, the more stable the catalyst's surface. The surface energy of the Pt_3Co was calculated to be 1.29 $J \cdot m^{-2}$, which is 11% lower than that of the pure Pt surface (1.45 $J \cdot m^{-2}$). Interestingly, doping of Ga into the Pt_3Co surface further lowers its surface energy to 1.17 $J \cdot m^{-2}$, rendering the Ga-doped Pt_3Co surface even more stable. Yuge et al. showed that the stable alloy surfaces exhibited weaker CO binding compared to the pure Pt surface [94]. Therefore, Ga doping on Pt_3Co surface can act as anti-CO poisoning sites for improved EOR performance. Consequently, the 4% Ga–Pt_3Co/C delivered the highest electrocatalytic performance with a specific activity of 4.2 $mA \cdot cm^{-2}$ and a mass activity of 2.0 $A \cdot mg^{-1}$, respectively (Figure 7d). Moreover, Ga–Pt_3Co NWs retained ~60% of their activity after 36,000 s, highlighting their remarkable durability. Mao et al. reported the Mo-doped PtNi NWs with a diameter of ~2.5 nm, where the addition of Ni produces surface defects and Mo can stabilize Ni and Pt atoms, leading to superior EOR performance [97]. The incorporation of 3d transition metals (Ni) into the Pt lattice to form ternary Pt–Mo–Ni NWs can promote the adsorption of hydroxyl species from water and remove the poisoned CO intermediates at a lower potential compared to Pt/C catalysts. Spatial confinement and energetic preference allow Mo to be permanently retained in Pt–Ni NWs. Hence, the subsurface Mo atoms will increase the cohesive atomic energies of the Ni by 0.27 eV and the Pt by 0.29 eV. This indicates that Mo has a stabilizing effect on undercoordinated sites of Pt–Ni NWs, which are the available sites for reactions.

In addition, Pt/Pd-based nanocatalysts with trimetallic surfaces exhibited more anti-CO poisoning properties than bimetallic surfaces due to the electron charge donor effect, accelerated C–C bond cleavage, and improved selectivity to CO_2 formation. For example, Dai et al. showed a set of earth-abundant elements, namely group IIIA and IVA metals (Ga, In, Sn, Pb) and late 3d transition metals (Fe, Co, Ni, Cu) to partially dope the noble metals such as Pt and Rh surface for the construction of trimetallic Pt–Rh–M nanoalloys and to uncover their EOR reactivity and CO_2 selectivity [38]. For those alloyed systems, a representative trimetallic Pt_3RhSn/C catalyst is considered, where HAADF-STEM and EDS line mapping demonstrated that the Pt_3RhM/C catalysts shared similar elemental distributions (Figure 7e). Pt_3RhSn/C is reported to show 67 and 7 times increment in EOR specific activity and mass activity, respectively, at 0.45 V (vs. RHE) compared with a commercial Pt/C catalyst in acidic conditions (Figure 7f). The group investigated the intermediates and products of EOR utilizing the in-situ FTIR (Figure 7g–i). Catalysts were typically swept at a potential ranging from 0.15 V to 0.95 V. The signature peak of CO_2 (2343 cm^{-1}) corresponds to the complete oxidation of ethanol, which indicates the breakage of the C–C bond in ethanol. Among those reported Pt–Rh–M catalysts, the early CO_2 peak implied that Pt_3RhSn/C performed complete EOR at low potential. The anti-CO poisoning property of Pt_3RhSn/C was also observed as there was no linearly adsorbed CO (CO_L) located at 2047 cm^{-1}, suggests that the adsorption of poisonous CO_L was weakened by the optimized electronic structure of Pt_3RhSn/C (Figure 7i).

An abundant source of OH_{ads} species resulting from decorated metals can accelerate the removal of adsorbed CO species from the surface. Therefore, the superior anti-CO poisoning species on the surface can also offer a catalytic boost for EOR performance by facilitating the oxidative removal of carbon-containing species. Following

this concept, Yuan et al. reported $Bi(OH)_3$ decorated PdBi nanochains where strongly coupled $Bi(OH)_3$ played an important role in determining the anti-poisoning property [56]. The OH_{ad} species formed on $Bi(OH)_3$ paved an efficient way to accelerate the oxidative removal of CO or other intermediates on Pd active sites (Figure 7j). CO stripping analysis in the range from 0.7 to 0.8 V indicates that the onset potential of CO oxidation on PdBi-$Bi(OH)_3$ nanochains shifted 100 mV in the negative direction compared to that of Pd/C, indicating the Pd d-band center was downshifted (Figure 7k). The EOR performance of PdBi–$Bi(OH)_3$ and Pd/C was evaluated in 1 M NaOH containing 1 M ethanol, as shown in Figure 7l. The ratio between the intensity of the forward scan peak (I_f) and the reverse scan peak (I_r) relates to the degree of EOR and the tolerance toward CO poisoning [96]. The I_f/I_r value of PdBi–$Bi(OH)_3$ nanochains was nearly 2.5, which was much higher than that of Pd/C (0.9), indicating a more robust tolerance against poisoning by intermediate species (Figure 7l) [56].

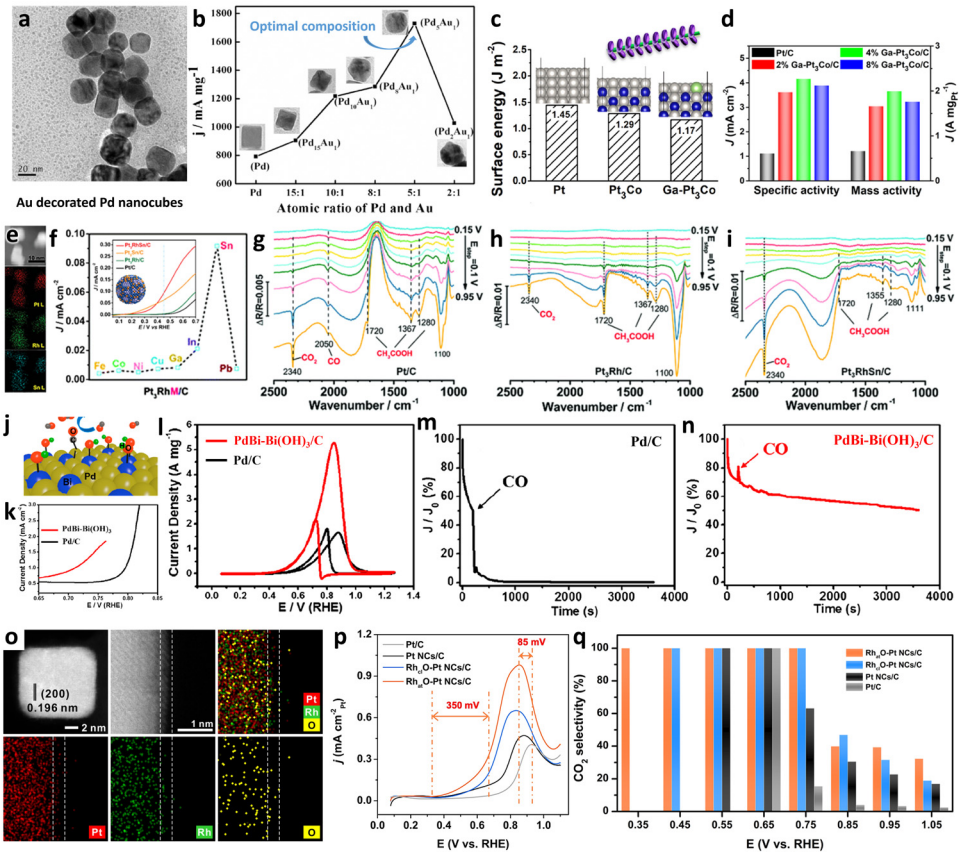

Figure 7. (**a**) TEM images of Au-decorated Pd nanocubes (Pd_5Au_1) and (**b**) relationship between the composition of the catalysts and their corresponding EOR mass activity. Reproduced with permission [55]. Copyright 2016, The Royal Society of Chemistry. (**c**) Surface energy of pure Pt, Pt_3Co, and Ga-doped Pt_3Co (111) surfaces. Gray, blue, green, and red spheres represent Pt, Co, Ga, and O atoms, respectively. (**d**) Specific activities and mass activities of different Ga-doped Pt_3Co NWs and commercial Pt/C catalysts in 0.1 M $HClO_4$ containing 0.5 M CH_3CH_2OH. Reproduced with permission [96]. Copyright 2020, American Chemical Society. (**e**) HAADF–STEM–EDS mapping scans (right side) of Pt_3RhSn/C catalyst. (**f**) EOR curves of trimetallic Pt–Rh–M nanoalloys and their specific activities at 0.45 V. In-situ FTIR spectra recorded during the EOR on (**g**) Pt/C, (**h**) Pt_3Rh/C, and (**i**) Pt_3RhSn/C at continuous stepped potentials from 0.15 V to 0.95 V in a mixture containing 0.1 M $HClO_4$ and 0.5 M CH_3CH_2OH. Reproduced with permission [38]. Copyright 2018, The Royal Society of Chemistry. (**j**) Schematic illustration of the oxidative removal mechanism of CO on PdBi–$Bi(OH)_3$ nanochains sites in which yellow, blue, red, green, and gray spheres represent Pd, Bi, O, H, and C, respectively. (**k**) Enlarged CO-stripping curves at potentials from 0.65 to 0.85 V. (**l**) EOR performances of PdBi–$Bi(OH)_3$ nanochains and commercial Pd/C catalysts in 1 M NaOH containing 1.0 M CH_3CH_2OH. Chronoamperometric response of (**m**) commercial Pd/C and (**n**) PdBi-$Bi(OH)_3$ nanochains in a solution of 1 M NaOH containing 1 M ethanol at 0.86 V. CO gas was purged into the electrolytes at 200 s. Reproduced with permission [56]. Copyright 2019, American Chemical Society. (**o**) CV profiles of the synthesized electrocatalysts measured in Ar-saturated 0.1 M $HClO_4$ solution. (**p**) EOR curves of $Rh_{at}O$-Pt NCs and commercial Pt/C catalysts in 0.1 M $HClO_4$ containing 0.2 M CH_3CH_2OH. (**q**) The CO_2 selectivity of all samples ranging from 0.25 to 1.05 V obtained from in-situ IRRAS spectra. Reproduced with permission [41]. Copyright 2022, The National Academy of Sciences.

The mass normalized current density of PdBi–$Bi(OH)_3$ nanochains was 5.30 $A \cdot mg_{pd}^{-1}$, which was 4.6 times higher than that of Pd/C. The authors also tried to demonstrate the enhanced CO tolerance of PdBi-$Bi(OH)_3$ during EOR by purging CO gas into the electrolytes at 200 s (Figure 7m,n). The poor CO tolerance for commercial Pd/C was observed as the EOR current density swiftly dropped to zero. On the other hand, PdBi–$Bi(OH)_3$ sample showed superior tolerance as 50% of the EOR current density could still be observed after 3600 s. In addition, the authors showed that the PdBi–$Bi(OH)_3$ could be reactivated electrochemically in a fresh electrolyte after each 20,000 s stability test. After reactivation, PdBi–$Bi(OH)_3$ could retain its original EOR activity. It was concluded that $Bi(OH)_3$ decoration can act as an anti-CO poisoning site which enhances the activity and stability of the EOR process. The high EOR activity and excellent stability made PdBi–$Bi(OH)_3$ one of the best reported EOR electrocatalysts.

Metal dopants can also act as the active component for complete EOR process. For example, Qiaowan et al. showed that partially oxidized Rh decorated on the Pt nanocube surface could completely oxidize ethanol to CO_2 at a record-breaking low potential of 0.35 V. A controlled decoration of partially oxidized single Rh on the (100) surface of Pt nanocubes ($Rh_{at}O$-Pt NCs) was achieved (Figure 5a) [41]. CV curves showed Pt NCs/C with typical Pt(100) H adsorption/desorption (0.08–0.45 V vs RHE). $Rh_{at}O$-Pt NCs/C exhibited Pt–O (0.75–1.0 V) and Rh–O (0.45–0.65 V) reduction peaks, while $Rh_{cl}O$-Pt NCs/C lacked Pt–O reduction, indicating an Rh-dominated surface (Figure 7o). EOR analysis indicates that compared to Pt/C, the $Rh_{at}O$-Pt NCs/C nanocatalyst showed negative shifts of the main peak and EOR onset potentials by 85 and 350 mV, respectively (Figure 7p). Additionally, the EOR current densities of $Rh_{at}O$-Pt NCs/C showed 11.4 times more enhancement than Pt/C at 0.75 V (Figure 7p). The role of Rh doping was unveiled by infrared reflection absorption spectroscopy (IRRAS). From the IRRAS peak integration, EOR products were quantitatively determined at a potential range of 0.35 to 1.05 V (Figure 7q). The Rh decoration remarkably improved the CO_2 selectivity. The $Rh_{at}O$-Pt NCs/C catalyst showed CO_2 selectivity of >99.9% from 0.35 to 0.75 V, revealing its strong C–C bond scission ability of ethanol in a wide range of potentials. From the IRRAS results, the authors concluded that Rh is the active component for C–C bond scission in ethanol, while Pt is the active center for the overall EOR performance. Therefore, Rh–O–Pt has the combination of EOR activity of Rh and Pt and assists in the formation of OH_{ad}, which removes the adsorbed CO_{ad}. Finally, as shown in Table 3, decorated nanocatalysts demonstrated superior EOR performances compared to commercially available Pt/Pd nanocatalysts.

Table 3. Comparison of EOR performance of various state-of-the-art decorated nanocatalysts.

Catalyst	MA [a] ($A \cdot mg_{Pt/Pd}^{-1}$)	MA Enhancement vs. Pt/C	SA [b] ($mA \cdot cm^{-2}$)	SA Enhancement vs. Pt/C	CA Stability [c]	Electrolyte	Ref.
Au-decorated Pd	1.74	2.2 (vs. Pd)	2.85	~1	~5% (0.02 $A \cdot mg^{-1}$) activity retention after 2000 s	1.0 M C_2H_5OH + 1.0 M KOH	[55]
Pt_3RhSn	0.02	7	0.09	67	~10% (0.01 $mA \cdot cm^{-2}$) activity retention after 36,000 s	0.5 M C_2H_5OH + 0.1 M $HClO_4$	[38]
Ga-doped Pt_3Co NWs	2.00	4	4.20	4	59.8% (0.01 $mA \cdot cm^{-2}$) activity retention after 36,000 s	0.5 M C_2H_5OH + 0.1 M $HClO_4$	[96]
Mo-doped PtNi NWs	0.87	6.3	2.57	13.4	~17% (0.4 $mA \cdot cm^{-2}$) activity retention after 1500 s	2.0 M C_2H_5OH + 0.5 M H_2SO_4	[97]
$Ni(OH)_2$ decorated Pt–Cu octahedra	1.97	5	8.40	~13	N/A	1.0 M C_2H_5OH + 0.1 M $HClO_4$	[98]
$Bi(OH)_3$ decorated PdBi nanochains	5.30	4.6 (vs. Pd/C)	N/A	N/A	36% (1.00 $A \cdot mg^{-1}$) activity retention after 20,000 s	1.0 M C_2H_5OH + 1.0 M NaOH	[56]
SnO_2 patched ultrathin PtRh NWs	3.16	5.3	5.63	4.3	~10% (0.05 $A \cdot mg^{-1}$) activity retention after 1000 s	1.0 M C_2H_5OH + 1.0 M NaOH	[99]
SnO_2 decorated PtRhNi nanoframes	0.13	6	0.72	10	~20% (0.03 $A \cdot mg^{-1}$) activity retention after 1500 s	0.5 M C_2H_5OH + 0.1 M $HClO_4$	[100]
Single Rh decorated Pt nanocubes	0.21	5	0.73	11.4	~24% activity retention after 600 s	0.2 M C_2H_5OH + 0.1 M $HClO_4$	[41]

[a] Mass activity, [b] Specific activity, [c] Chronoamperometry.

Surface decoration has proven to be one of the effective routes for improving EOR kinetics by facilitating C–C bond cleavage, enhancing OH_{ad} availability, and suppressing CO poisoning intermediates. This review summarized that electronic modulation of the Pt/Pd surface can dramatically shift reaction pathways toward

complete EOR oxidation. However, achieving high CO_2 selectivity at low potentials while maintaining long-term stability remains challenging. We believe that future research should focus on new metal dopant that stabilize active facets, suppress metal leaching, and enable rapid desorption of carbonaceous intermediates.

4.3. FAOR Performance

Direct formic acid fuel cells (DFAFCs) are regarded as one of the most promising liquid fuel cells due to the high power densities, nontoxicity, and low fuel crossover through the Nafion membrane [9,101–104]. Pt-/Pd-based catalysts have been considered the most suitable catalyst for the anodic FAOR in DFACFs. FAOR proceeds on the surface Pt and Pd through a widely accepted dual-path mechanism [105–107]. A detailed mechanism has been discussed in Section 2, which revealed that decorated metal and metal oxide species could play a key role as anti-CO poisoning species during FAOR. Moreover, in acidic conditions, monometallic Pd and Pt catalysts suffer from deactivation and shape deformation during FAOR. Surface decoration can improve activity, preserve the shape, and enable superior stability during FAOR. For instance, Rettenmaier et al. reported SnO_2 decorated Pd (SnO_2@Pd) NCs, improving the electrocatalytic FAOR activity compared to Pd NCs due to a decrease in the oxidizing potential of CO intermediates while maintaining the Pd sites free of poisoning [108]. Figure 8a shows HRTEM images of SnO_2@Pd NC supported on carbon powder where the SnO_2 agglomerates were found on Pd cubes. The authors demonstrated that with SnO_2 decoration, the Pd oxidation state does not change during FAOR. To support their claim, the authors conducted *in-operando* X-ray absorption fine structure (XAFS) measurements during FAOR to obtain the chemical state of Pd and Sn (Figure 8b–d). The X-ray absorption near edge structure (XANES) analysis at the Sn K-edge (Figure 8b) reveals that the local structure and oxidation state around Sn in the SnO_2@Pd NC catalyst can be related to the SnO_2 reference material, and no change occurred during the FAOR operation. An analysis of the Pd K-edge data in Figure 8c indicates that the Pd oxidation state and local structure do not alter during FAOR, revealing superior stability SnO_2@Pd NC during FAOR. It was also revealed that Pd in the Pd NCs and SnO_2@Pd NCs catalysts were in a reduced state and matched with metallic fcc-Pd. Similar to the XANES data analysis, the Fourier-transform extended X-ray absorption fine structure (FT-EXAFS) analysis (Figure 8d) revealed that before the FAOR and during the FAOR, catalysts are in the reduced state and match with a local structure similar to that of pure metallic Pd. This analysis shows that the decorated SnO_2 can stabilize the Pd surface and the electron relocation effect remains intact during and after FAOR. As a result, the SnO_2@Pd NC exhibited good FAOR performance, as revealed by the CV (Figure 8e).

From the CV, the peak potential for SnO_2@Pd NCs was found at 0.55 V (vs. RHE), which was shifted by 100 mV lower potential than that of Pd NCs. SnO_2@Pd NCs showed a 5.8-fold enhanced current density at 0.55 V (vs. RHE) compared to the Pd NCs. Moreover, the authors performed in-situ FTIR during FAOR and compared the CO_2 evolution (Figure 8f–h). The vibrational frequency of dissolved CO_2 was recorded at 2345 cm^{-1} (C–O stretch) [109]. It can be seen that the CO_2 signal generated from FAOR starts to evolve at 0.21 V for Pd NCs (Figure 8f), while the CO_2 signal can be observed at 0.01 V for the SnO_2@Pd NCs (Figure 8g). Interestingly, the advantages of in-situ FTIR measurements for FAOR can be realized as the onset potentials for the catalytic activities were 140 mV lower than the onset potentials measured by the CV technique (Figure 8h). This analysis reveals the higher sensitivity of the in-situ FTIR measurements for FAOR, which can be utilized for detecting the catalytic activity of SnO_2@Pd NC at a lower potential.

The superior FAOR performance of the catalyst was also attributed to improved CO tolerance. Therefore, the authors have demonstrated CO stripping analysis to evaluate the anti-CO properties of the catalyst utilizing conventional CO stripping analysis and in-situ FTIR analysis. From the CO stripping analysis (Figure 8i), similar peak potentials were observed for both the catalysts (0.86 V), suggesting the absence of strain effect by decorating SnO_2 on the Pd lattice. Interestingly, the onset potential for CO oxidation was lower for SnO_2@Pd NCs (0.61 V) than Pd NCs (0.73 V). The potential was lowered due to the oxophilic sites providing oxygen at a lower Sn oxidation potential. Also, the oxidative current in the potential range of 0.6 to 1.0 V (vs. RHE) indicates a more facile CO oxidation, surface heterogeneity, and a slower CO surface diffusion toward the reactive Pd sites on SnO_2@Pd NCs [110–113]. Additionally, the vibrational frequency of bridge-bonded CO_B (C–O stretch) is recorded between 1900–1955 cm^{-1}. In the case of Pd NCs (Figure 8j), the CO_B band primarily appears at 1945 cm^{-1} and starts shifting as the potential changes from 1951 cm^{-1} (0.16 V) to 1958 cm^{-1} (0.71 V). The shifting is also observed for SnO_2@Pd NCs (Figure 8k), but the peak intensity starts to decline at 0.66 V (vs. RHE), suggesting the earlier CO oxidation of the SnO_2@Pd NCs. The integrated band intensities of the CO_2 formation in Figure 8l also suggest the lowered onset potential for SnO_2@Pd NCs (0.66 V) than Pd NCs (0.71 V), matching with previous CO stripping data.

Scofield et al. reported ultrathin Fe-doped PtRu NWs and utilized the decorated material toward FAOR [114]. They prepared several PtRuFe compositions and investigated their performance toward MOR and FAOR. Among those prepared ultrathin Fe-doped PtRu NWs catalysts, $Pt_7Ru_{1.5}Fe_{1.5}$ NWs showed the highest FAOR performance.

The authors concluded that the corresponding Fe content primarily impacts FAOR within the ternary metal alloy nanowire. Vidal-Iglesias et al. reported that the highest FAOR could be achieved for Pt(100) electrodes decorated by Pd adatoms, owing to the decreased CO poisoning and the lowering of the onset potential for FAOR at 0.12 V (vs. RHE) [115]. A comprehensive FAOR performance comparison of previously reported catalysts with the metal-doped surface is shown in Table 4.

Decorated Pt/Pd catalysts have shown clear advantages in FAOR by lowering CO oxidation potentials, stabilizing active surfaces, and preserving the morphology of the catalysts during extended operation. These findings confirm that controlled electronic tuning of the surface can shift the FAOR pathway toward efficient dehydrogenation while minimizing poisoning. Future studies should include a deeper integration of in-situ/operando XAFS, FTIR, and SEIRA techniques to directly correlate surface chemistry with FAOR activity.

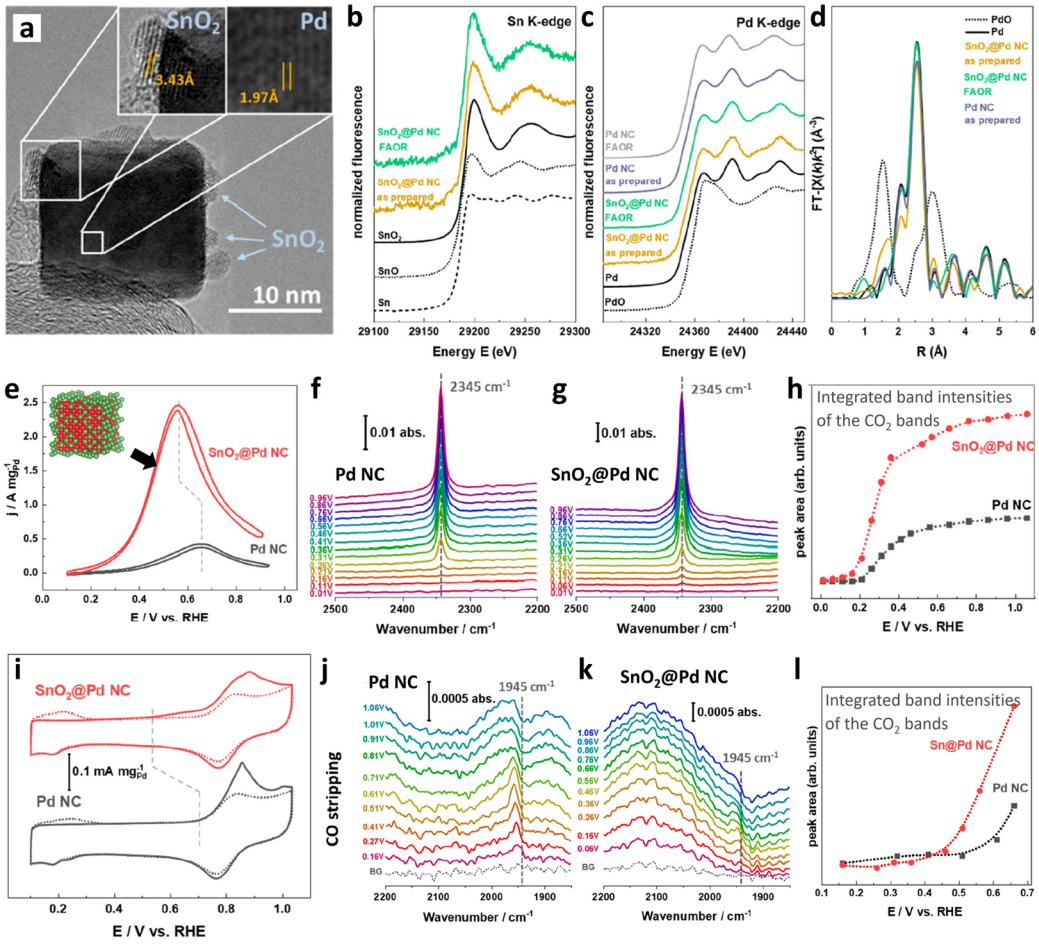

Figure 8. (**a**) HRTEM images of SnO_2@Pd NCs. XANES spectra at the (**b**) Sn K-edge of SnO_2@Pd NCs and (**c**) Pd K-edge for the Pd NCs, and SnO_2@Pd NCs in the as-prepared state and *in-operando* spectra collected during 3 h of the FAOR in 0.1 M $HClO_4$ + 0.5 M HCOOH at 0.45 V vs. RHE. (**d**) Fourier-transformed (FT) k2-weighted Pd K-edge EXAFS spectra for both catalysts in the as-prepared state and during the reaction. (**e**) CV for FAOR of the SnO_2@Pd NC and Pd NC (gray) in 0.1 M $HClO_4$ + 0.5 M HCOOH at 50 $mV \cdot s^{-1}$. In-situ FTIR of FAOR showing CO_2 bands during FAOR for (**f**) Pd NCs and (**g**) SnO_2@Pd NCs; (**h**) integrated band intensities of the CO_2 bands during FAOR. Reference spectra were taken at −0.04 V vs. RHE on glassy carbon electrode in 0.1 M $HClO_4$ and 25 mM HCOOH. (**i**) CO-stripping voltammograms of SnO_2@Pd catalysts (red) and Pd catalysts (gray) in 0.1 M $HClO_4$ at 20 $mV \cdot s^{-1}$. In-situ FTIR of the CO-stripping experiments in the CO regime of (**j**) Pd NCs and (**k**) SnO_2@Pd NCs; (**l**) integrated intensities of the corresponding CO_2 bands. Reference spectra taken at 0.06 V vs. RHE taken on Au foil in 0.1 M $HClO_4$. Reproduced with permission [108]. Copyright 2020, American Chemical Society.

Table 4. Comparison of FAOR performance of various decorated nanocatalysts.

Catalyst	MA [a] ($A \cdot mg_{Pt/Pd}^{-1}$)	MA Enhancement vs. Pt/C or Pd/C	SA [b] ($mA \cdot cm^{-2}$)	SA Enhancement vs. Pt/C or Pd/C	CA Stability [c]	Electrolyte	Ref.
SnO_2 decorated Pd cubes	2.46	5.8	27	~5	~60% mass activity retention after 10,800 s	0.5 M HCOOH + 0.1 M $HClO_4$	[108]
Fe-doped PtRu NWs	N/A	N/A	2.15	4 (Pt NWs)	N/A	0.5 M HCOOH + 0.1 M $HClO_4$	[114]
Au decorated PtNi	3.44	9.5	4.54	2.52	~40% mass activity retention after 4000 s	0.5 M HCOOH + 0.1 M $HClO_4$	[49]
Pd adatom decorated Pt	N/A	N/A	~1.5	~5	~20% specific activity retention after 600 s	0.1 M HCOOH + 0.5 M H_2SO_4	[115]
Pt decorated PdFe	1.93	1.52 (vs. 1.52)	N/A	N/A	~20% mass activity retention after 2100 s	0.5 M HCOOH + 0.1 M $HClO_4$	[110]
Sn-doped PdCu	2.42	3.94	N/A	N/A	102.3 times mass activity than Pd/C after 3600 s	0.5 M HCOOH + 0.5 M H_2SO_4	[116]
(Y–Pt)–$PtTe_2$ HPNT/C	6.4	49.2	5.4	25.7	~80.4% mass activity retention after 36,000 s	0.5 M HCOOH + 0.5 M H_2SO_4	[117]
Sb-decorated Pt octahedral NPs	NA	NA	~2.8	NA	88% mass activity retention after 600 s	0.5 M HCOOH + 0.5 M H_2SO_4	[118]

[a] Mass activity, [b] Specific activity, [c] Chronoamperometry.

4.4. EGOR Performance

Ethylene glycol (EG), produced from cellulose, is an attractive energy carrier for electrocatalytic applications. Due to its high boiling point of 198 °C, coupled with theoretical capacity (4.8 Ah/mL) and a higher boiling point than methanol (64.7 °C), it renders an advantageous and safe candidate alternative to methanol and ethanol, which can be fed in direct alcohol fuel cells [54,119,120]. In addition, EG is less volatile than ethanol, reducing raw-material wastage [121]. Pt has been considered a promising electrocatalyst for EGOR, and there are two pathways for EGOR, which we have discussed in chapter 2.4 [42,122,123]. However, one pathway will lead to poisoning the catalyst surface and making the Pt surface inactive for further reaction. These led to studies on surface decoration protocols with various metal atoms, which not only enhance the EGOR but also act as anti-CO sites for long-time stability of EGOR.

One current strategy to improve the electrocatalytic activity of Pt is to generate a catalytic surface with high-index facets (HIFs). Reports reveal that HIFs with high-density steps and kinks improve LFOR by lowering the potential for CO oxidation [124–127]. For example, Wang et al. unveiled that doping non-noble metal or nonmetals into the near-surface of the Pt-based nanocrystals bound with HIFs exhibits high activity and stability toward EGOR [124]. The metal dopant in the catalytic surface of Pt can change the electrochemical properties. Furthermore, the metal dopants also assist in stabilizing the crystal surface structure of Pt-based nanocrystals. The group also reported Mo doping on the HIF of Pt_3Mn catalyst, which showed advantages such as easier C–C cleavage of EG, the direct conversion of carbonaceous species to CO_2, and suppressing CO_L poison formation species [128]. A schematic illustration of Mo-doped Pt_3Mn is shown in Figure 9a, where the Mo component is doped into the surface lattice of Pt_3Mn outer layer.

EGOR analysis for different Mo-doped Pt_3Mn and commercial Pt/C was conducted in 0.1 M $HClO_4$ solution containing 0.5 M EG. It was found that the specific activities (Figure 9b) of 1.8%Mo/Pt_3Mn, 0.4%Mo/Pt_3Mn, and 0.07%Mo/Pt_3Mn were 0.95, 1.23, and 0.86 $mA \cdot cm^{-2}$, which are 2.2, 2.9, and 2.0 times higher than that of Pt_3Mn catalyst (0.43 $mA \cdot cm^{-2}$), respectively. It is evident from the above results that an optimum amount of Mo doping is necessary for maximizing EGOR performance. In-situ FTIR spectroscopy was utilized to measure the effects of Mo doping for EGOR performance in 0.1 M $HClO_4$ + 0.5 M EG solution, and the results are displayed in Figures 9c and d, for Pt_3Mn and 0.4% Mo-doped Pt_3Mn, respectively. The negative band at 2343 cm^{-1} represents the CO_2 formation found after applying more than 0.6 V (vs. RHE) [129,130]. Moreover, the band observed at about 2050 cm^{-1} corresponds to the linearly bonded CO (CO_L) [130–132], which was undetectable for 0.4% Mo-doped Pt_3Mn, confirming that the formation of CO was deterred. Therefore, no signals of CO_L in 0.4% Mo-doped Pt_3Mn spectra imply that the catalyst follows a direct pathway where the C_1 species are directly oxidized to CO_2 without forming CO_L species. To confirm the above claim, the authors also analyzed attenuated total reflection surface-enhanced infrared absorption spectroscopy (ATR-SEIRA) during EGOR at 0.5 V (vs. RHE) (Figure 9e,f). First, the intensity of CO_2 signals at 2343 cm^{-1} for 0.4% Mo-doped Pt_3Mn is higher than Pt_3Mn, revealing better EGOR performance. The authors have collected CO_2 after 35 s, and the amount per unit catalyst surface area is nearly two times higher

for the 0.4% Mo-doped Pt_3Mn catalyst than Pt_3Mn catalyst. Secondly, the CO_L band at 2050 cm^{-1} broadens at Pt_3Mn surface with time, while the band is suppressed on the 0.4% Mo-doped Pt3Mn surface. Therefore, Mo doping inhibits CO_L species formation and acts as anti-CO sites on Pt_3Mn surface.

Interestingly, authors have analyzed CV curves of Pt_3Mn and 4% Mn-doped Pt_3Mn after the chronoamperometric test (Figure 9g,h) and correlated the voltammetric profile peaks with surface structure evolution. During the first cycle, the hydrogen adsorption/desorption peaks were weaker, and two apparent peaks at 0.11 and 0.24 V belong to (110) and (100) facets, respectively. For Pt_3Mn catalyst (Figure 9g), the (100) peak (terrace) exhibits a rapid downtrend with time, compared with the (110) peak (step). This phenomenon may originate from the fact that in bimetallic Pt nanocrystals, Pt atoms tend to be located on peaks and edges while transition metal atoms occupy the crystal facet [124]. On the contrary, 4% Mn-doped Pt_3Mn showed a gentler downtrend with time for the peaks related to (110) and (100) facets (Figure 9h). Also, at 0.7 V, Pt_3Mn shows a shift in onset potential for OH adsorption with time, signifying the leaching of Mn from the Pt surface. But, on the 4% Mn-doped Pt_3Mn, the slight changes reveal that doped Mo can stabilize Pt_3Mn during the stability test. To further confirm the stabilizing effect, the authors have conducted DFT calculations on different Mo-doped surfaces (Figure 9i). When Mo was doped on Pt_3Mn alloy, the binding energy of Pt changed from 5.82 to 5.84 eV (Mo doping on the surface) or 5.71 eV (Mo doping on the subsurface), while the binding energy of Mn changed from 5.14 to 6.49 eV (Mo doping on the surface) or 6.30 eV (Mo doping on the subsurface). Based on the binding energy, the authors expressed that Mo doping on Pt_3Mn creates strongly bonded Mo-Mn instead of Pt-Mn and Pt-Mo bonds, and this phenomenon leads to the anti-dissolution of Mn during EGOR.

In a similar study by Wang et al., Bi-decorated Pd concave nanocubes (CNCs) exhibited improved EGOR performance by following the C1 pathway compared to bare Pd CNCs in a 1 M NaOH + 1 M EG solution [133]. The Bi-decorated Pd CNC showed an increased specific activity of 2.44 times compared to the Pd CNC electrode toward EGOR in alkaline media. Earlier, OH_{ad} was regarded as a reactive pair in the LFOR in alkaline media [134,135]. Therefore, the promoted EGOR on Bi-decorated Pd CNCs may be ascribed to the modification of the electronic state of Pd by oxophilic Bi adatoms, assisting in the formation of OH_{ads}. Finally, the bifunctional mechanism is followed for eliminating CO_{ads} species to CO_2. However, the authors also pointed out that the formation of adsorbed CO_{ads} during the EGOR should not be simply defined as a poisoning species rather than an active intermediate to be converted to CO_2 (HCO_3^- and CO_3^{2-}) [136].

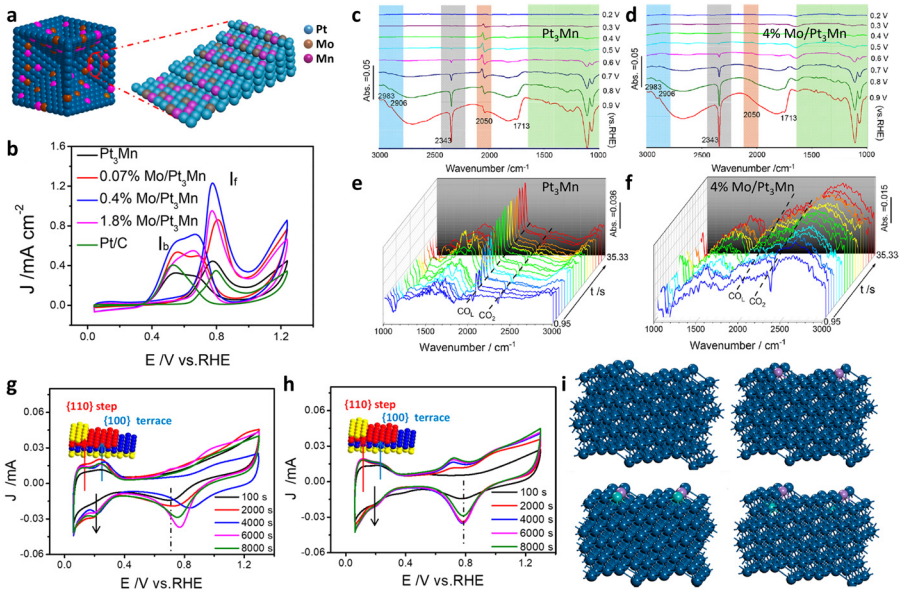

Figure 9. (**a**) Surface Illustration of the Mo-doped Pt_3Mn catalyst. (**b**) CV for EGOR of Pt_3Mn, 0.4% Mo-doped Pt_3Mn, and commercial Pt/C in 0.1 M $HClO_4$ + 0.5 M EG solution at a scan rate of 50 $mV \cdot s^{-1}$. In-situ FTIR spectra for EGOR on (**c**) Pt_3Mn and (**d**) 0.4% Mo-doped Pt_3Mn catalyst in 0.1 M $HClO_4$ + 0.5 M EG solution. Real-time ATR-SEIRA spectra of (**e**) Pt_3Mn and (**f**) 0.4% Mo-doped Pt_3Mn catalyst in 0.1 M $HClO_4$ + 0.5 M EG solution at 500 mV vs. RHE (temporal resolution 0.95 s/spectrum). CV curves of (**g**) Pt_3Mn and (**h**) 0.4% Mo-doped Pt_3Mn after different chronoamperometric tests. (**i**) Geometrical structures of Pt (410) surface (**left top**), Pt_3Mn step edge (**right top**), surface Mo-doped Pt_3Mn step edge (**left bottom**), subsurface Mo-doped Pt_3Mn step edge (**right bottom**). The indigo, purple, and grass green balls denote the Pt, Mn, and Mo atoms, respectively. Reproduced with permission [124]. Copyright 2019, American Chemical Society.

Interestingly, Ir decoration on Pd nanosheet can also lead to higher EGOR performance, which was discussed by Wang et al. [137]. The introduction of Ir as a dopant into the Pd surface can effectively reform the Pd–Pd bond, favoring the downshift of the d-band center. These led to the faster adsorption of H_2O, and CO_{ads} was removed easily from the surface during EGOR. An overall comparison of the EGOR performance of various decorated nanocatalysts is shown in Table 5.

Table 5. Comparison of the EGOR performance of various decorated nanocatalysts.

Catalyst	MA [a] ($A \cdot mg_{Pt/Pd}^{-1}$)	MA Enhancement vs. Pt/C or Pd/C	SA [b] ($mA \cdot cm^{-2}$)	SA Enhancement vs. Pt/C or Pd/C	CA Stability [c]	Electrolyte	Ref.
Mo doped Pt_3Mn	0.23	~2	1.23	~3	~20% specific activity retention after 2000 s	0.5 M $(CH_2OH)_2$ + 0.1 M $HClO_4$	[124]
Bi decorated Pd CNC	N/A	N/A	N/A	~2.44 (apparent SA vs. Pd CNC)	N/A	1.0 M $(CH_2OH)_2$ + 1.0 M NaOH	[133]
Ir doped Pd NSAs	4.32	3.64 (vs. Pd/C)	3.29	2.78 (vs. Pd/C)	~30% mass activity retention after 4000 s	1.0 M $(CH_2OH)_2$ + 1.0 M KOH	[137]
Pt_3Mn–Ru CNCs	0.24	2.05	1.32	3.77	N/A	0.5 M $(CH_2OH)_2$ + 0.1 M $HClO_4$	[138]
Se doped Pd-PdSe HNSs	8.60	6.6	15.7	5.5	~60% mass activity retention after 5000 s	1.0 M $(CH_2OH)_2$ + 1.0 M KOH	[139]
Au-Doped PtBi	28.72	8.65	N/A	N/A	~20% mass activity retention after 3600 s	0.5 M $(CH_2OH)_2$ + 1.0 M KOH	[140]

[a] Mass activity, [b] Specific activity, [c] Chronoamperometry.

Surface decoration significantly enhances EGOR by weakening C–C bond in EG, stabilizing high-index facets, and suppressing strongly adsorbed CO-like species. Studies demonstrate that dopant placement can shift the mechanism toward direct oxidation with minimal poisoning. Nonetheless, the structural evolution of decorated surfaces under EGOR conditions-especially dissolution or migration of dopants remains an unresolved challenge. In this view, designing dopants that anchor strongly to step/kink sites and resist leaching will be the key to overcome EGOR. Future work should also combine DFT insights with real-time spectroscopic tracking to fully understand the mechanism between dopant distribution, surface reconstruction, and EGOR pathway selectivity.

5. Conclusions and Outlook

We have summarized synthesis protocols and outlined the properties of anti-CO sites affecting the LFOR of catalysts to achieve maximum performance. The indirect pathway or failure to split the C–C bond in liquid fuel will result in CO adsorption on the catalytic surface. Continuous Pt or Pd sites are more favorable for bridge CO_{ads}, which require more energy to free the catalyst surface from CO_{ads}. As discussed in this review, this phenomenon can be minimized by decorating the Pt surface with metal dopants. To date, synthetic strategies have made impressive progress in decorating noble metal and non-noble metal catalysts for efficient LFOR. Figure 10 delivers an overview of the reported metal dopants for decorating Pt or Pd surface utilized for LFOR. The scientific community is still investigating LFOR performance enhancement for the vast commercialization of DLFCs.

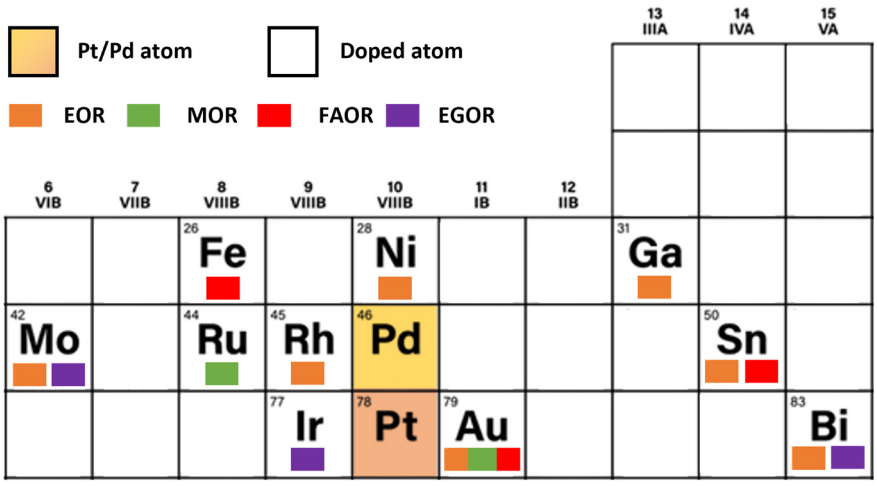

Figure 10. Overview of reported metal dopants for decorating Pt or Pd surface utilized for various LFOR.

To provide insight into the influential roles of those anti-CO sites on LFOR, we have compared all the catalysts that have been reported so far. As the experimental operation conditions are different for each study, one way to compare nanocatalysts is in terms of the shift in the onset of the CO stripping experiment versus mass activity enhancement compared to commercial Pt/C. It is evident that the more the deviation from the CO stripping onset compared to Pt/C, the better the LFOR performance of the catalyst. Although a decorated nanocatalyst has shown improved LFOR performance, many challenges remain to be addressed regarding (i) synthesis, (ii) optimization of catalytic performance, (iii) dissolution of metal during electrocatalysis, and (iv) combination of theoretical and experimental approaches to further understand the reaction mechanisms. As an outlook for the field, we highlight a few crucial challenges for further developing decorated nanocatalysts toward LFOR.

(i) *Easier regeneration of active sites after stability test.* Catalyst deactivation is the most common and consistent issue for LFOR. This review shows that the deactivation of catalysts during LFOR stability performance can be minimized by decorating the catalyst's surface, but cannot be eliminated entirely. CO can still be adsorbed on the decorated surface and deteriorate the electrocatalytic performance over time, as seen in every chronoamperometric stability test. Therefore, a catalyst with easier regeneration of active sites may address the problem. For example, $Bi(OH)_2$ decorated PdBi showed that the active anti-CO species could be regenerated easily on cycling in 1M NaOH solution while retaining its activity. Therefore, developing such nanocatalysts for long-term LFOR performance is desirable.

(ii) *Multi-metallic surface decoration.* The anti-CO poisoning effect can be enhanced by decorating three or more transition metals on the noble metal surface. For example, Rh and Sn decorated Pt toward EOR, Au decorated PtFe, Fe-doped PtRu NWs for FAOR, and Mo-doped Pt_3Mn for EGOR have been investigated. Interestingly, these catalysts showed superior electrocatalytic performance than commercial Pt/C. Therefore, it is an endless possibility to explore different decorated structures suitable for LFOR. Of course, the theoretical analysis would reveal if the catalyst is ideal for breaking C–C bonds of liquid fuels and the reaction pathways before practical research is conducted.

(iii) *Synthesis protocol.* Although hundreds of studies are pouring in for bimetallic surface synthesis toward LFOR, only a few are good enough to design and tailor electrocatalysts with a preferentially decorated structure. That is to say, that synthesis may have resulted in a decorated surface, but if there is too much active site coverage by anti-CO sites, it may interrupt the whole reaction, as reactants will not adsorb on the catalyst surface. Therefore, the degree of decoration or optimal surface composition must be considered when decorating the catalytic surface with dopants.

(iv) *Robust analytical techniques for the determination of roles of anti-CO-sites.* With current cutting-edge technology, it is possible to identify the doped/decorated metal using XPS, ICP-AES, HRTEM, and EDX analysis. However, detecting the decorated metal acting as an anti-CO poisoning species would be interesting to analyze and report. Few studies reported in-situ FTIR analysis during LFOR, but the metal oxidation state was unknown during the reaction. In-situ XAS, which has often been used to reveal the structural changes (including the metal oxidation state, bond distances, and coordination numbers) and their dependence on potential, might also become a powerful tool in disclosing the role of decorated metal as anti-CO poisoning sites for improved activity and stability.

Author Contributions: M.K.K.: Conceptualization, writing—original draft preparation. J.K.: Conceptualization, writing—original draft preparation. S.S.: Writing—reviewing. S.-I.C.: Conceptualization, supervision, writing—reviewing, and editing. All authors have read and agreed to the published version of the manuscript.

Funding: This study was supported by the National Research Foundation of Korea (RS-2024-00346153, RS-2025-02215028).

Data Availability Statement: Not applicable.

Conflicts of Interest: The authors declare no conflict of interest.

Use of AI and AI-Assisted Technologies: No AI tools were utilized for this paper.

References

1. Cheng, H.; Wang, J.; Wu, C.; Liu, Z. Electrocatalysts for Formic Acid-Powered PEM Fuel Cells: Challenges and Prospects. *Energy Mater. Adv.* **2025**, *4*, 67.
2. Chang, J.; Wang, G.; Zhang, W.; Yang, Y. Atomically Dispersed Catalysts for Small Molecule Electrooxidation in Direct Liquid Fuel Cells. *J. Energy Chem.* **2022**, *68*, 439–453.
3. Ramli, Z.A.C.; Pasupuleti, J.; Samidin, S.; Saharuddin, T.S.T.; Isahak, W.N.R.W.; Sofiah, A.G.N.; Koh, S.P.; Kiong, S.T. Recent Advances of Two-Dimensional-Based (2D) Materials as Electrocatalysts in DLFC: An Overview. *Fuel* **2025**, *387*, 134386.

4. Li, Y.; Yao, M.-S.; He, Y.; Du, S. Recent Advances of Electrocatalysts and Electrodes for Direct Formic Acid Fuel Cells: From Nano to Meter Scale Challenges. *Nano-Micro Lett.* **2025**, *17*, 148.
5. Shaari, N.; Kamarudin, S.K.; Bahru, R.; Osman, S.H.; Md Ishak, N.A.I. Progress and Challenges: Review for Direct Liquid Fuel Cell. *Int. J. Energy Res.* **2021**, *45*, 6644–6688.
6. Altarawneh, R.M. Overview on the Vital Step toward Addressing Platinum Catalyst Poisoning Mechanisms in Acid Media of Direct Ethanol Fuel Cells (DEFCs). *Energy Fuels* **2021**, *35*, 11594–11612.
7. Cai, B.; Chen, X.; Wang, L.; Fu, H. Advanced Progress for Promoting Anodic Hydrogen Oxidation Activity and Anti-CO Poisoning in Fuel Cells. *ACS Catal.* **2024**, *14*, 13602–13629.
8. Chen, A.; Ostrom, C. Palladium-Based Nanomaterials: Synthesis and Electrochemical Applications. *Chem. Rev.* **2015**, *115*, 11999–12044.
9. Kabiraz, M.K.; Kim, J.; Lee, W.-J.; Ruqia, B.; Kim, H.C.; Lee, S.-U.; Kim, J.-R.; Paek, S.-M.; Hong, J.W.; Choi, S.-I. Ligand Effect of Shape-Controlled β-Palladium Hydride Nanocrystals on Liquid-Fuel Oxidation Reactions. *Chem. Mater.* **2019**, *31*, 5663–5673.
10. Antolini, E. Palladium in Fuel Cell Catalysis. *Energy Environ. Sci.* **2009**, *2*, 915–931.
11. Zhang, H.; Jin, M.; Xia, Y. Enhancing the Catalytic and Electrocatalytic Properties of Pt-Based Catalysts by Forming Bimetallic Nanocrystals with Pd. *Chem. Soc. Rev.* **2012**, *41*, 8035–8049.
12. Wu, C.; Zhang, Y.; Yang, H.Y. Rational Design and Facile Preparation of Palladium-Based Electrocatalysts for Small Molecules Oxidation. *ChemSusChem* **2025**, *18*, e202401127.
13. Neto, A.O.; Dias, R.R.; Tusi, M.M.; Linardi, M.; Spinacé, E.V. Electro-Oxidation of Methanol and Ethanol Using PtRu/C, PtSn/C and PtSnRu/C Electrocatalysts Prepared by an Alcohol-Reduction Process. *J. Power Sources* **2007**, *166*, 87–91.
14. Busó-Rogero, C.; Herrero, E.; Feliu, J.M. Ethanol Oxidation on Pt Single-Crystal Electrodes: Surface-Structure Effects in Alkaline Medium. *ChemPhysChem* **2014**, *15*, 2019–2028.
15. Ozoemena, K.I. Nanostructured Platinum-Free Electrocatalysts in Alkaline Direct Alcohol Fuel Cells: Catalyst Design, Principles and Applications. *RSC Adv.* **2016**, *6*, 89523–89550.
16. Liao, Y.; Chen, W.; Ding, Y.; Xie, L.; Yang, Q.; Wu, Q.; Liu, X.; Zhu, J.; Feng, R.; Fu, X.-Z. Boosting Alcohol Oxidation Electrocatalysis with Multifactorial Engineered Pd1/Pt Single-Atom Alloy-BiOx Adatoms Surface. *Nano-Micro Lett.* **2025**, *17*, 172.
17. Mai, Q.; Mai, Y.; Zhong, Y.; Xue, R.; Jia, B.; Guan, X.; Du, W.; Pan, H.; Li, Y.; Zhang, Z. Intermetallic Electrocatalysts for Small-Molecule Fuel Oxidation. *Adv. Energy Mater.* **2025**, *15*, 2500415.
18. Kwon, T.; Kim, T.; Son, Y.; Lee, K. Dopants in the Design of Noble Metal Nanoparticle Electrocatalysts and Their Effect on Surface Energy and Coordination Chemistry at the Nanocrystal Surface. *Adv. Energy Mater.* **2021**, *11*, 2100265.
19. Chen, Q.-S.; Vidal-Iglesias, F.J.; Solla-Gullón, J.; Sun, S.-G.; Feliu, J.M. Role of Surface Defect Sites: From Pt Model Surfaces to Shape-Controlled Nanoparticles. *Chem. Sci.* **2012**, *3*, 136–147.
20. Bommersbach, P.; Chaker, M.; Mohamedi, M.; Guay, D. Physico-Chemical and Electrochemical Properties of Platinum−Tin Nanoparticles Synthesized by Pulsed Laser Ablation for Ethanol Oxidation. *J. Phys. Chem. C* **2008**, *112*, 14672–14681.
21. Hsieh, C.-T.; Lin, J.-Y. Fabrication of Bimetallic Pt–M (M=Fe, Co, and Ni) Nanoparticle/Carbon Nanotube Electrocatalysts for Direct Methanol Fuel Cells. *J. Power Sources* **2009**, *188*, 347–352.
22. Kowal, A.; Li, M.; Shao, M.; Sasaki, K.; Vukmirovic, M.B.; Zhang, J.; Marinkovic, N.S.; Liu, P.; Frenkel, A.I.; Adzic, R.R. Ternary Pt/Rh/SnO_2 Electrocatalysts for Oxidizing Ethanol to CO_2. *Nat. Mater.* **2009**, *8*, 325–330.
23. Koper, M.T.M. Structure Sensitivity and Nanoscale Effects in Electrocatalysis. *Nanoscale* **2011**, *3*, 2054–2073.
24. Erini, N.; Rudi, S.; Beermann, V.; Krause, P.; Yang, R.; Huang, Y.; Strasser, P. Exceptional Activity of a Pt–Rh–Ni Ternary Nanostructured Catalyst for the Electrochemical Oxidation of Ethanol. *ChemElectroChem* **2015**, *2*, 903–908.
25. Ong, B.C.; Kamarudin, S.K.; Basri, S. Direct Liquid Fuel Cells: A Review. *Int. J. Hydrogen Energy* **2017**, *42*, 10142–10157.
26. Karim, N.A.; Kamarudin, S.K. *Chapter 2—Introduction to Direct Alcohol Fuel Cells (DAFCs)*; Akay, R.G., Akay, R.G., Yurtcan, A.B., Eds.; Academic Press: London, UK, 2021; pp. 49–70.
27. Ponmani, K.; Durga, S.; Arun, A.; Kiruthika, S.; Muthukumaran, B. Development of Membraneless Sodium Perborate Fuel Cell for Media Flexible Power Generation. *Int. J. Electrochem.* **2014**, *2014*, 962161.
28. Arenz, M.; Mayrhofer, K.J.J.; Stamenkovic, V.; Blizanac, B.B.; Tomoyuki, T.; Ross, P.N.; Markovic, N.M. The Effect of the Particle Size on the Kinetics of CO Electrooxidation on High Surface Area Pt Catalysts. *J. Am. Chem. Soc.* **2005**, *127*, 6819–6829.
29. Li, X.; Haunold, T.; Werkovits, S.; Marks, L.D.; Blaha, P.; Rupprechter, G. CO Adsorption and Disproportionation on Smooth and Defect-Rich Ir(111). *J. Phys. Chem. C* **2022**, *126*, 6578–6589.
30. Fang, Q.; Zhang, Z.; Yang, X.; Cheng, T.; Ma, X.; Tang, J. Cu_2O Nanoparticles with Controlled Surface Roughness for CO_2 Electroreduction towards C_{2+} Products. *Chem. Eng. J.* **2025**, *515*, 163293.
31. Cao, L.; Soto, F.A.; Li, D.; Deng, T.; Hu, E.; Lu, X.; Cullen, D.A.; Eidson, N.; Yang, X.-Q.; He, K.; et al. Pd-Ru Pair on Pt Surface for Promoting Hydrogen Oxidation and Evolution in Alkaline Media. *Nat. Commun.* **2024**, *15*, 7245.

32. Long, D.; Liu, Y.; Ping, X.; Chen, F.; Tao, X.; Xie, Z.; Wang, M.; Wang, M.; Li, L.; Guo, L.; et al. Constructing CO-Immune Water Dissociation Sites around Pt to Achieve Stable Operation in High CO Concentration Environment. *Nat. Commun.* **2024**, *15*, 8105.
33. Huang, H.; Hayes, E.T.C.; Gianolio, D.; Cibin, G.; Hage, F.S.; Ramasse, Q.M.; Russell, A.E. Role of SnO2 in the Bifunctional Mechanism of CO Oxidation at Pt-SnO_2 Electrocatalysts. *ChemElectroChem* **2021**, *8*, 2572–2582.
34. Berretti, E.; Osmieri, L.; Baglio, V.; Miller, H.A.; Filippi, J.; Vizza, F.; Santamaria, M.; Specchia, S.; Santoro, C.; Lavacchi, A. Direct Alcohol Fuel Cells: A Comparative Review of Acidic and Alkaline Systems. *Electrochem. Energy Rev.* **2023**, *6*, 30.
35. Li, M.; Adzic, R.R. *Low-Platinum-Content Electrocatalysts for Methanol and Ethanol Electrooxidation BT—Electrocatalysis in Fuel Cells: A Non- and Low-Platinum Approach*; Shao, M., Ed.; Springer: London, UK, 2013; pp. 1–25.
36. Wang, Y.; Zou, S.; Cai, W.-B. Recent Advances on Electro-Oxidation of Ethanol on Pt- and Pd-Based Catalysts: From Reaction Mechanisms to Catalytic Materials. *Catalysts* **2015**, *5*, 1507–1534.
37. Flórez-Montaño, J.; García, G.; Guillén-Villafuerte, O.; Rodríguez, J.L.; Planes, G.A.; Pastor, E. Mechanism of Ethanol Electrooxidation on Mesoporous Pt Electrode in Acidic Medium Studied by a Novel Electrochemical Mass Spectrometry Set-Up. *Electrochim. Acta* **2016**, *209*, 121–131.
38. Dai, L.-X.; Wang, X.-Y.; Yang, S.-S.; Zhang, T.; Ren, P.-J.; Ye, J.-Y.; Nan, B.; Wen, X.-D.; Zhou, Z.-Y.; Si, R.; et al. Intrinsic Composition and Electronic Effects of Multicomponent Platinum Nanocatalysts with High Activity and Selectivity for Ethanol Oxidation Reaction. *J. Mater. Chem. A* **2018**, *6*, 11270–11280.
39. Asiri, H.A.; Anderson, A.B. Mechanisms for Ethanol Electrooxidation on Pt(111) and Adsorption Bond Strengths Defining an Ideal Catalyst. *J. Electrochem. Soc.* **2015**, *162*, F115.
40. Yang, Y.-Y.; Ren, J.; Li, Q.-X.; Zhou, Z.-Y.; Sun, S.-G.; Cai, W.-B. Electrocatalysis of Ethanol on a Pd Electrode in Alkaline Media: An in Situ Attenuated Total Reflection Surface-Enhanced Infrared Absorption Spectroscopy Study. *ACS Catal.* **2014**, *4*, 798–803.
41. Chang, Q.; Hong, Y.; Lee, H.J.; Lee, J.H.; Ologunagba, D.; Liang, Z.; Kim, J.; Kim, M.J.; Hong, J.W.; Song, L.; et al. Achieving Complete Electrooxidation of Ethanol by Single Atomic Rh Decoration of Pt Nanocubes. *Proc. Natl. Acad. Sci. USA* **2022**, *119*, e2112109119.
42. Schnaidt, J.; Heinen, M.; Jusys, Z.; Behm, R.J. Mechanistic Aspects of the Electro-Oxidation of Ethylene Glycol on a Pt-Film Electrode: A Combined in Situ IR Spectroscopy and Online Mass Spectrometry Study of Kinetic Isotope Effects. *Catal. Today* **2013**, *202*, 154–162.
43. Liu, Y.; Hu, P.; Wei, M.; Wang, C. Electrocatalytic Study of Ethylene Glycol Oxidation on Pt3Sn Alloy Nanoparticles. *ChemElectroChem* **2019**, *6*, 1004–1008.
44. Kabiraz, M.K.; Wahidah, H.; Hong, J.W.; Choi, S.-I. Platinum Metallenes: Advanced Electrocatalysts for Sustainable Energy Solutions. *Small* **2025**, *21*, 2500858.
45. Tong, Y.; Yan, X.; Liang, J.; Dou, S.X. Metal-Based Electrocatalysts for Methanol Electro-Oxidation: Progress, Opportunities, and Challenges. *Small* **2021**, *17*, 1904126.
46. Ayán-Varela, M.; Ruiz-Rosas, R.; Villar-Rodil, S.; Paredes, J.I.; Cazorla-Amorós, D.; Morallón, E.; Martínez-Alonso, A.; Tascón, J.M.D. Efficient Pt Electrocatalysts Supported onto Flavin Mononucleotide-Exfoliated Pristine Graphene for the Methanol Oxidation Reaction. *Electrochim. Acta* **2017**, *231*, 386–395.
47. Mu, Y.; Liang, H.; Hu, J.; Jiang, L.; Wan, L. Controllable Pt Nanoparticle Deposition on Carbon Nanotubes as an Anode Catalyst for Direct Methanol Fuel Cells. *J. Phys. Chem. B* **2005**, *109*, 22212–22216.
48. Watanabe, M.; Motoo, S. Electrocatalysis by Ad-Atoms: Part III. Enhancement of the Oxidation of Carbon Monoxide on Platinum by Ruthenium Ad-Atoms. *J. Electroanal. Chem. Interfacial Electrochem.* **1975**, *60*, 275–283.
49. Pei, A.; Ruan, L.; Liu, B.; Chen, W.; Lin, S.; Chen, B.; Liu, Y.; Zhu, L.H.; Chen, B.H. Ultra-Low Au Decorated PtNi Alloy Nanoparticles on Carbon for High-Efficiency Electro-Oxidation of Methanol and Formic Acid. *Int. J. Hydrogen Energy* **2020**, *45*, 22893–22905.
50. Bhalothia, D.; Huang, T.-H.; Chou, P.-H.; Wang, K.-W.; Chen, T.-Y. Promoting Formic Acid Oxidation Performance of Pd Nanoparticles via Pt and Ru Atom Mediated Surface Engineering. *RSC Adv.* **2020**, *10*, 17302–17310.
51. Bhalothia, D.; Huang, T.-H.; Chou, P.-H.; Chen, P.-C.; Wang, K.-W.; Chen, T.-Y. CO-Reductive and O_2-Oxidative Annealing Assisted Surface Restructure and Corresponding Formic Acid Oxidation Performance of PdPt and PdRuPt Nanocatalysts. *Sci. Rep.* **2020**, *10*, 8457.
52. Xia, S.; Wu, F.; Liu, Q.; Gao, W.; Guo, C.; Wei, H.; Hussain, A.; Zhang, Y.; Xu, G.; Niu, W. Steering the Selective Production of Glycolic Acid by Electrocatalytic Oxidation of Ethylene Glycol with Nanoengineered PdBi-Based Heterodimers. *Small* **2024**, *20*, 2400939.
53. Schnaidt, J.; Heinen, M.; Jusys, Z.; Behm, R.J. Oxidation of the Partly Oxidized Ethylene Glycol Oxidation Products Glycolaldehyde, Glyoxal, Glycolic Acid, Glyoxylic Acid, and Oxalic Acid on Pt Electrodes: A Combined ATR-FTIRS and DEMS Spectroelectrochemical Study. *J. Phys. Chem. C* **2013**, *117*, 12689–12701.

54. Yue, H.; Zhao, Y.; Ma, X.; Gong, J. Ethylene Glycol: Properties, Synthesis, and Applications. *Chem. Soc. Rev.* **2012**, *41*, 4218–4244.
55. Zhong, J.; Bin, D.; Feng, Y.; Zhang, K.; Wang, J.; Wang, C.; Guo, J.; Yang, P.; Du, Y. Synthesis and High Electrocatalytic Activity of Au-Decorated Pd Heterogeneous Nanocube Catalysts for Ethanol Electro-Oxidation in Alkaline Media. *Catal. Sci. Technol.* **2016**, *6*, 5397–5404.
56. Yuan, X.; Zhang, Y.; Cao, M.; Zhou, T.; Jiang, X.; Chen, J.; Lyu, F.; Xu, Y.; Luo, J.; Zhang, Q.; et al. $Bi(OH)_3$/PdBi Composite Nanochains as Highly Active and Durable Electrocatalysts for Ethanol Oxidation. *Nano Lett.* **2019**, *19*, 4752–4759.
57. Gao, L.; Yang, Z.; Sun, T.; Tan, X.; Lai, W.; Li, M.; Kim, J.; Lu, Y.-F.; Choi, S.-I.; Zhang, W.; et al. Autocatalytic Surface Reduction-Assisted Synthesis of PtW Ultrathin Alloy Nanowires for Highly Efficient Hydrogen Evolution Reaction. *Adv. Energy Mater.* **2022**, *12*, 2103943.
58. Wasmus, S.; Küver, A. Methanol Oxidation and Direct Methanol Fuel Cells: A Selective Review. *J. Electroanal. Chem.* **1999**, *461*, 14–31.
59. Tiwari, J.N.; Tiwari, R.N.; Singh, G.; Kim, K.S. Recent Progress in the Development of Anode and Cathode Catalysts for Direct Methanol Fuel Cells. *Nano Energy* **2013**, *2*, 553–578.
60. Park, J.; Kwon, T.; Kim, J.; Jin, H.; Kim, H.Y.; Kim, B.; Joo, S.H.; Lee, K. Hollow Nanoparticles as Emerging Electrocatalysts for Renewable Energy Conversion Reactions. *Chem. Soc. Rev.* **2018**, *47*, 8173–8202.
61. Aricò, A.S.; Srinivasan, S.; Antonucci, V. DMFCs: From Fundamental Aspects to Technology Development. *Fuel Cells* **2001**, *1*, 133–161.
62. Yuda, A.; Ashok, A.; Kumar, A. A Comprehensive and Critical Review on Recent Progress in Anode Catalyst for Methanol Oxidation Reaction. *Catal. Rev.* **2022**, *64*, 126–228.
63. Liu, M.; Zhang, Z.; Li, C.; Jin, S.; Zhu, K.; Fan, S.; Li, J.; Liu, K. High-Entropy Alloyed Single-Atom Pt for Methanol Oxidation Electrocatalysis. *Nat. Commun.* **2025**, *16*, 6359.
64. Li, P.; Hu, Q.; Fan, W.; Li, M.; Zhou, C.; Zhang, H.; Chen, L.; Pan, Z.; Jiao, X.; Chen, Q. Synergistic Multi-Active Sites in High-Entropy Alloy Nanowires Enhances the Methanol Oxidation Reaction Performances. *Small* **2025**, *21*, 2506472.
65. Xing, S.; Liu, Z.; Jiang, Y.; Tang, P.; Zhang, J.; Chen, J.; Li, H.; Li, C. Platinum-Copper Nanowire Networks with Enhanced CO Tolerance toward Methanol Oxidation Electrocatalysis. *Chem. Sci.* **2025**, *16*, 9311–9319
66. Lin, Z.; Chen, W.; Jiang, Y.; Bian, T.; Zhang, H.; Wu, J.; Wang, Y.; Yang, D. Facile Synthesis of Ru-Decorated Pt Cubes and Icosahedra as Highly Active Electrocatalysts for Methanol Oxidation. *Nanoscale* **2016**, *8*, 12812–12818.
67. Maiyalagan, T.; Alaje, T.O.; Scott, K. Highly Stable Pt–Ru Nanoparticles Supported on Three-Dimensional Cubic Ordered Mesoporous Carbon (Pt–Ru/CMK-8) as Promising Electrocatalysts for Methanol Oxidation. *J. Phys. Chem. C* **2012**, *116*, 2630–2638.
68. Takeguchi, T.; Yamanaka, T.; Asakura, K.; Muhamad, E.N.; Uosaki, K.; Ueda, W. Evidence of Nonelectrochemical Shift Reaction on a CO-Tolerant High-Entropy State Pt–Ru Anode Catalyst for Reliable and Efficient Residential Fuel Cell Systems. *J. Am. Chem. Soc.* **2012**, *134*, 14508–14512.
69. Nilekar, A.U.; Sasaki, K.; Farberow, C.A.; Adzic, R.R.; Mavrikakis, M. Mixed-Metal Pt Monolayer Electrocatalysts with Improved CO Tolerance. *J. Am. Chem. Soc.* **2011**, *133*, 18574–18576.
70. Gasteiger, H.A.; Markovic, N.; Ross, P.N.; Cairns, E.J. Methanol Electrooxidation on Well-Characterized Platinum-Ruthenium Bulk Alloys. *J. Phys. Chem.* **1993**, *97*, 12020–12029.
71. Zhao, X.; Yin, M.; Ma, L.; Liang, L.; Liu, C.; Liao, J.; Lu, T.; Xing, W. Recent Advances in Catalysts for Direct Methanol Fuel Cells. *Energy Environ. Sci.* **2011**, *4*, 2736–2753.
72. Yajima, T.; Wakabayashi, N.; Uchida, H.; Watanabe, M. Adsorbed Water for the Electro-Oxidation of Methanol at Pt–Ru Alloy. *Chem. Commun.* **2003**, *7*, 828–829.
73. Pelliccione, C.J.; Timofeeva, E.V.; Katsoudas, J.P.; Segre, C.U. In Situ Ru K-Edge X-Ray Absorption Spectroscopy Study of Methanol Oxidation Mechanisms on Model Submonolayer Ru on Pt Nanoparticle Electrocatalyst. *J. Phys. Chem. C* **2013**, *117*, 18904–18912.
74. Cai, Z.; Lu, Z.; Bi, Y.; Li, Y.; Kuang, Y.; Sun, X. Superior Anti-CO Poisoning Capability: Au-Decorated PtFe Nanocatalysts for High-Performance Methanol Oxidation. *Chem. Commun.* **2016**, *52*, 3903–3906.
75. Gu, J.; Liu, W.-C.; Zhao, Z.-Q.; Lan, G.-X.; Zhu, W.; Zhang, Y.-W. Pt/Ru/C Nanocomposites for Methanol Electrooxidation: How Ru Nanocrystals' Surface Structure Affects Catalytic Performance of Deposited Pt Particles. *Inorg. Chem. Front.* **2014**, *1*, 109–117.
76. Freitas, R.G.; Marchesi, L.F.Q.; Forim, M.R.; Bulhões, L.O.; Pereira, E.C.; Santos, M.C.; Oliveira, R.T. Ethanol Electrooxidation Using Ti/$(RuO_2)_{(x)}Pt_{(1-x)}$ Electrodes Prepared by the Polymeric Precursor Method. *J. Braz. Chem. Soc.* **2011**, *22*, 1709–1717.
77. Freitas, R.G.; Marchesi, L.F.; Oliveira, R.T.S.; Mattos-Costa, F.I.; Pereira, E.C.; Bulhoes, L.O.S.; Santos, M.C. Methanol Oxidation Reaction on Ti/$(RuO_2)_{(x)}Pt_{(1-x)}$ Electrodes Prepared by the Polymeric Precursor Method. *J. Power Sources* **2007**, *171*, 373–380.

78. Park, J.; Kim, H.J.; Oh, A.; Kwon, T.; Baik, H.; Choi, S.-I.; Lee, K. RuO X-Decorated Multimetallic Hetero-Nanocages as Highly Efficient Electrocatalysts toward the Methanol Oxidation Reaction. *Nanoscale* **2018**, *10*, 21178–21185.
79. Qiao, B.; Wang, A.; Yang, X.; Allard, L.F.; Jiang, Z.; Cui, Y.; Liu, J.; Li, J.; Zhang, T. Single-Atom Catalysis of CO Oxidation Using Pt_1/FeO_X. *Nat. Chem.* **2011**, *3*, 634–641.
80. Fu, Q.; Li, W.-X.; Yao, Y.; Liu, H.; Su, H.-Y.; Ma, D.; Gu, X.-K.; Chen, L.; Wang, Z.; Zhang, H. Interface-Confined Ferrous Centers for Catalytic Oxidation. *Science* **2010**, *328*, 1141–1144.
81. Pedersen, M.Ø.; Helveg, S.; Ruban, A.; Stensgaard, I.; Lægsgaard, E.; Nørskov, J.K.; Besenbacher, F. How a Gold Substrate Can Increase the Reactivity of a Pt Overlayer. *Surf. Sci.* **1999**, *426*, 395–409.
82. Koenigsmann, C.; Semple, D.B.; Sutter, E.; Tobierre, S.E.; Wong, S.S. Ambient Synthesis of High-Quality Ruthenium Nanowires and the Morphology-Dependent Electrocatalytic Performance of Platinum-Decorated Ruthenium Nanowires and Nanoparticles in the Methanol Oxidation Reaction. *ACS Appl. Mater. Interfaces* **2013**, *5*, 5518–5530.
83. Marinkovic, N.S.; Li, M.; Adzic, R.R. Pt-based Catalysts for Electrochemical Oxidation of Ethanol. *Electrocatalysis* **2019**, *377*, 11.
84. Li, G.; Pickup, P.G. Analysis of Performance Losses of Direct Ethanol Fuel Cells with the Aid of a Reference Electrode. *J. Power Sources* **2006**, *161*, 256–263.
85. Xu, Y.; Zhang, B. Recent Advances in Porous Pt-Based Nanostructures: Synthesis and Electrochemical Applications. *Chem. Soc. Rev.* **2014**, *43*, 2439–2450.
86. Zhu, W.; Ke, J.; Wang, S.-B.; Ren, J.; Wang, H.-H.; Zhou, Z.-Y.; Si, R.; Zhang, Y.-W.; Yan, C.-H. Shaping Single-Crystalline Trimetallic Pt–Pd–Rh Nanocrystals toward High-Efficiency C–C Splitting of Ethanol in Conversion to CO_2. *ACS Catal.* **2015**, *5*, 1995–2008.
87. Kim, H.J.; Ruqia, B.; Kang, M.S.; Lim, S.B.; Choi, R.; Nam, K.M.; Seo, W.S.; Lee, G.; Choi, S.-I. Shape-Controlled Pt Nanocubes Directly Grown on Carbon Supports and Their Electrocatalytic Activity toward Methanol Oxidation. *Sci. Bull.* **2017**, *62*, 943–949.
88. Kim, K.S.; Hong, Y.; Kim, H.C.; Choi, S.; Hong, J.W. Ultrathin-Polyaniline-Coated Pt–Ni Alloy Nanooctahedra for the Electrochemical Methanol Oxidation Reaction. *Chem. Eur. J.* **2019**, *25*, 7185–7190.
89. Zhang, Z.; Liu, J.; Zhu, S.; Wang, Y.; Wang, J.; Xu, M.; Zhao, J.; Wang, Z.; Zeng, D.; Zeng, J. Dizygotic Atomic Platinum and Palladium on Carbon for High-Performance Ethanol and Methanol Electro-Oxidation. *Angew. Chem. Int. Ed.* **2025**, *64*, e202502348.
90. Kim, H.J.; Ahn, Y.-D.; Kim, J.; Kim, K.-S.; Jeong, Y.U.; Hong, J.W.; Choi, S.-I. Surface Elemental Distribution Effect of Pt-Pb Hexagonal Nanoplates for Electrocatalytic Methanol Oxidation Reaction. *Chin. J. Catal.* **2020**, *41*, 813–819.
91. Zhang, K.; Bin, D.; Yang, B.; Wang, C.; Ren, F.; Du, Y. Ru-Assisted Synthesis of Pd/Ru Nanodendrites with High Activity for Ethanol Electrooxidation. *Nanoscale* **2015**, *7*, 12445–12451.
92. Wu, Z.; Duan, R.; Cui, J.; Ye, C.; Zhang, S.; Yan, S. An Overview of the Pd Based Electrocatalysts Utilized in Direct Alcohol Fuel Cells. *Electrocatalysis* **2025**, *16*, 197–223.
93. Cui, Y.; Ma, K.; Chen, Z.; Yang, J.; Geng, Z.; Zeng, J. Atomic-Level Insights into Strain Effect on p-Nitrophenol Reduction via Au@Pd Core–Shell Nanocubes as an Ideal Platform. *J. Catal.* **2020**, *381*, 427–433.
94. Yuge, K.; Koyama, Y.; Kuwabara, A.; Tanaka, I. Surface Design of Alloy Protection against CO-Poisoning from First Principles. *J. Phys. Condens. Matter* **2014**, *26*, 355006.
95. Nguyen, M.T.X.; Nguyen, M.-K.; Pham, P.T.T.; Huynh, H.K.P.; Pham, H.H.; Vo, C.C.; Nguyen, S.T. High-Performance Pd-Coated Ni Nanowire Electrocatalysts for Alkaline Direct Ethanol Fuel Cells. *J. Electroanal. Chem.* **2021**, *888*, 115180.
96. Li, M.; Zhao, Z.; Xia, Z.; Yang, Y.; Luo, M.; Huang, Y.; Sun, Y.; Chao, Y.; Yang, W.; Yang, W.; et al. Lavender-Like Ga-Doped Pt3Co Nanowires for Highly Stable and Active Electrocatalysis. *ACS Catal.* **2020**, *10*, 3018–3026.
97. Mao, J.; Chen, W.; He, D.; Wan, J.; Pei, J.; Dong, J.; Wang, Y.; An, P.; Jin, Z.; Xing, W. Design of Ultrathin Pt-Mo-Ni Nanowire Catalysts for Ethanol Electrooxidation. *Sci. Adv.* **2017**, *3*, e1603068.
98. Hong, Y.; Kim, H.J.; Lee, H.J.; Kim, J.; Choi, S.-I. $Ni(OH)_2$ Decorated Pt–Cu Octahedra for Ethanol Electrooxidation Reaction. *Front. Chem.* **2019**, *7*, 608.
99. Fan, X.; Tang, M.; Wu, X.; Luo, S.; Chen, W.; Song, X.; Quan, Z. SnO_2 Patched Ultrathin PtRh Nanowires as Efficient Catalysts for Ethanol Electrooxidation. *J. Mater. Chem. A* **2019**, *7*, 27377–27382.
100. Gruzeł, G.; Szmuc, K.; Drzymała, E.; Piekarz, P.; Pajor-Świerzy, A.; Budziak, A.; Pastor, E. Thin Layer vs. Nanoparticles: Effect of SnO_2 Addition to PtRhNi Nanoframes for Ethanol Oxidation Reaction. *Int. J. Hydrogen Energy* **2022**, *47*, 14823–14835.
101. Yu, X.; Pickup, P.G. Recent Advances in Direct Formic Acid Fuel Cells (DFAFC). *J. Power Sources* **2008**, *182*, 124–132.
102. Rhee, Y.-W.; Ha, S.Y.; Masel, R.I. Crossover of Formic Acid through Nafion® Membranes. *J. Power Sources* **2003**, *117*, 35–38.
103. Demirci, U.B. Direct Liquid-Feed Fuel Cells: Thermodynamic and Environmental Concerns. *J. Power Sources* **2007**, *169*, 239–246.

104. Aslam, N.M.; Masdar, M.S.; Kamarudin, S.K.; Daud, W.R.W. Overview on Direct Formic Acid Fuel Cells (DFAFCs) as an Energy Sources. *Apcbee Procedia* **2012**, *3*, 33–39.
105. Capon, A.; Parson, R. The Oxidation of Formic Acid at Noble Metal Electrodes: I. Review of Previous Work. *J. Electroanal. Chem. Interfacial Electrochem.* **1973**, *44*, 1–7.
106. Capon, A.; Parsons, R. The Oxidation of Formic Acid on Noble Metal Electrodes: II. A Comparison of the Behaviour of Pure Electrodes. *J. Electroanal. Chem. Interfacial Electrochem.* **1973**, *44*, 239–254.
107. Fayette, M.; Nutariya, J.; Vasiljevic, N.; Dimitrov, N. A Study of Pt Dissolution during Formic Acid Oxidation. *Acs Catal.* **2013**, *3*, 1709–1718.
108. Rettenmaier, C.; Arán-Ais, R.M.; Timoshenko, J.; Rizo, R.; Jeon, H.S.; Kühl, S.; Chee, S.W.; Bergmann, A.; Roldan Cuenya, B. Enhanced Formic Acid Oxidation over SnO_2-Decorated Pd Nanocubes. *ACS Catal.* **2020**, *10*, 14540–14551.
109. Miyake, H.; Okada, T.; Samjeské, G.; Osawa, M. Formic Acid Electrooxidation on Pd in Acidic Solutions Studied by Surface-Enhanced Infrared Absorption Spectroscopy. *Phys. Chem. Chem. Phys.* **2008**, *10*, 3662–3669.
110. Zhou, Y.; Du, C.; Han, G.; Gao, Y.; Yin, G. Ultra-Low Pt Decorated PdFe Alloy Nanoparticles for Formic Acid Electro-Oxidation. *Electrochim. Acta* **2016**, *217*, 203–209.
111. Wang, J.-Y.; Kang, Y.-Y.; Yang, H.; Cai, W.-B. Boron-Doped Palladium Nanoparticles on Carbon Black as a Superior Catalyst for Formic Acid Electro-Oxidation. *J. Phys. Chem. C* **2009**, *113*, 8366–8372.
112. Xu, H.; Yan, B.; Zhang, K.; Wang, C.; Zhong, J.; Li, S.; Yang, P.; Du, Y. Facile Synthesis of Pd–Ru–P Ternary Nanoparticle Networks with Enhanced Electrocatalytic Performance for Methanol Oxidation. *Int. J. Hydrogen Energy* **2017**, *42*, 11229–11238.
113. Lv, H.; Xu, D.; Sun, L.; Henzie, J.; Suib, S.L.; Yamauchi, Y.; Liu, B. Ternary Palladium-Boron-Phosphorus Alloy Mesoporous Nanospheres for Highly Efficient Electrocatalysis. *ACS Nano* **2019**, *13*, 12052–12061.
114. Scofield, M.E.; Koenigsmann, C.; Wang, L.; Liu, H.; Wong, S.S. Tailoring the Composition of Ultrathin, Ternary Alloy PtRuFe Nanowires for the Methanol Oxidation Reaction and Formic Acid Oxidation Reaction. *Energy Environ. Sci.* **2015**, *8*, 350–363.
115. Vidal-Iglesias, F.J.; Solla-Gullón, J.; Herrero, E.; Aldaz, A.; Feliu, J.M. Pd Adatom Decorated (100) Preferentially Oriented Pt Nanoparticles for Formic Acid Electrooxidation. *Angew. Chem. Int. Ed.* **2010**, *49*, 6998–7001.
116. Yang, F.-K.; Fang, Y.; Li, F.-F.; Qu, W.-L.; Deng, C. Sn-Doped PdCu Alloy Nanosheet Assemblies as an Efficient Electrocatalyst for Formic Acid Oxidation. *Dalt. Trans.* **2023**, *52*, 14428–14434.
117. Lin, X.; Geng, S.; Du, X.; Wang, F.; Zhang, X.; Xiao, F.; Xiao, Z.; Wang, Y.; Cheng, J.; Zheng, Z.; et al. Efficient Direct Formic Acid Electrocatalysis Enabled by Rare Earth-Doped Platinum-Tellurium Heterostructures. *Nat. Commun.* **2025**, *16*, 147.
118. Vidal-Iglesias, F.J.; López-Cudero, A.; Solla-Gullón, J.; Feliu, J.M. Towards More Active and Stable Electrocatalysts for Formic Acid Electrooxidation: Antimony-Decorated Octahedral Platinum Nanoparticles. *Angew. Chem. Int. Ed.* **2013**, *52*, 964–967.
119. Serov, A.; Kwak, C. Recent Achievements in Direct Ethylene Glycol Fuel Cells (DEGFC). *Appl. Catal. B Environ.* **2010**, *97*, 1–12.
120. Gao, J.; Mao, M.; Li, P.; Liu, R.; Song, H.; Sun, K.; Zhang, S. Segmentation and Re-Encapsulation of Porous PtCu Nanoparticles by Generated Carbon Shell for Enhanced Ethylene Glycol Oxidation and Oxygen-Reduction Reaction. *ACS Appl. Mater. Interfaces* **2020**, *12*, 6298–6308.
121. An, L.; Chen, R. Recent Progress in Alkaline Direct Ethylene Glycol Fuel Cells for Sustainable Energy Production. *J. Power Sources* **2016**, *329*, 484–501.
122. Chang, S.C.; Ho, Y.; Weaver, M.J. Applications of Real-Time FTIR Spectroscopy to the Elucidation of Complex Electroorganic Pathways: Electrooxidation of Ethylene Glycol on Gold, Platinum, and Nickel in Alkaline Solution. *J. Am. Chem. Soc.* **1991**, *113*, 9506–9513.
123. Schnaidt, J.; Heinen, M.; Jusys, Z.; Behm, R.J. Electro-Oxidation of Ethylene Glycol on a Pt-Film Electrode Studied by Combined in Situ Infrared Spectroscopy and Online Mass Spectrometry. *J. Phys. Chem. C* **2012**, *116*, 2872–2883.
124. Wang, Y.; Zhuo, H.; Sun, H.; Zhang, X.; Dai, X.; Luan, C.; Qin, C.; Zhao, H.; Li, J.; Wang, M. Implanting Mo Atoms into Surface Lattice of Pt_3Mn Alloys Enclosed by High-Indexed Facets: Promoting Highly Active Sites for Ethylene Glycol Oxidation. *ACS Catal.* **2018**, *9*, 442–455.
125. Bai, S.; Wang, C.; Deng, M.; Gong, M.; Bai, Y.; Jiang, J.; Xiong, Y. Surface Polarization Matters: Enhancing the Hydrogen-evolution Reaction by Shrinking Pt Shells in Pt–Pd–Graphene Stack Structures. *Angew. Chem. Int. Ed.* **2014**, *53*, 12120–12124.
126. Li, C.; Yuan, Q.; Ni, B.; He, T.; Zhang, S.; Long, Y.; Gu, L.; Wang, X. Dendritic Defect-Rich Palladium–Copper–Cobalt Nanoalloys as Robust Multifunctional Non-Platinum Electrocatalysts for Fuel Cells. *Nat. Commun.* **2018**, *9*, 3702.
127. Robinson, A.M.; Mark, L.; Rasmussen, M.J.; Hensley, J.E.; Medlin, J.W. Surface Chemistry of Aromatic Reactants on Pt-and Mo-Modified Pt Catalysts. *J. Phys. Chem. C* **2016**, *120*, 26824–26833.

128. Demarconnay, L.; Brimaud, S.; Coutanceau, C.; Léger, J.-M. Ethylene Glycol Electrooxidation in Alkaline Medium at Multi-Metallic Pt Based Catalysts. *J. Electroanal. Chem.* **2007**, *601*, 169–180.
129. Yang, Y.-Y.; Ren, J.; Zhang, H.-X.; Zhou, Z.-Y.; Sun, S.-G.; Cai, W.-B. Infrared Spectroelectrochemical Study of Dissociation and Oxidation of Methanol at a Palladium Electrode in Alkaline Solution. *Langmuir* **2013**, *29*, 1709–1716.
130. Hahn, F.; Beden, B.; Kadirgan, F.; Lamy, C. Electrocatalytic Oxidation of Ethylene Glycol: Part III. In-Situ Infrared Reflectance Spectroscopic Study of the Strongly Bound Species Resulting from Its Chemisorption at a Platinum Electrode in Aqueous Medium. *J. Electroanal. Chem. Interfacial Electrochem.* **1987**, *216*, 169–180.
131. Leung, L.W.H.; Weaver, M.J. Real-Time FTIR Spectroscopy as a Quantitative Kinetic Probe of Competing Electrooxidation Pathways of Small Organic Molecules. *J. Phys. Chem.* **1988**, *92*, 4019–4022.
132. Christensen, P.A.; Hamnett, A. The Oxidation of Ethylene Glycol at a Platinum Electrode in Acid and Base: An in Situ FTIR Study. *J. Electroanal. Chem. Interfacial Electrochem.* **1989**, *260*, 347–359.
133. Wang, H.; Jiang, B.; Zhao, T.-T.; Jiang, K.; Yang, Y.-Y.; Zhang, J.; Xie, Z.; Cai, W.-B. Electrocatalysis of Ethylene Glycol Oxidation on Bare and Bi-Modified Pd Concave Nanocubes in Alkaline Solution: An Interfacial Infrared Spectroscopic Investigation. *ACS Catal.* **2017**, *7*, 2033–2041.
134. Wang, P.; Lin, X.; Yang, B.; Jin, J.-M.; Hardacre, C.; Yu, N.-F.; Sun, S.-G.; Lin, W.-F. Activity Enhancement of Tetrahexahedral Pd Nanocrystals by Bi Decoration towards Ethanol Electrooxidation in Alkaline Media. *Electrochim. Acta* **2015**, *162*, 290–299.
135. Bambagioni, V.; Bevilacqua, M.; Bianchini, C.; Filippi, J.; Marchionni, A.; Vizza, F.; Wang, L.Q.; Shen, P.K. Ethylene Glycol Electrooxidation on Smooth and Nanostructured Pd Electrodes in Alkaline Media. *Fuel Cells* **2010**, *10*, 582–590.
136. Cheng, J.; Tu, Y.; Xiang, Y.; Ni, J.; Guo, T.; Huang, X.; Liu, B.; Wei, Z. Anti-Poisoning of CO and Carbonyl Species over Pd Catalysts during the Electrooxidation of Ethylene Glycol to Glycolic Acid at Elevated Current Density. *Chem. Sci.* **2025**, *16*, 4303–4310.
137. Wang, C.; Xu, H.; Shang, H.; Jin, L.; Chen, C.; Wang, Y.; Yuan, M.; Du, Y. Ir-Doped Pd Nanosheet Assemblies as Bifunctional Electrocatalysts for Advanced Hydrogen Evolution Reaction and Liquid Fuel Electrocatalysis. *Inorg. Chem.* **2020**, *59*, 3321–3329.
138. Wang, Y.; Zheng, M.; Sun, H.; Zhang, X.; Luan, C.; Li, Y.; Zhao, L.; Zhao, H.; Dai, X.; Ye, J.-Y.; et al. Catalytic Ru Containing Pt3Mn Nanocrystals Enclosed with High-Indexed Facets: Surface Alloyed Ru Makes Pt More Active than Ru Particles for Ethylene Glycol Oxidation. *Appl. Catal. B Environ.* **2019**, *253*, 11–20.
139. Qin, Y.; Zhang, W.; Wang, F.; Li, J.; Ye, J.; Sheng, X.; Li, C.; Liang, X.; Liu, P.; Wang, X. Extraordinary p–d Hybridization Interaction in Heterostructural Pd-PdSe Nanosheets Boosts C–C Bond Cleavage of Ethylene Glycol Electrooxidation. *Angew. Chem. Int. Ed.* **2022**, *61*, e202200899.
140. Yang, X.; Yao, K.X.; Ye, J.Y.; Yuan, Q.; Zhao, F.; Li, Y.; Zhou, Z. Interface-Rich Three-Dimensional Au-Doped PtBi Intermetallics as Highly Effective Anode Catalysts for Application in Alkaline Ethylene Glycol Fuel Cells. *Adv. Funct. Mater.* **2021**, *31*, 2103671.

Article

Magnetic Assembly of Nonuniform Nanocrystal Clusters into Responsive Photonic Crystals

Fenglian Qi [1,2], Qingsong Fan [2], Chaolumen Wu [2], and Yadong Yin [2,*]

[1] College of Chemistry and Molecular Engineering, Qingdao University of Science and Technology, Qingdao 266042, China
[2] Department of Chemistry, University of California, Riverside, CA 92521, USA
* Correspondence: yadong.yin@ucr.edu
Received: 5 December 2025; Revised: 23 December 2025; Accepted: 25 December 2025; Published: 26 December 2025

Abstract: Colloidal assembly of photonic crystals typically relies on uniform building blocks to achieve the required periodicity. However, the difficulties in large-scale production of uniform particles limit the practical use of colloidal photonic crystals in many exciting applications. Here, we show that this uniformity requirement can be relaxed by increasing the interparticle spacing during colloidal magnetic assembly, enabling the formation of responsive photonic crystals from particles with a broader size range. Specifically, we demonstrate that magnetite nanocrystal clusters with a wide size range of 40–60 nm, formed by breaking their large aggregates via ultrasonication in the presence of polymeric ligands, can be magnetically assembled in solution into one-dimensional photonic crystals with tunable optical diffraction across the entire visible spectrum. The strong electrostatic repulsion imparted by the polymeric ligands results in large interparticle separation, reducing the negative impact of low particle uniformity and enabling the required periodicity for notable diffraction and broad spectral tunability.

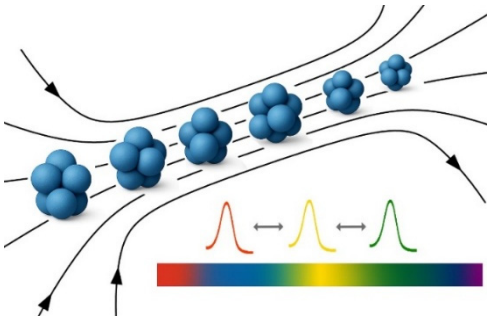

Keywords: nonuniformity; nanocrystal clusters; magnetic assembly; one-dimensional; photonic crystals; poly(acrylic acid)

1. Introduction

Photonic crystals are functional materials with periodically modulated refractive indices [1–3]. Their strong interaction with light induces constructive and destructive interference, producing optical diffraction that is determined by the crystals' order and periodicity [4]. Conventional methods for preparing colloidal photonic crystals rely on uniform building blocks of appropriate sizes to achieve bright structural colors and tunable optical diffraction [5]. As determined by Bragg's law, colloidal particles with uniform sizes in the range from 150 to 300 nm are commonly employed as ideal building blocks for preparing close-packed crystals with diffraction in the visible range [6–9]. Various materials, such as SiO_2 [6,10], polymers [11–13], and polysulfide [5], have been prepared as uniform colloidal spheres for photonic crystal assembly. Besides particle size, the refractive indices of materials also contribute to determining the diffraction wavelength. For materials with low refractive indices, such as SiO_2, a particle diameter of 200–300 nm is required to produce visible diffraction [14]. This contrasts with materials like CeO_2, which have higher refractive indices and can produce visible responses with particles as small as 125 nm [15].

For non-close-packed photonic crystals, the building-block size can be reduced further to below 100 nm due to interparticle separations. Earlier research by Asher et al. demonstrated that highly charged polystyrene beads of 110 and 120 nm could self-assemble into crystalline colloidal arrays [16,17], relying on electrostatic repulsion to maintain structural order. Another example involves the magnetic assembly of superparamagnetic nanocrystal clusters of magnetite (Fe_3O_4), first developed in our group [18,19] and then followed by several other groups [20,21]. In these cases, strong electrostatic repulsion could create large interparticle separations, enabling small particles to be assembled into one-dimensional (1D) arrays with bright, magnetically responsive structural colors.

Copyright: © 2025 by the authors. This is an open access article under the terms and conditions of the Creative Commons Attribution (CC BY) license (https://creativecommons.org/licenses/by/4.0/).
Publisher's Note: Scilight stays neutral with regard to jurisdictional claims in published maps and institutional affiliations.

This work aims to highlight another key benefit of the magnetic assembly approach for forming non-close-packed structures: reducing the negative impact of nonuniformity in the building blocks. We show that large separations induced by strong electrostatic repulsion can offset the effects of particle-size polydispersity, enabling the formation of the periodicity required for optical diffraction. Starting with bulk aggregates of Fe_3O_4 nanocrystals produced via solvothermal processing, we found that ultrasonication could break them into nanocrystal clusters of 40–60 nm. Despite their low size uniformity, these clusters could still be assembled in aqueous solution into 1D arrays with magnetically responsive structural colors of notable brightness. Polyacrylic acid (PAA) was used as a capping ligand during ultrasonication to stabilize nanocrystal clusters formed from aggregate breakage and to promote strong electrostatic repulsion during magnetic assembly. Since the initial solvothermal synthesis of bulk nanocrystal aggregates is easily scalable, their convenient transformation into nanocrystal clusters, combined with the high tolerance to nonuniformity of the magnetic assembly process, makes this approach promising for applications that require large amounts of material over wide areas, while maximum brightness in structural color isn't essential.

2. Experimental Section

2.1 Materials

$FeCl_3 \cdot 6H_2O$, sodium formate, polyvinylpyrrolidone (PVP, M_w. 40,000), PAA (M_w. 1800), EG, PG, resorcinol, and formaldehyde solution (37 wt % in water) were purchased from Sigma-Aldrich (St. Louis, MI, USA). $NH_3 \cdot H_2O$ was purchased from Fisher (Pittsburgh, PL, USA). All chemicals were used as received without further purification.

2.2 Synthesis of PAA-Modified Magnetic Clusters

Magnetic clusters were prepared using a modified solvothermal polyol method [22]. $FeCl_3 \cdot 6H_2O$ (16 mmol), sodium formate (29 mmol), and PVP (2.0 g) were dissolved in a mixture of ethylene glycol (35 mL) and 1,2-propylene glycol (5 mL) under vigorous stirring. The solution was sealed in a 100 mL Teflon-lined stainless-steel autoclave and heated at 210 °C for 8 h. After cooling to room temperature overnight, the black product was collected by centrifugation and washed three times with water. The resulting material was re-dispersed in 50 mL of water, followed by the addition of 10 mL of PAA solution (7.2 mg/mL). The mixture was sonicated for 30 min, washed three times with water, and separated overnight using a magnet. Finally, the clusters were re-dispersed in 30 mL of water.

2.3 Centrifugal Separation of PAA-Modified Magnetic Clusters

Four representative samples of PAA-modified magnetic clusters were obtained through sequential centrifugation. Prior to separation, the dispersion was sonicated for 20 min. The first fraction (M1) was collected from the supernatant after centrifugation at 11,000 rpm for 3 min. The remaining precipitate was re-dispersed in 30 mL of water by ultrasonication, and subsequent fractions (M2, M3, and M4) were obtained by centrifugation at 9000, 7000, and 5000 rpm for 3 min, respectively. All samples were then concentrated to 10 mg/mL in water for further characterization.

2.4 Fixation of 1D Assemblies of Nanocrystal Clusters

1D assemblies were stabilized using a conformal coating of phenolic resin with slight modifications to the reported procedure [23]. Two precursor solutions were prepared separately: one by dissolving 5 mg of resorcinol in 1 mL of water, and the other by mixing 7 μL of formaldehyde (37 wt % in water) with 293 μL of water. Subsequently, 30 μL of resorcinol solution and 9 μL of diluted formaldehyde solution were combined with 100 μL of sample M1 (≈0.8 mg/mL) in a well of a 96-well plate. After ultrasonication for 3 min, the mixture was placed under a parallel magnetic field by positioning it adjacent to a neodymium magnet (25 mm × 25 mm × 9 mm, ≈2020 G) for 5 min. Then, 13 μL of $NH_3 \cdot H_2O$ (0.28%) was added slowly without disturbing the system, and the reaction continued for an additional 20 min under the same field. Following completion, the magnetic chains were separated from the solution using a magnetic field and then redispersed in 50 μL of water. The M2-based nanocluster chains were fixed using the same method and conditions as described above. The M3-based nanocluster chains were fixed with the same method, but the distance between the sample and the magnet was adjusted to 0.85 cm (magnetic strength: ca. 1380 Gauss). The M4-based nanocluster chains were fixed using the same method, with the M4 sample concentration reduced to 0.4 mg/mL and the distance between the sample and the magnet increased to 3.20 cm (magnetic strength: ca. 490 Gauss).

2.5 Sample Characterization

Dark-field optical images were obtained using a Zeiss AXIO Imager microscope (Oberkochen, Germany). SEM images of PAA-modified magnetic clusters were captured with a Zeiss G300 scanning electron microscope, and TEM images were recorded on a Tecnai T12 transmission electron microscope operating at 120 kV. Dynamic light scattering (DLS) and zeta potential measurements were performed using a Delsa NanoC Particle Analyzer and Zeta-Potential Analyzer (Beckman Coulter, Brea, CA, USA), respectively. Magnetic properties were characterized with a MicroMag 3900 Series (Lake Shore, Westerville, OH, USA) vibrating sample magnetometer under applied fields ranging from −20 to 20 kOe at 298 K. Reflection spectra were collected using an Ocean Optics HR2000 CG-UV-NIR spectrometer coupled with a six-around-one reflection probe, with incident and reflection angles fixed at 0° and the magnetic field oriented parallel to the incident light. Structural colors of photonic crystals were documented using a digital camera under the same magnetic field alignment.

3. Results and Discussion

Fe_3O_4 nanocrystal clusters were synthesized via a solvothermal process [22]. Ethylene glycol (EG) and 1,2-propylene glycol (PG) were employed as both the solvents and reducing agents during the reaction. In the presence of sodium formate, ferric ions were first hydrolyzed to form ferric hydroxide precipitates, which were then reduced to Fe_3O_4 nanocrystals by EG and PG at high temperature [22]. Due to the absence of capping ligands, the initial product appeared as bulk aggregates that quickly settled from the solution, as shown in the optical microscopy image and photo in Figure 1a. Ultrasonication of the aqueous solution containing these aggregates and PAA produced a colloidal dispersion of nanocrystal clusters [20,24]. During this process, PAA binds to the surface of the magnetic clusters through strong coordination between its carboxylate groups and the iron ions on the nanocrystal surface. As discussed later, it also provides large surface charges, resulting in strong electrostatic repulsion between the clusters [25]. As shown in Figure 1b, large aggregates disappeared after ultrasonication, confirming their effective breakage into small nanocrystal clusters, which also exhibited greatly improved colloidal stability compared to their original aggregate form. The scanning electron microscopy (SEM) image in Figure 1c shows their quasi-spherical shape with an average size below 100 nm. The transmission electron microscopy (TEM) image in Figure 1d indicates individual nanocrystals with an average size of around 20 nm, although it is difficult to distinguish between clusters when they are connected.

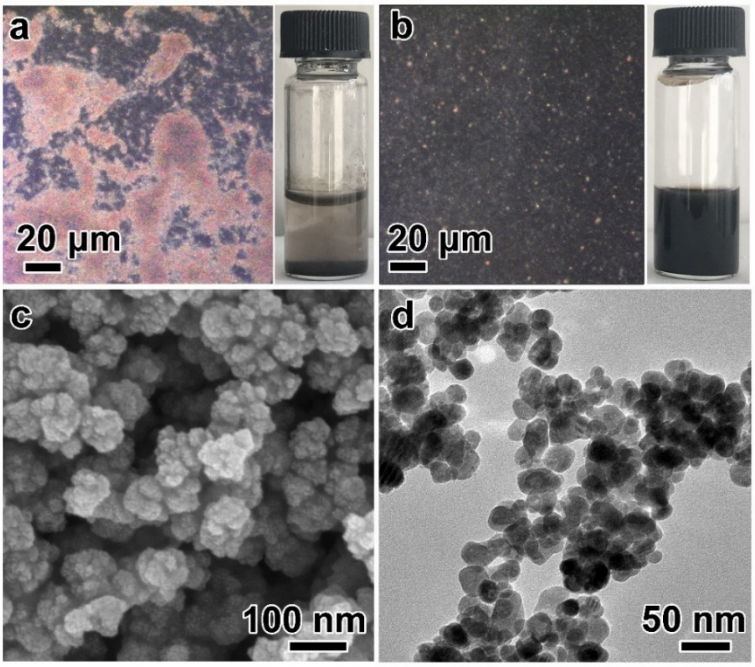

Figure 1. (**a**) Dark-field optical microscopy image of Fe_3O_4 nanocrystal aggregates synthesized via a solvothermal process, with the inset photo showing the sample in water; (**b**) Dark-field optical microscopy image of nanocrystal clusters formed after sonicating the aqueous mixture of aggregates and PAA, with the inset photo showing the particle dispersion after sitting for 30 min; (**c**,**d**) SEM image (**c**) and TEM image (**d**) of the PAA-modified nanocrystal clusters.

While effective at breaking nanocrystal aggregates, ultrasonication has limited capability to control cluster sizes. To obtain distinct structural colors, centrifugation-based size selection was performed by collecting nanocrystal clusters that remained in the supernatant after centrifugation at a specific speed. Specifically, four samples, M1, M2, M3, and M4, were collected from the supernatants after the initial product was centrifuged at 11,000, 9000, 7000, and 5000 rpm, respectively. Dynamic light scattering (DLS) study (Figure 2a,b) shows that the cluster sizes increase gradually from 83 nm (M1) to 104 nm (M2), 115 nm (M3), and finally 136 nm (M4). Their measured polydispersity indices (PDIs), which define the breadth of size distribution, range from 0.06 to 0.10 (Figure 2b), indicating relatively broad size distribution as compared with near-monodisperse spheres (e.g., PDI = 0.016) used in preparing conventional close-packed photonic crystals [5] or uniform magnetite nanocrystal clusters prepared in our previous work [18].

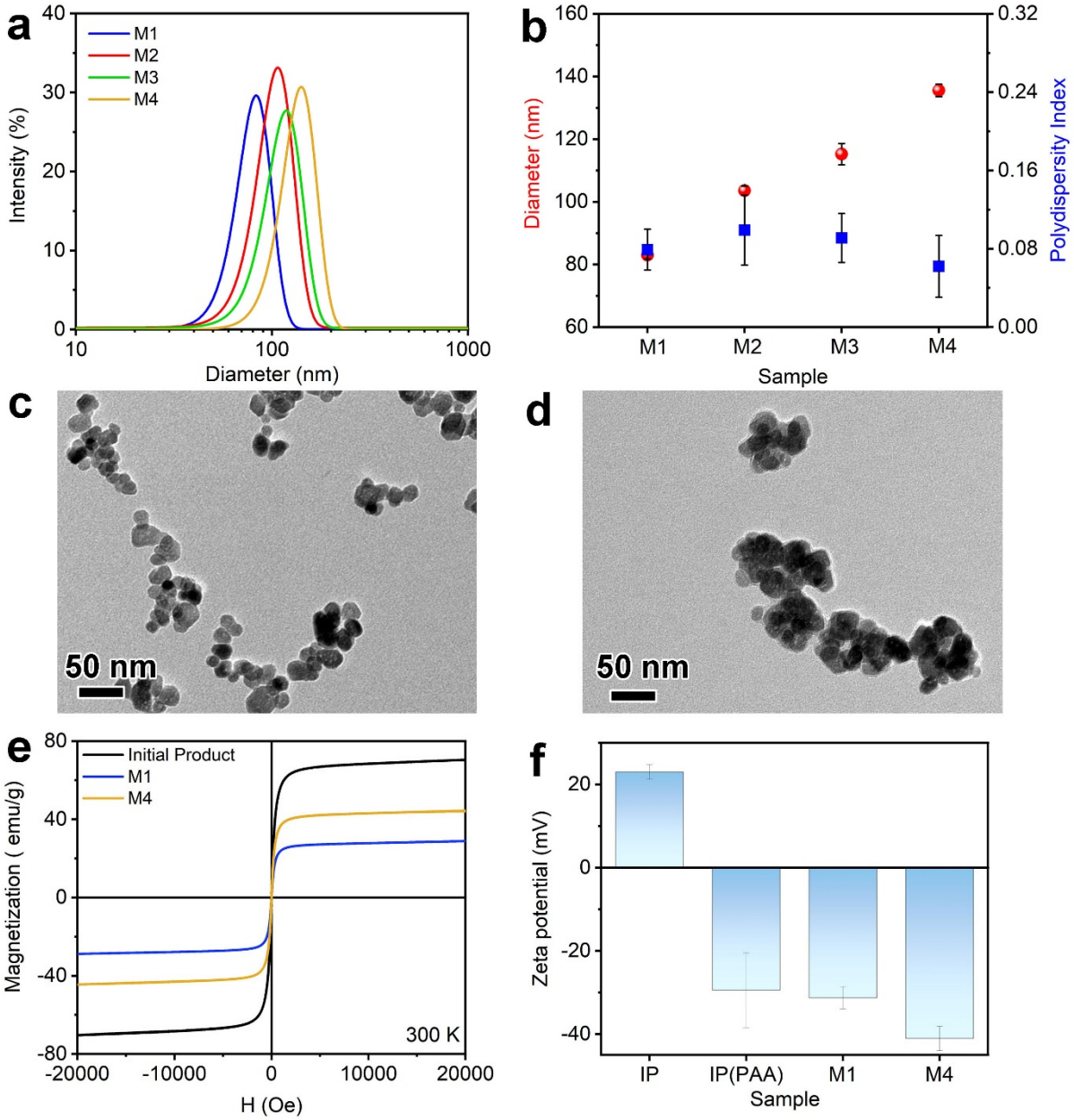

Figure 2. (**a**,**b**) DLS measurement of samples M1, M2, M3 and M4: size distribution (**a**) and corresponding diameter and PDI (**b**); (**c**,**d**) TEM images of samples M1 (**c**) and M4 (**d**); (**e**) Magnetic hysteresis loops of the initial nanocrystal aggregates and samples M1 and M4; (**f**) ζ-potential values of the initial product of nanocrystal aggregates (IP), PAA-modified cluster before size selection (IP(PAA)), and samples M1 and M4.

Using the smallest (M1) and largest (M4) magnetic clusters as examples, we systematically studied their morphologies and magnetically responsive optical properties. The TEM images in Figure 2c,d demonstrate the nonuniform size and irregular shape of the clusters, with M1 size below 50 nm and M4 ~60 nm. The size

discrepancies between TEM and DLS measurements are expected, as TEM measures the physical size of clusters in a dry state, while DLS measures the hydrodynamic diameter, which includes contributions from the solvent layer around the particles, surface ligands, and the diffuse ionic layer. Due to their small grain sizes, these clusters are superparamagnetic. The hysteresis curves in Figure 2e suggest superparamagnetic behavior, with coercivities of 24, 16, and 19 Oe for the initial aggregates, sample M1, and sample M4, respectively, which are smaller than the typical superparamagnetic limit of 30 Oe [24,25]. Moreover, the saturation magnetization is 29 emu/g for sample M1 and 44 emu/g for sample M4 at room temperature, in good agreement with the average particle size observed in Figure 2c,d [25]. The lower saturation magnetization of M1 and M4 than that of the initial aggregates (70 emu/g) is attributed to the contribution of PAA to the sample mass and to reduced domain interactions within the clusters.

Modification of the nanocrystal clusters with PAA confers negative surface charges, as shown by the ζ-potential measurements in Figure 2f. Before PAA modification, the ζ-potential of the initial aggregates was +23 mV, likely due to surface-bound iron ions. After modification, the ζ-potential shifted to −29 mV because of the abundant negative charges carried by carboxylate groups. At a pH near 7, PAA's carboxyl groups are significantly deprotonated, thanks to its pK_a of ~4.5 [26,27], which provides the nanocrystal surface with negative charges. These negative surface charges remained after size selection, with a ζ-potential of −31 mV for sample M1 and −41 mV for sample M4. The differences in ζ-potential between M1 and M4 may result from the differences in cluster size and the number of primary nanocrystals within. For smaller clusters, neighboring ligands are closer to each other and therefore experience more electrostatic repulsion, leading to a lower overall ligand density. A smaller number of primary nanocrystals in a cluster may also decrease surface complexity, allowing fewer ligands to bind.

The 1D assembly of magnetic clusters under magnetic fields was verified by coating the assembled structures with a resorcinol-formaldehyde resin via a sol-gel-like process in water [28,29]. The phenolic resin was used, instead of silica in our previous study, to avoid the need for ethanol as a solvent [19,30,31], which tends to cause severe aggregation of the current magnetic clusters. Further, we applied a strong magnetic field during coating to mitigate the challenges posed by the large separations within the assemblies.

The phenolic resin fixation of samples M1, M2, M3, and M4 was performed under 2020 G, 2020 G, 1380 G, and 490 G of magnetic fields, respectively. Figure 3a–d clearly confirmed the 1D periodic configurations of the magnetic nanoclusters. After the addition of phenolic resin precursor, the diffraction of the assemblies blueshifted owing to the increase in ionic strength (Figure S1). Relatively strong magnetic fields were applied to all four samples to decrease the inter-cluster spacings, making it easier to encapsulate the entire chains. Figure 3e further shows the electron tomography TEM images of a 1D chain assembled from sample M4, taken by rotating the chain from -45° to 45° counterclockwise along its long axis. Distinct gaps between neighboring nanocrystal clusters can be observed, indicating that the chain is assembled from discrete clusters rather than a continuous aggregation of individual nanocrystals. Treating individual nanocrystals as spheres, 20 nm in diameter as estimated from Figure 1d, allows us to estimate the average cluster size and the number of nanocrystals within each cluster. As summarized in Figure 3f, the average size of clusters increases from 40 nm (M1) to 53 nm (M2), 56 nm (M3), and finally 60 nm (M4), with the average number of nanocrystals in each cluster increasing from 2 to 5, 7, and 9, respectively. We further constructed a simple model (Figure 3g) to help illustrate the number of nanocrystals and their configuration within magnetic clusters of varying sizes.

Although the nanocrystal clusters were nonuniform in size and irregular in shape, we still observed tunable structural colors when their dispersions were exposed to magnetic fields. Figure 4a shows photos of the four samples in round glass vials (10 mg/mL) captured from the front direction, under a magnetic field aligned at the same angle (Figure S2). When the magnetic field decreases from 2020 G to 200 G, the structural color of sample M1 shifts from purple to green due to increased interparticle spacing. When the field is further reduced to 180 G, the color returns to its original grey, due to the disassembly of photonic chains under such a weak magnetic field. Similar trends in structural color changes are seen in samples M2, M3, and M4. At the same magnetic field strength, the structural color redshifts as the cluster size increases from M1 to M4. Smaller clusters, especially M1, diffract only short-wavelength light, from ~414 nm to 584 nm, with relatively weak, broad peaks (Figure 4b). Larger clusters exhibit higher diffraction intensity and a broader tuning range, primarily due to stronger magnetic interactions and larger scattering cross-sections [19]. Notably, M4 displays a much brighter structural color compared to the other samples, demonstrating wide spectral tuning of optical diffraction in the visible range, from 540 nm to 652 nm (Figure 4c). To compare the diffraction positions and intensities of the four samples, their reflection spectra under a magnetic field of 490 G are shown in Figure 4d. As the cluster size increases from 40 nm (M1) to 60 nm (M4), the peaks shift from 443 nm to 553 nm, respectively. The correlation between peak position and sample size is summarized in Figure 4e. When decreasing the magnetic field strength from 2020 G to 490 G by increasing the sample-magnet distance, we observed an initial slow and then rapid redshift in the diffraction peaks for all four samples.

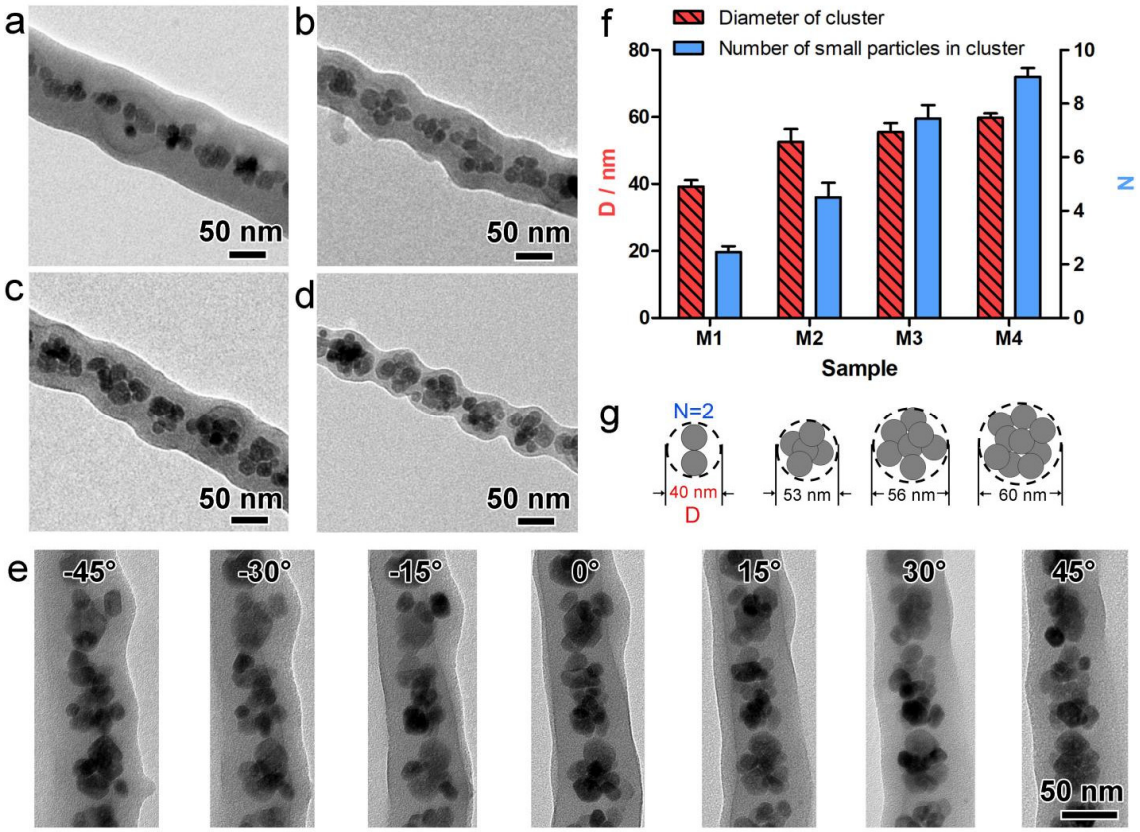

Figure 3. (**a**–**d**) TEM images of the magnetic assemblies of nanocrystal clusters of samples M1 (**a**), M2 (**b**), M3 (**c**), and M4 (**d**), all fixed by a phenolic resin coating; (**e**) Electron tomography images of a fixed M4 chain rotated along its long axis for various angles; (**f**) Estimated mean diameter of the magnetic clusters and the number of contained nanocrystals; (**g**) Scheme illustrating the configuration in nanocrystal clusters, from left to right: M1, M2, M3, and M4.

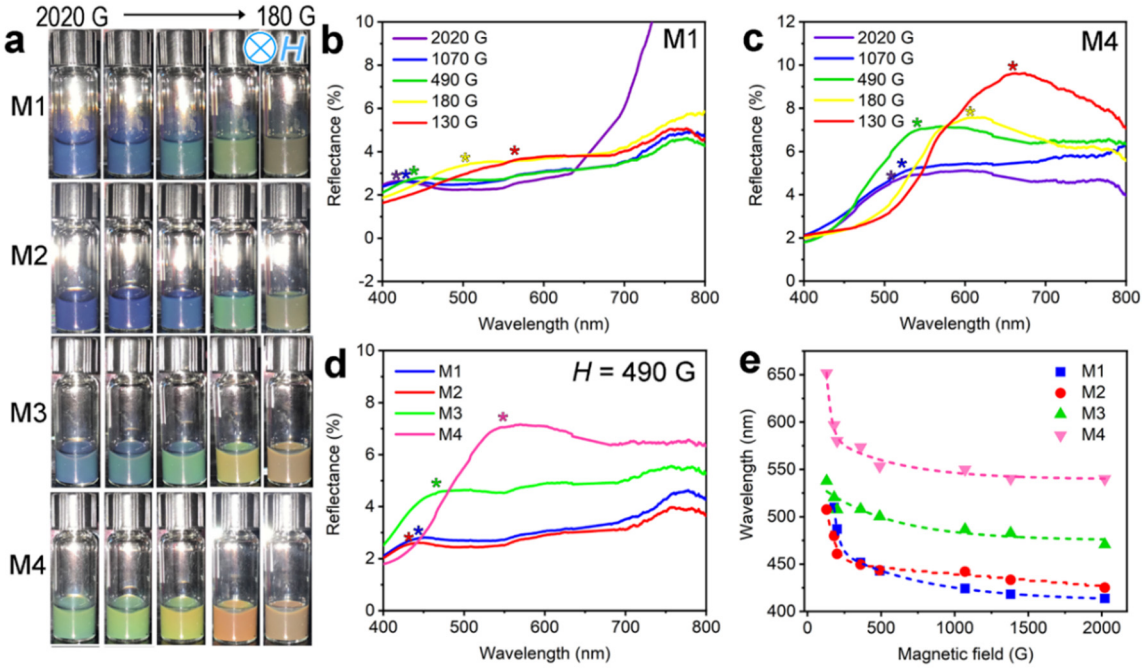

Figure 4. (**a**) Photographs of samples M1, M2, M3, and M4 under varying magnetic fields; (**b**,**c**) Reflection spectra of samples M1 (**b**) and M4 (**c**) under different magnetic fields; (**d**) Reflection spectra of all four samples at a magnetic field of 490 G; (**e**) Change in peak position with magnetic field strength. The concentration of each sample is 10 mg/mL. The symbol '*' in figures b–d indicates the position of the main reflection peaks.

We further optimized the concentration of sample M4 to enable full-range optical diffraction tuning. An increase in sample concentration results in a blueshift in diffraction and improved response at lower field strengths, broadening the range of structural color changes (Figure S3). At 20 mg/mL, the reflection spectra show a peak shift from 470 nm to 663 nm as the magnetic field decreases from 2020 G to 60 G, accompanied by a color transition from blue to red (Figure 5a). Unlike our previous work where uniform magnetic particles of similar size produced only blue light [18], the broad size distribution of magnetic clusters in this study allows for a significantly wider tuning range [19].

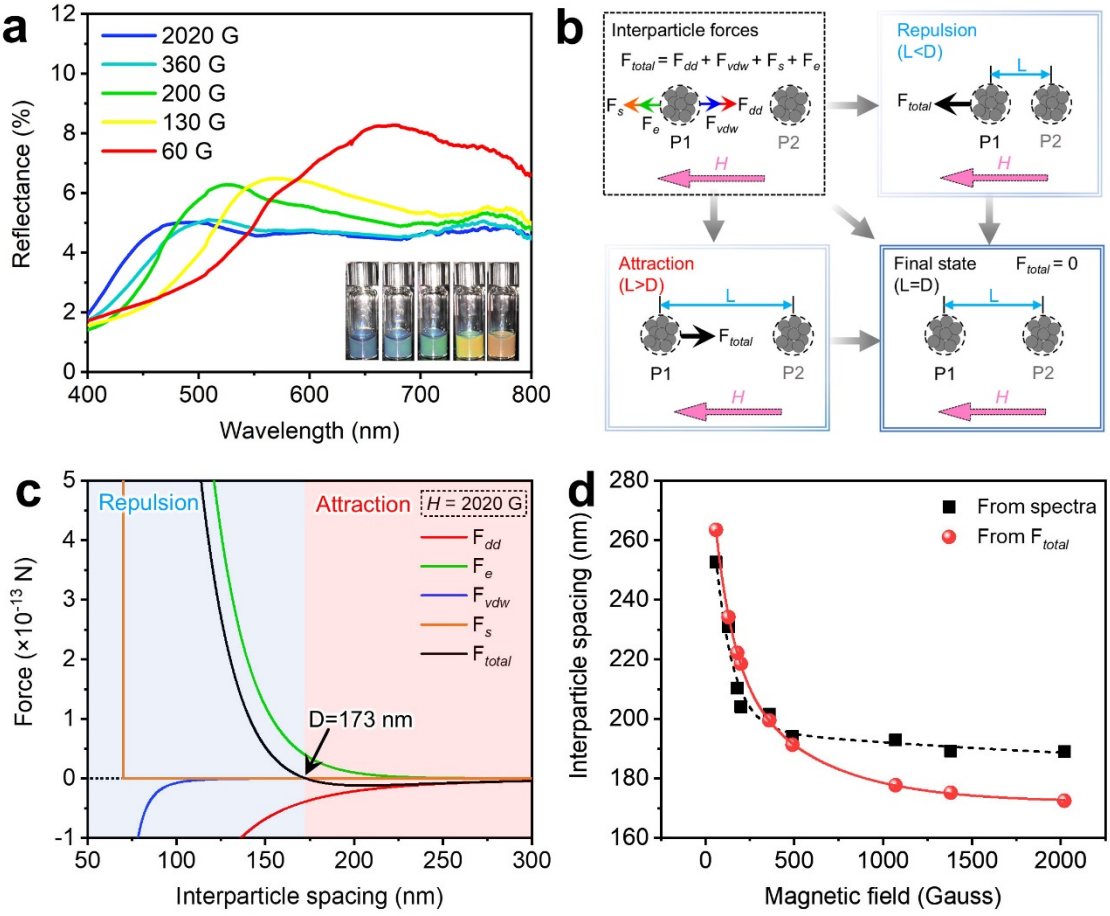

Figure 5. (**a**) Reflection spectra and corresponding color changes of sample M4 (20 mg/mL) under varying magnetic fields; (**b**) Schematic of positional adjustment of the magnetic clusters driven by interparticle forces during magnetic assembly, with the pink arrows indicating the direction of magnetic fields; (**c**) Simulated force profile at 2020 G as interparticle spacing varies; (**d**) Comparison of spacing derived from spectral data (black) and force equilibrium calculations (red) across magnetic field strengths.

To investigate the periodicity and driving forces behind photonic crystal formation with small clusters, we calculated the interparticle spacing of sample M4 (10 mg/mL) using Bragg's law and force dynamics analysis. Based on Figure 3f,g, each cluster is modeled as a 60-nm sphere comprising nine 20-nm magnetic nanocrystals. In addition to Bragg's law [32], we analyzed the forces governing equilibrium spacing between adjacent clusters. As shown in Figure 5b, four interactions were considered: magnetic dipole–dipole attraction ($\vec{F}_{dd}$), van der Waals forces ($\vec{F}_{vdw}$), electrostatic repulsion ($\vec{F}_e$), and steric repulsion($\vec{F}_s$). Under a uniform magnetic field, the dipole moment ($\vec{m}$) of a cluster is given by $\vec{m} = \chi \vec{H} V$, where χ is the volume magnetic susceptibility, $\vec{H}$ the applied field, and V the cluster volume. In the 1D photonic arrays as shown in Figure 3d, the dipole-dipole attractive interaction between two clusters with an interparticle spacing of d_{12} can be described as: $\vec{F}_{dd} = -\nabla U_{dd}$ [33], where U_{dd} is the dipole-dipole potential that can be calculated by $U_{dd,12} = -\frac{\mu_{water}}{4\pi}\left(\frac{3(\vec{m}_1 \cdot \vec{d}_{12})(\vec{m}_2 \cdot \vec{d}_{12})}{d_{12}^5} - \frac{\vec{m}_1 \cdot \vec{m}_2}{d_{12}^3}\right)$, with μ_{water} being the permeability of the solution. The van der Waals force ($\vec{F}_{vdw}$) can be calculated by $\vec{F}_{vdw} = -\nabla U_{vdw}$ [33], where U_{vdw} is the van der Waals potential and it can be obtained by $U_{vdw,12} = -\frac{A}{6}\left(\frac{2R^2}{d_{12}^2 - 4R^2} + \frac{2R^2}{d_{12}^2} + ln\frac{d_{12}^2 - 4R^2}{d_{12}^2}\right)$, with A being the Hamaker constant and R the radius of the cluster.

Due to the presence of PAA on the cluster surface, both electrostatic repulsion from surface charges and steric repulsion from the polymer volume were included in the calculations. The deprotonation of carboxyl groups on PAA impart strong negative charges, promoting inter-cluster repulsion. This electrostatic interaction between adjacent clusters is primarily governed by double-layer forces, as described by DLVO theory: $\vec{F}_e = -\nabla U_e$, and $U_e = 2\pi\epsilon_0\epsilon_r R\zeta^2 \ln\left(1 + e^{-\frac{d_{12}-2R}{\kappa^{-1}}}\right)$, where ϵ_0 is the permittivity of free space, ϵ_r the relative permittivity, and ζ the zeta potential [34]. From Figure 2f, ζ is determined to be -41 mV for sample M4. The cluster radius (R) is approximately 30 nm, based on the average size of sample M4 in Figure 3g. The Debye-Hückel length κ^{-1} is calculated using [34]: $\kappa^{-1} = \sqrt{\varepsilon_r\varepsilon_0 k_B T/2000 N_A e^2 I}$, where k_B is Boltzmann constant, T the temperature in kelvins, N_A Avogadro's number, e the elementary charge, and I the ionic strength. The ionic strength for sample M4, estimated from a pure PAA solution at the same pH, is 2.38×10^{-4} mol/L.

The steric repulsion between two adjacent clusters is calculated by $F_s = -\nabla U_s$ [33], where the potential U_s is defined as $U_s = 2\pi R^2 N_s k_B T\left\{2 - \frac{d_{12}-2R}{\delta} - \frac{d_{12}}{\delta}\ln\left(\frac{2R+2\delta}{d_{12}}\right)\right\}$, where δ and N_s represent the thickness of the PAA layer and the surface density of PAA, respectively.

Figure 5c illustrates the simulated force profile as interparticle spacing varies under a 2020 G magnetic field. At 173 nm, the net force reaches zero, indicating the equilibrium position between the two clusters. Spacing below this threshold produces repulsive forces, while larger spacing results in attraction, driving assembly. As the magnetic field decreases from 2020 G to 60 G, the equilibrium spacing expands from 173 nm to 264 nm. As shown in Figure 5d, these theoretical values align closely with Bragg's law and experimental measurements. The model also explains the diffraction behavior: strong fields cause minor peak shifts, whereas weak fields (<500 G) lead to rapid redshifts. The calculations confirm that large inter-cluster gaps—much greater than cluster radius—minimize size variation effects, enabling stable 1D photonic chains with vivid, tunable colors across the visible spectrum.

4. Conclusions

This study demonstrates that magnetic assembly can effectively produce one-dimensional photonic crystals from nonuniform Fe_3O_4 nanocrystal clusters. By leveraging PAA modification to impart strong electrostatic repulsion, large interparticle separations were achieved, mitigating the impact of size polydispersity and enabling periodic structures with tunable optical diffraction across the visible spectrum. Experimental results and force-dynamics modeling confirm that magnetic, electrostatic, van der Waals, and steric interactions collectively govern the assembly behavior, with equilibrium spacing significantly exceeding cluster size. This relaxed requirement for particle uniformity, combined with scalable synthesis and broad spectral tunability, offers a practical route for fabricating responsive photonic materials over large areas. These findings pave the way for cost-effective, magnetically responsive optical devices for sensing, display, and adaptive photonics.

Supplementary Materials: The following supporting information can be downloaded at: https://media.sciltp.com/articles/others/2512261112538084/MI-25120043-Supplementary_Materials.pdf, Figure S1: (a) The photographs of sample M4 during RF fixation; (b) the possibly corresponding assembly behaviors. Figure S2: The observation angle and magnetic field direction in Figure 4a. Figure S3: The reflection peak wavelength and structural color comparison of sample M4 with concentrations of 10 mg/mL and 20 mg/mL upon exposure to magnetic fields.

Author Contributions: Y.Y.: conceptualization, supervision, writing—reviewing and editing; F.Q.: methodology, investigation, data curation, visualization, writing—original draft preparation; Q.F.: simulation, software, validation; C.W.: investigation. All authors have read and agreed to the published version of the manuscript.

Funding: This work was supported by the U.S. National Science Foundation (CHE-2203972).

Data Availability Statement: Data are available from the corresponding author upon reasonable request.

Conflicts of Interest: The authors declare no conflict of interest.

Use of AI and AI-Assisted Technologies: No AI tools were used to prepare this paper.

References

1. Ge, J.; Yin, Y. Responsive photonic crystals. *Angew. Chem. Int. Ed.* **2011**, *50*, 1492–1522.
2. Li, Z.; Yin, Y. Stimuli-Responsive Optical Nanomaterials. *Adv. Mater.* **2019**, *31*, 1807061.
3. Li, Z.; Yang, F.; Yin, Y. Smart materials by nanoscale magnetic assembly. *Adv. Funct. Mater.* **2020**, *30*, 1903467.
4. Hou, J.; Li, M.; Song, Y. Patterned colloidal photonic crystals. *Angew. Chem. Int. Ed.* **2018**, *57*, 2544–2553.
5. Li, F.H.; Tang, B.T.; Wu, S.L.; Zhang, S.F. Facile Synthesis of Monodispersed Polysulfide Spheres for Building Structural Colors with High Color Visibility and Broad Viewing Angle. *Small* **2017**, *13*, 1602565. https://doi.org/10.1002/smll.201602565.

6. Zhang, Y.; Fu, Q.; Ge, J. Test-Paper-Like Photonic Crystal Viscometer. *Small* **2017**, *13*, 1603351. https://doi.org/10.1002/smll.201603351.
7. Hou, K.; Ali, W.; Lv, J.; Guo, J.; Shi, L.; Han, B.; Wang, X.; Tang, Z. Optically Active Inverse Opal Photonic Crystals. *J. Am. Chem. Soc.* **2018**, *140*, 16446–16449. https://doi.org/10.1021/jacs.8b10977.
8. Shang, L.R.; Fu, F.F.; Cheng, Y.; Yu, Y.R.; Wang, J.; Gu, Z.Z.; Zhao, Y.J. Bioinspired Multifunctional Spindle-Knotted Microfibers from Microfluidics. *Small* **2017**, *13*, 1600286. https://doi.org/10.1002/smll.201600286.
9. Fenzl, C.; Hirsch, T.; Wolfbeis, O.S. Photonic Crystals for Chemical Sensing and Biosensing. *Angew. Chem.-Int. Ed.* **2014**, *53*, 3318–3335. https://doi.org/10.1002/anie.201307828.
10. Fu, F.; Chen, Z.; Zhao, Z.; Wang, H.; Shang, L.; Gu, Z.; Zhao, Y. Bio-inspired self-healing structural color hydrogel. *Proc. Natl. Acad. Sci. USA* **2017**, *114*, 5900–5905. https://doi.org/10.1073/pnas.1703616114.
11. Wang, J.; Sultan, U.; Goerlitzer, E.S.A.; Mbah, C.F.; Engel, M.; Vogel, N. Structural Color of Colloidal Clusters as a Tool to Investigate Structure and Dynamics. *Adv. Funct. Mater.* **2019**, *30*, 1907730. https://doi.org/10.1002/adfm.201907730.
12. Lu, W.; Asher, S.A.; Meng, Z.H.; Yan, Z.Q.; Xue, M.; Qiu, L.L.; Yi, D. Visual detection of 2,4,6-trinitrotolune by molecularly imprinted colloidal array photonic crystal. *J. Hazard. Mater.* **2016**, *316*, 87–93. https://doi.org/10.1016/j.jhazmat.2016.05.022.
13. Qin, M.; Huang, Y.; Li, Y.; Su, M.; Chen, B.; Sun, H.; Yong, P.; Ye, C.; Li, F.; Song, Y. A Rainbow Structural-Color Chip for Multisaccharide Recognition. *Angew. Chem.* **2016**, *55*, 6911–6914. https://doi.org/10.1002/anie.201602582.
14. Zhao, Z.; Wang, H.; Shang, L.; Yu, Y.; Fu, F.; Zhao, Y.; Gu, Z. Bioinspired Heterogeneous Structural Color Stripes from Capillaries. *Adv. Mater.* **2017**, *29*, 1704569. https://doi.org/10.1002/adma.201704569.
15. Fu, Q.; Zhu, H.; Ge, J. Electrically Tunable Liquid Photonic Crystals with Large Dielectric Contrast and Highly Saturated Structural Colors. *Adv. Funct. Mater.* **2018**, *28*, 1804628. https://doi.org/10.1002/adfm.201804628.
16. Reese, C.E.; Baltusavich, M.E.; Keim, J.P.; Asher, S.A. Development of an intelligent polymerized crystalline colloidal array colorimetric reagent. *Anal. Chem.* **2001**, *73*, 5038–5042.
17. Ward Muscatello, M.M.; Stunja, L.E.; Thareja, P.; Wang, L.; Bohn, J.J.; Velankar, S.S.; Asher, S.A. Dependence of photonic crystal nanocomposite elasticity on crystalline colloidal array particle size. *Macromolecules* **2009**, *42*, 4403–4406.
18. Ge, J.; Hu, Y.; Yin, Y. Highly tunable superparamagnetic colloidal photonic crystals. *Angew. Chem.* **2007**, *46*, 7428–7431. https://doi.org/10.1002/anie.200701992.
19. Ge, J.; Hu, Y.; Zhang, T.; Huynh, T.; Yin, Y. Self-assembly and field-responsive optical diffractions of superparamagnetic colloids. *Langmuir* **2008**, *24*, 3671–3680. https://doi.org/10.1021/la7039493.
20. Luo, W.; Ma, H.; Mou, F.; Zhu, M.; Yan, J.; Guan, J. Steric-Repulsion-Based Magnetically Responsive Photonic Crystals. *Adv. Mater.* **2014**, *26*, 1058–1064. https://doi.org/10.1002/adma.201304134.
21. Li, Z.; Yin, S.; Cheng, L.; Yang, K.; Li, Y.; Liu, Z. Magnetic targeting enhanced theranostic strategy based on multimodal imaging for selective ablation of cancer. *Adv. Funct. Mater.* **2014**, *24*, 2312–2321.
22. Cheng, C.; Xu, F.; Gu, H. Facile synthesis and morphology evolution of magnetic iron oxide nanoparticles in different polyol processes. *New J. Chem.* **2011**, *35*, 1072–1079. https://doi.org/10.1039/c0nj00986e.
23. Chen, J.; Feng, J.; Li, Z.; Xu, P.; Wang, X.; Yin, W.; Wang, M.; Ge, X.; Yin, Y. Space-Confined Seeded Growth of Black Silver Nanostructures for Solar Steam Generation. *Nano Lett.* **2019**, *19*, 400–407. https://doi.org/10.1021/acs.nanolett.8b04157.
24. Xu, W.; Wang, M.; Li, Z.; Wang, X.; Wang, Y.; Xing, M.; Yin, Y. Chemical Transformation of Colloidal Nanostructures with Morphological Preservation by Surface-Protection with Capping Ligands. *Nano Lett.* **2017**, *17*, 2713–2718. https://doi.org/10.1021/acs.nanolett.7b00758.
25. Ge, J.; Hu, Y.; Biasini, M.; Beyermann, W.P.; Yin, Y. Superparamagnetic Magnetite Colloidal Nanocrystal Clusters. *Angew. Chem. Int. Ed.* **2007**, *46*, 4342–4345. https://doi.org/10.1002/anie.200700197.
26. Das, K.K.; Somasundaran, P. Ultra-low dosage flocculation of alumina using polyacrylic acid. *Colloids Surf. Physicochem. Eng. Asp.* **2001**, *182*, 25–33. https://doi.org/10.1016/S0927-7757(00)00735-4.
27. Liu, L.; Luo, S.-Z.; Wang, B.; Guo, Z. Investigation of small molecular weight poly(acrylic acid) adsorption on γ-alumina. *Appl. Surf. Sci.* **2015**, *345*, 116–121. https://doi.org/10.1016/j.apsusc.2015.03.145.
28. Liu, S.; Ye, Z.; Yin, Y. Seeded Growth of Plasmonic Nanostructures in Deformable Polymer Confinement. *Langmuir* **2024**, *40*, 8760–8770. https://doi.org/10.1021/acs.langmuir.4c00706.
29. Ye, Z.; Tai, Y.; Han, Z.; Liu, S.; Etheridge, M.L.; Pasek-Allen, J.L.; Shastry, C.; Liu, Y.; Li, Z.; Chen, C.; et al. Engineering Magnetic Nanoclusters for Highly Efficient Heating in Radio-Frequency Nanowarming. *Nano Lett.* **2024**, *24*, 4588–4594. https://doi.org/10.1021/acs.nanolett.4c00721.
30. Hu, Y.; He, L.; Yin, Y. Magnetically Responsive Photonic Nanochains. *Angew. Chem.-Int. Ed.* **2011**, *50*, 3747–3750. https://doi.org/10.1002/anie.201100290.

31. Li, Z.; Wang, M.; Zhang, X.; Wang, D.; Xu, W.; Yin, Y. Magnetic Assembly of Nanocubes for Orientation-Dependent Photonic Responses. *Nano Lett.* **2019**, *19*, 6673–6680. https://doi.org/10.1021/acs.nanolett.9b02984.
32. Li, Z.; Liu, Y.; Marin, M.; Yin, Y. Thickness-dependent wrinkling of PDMS films for programmable mechanochromic responses. *Nano Res.* **2020**, *13*, 1882–1888.
33. Xue, X.; Furlani, E.P. Analysis of the Dynamics of Magnetic Core–Shell Nanoparticles and Self-Assembly of Crystalline Superstructures in Gradient Fields. *J. Phys. Chem. C* **2015**, *119*, 5714–5726. https://doi.org/10.1021/jp513025w.
34. Liu, Y.; Han, X.; He, L.; Yin, Y. Thermoresponsive Assembly of Charged Gold Nanoparticles and Their Reversible Tuning of Plasmon Coupling. *Angew. Chem.-Int. Ed.* **2012**, *51*, 6373–6377.

Article

AuCu-Based Solid-Hollow Hybrid Nanostructures for Efficient Photothermal Therapy against Multidrug-Resistant Bacteria

Qiuping Yang [1,†], Qian Wu [2,†], Xiaowen Chen [3,†], Xiaoying Shen [4,†], Yi Wang [2,*], Xiaohu Wu [5,*], Yanyun Ma [6], Pu Zhang [4,*], and Yiqun Zheng [1,*]

[1] School of Chemistry, Chemical Engineering and Materials, Jining University, Qufu 273155, China
[2] Chongqing Key Laboratory of Green Synthesis and Applications, College of Chemistry, Chongqing Normal University, Chongqing 401331, China
[3] College of Electromechanical Engineering, Qingdao University of Science and Technology, Qingdao 266061, China
[4] Chongqing Research Center for Pharmaceutical Engineering, College of Pharmacy, Chongqing Medical University, Chongqing 400016, China
[5] Yangtze Laboratory, Wuhan 430205, China
[6] Jiangsu Key Laboratory of Advanced Negative Carbon Technologies, Institute of Functional Nano & Soft Materials (FUNSOM), Soochow University, Suzhou 215123, China
* Correspondence: ywang@cqnu.edu.cn (Y.W.); wuxiaohu@pku.org.cn (X.W.); zhangpu@cqmu.edu.cn (P.Z.); yzheng@jnxy.edu.cn (Y.Z.)
† These authors contributed equally to this work.
Received: 10 August 2025; Revised: 3 September 2025; Accepted: 25 December 2025; Published: 30 December 2025

Abstract: Hybrid nanostructures incorporating anisotropic structural components present promising opportunities for developing advanced photothermal agents. Here, we report the controlled synthesis of solid–hollow hybrid nanostructures based on gold–copper (Au–Cu) and demonstrate their photothermal antibacterial properties. Starting from Au nanoplate seeds, we achieve anisotropic deposition to synthesize AuCu and AuAgCu Janus nanostructures. The newly-deposited regions are subsequently transformed into porous architectures via a galvanic replacement reaction mediated by KCl and acetic acid. The introduced nanopores enhance near-infrared (NIR) absorption, thereby improving photothermal conversion efficiency under both 808 nm and 1064 nm laser irradiation and enabling the efficient eradication of multidrug-resistant bacteria. Finite-difference time-domain (FDTD) simulations confirm their optimized plasmonic properties. The current study underscores the potential of morphologically complex hybrid nanostructures for advanced photothermal applications.

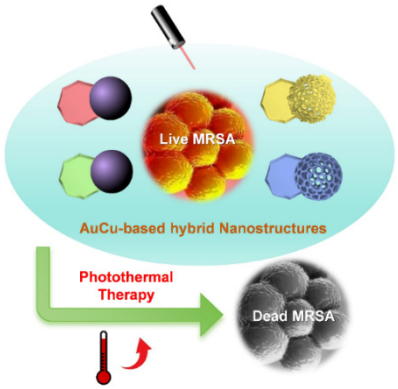

Keywords: hybrid; noble metal; two dimensional; porous; photothermal conversion; FDTD simulation

1. Introduction

Hybrid nanostructures have attracted considerable research interest owing to their unique asymmetric architectures and broad applicability in fields such as catalysis, biomedicine, energy storage, and environmental remediation [1–3]. These structures are defined by their integration of distinct material domains or morphological features within a single entity, enabling multifunctionality through compartmentalized or spatially varied properties [4]. In plasmonics, which exploits localized surface plasmon resonance (LSPR) to confine and enhance electromagnetic (EM) fields, hybrid nanostructures provide a versatile platform for tailoring optical responses beyond the limits of symmetric counterparts [5,6]. Their inherent structural or compositional asymmetry facilitates a non-uniform distribution of plasmonic fields, generating localized hotspots at designated regions [7,8]. This capability becomes especially valuable when structural features of varied morphologies—such as two-dimensional (2D) plates and zero-dimensional (0D) spheres—are integrated into one hybrid entity, enhancing their utility in applications like photothermal therapy and high-sensitivity optical sensing [9–12].

Copyright: © 2025 by the authors. This is an open access article under the terms and conditions of the Creative Commons Attribution (CC BY) license (https://creativecommons.org/licenses/by/4.0/).
Publisher's Note: Scilight stays neutral with regard to jurisdictional claims in published maps and institutional affiliations.

Previous research on hybrid nanostructures has largely emphasized compositional heterogeneity, combining materials such as metals, semiconductors, and polymers [13–15]. Recent advances have expanded the scope, shifting from compositional heterogeneity toward the integration of components with distinct morphological features. This focus on structural hybridity opens new avenues to modulate plasmonic behavior, enhance light–matter interaction, and introduce directional functionality [10,16–20].

However, integrating diverse morphological features into a single nanoentity remains synthetically challenging, primarily due to the competing growth kinetics and thermodynamic preferences involved in forming distinct architectures within one structure [21,22]. While conventional one-pot syntheses often lack the precision to simultaneously regulate these multiple structural parameters, the seeded growth approach offers a more controlled pathway [23,24]. This method enables site-specific deposition on preformed seeds, typically through symmetry breaking of face-centered cubic (*fcc*) metals combined with region-specific capping or kinetic modulation [25–28]. Furthermore, the synthetic strategy can be extended by post-synthetic modifications such as oxidative etching [29,30], which allows the solid domains readily converted into hollow ones, thereby introducing porosity, increasing surface area, and creating complex hybrid nanoentities [31].

Herein, we report the synthesis of gold-copper (AuCu)-based solid-hollow hybrid nanostructures that were achieved through controlled seeded growth followed by galvanic replacement. These nanostructures are subsequently applied to the photothermal eradication of multidrug-resistant bacteria. Our synthesis begins with the formation of plate-like Au nanoparticles as seeds, followed by the anisotropic deposition of Cu or CuAg to anchor quasi-spherical particles onto the plate seeds, yielding AuCu or AuAgCu Janus nanostructures, respectively. Subsequent treatment with an Au precursor ($HAuCl_4$) in a KCl/acetic acid (HAc) solution tempers and spatially confines the galvanic replacement reaction. This process preferentially oxidizes the newly deposited domains into porous, hollow architectures, while concurrently reducing Au^{3+} ions for deposition.

Compared to previous reports on AuCu-based systems, our methodology advances the field in several key aspects: (i) it achieves the hybrid integration of divergent morphological features, combining solid 2D plates with solid/hollow 0D quasi-spheres into single architectures; (ii) the use of KCl/HAc mildens the galvanic replacement process, allowing it to proceed in a controlled manner that is confined to the newly-deposited quasi-spherical domain while largely preserving the solid plate; and (iii) The introduction of Ag to the galvanic replacement reaction acts as a modulator, reducing the dimensions of the resulting nanopores within the hollow domain. These solid–hollow hybrid nanostructures exhibit satisfactory photothermal conversion efficiency and antibacterial properties due to their engineered asymmetry and porous morphology.

2. Experimental Details

2.1. Materials

Gold(III) chloride trihydrate ($HAuCl_4 \cdot 3H_2O$, 99.9%), copper(II) nitrate trihydrate ($Cu(NO_3)_2 \cdot 3H_2O$, 99%), ascorbic acid (AA, 99.0%), and hexadecyltrimethylammonium bromide (CTAB, 99%) were sourced from Aladdin Chemical (Shanghai, China) and utilized without further purification. Silver nitrate ($AgNO_3$, analytical grade), potassium chloride (KCl, analytical grade), and hexamethylenetetramine (HMTA, ≥98.0%) were all purchased from Sinopharm Group in Shanghai, China. Acetic acid (HAc, 99.8%) was obtained from Tianjin Fuyu Fine Chemical Co., Ltd. (Tianjin, China). Octadecyltrimethylammonium chloride (OTAC, 90%) was acquired from Lvsen Chemical (Linyi, China). For all experiments, deionized water with a resistivity of 18.2 MΩ·cm was employed, which was generated by an ultrapure water system from Ulupure (Beijing, China).

2.2. Synthesis of Au Nanoplates (Au NPs)

An aqueous solution of Au NPs was prepared according to the method described in our previous study [32]. It began with the combination of 5 mL of OTAC (10 mM) and 6 mL of $HAuCl_4$ (0.5 mM) at room temperature. The mixture was cooled in an ice-water bath for 10 min. Following this, 1 mL of ascorbic acid (AA, 10 mM) was added, inducing an immediate color change to light green. The solution was then allowed to age at ice-water bath for 30 min before use.

2.3. Synthesis of AuCu and AuAgCu Janus Nanostructures (JNSs)

For the synthesis of AuCu JNSs, 1.4 mL of CTAB (200 mM) was added to the aqueous Au NP suspension. Subsequently, 100 mg of solid AA was introduced, followed by the sequential addition of 1 mL of HMTA (100 mg mL^{-1}) and 0.1 mL of $Cu(NO_3)_2$ (50 mg mL^{-1}) solution. The mixture was homogenized by ultrasonication

and then aged in an oil bath at 80 °C for 3 h. the protocol remained identical except for the introduction of an $AgNO_3$ solution (2 mM, 0.625 mL) alongside the Cu precursor.

2.4. Synthesis of AuCu and AuAgCu Porous Hybrid Nanostructures (PHNSs)

The synthesis of AuCu PHNSs was initiated by adding 0.1 mL of KCl (30 mg mL^{-1}) to the aqueous suspension of as-prepared AuCu JNSs. Subsequently, 0.2 mL of acetic acid and 0.1 mL of $HAuCl_4$ (20 mM) were introduced. The mixture was dispersed uniformly via ultrasonication and then reacted under stirring at room temperature for 2 h. The procedure for AuAgCu PHNSs was identical, with the sole modification being the use of AuAgCu JNSs as the starting material.

2.5. Instruments

Transmission electron microscopy (TEM) images were captured using a HT7820 microscope (Hitachi, Tokyo, Japan) operated at 120 kV accelerating voltage. High-resolution TEM (HRTEM), selected-area electron diffraction (SAED), high angle annular dark field-scanning transmission electron microscopy (HAADF-STEM) and energy-dispersive X-ray STEM (EDX-STEM) mapping were performed using a Talos F200X (FEI, Hillsboro, OR, USA) microscope operated at 200 kV accelerating voltage. The crystalline structures were analyzed with a MiniFlex600 X-ray diffractometer (XRD, Rigaku Corporation, Tokyo, Japan). X-ray photoelectron spectroscopy (XPS) measurements were performed using a Thermo Fisher Scientific KALPHA XPS (Thermo Fisher Scientific Inc., Waltham, MA, USA) with monochromatic Al K_α radiation ($h\nu$ = 1486.6 eV). Extinction spectra were recorded using a UV2310II dual-beam UV-vis-NIR spectrometer (Techcomp Ltd., Shanghai, China). The thermal image was taken by FOTRIC 220s infrared thermal imager (JIUHENG, Shanghai, China). The 808 nm and 1064 nm lasers used in the experiments were models DS3-51512-K808DAHRN-10.00W and DS3-51512-K1064HAMRA-10.00W, respectively, supplied by BWT (Beijing, China).

2.6. Photothermal Measurement

The photothermal effect of the as-prepared products was measured using a laser (wavelength: 808 nm or 1064 nm) and an infrared thermal imager. Typically, the as-prepared products were purified, resuspended in water, and 1.7 mL of the resulting suspension was added to each well of a 48-well plate. The aqueous suspensions were completely covered by adjusting the size of the laser spot, followed by the irradiation under the laser (1 $W \cdot cm^{-2}$) for 10 min. Throughout the measurement, the solution temperature was monitored using an infrared thermal imager, data was recorded at the set interval of 10 s, and the *T-t* curve was simultaneously mapped.

2.7. Calculation of the Photothermal Conversion Efficiency

The photothermal conversion efficiency (η) was calculated according to the following formula proposed by Roper [33],

$$\eta = \frac{hA(\Delta T_{\max} - \Delta T_{H_2O})}{I(1 - 10^{-A_\lambda})}$$

where h is the heat transfer coefficient, A is the surface area for radiative heat transfer, $\Delta T_{\max}$ represents the maximum steady-state temperature in the presence of products relative to room temperature, ΔT_{H_2O} represents the maximum steady state temperature of water relative to room temperature, I is the power density of used laser, and A_λ is the absorbance of products at 808 or 1064 nm.

2.8. *FDTD Simulation*

Based on the Finite Element Method (FEM), the photothermal conversion characteristics were calculated. The refractive index of the material determines the optical properties of the nanoparticles, and the complex refractive indices of Au, Ag, and Cu used in the calculation were taken from previous studies [34]. Here, the real part, n, determines the propagation speed of light waves in the medium, while the imaginary part, k, represents the absorption performance of the medium for electromagnetic waves. The medium surrounding the nanoparticles is water, with a refractive index of 1.33. The incident light intensity was set to 10^9 W m^{-2} [35]. The spherical region outside the nanoparticles was set as a perfect matching layer (PML) to reduce the influence of boundary reflections.

3. Results and Discussion

3.1. Synthesis and Characterizations of AuCu-Based Hybrid Nanostructures

The synthesis proceeded in three steps, as outlined in Scheme 1. First, plate-like Au seeds were prepared according to our previous study (Figure S1) [36]. Next, Cu or CuAg atoms were deposited by reducing their precursors in the presence of CTAB, AA, and HMTA [37]. As shown in Figure S2, quasi-spherical particles formed asymmetrically on one side of the Au plates in both cases, with the underlying plate remaining visible—consistent with the formation of Janus nanostructures (JNSs). EDX-STEM mapping of the products revealed distinct compositional profiles. For Cu-only deposition, Cu localized predominantly on the quasi-spherical particles, leaving the plate region Au-rich (Figure S3). In contrast, co-deposition of Cu and Ag resulted in Cu-enriched quasi-spherical particles, whereas the plate region contained both Au and Ag (Figure S4). This suggests that Ag readily alloys with Au, likely due to their close lattice matching, whereas the significant Au/Cu lattice mismatch promotes heterogeneous Cu deposition. Based on their composition, these two types of products are designated as AuCu JNSs and AuAgCu JNSs, respectively.

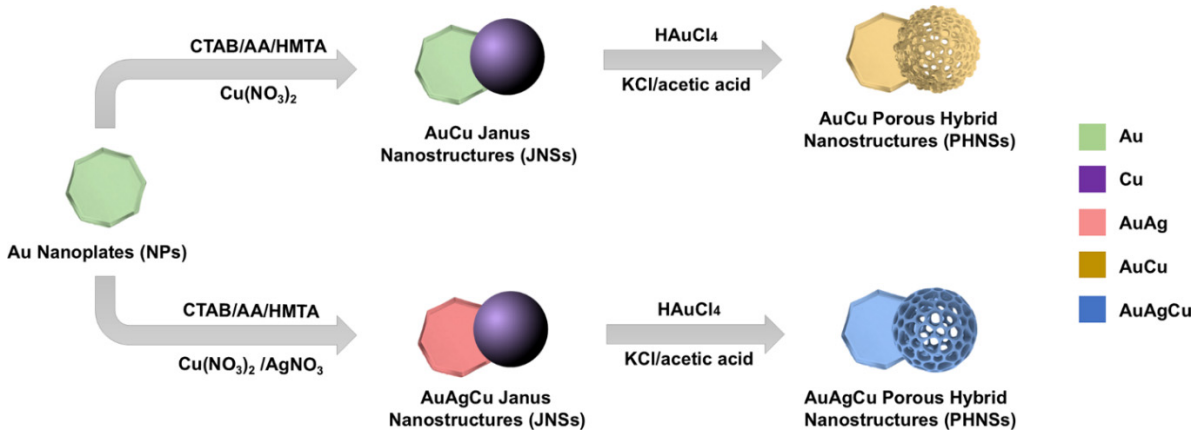

Scheme 1. Schematic illustration showing the formation process of AuCu-based hybrid nanostructures.

The third step involved a galvanic replacement reaction, where AuCu JNSs and AuAgCu JNSs were reacted with $HAuCl_4$ in the presence of KCl and acetic acid. For both cases, the quasi-spherical component transformed into a porous structure while the plate-like seeds were retained, as confirmed by TEM (Figures 1a–c and 2a–c) and HAADF-STEM images (Figures 1f and 2f). For the product derived from AuCu JNSs, lattice fringes of the solid and hollow regions measured 0.23 nm (Figure 1d) and 0.20 nm (Figure 1e), corresponding to the (111) planes of Au and a Cu/Au alloy, respectively. For the products from AuAgCu JNSs, the hollow and solid regions exhibited lattice fringes of 0.21 nm (Figure 2d) and 0.22 nm (Figure 2e), corresponding to the (111) planes of a Cu/Ag/Au alloy and Au, respectively. For both types of products, EDX-STEM elemental mapping images (Figures 1g–i and 2g–j, Figure S5a,b) demonstrated a roughly homogeneous distribution of the constituent metals. The distinct lattice spacings, however, indicate the formation of local compositional gradients, resulting in regions with Au-rich and alloy-dominated crystalline phases. This redistribution and phase evolution are attributed to the etching and in situ regrowth occurring during the galvanic replacement reaction. Given their distinct structural features and compositions, the final products shown in Figures 1 and 2 are designated as AuCu porous hybrid nanostructures (PHNSs) and AuAgCu PHNSs, respectively.

Pore size analysis (Figure S6) revealed average diameters of 7.5 ± 3.9 nm for AuAgCu PHNSs and 58.8 ± 20.7 nm for AuCu PHNSs. This variation in pore size is attributed to the dual galvanic replacement reactions enabled by the participation of Ag. When Cu and Ag are both present, their differing standard reduction potentials and reaction kinetics with $AuCl_4^-$ result in a competitive yet synergistic process of etching and redeposition. This complex in situ regrowth, involving two sacrificial metals, governs the final scale of the porous architecture.

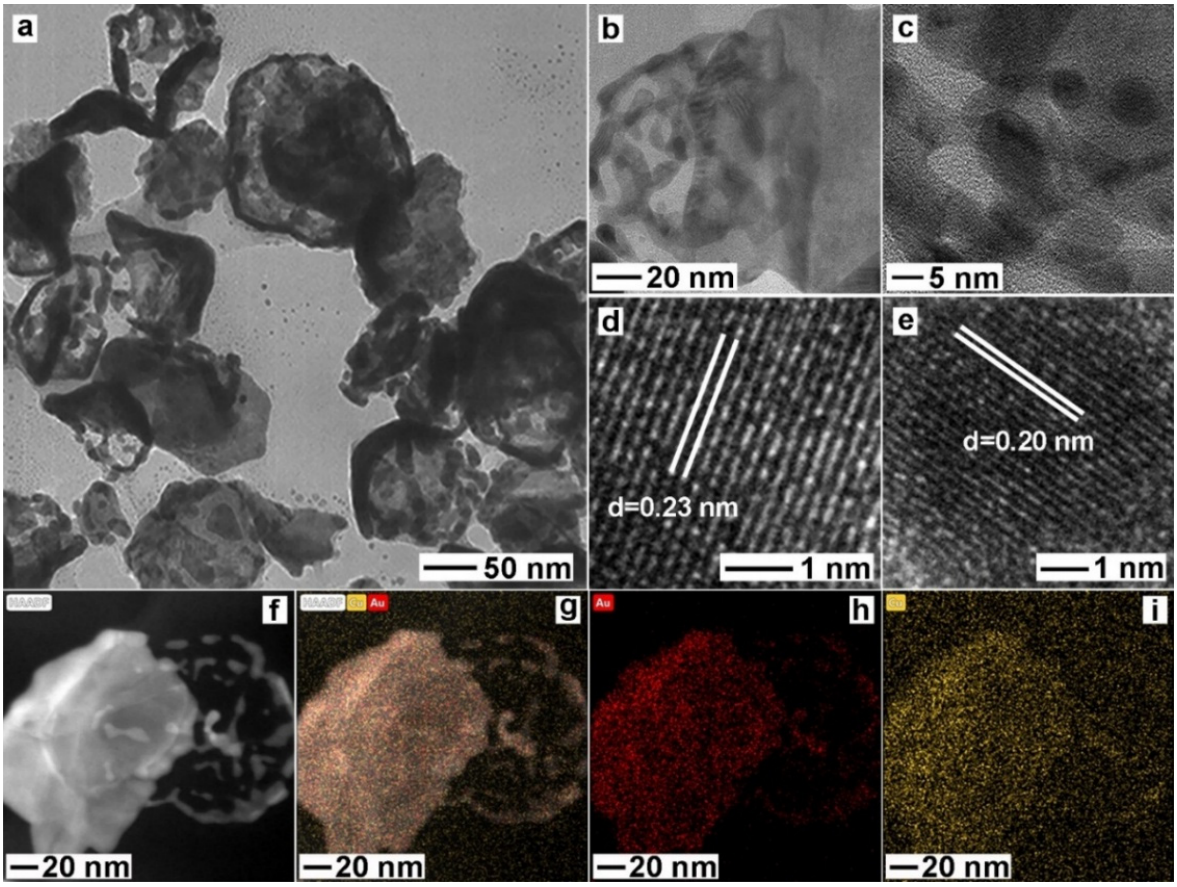

Figure 1. Morphology and structural characterizations of AuCu PHNSs: (**a**–**c**) TEM; (**d**,**e**) HRTEM; (**f**) HAADF-STEM; (**g**–**i**) EDX-STEM mapping; (**g**) HAADF + Cu + Au; (**h**) Au; and (**i**) Cu.

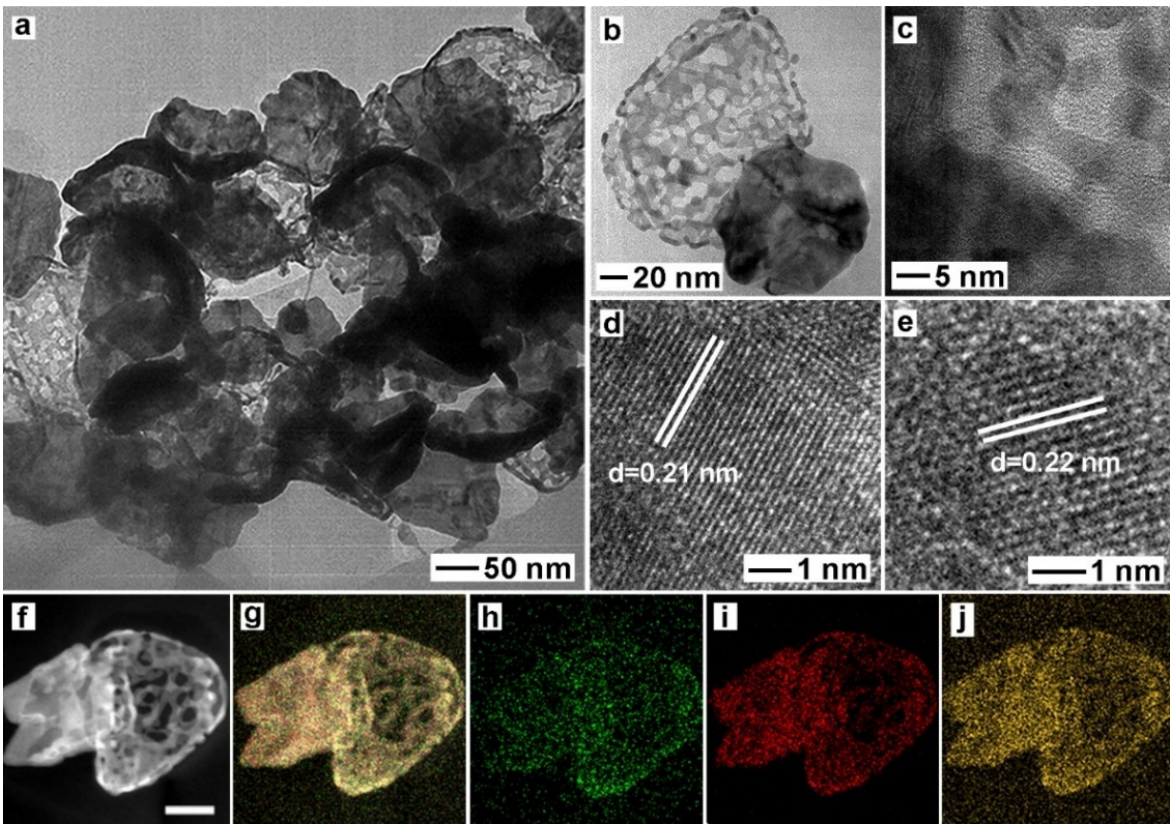

Figure 2. Morphology and structural characterizations of AuAgCu PHNSs: (**a**–**c**) TEM; (**d**,**e**) HRTEM; (**f**) HAADF-STEM; (**g**–**j**) EDX-STEM mapping; (**g**) HAADF + Cu + Ag + Au; (**h**) Ag; (**i**) Au; (**j**) Cu. The scale bar in (**f**) is 50 nm and applies to (**g**–**j**).

3.2. XRD and XPS Characterizations

To gain further insights into the structural properties, an array of characterizations was conducted. EDS measurements of four types of products were conducted. As shown in Figure S7, the Au/Cu atomic ratio of AuCu JNSs and AuCu PHNSs was 89.0:11.0 and 74.2:25.8, respectively. The atomic ratio of Au/Ag/Cu atomic ratio of AuAgCu JNSs and AuAgCu PHNSs was 82.4:14.2:3.3 and 66.8:23.4:9.8, respectively.

XRD measurements were conducted and the diffraction peaks observed for all products were compared with standard references for Au, Ag, and Cu, as shown in Figure 3. The results indicate good consistency with the face-centered cubic (*fcc*) structure of these metals. For the patterns of AuCu-based NSs, two distinct sets of diffraction peaks were observed, corresponding to *fcc*-Cu and *fcc*-Au/Ag, respectively (Table S1). X-ray photoelectron spectroscopy (XPS) measurements were performed to investigate the valence electronic states of elements in the four products. The Cu 2p spectra (Figure 4a–d) were deconvoluted into two components: the lower binding energy component at 931–932 eV was assigned to two possible valence states, Cu(I) or Cu(0), while the peaks at higher binding energies of 933–934 eV were attributed to $Cu(OH)_2$. The presence of weak satellite peaks in the binding energy range of 940 to 948 eV, corresponding to shake-up structures, further confirms the minimal presence of Cu(II) species. In the corresponding Cu LMM spectra (Figure 4e–h), the kinetic energy peaks centered at 915 eV were assigned to Cu(I) species. Since no Cu(I) species were detected in the XRD patterns, their presence is likely due to the oxidation of metallic nano-Cu under ambient conditions. The deconvolution of the doublets in the Au 4f spectra (Figure 4i–l) and Ag 3d spectrum (Figure S8) were performed. Specifically, the major presence of a doublet with the binding energy peaks located at around 88 eV (Au $4f_{5/2}$), 84 eV (Au $4f_{7/2}$), 374 eV (Ag $3d_{3/2}$), and 368 eV (Ag $3d_{5/2}$) confirmed the predominance of Au and Ag atoms in their zerovalent states. The slight shift in B.E. peak positions should be attributed to the electronic interactions among these metals. All the obtained data are summarized in Table S2.

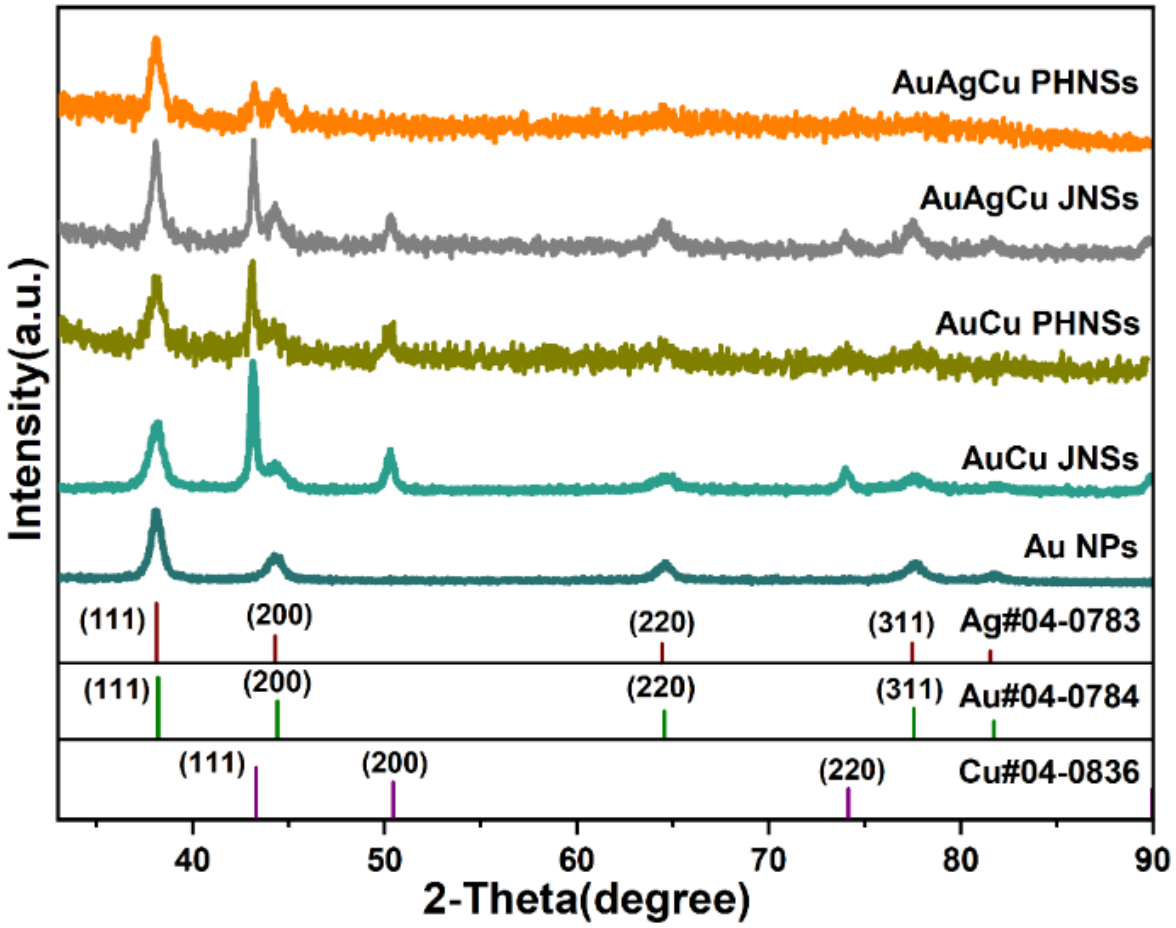

Figure 3. XRD patterns of AuCu JNSs, AuAgCu JNSs, AuCu PHNSs, and AuAgCu PHNSs. Reference peak positions for metallic Cu, Ag, and Au are indicated for comparison.

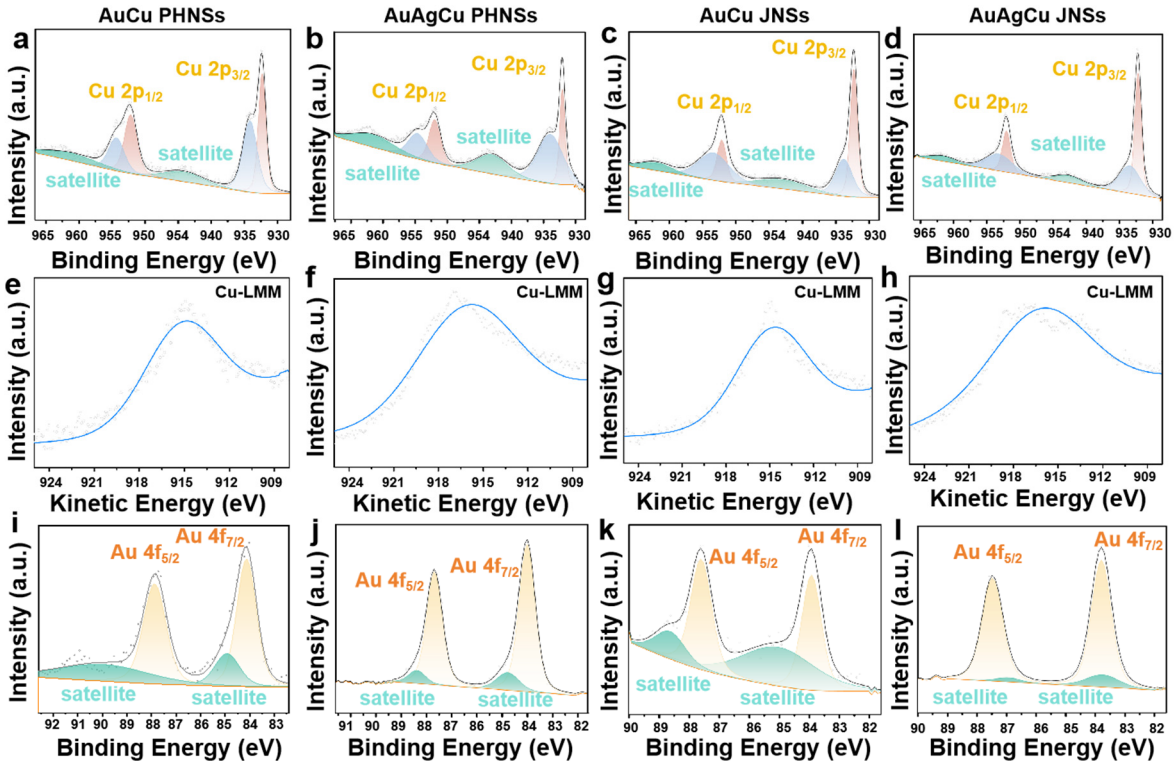

Figure 4. XPS spectra for (**a**–**d**) Cu 2p; (**e**–**h**) Cu LMM; and (**i**–**l**) Au 4f regions. From left to right, the columns correspond to (**a**,**e**,**i**) AuCu PHNSs; (**b**,**f**,**j**) AuAgCu PHNSs; (**c**,**g**,**k**) AuCu JNSs; and (**d**,**h**,**l**) AuAgCu JNSs.

3.3. Formation Mechanism

The selective etching of the quasi-spherical regions, while preserving the plate-like part, is fundamentally driven by electrochemical potential differences. Thermodynamically, the higher reduction potential of Au^{3+}/Au (+1.50 V vs. SHE) compared to Cu^{2+}/Cu (+0.34 V vs. SHE) and Ag^{+}/Ag (+0.80 V vs. SHE) drives the galvanic replacement, rendering the less noble Cu/CuAg regions sacrificial anodes. Control experiments established the essential roles of KCl and acetic acid in the formation of solid-hollow hybrid nanostructures (Figure S9). The quasi-spherical domains in both AuCu and AuAgCu JNSs underwent significant dissolution and structural collapse in the absence of either KCl or HAc. This confirms that both components are essential for achieving controlled synthesis and well-reserved porous architectures. Chloride ions stabilize the oxidized Cu/CuAg species as soluble chloro-complexes, facilitating their removal and modulating local reactivity, while oxygen acts as a co-oxidant to enhance and regulate the overall etching kinetics. Acetic acid fine-tunes this environment through its dual role as a pH buffer and a coordination modulator (via Ac^{-} anions), thereby preventing uncontrolled dissolution and promoting the development of spatially confined porosity. In addition, consistent with this mechanism, XRD analysis shows no detectable alloy phases, confirming that the resulting porosity arises from the controlled etching pathway mediated by $HAuCl_4$ and its synergistic auxiliaries, not from bulk alloy formation or interfacial intermixing.

3.4. LSPR Properties and Photothermal Conversion

The aqueous solution of Au NPs and AuCu-based hybrid nanostructures were investigated using UV-vis-NIR, revealing strong LSPR absorption in the NIR region for each product, indicating that they are all ideal photothermal conversion materials (Figure 5a). We further explored the NIR photothermal conversion performance of the five products using a laser and an infrared thermal imager, detecting their temperature changes under 808 nm laser irradiation. From the temperature rise and cooling curves of the five products, it was evident that all five products showed a significant temperature increase compared to the solvent water, with AuAgCu PHNSs showing the highest temperature increase, indicating that the products can effectively convert light energy into heat (Figure 5b). The thermographs also showed that the blank group did not change much in color after 20 min of 808 nm laser irradiation. In contrast, the thermographs of Au NPs, AuCu JNSs, AuCu PHNSs, AuAgCu JNSs, and AuAgCu PHNSs showed color changes from deep blue to orange-yellow to varying degrees (Figure 5c). The calculated ΔT values for Au NPs, AuCu JNSs, AuCu PHNSs, AuAgCu JNSs, and AuAgCu PHNSs were 27, 23.3, 27.8, 27.1, and 29.6 °C, respectively (Figure 5d). Additionally, the corresponding photothermal conversion efficiencies were calculated as

69.49%, 77.86%, 65.19%, 69.17%, and 67.15% (Figure S10, Table S3). Compared to the other four materials, AuAgCu PHNSs had stronger LSPR absorption at 808 nm, thus able to absorb more incident light, and its −ln(q) also showed a good linear relationship with time (Figure 5e). Since the photothermal conversion efficiency is influenced by multiple variables including ΔT_{max} and A_λ, its photothermal conversion efficiency is not necessarily the highest. Further, after performing five temperature rise-cooling cycles on AuAgCu PHNSs, the ΔT value did not decrease, indicating its excellent photothermal stability (Figure 5f).

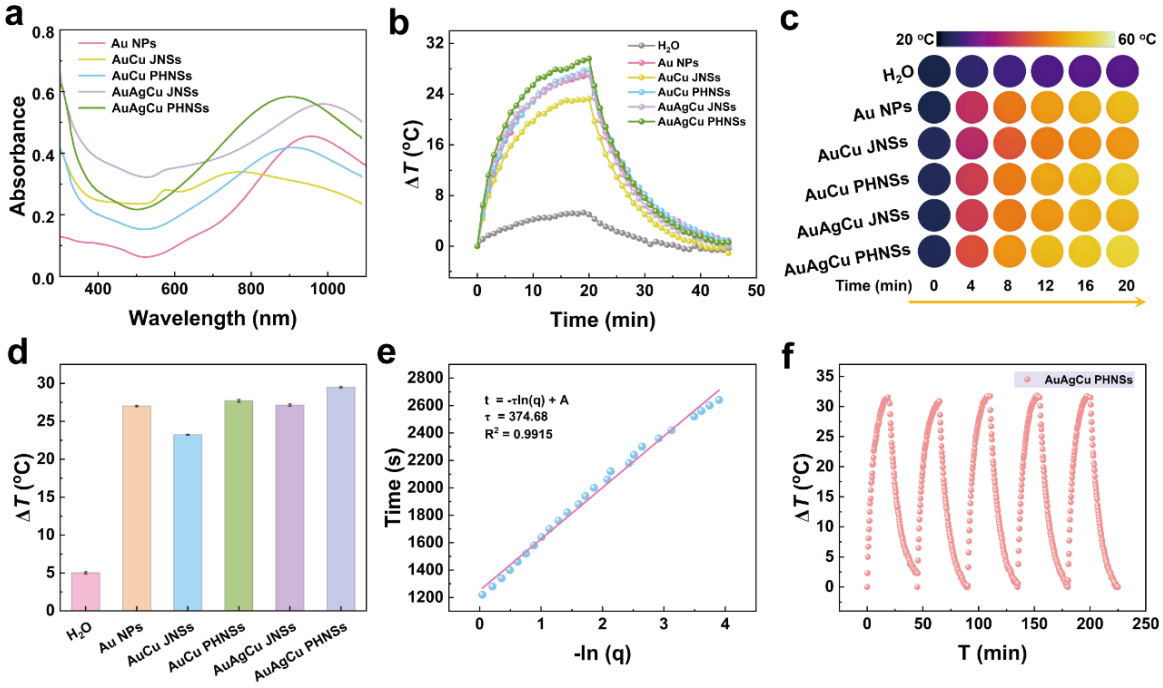

Figure 5. (**a**) UV-vis-NIR absorption spectra; (**b**) Temperature change (ΔT) over time during 20 min of 808 nm laser irradiation (1 W·cm^{-2}) followed by 25 min of cooling; (**c**) Infrared thermographic image under 808 nm laser irradiation; (**d**) Maximum temperature change (ΔT) after 20 min of irradiation; (**e**) Linear fitting of the cooling curve plotted as −ln(θ) versus time for AuAgCu PHNSs; (**f**) Photothermal stability of AuAgCu PHNSs assessed over five consecutive laser on/off cycles.

We further explored the photothermal performance of the five products in the NIR-II region. Under 20 min of 1064 nm laser irradiation, both the solvent water and the five products showed obvious temperature increase, with AuAgCu PHNSs showing the highest temperature increase (Figure 6a). The thermograph of the blank group changed from deep blue to red, while the thermographs of Au NPs, AuCu JNSs, AuCu PHNSs, AuAgCu JNSs, and AuAgCu PHNSs showed color changes from deep blue to orange-yellow (Figure 6b). The calculated ΔT values for Au NPs, AuCu JNSs, AuCu PHNSs, AuAgCu JNSs, and AuAgCu PHNSs were 25.9, 20.1, 24.6, 24.6, and 26.7 °C, respectively (Figure 6c), with corresponding photothermal conversion efficiencies of 32.11%, 30.40%, 31.72%, 31.64%, and 31.35% (Figure S11, Table S3). From Figure 6d, it can be seen that the −ln(q) of AuAgCu PHNSs still has a good linear relationship with time. However, unlike under 808 nm laser irradiation, AuAgCu JNSs has an absorption peak closer to the NIR-II region and has a higher absorbance. In addition, under 1064 nm laser irradiation, the photothermal stability of AuAgCu PHNSs was tested, and after five temperature rise-cooling cycles, it was found that the ΔT value of AuAgCu PHNSs did not change significantly in each cycle, indicating its excellent photothermal stability (Figure 6e). By comparing the results of recent studies on Au-based photothermal materials, the photothermal conversion efficiency of AuAgCu PHNSs is quite competitive (Table S4).

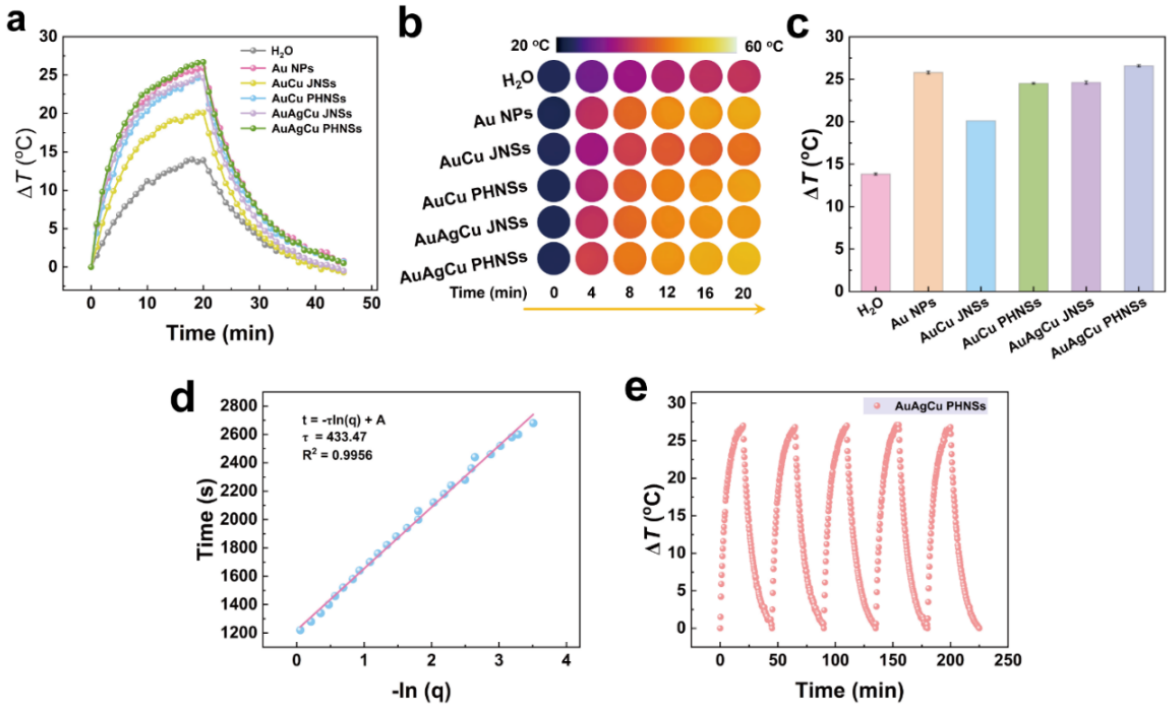

Figure 6. (**a**) Temperature change (ΔT) over time during 20 min of 1064 nm laser irradiation (1 W·cm^{-2}) followed by 25 min of cooling; (**b**) Infrared thermographic image under 1064 nm laser irradiation; (**c**) Maximum temperature change (ΔT) after 20 min of irradiation; (**d**) Linear fitting of the cooling curve plotted as –ln(θ) versus time for AuAgCu PHNSs; (**e**) Photothermal stability of AuAgCu PHNSs assessed over five consecutive laser on/off cycles.

3.5. *FDTD* Simulation

Figure S12 schematically illustrates the five numerical simulation models constructed to systematically investigate their near-infrared (NIR) photothermal properties. The models include Au nanoplate (Model Au NPs); a Cu nanosphere anchored with a Au nanoplate (Model AuCu JNSs); a Cu nanosphere anchored with a AuAg nanoplate (Model AuAgCu JNSs); and two porous hybrid nanostructures (Model AuCu PHNSs-I and AuCu PHNSs-II) composed of a Au nanosheet and a Cu nanosphere with pores of varying sizes. This series was designed to isolate the effects of material composition, heterojunction interfaces, and nanoscale porosity on plasmonic excitation and heat generation under NIR irradiation.

Due to the asymmetric structure, the absorption and scattering characteristics for multiple incident polarization directions were calculated and averaged, as shown in Figure 7. Figure 7a,c show that within the range of 300 to 1200 nm, Model Au NPs exhibit two absorption peaks under continuous illumination, but the absorption intensity is relatively low within the visible light range. For Model AuCu JNSs and Model AuAgCu JNSs, two small peaks can be observed within the range of 700 to 1050 nm, and a strong peak at 1100–1200 nm. The absorption peak of Model AuAgCu JNSs shifts slightly towards the blue compared to Model AuCu JNSs, which is attributed to the addition of Ag. Model AuCu PHNSs has three or more absorption peaks within the range of 300 to 1200 nm, and the absorption cross-section shows a significant increase. Particularly, the absorbance of Model AuCu PHNSs-II is relatively high in the range of 300–1200 nm. In Figure 7b,d, it can be observed that within the range of 600–900 nm, the scattering cross-section of Model AuCu PHNSs-II is significantly higher than that of other structures, which is unfavorable for its absorption performance. Considering the absorption and scattering effects throughout the entire range, Model AuCu PHNSs-I exhibits the strongest light harvesting capacity.

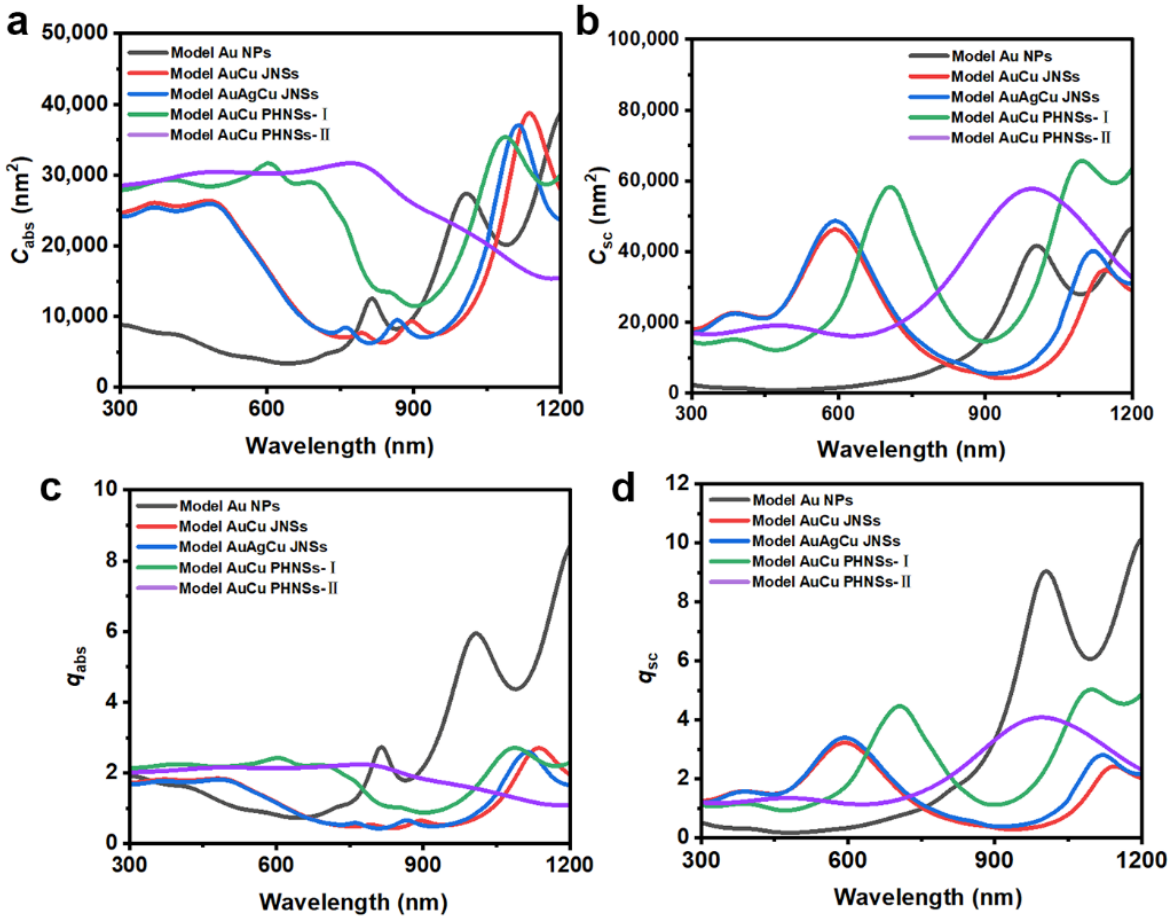

Figure 7. (**a**) absorption cross section; (**b**) scattering cross section; (**c**) absorption coefficient and (**d**) scattering coefficient of Model Au NPs, Model AuCu JNSs, Model AuAgCu JNSs, Model AuCu PHNSs-I, and Model AuCu PHNSs-II.

As shown in the electric and magnetic field energy distributions in Figure 8, a distinct electrical response appears at the edge of the Au NPs due to the concentration of electrons, resulting in local surface plasmon resonance (LSPR) [38]. In Model AuCu JNSs, the coupling effect between Au nanoplate and Cu nanosphere enhances the electromagnetic field. In contrast, for Model AuAgCu JNSs, when the Au nanoplate transforms into the AuAg nanoplate, the EM field distribution does not show any significant change. It is worth noting that in Model AuCu PHNSs-I and Model AuCu PHNSs-II, the cavity in the caged structure guides more electric fields into its interior, further enhancing the LSPR effect [39]. At the same time, the interaction between light and surface electrons increases, thereby improving light absorption capacity. Due to the smaller pores of Model AuCu PHNSs-II, the shortened path of light action, compared with Model AuCu PHNSs-I, the electric field is weaker.

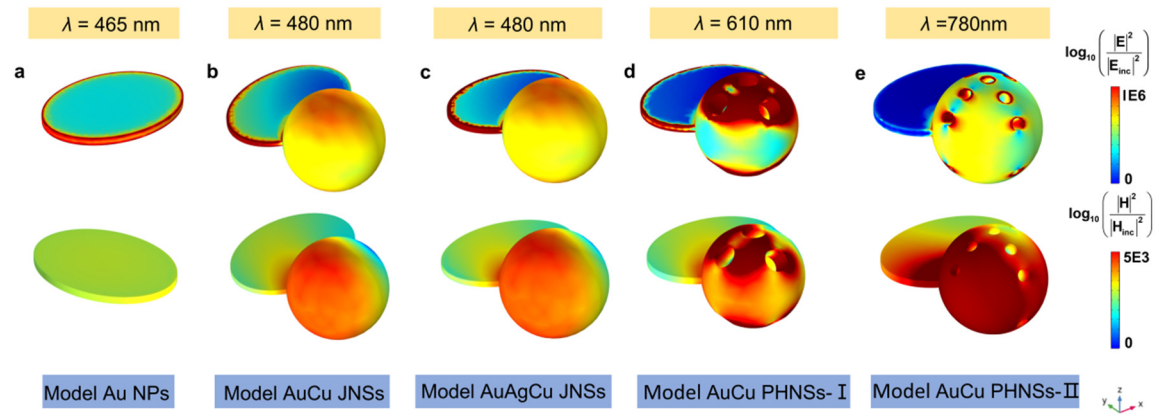

Figure 8. Electric field (top) and magnetic field (bottom) at the absorption peak in the x incident −z polarization direction for (**a**) Model Au NPs; (**b**) Model AuCu JNSs; (**c**) Model AuAgCu JNSs; (**d**) Model AuCu PHNSs-I and (**e**) Model AuCu PHNSs-II.

To visualize the photothermal response more clearly, we analyzed the two-dimensional temperature distributions (in x–y and z–y sections) of these models and the surrounding medium (Figure 9). Model AuCu PHNSs-I exhibited the greatest temperature rise of 44.1 K. In comparison, Models AuCu JNSs and AuAgCu JNSs showed increases of 32.8 K and 32.5 K, respectively. The temperature increase for Model AuCu PHNSs-II was more moderate at 8.5 K, due to its higher scattering efficiency. Model Au NPs showed only a minimal temperature rise of 5.4 K.

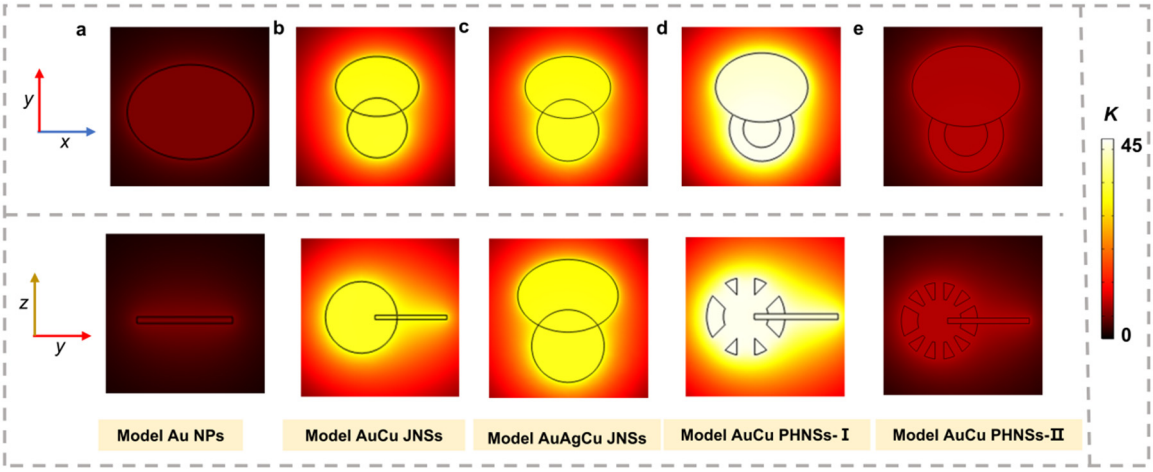

Figure 9. Temperature profiles of (**a**) Model Au NPs; (**b**) Model AuCu JNSs; (**c**) Model AuAgCu JNSs; (**d**) Model AuCu PHNSs-I and (**e**) Model AuCu PHNSs-II.

3.6. Photothermal Antibaceterial Test

The synthesized AuCu PHNSs and AuAgCu PHNSs represent promising NIR photothermal conversion agents capable of combating multidrug-resistant bacteria via photothermal therapy (PTT). The photothermal antimicrobial capability of these nanostructures was evaluated using the representative multidrug-resistant Gram-positive strain MRSA. Figure 10a demonstrates that even without NIR irradiation, both AuCu PHNSs and AuAgCu PHNSs exhibited significant antibacterial effects compared to the PBS control group. Notably, AuCu PHNSs showed superior intrinsic antibacterial activity, comparable to its performance under NIR irradiation. In contrast, AuAgCu PHNSs displayed markedly enhanced antibacterial efficacy only upon NIR irradiation for 10 min. Complete eradication of colonies (no growth) was observed for AuCu PHNSs diluted to 0.17×10^9 particles/mL, identifying this concentration as its MBC. These results indicate that the antimicrobial mechanism involves not only hyperthermia generated by the photothermal effect under NIR light but also significant growth inhibition mediated by the released Cu^{2+} ions at high concentrations. This synergistic effect is further corroborated by the data presented in Figure 10b,c. Given its optimal performance, AuCu PHNSs was selected for evaluating broad-spectrum antimicrobial efficacy. Testing againstrevealed that AuCu PHNSs, under NIR irradiation, effectively inhibited the growth of both Gram-positive and Gram-negative bacteria, achieving inhibition rates exceeding 99.9% in all cases (Figure 10d,e). Even in the absence of NIR irradiation, the AuCu PHNSs group exhibited substantially fewer bacterial colonies compared to the PBS group, with inhibition rates consistently above 60%. These findings further demonstrate that the potent antibacterial action of our material stems from the synergistic interplay between photothermal ablation and Cu^{2+} ion-mediated inhibition.

While the measured photothermal conversion efficiency of the AuCu-based hybrid nanostructures was comparable to that of pure Au nanoplates, the principal rationale for developing these complex architectures lies in their multimodal antibacterial action. In contrast to Au nanoplates, which function primarily as photothermal agents, the AuCu-based systems integrate photothermal therapy (PTT) with additional therapeutic mechanisms. Specifically, the porous, Cu-containing domains enable the sustained release of biocidal metal ions (e.g., Cu^{2+}, Ag^{+}), introducing a potent chemodynamic therapy (CDT) component. This synergistic PTT/CDT approach targets bacteria through concurrent physical and chemical pathways, which is anticipated to mitigate heat-shock resistance and lower the required laser irradiation dose for effective bacterial eradication.

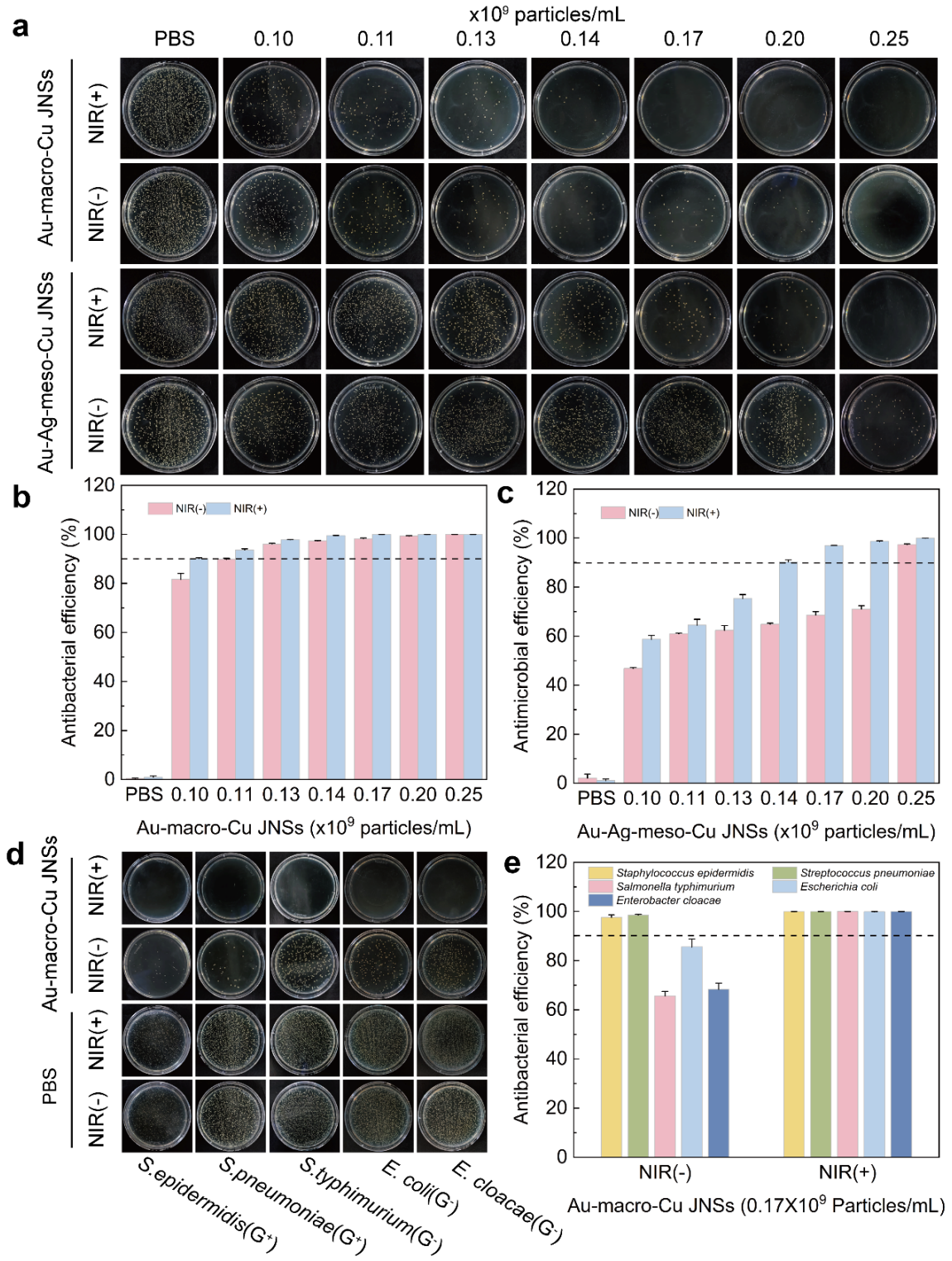

Figure 10. *In vitro* photothermal antibacterial performance of different materials. (**a**–**c**) Growth inhibition of MRSA on LB agar and antibacterial efficiency mediated by AuCu PHNSs and AuAgCu PHNSs treated with different concentrations, without or with NIR irradiation; (**d**,**e**) Broad-spectrum antimicrobial performance of AuCu PHNSs (0.17×10^9 particles/mL) without or with NIR irradiation.

4. Conclusions

In summary, we have developed a combined seeded growth and galvanic replacement strategy to synthesize AuCu-based solid–hollow hybrid nanostructures. The synthetic process—featuring unconformal deposition of quasi-spherical domains onto plate-like seeds, followed by spatially confined galvanic replacement moderated by KCl/acetic acid—yields porous hollow architectures integrated with solid Au plates. FDTD simulations confirm that the introduced porosity and structural asymmetry significantly enhance near-field plasmonic coupling and

broadband absorption, particularly in the NIR region. These characteristics correlate with the observed high photothermal conversion efficiencies of 77.86% at 808 nm and 32.11% at 1064 nm, enabling effective eradication of multidrug-resistant bacteria under NIR irradiation. This work not only provides a versatile route to structurally tunable hybrid nanomaterials but also demonstrates, through both simulation and experiment, their promising potential as efficient photothermal agents for biomedical applications.

Supplementary Materials: The following supporting information can be downloaded at: https://media.sciltp.com/articles/others/2512301119183915/MI-25120148-Supplementary-Materials.pdf. Figure S1: TEM image of Au nanoplates (NPs). Figure S2: (**a**,**c**) SEM and (**b**,**d**) TEM images of (**a**,**b**) AuCu JNSs and (**c**,**d**) AuAgCu JNSs. Figure S3: EDX-STEM elemental maps of the AuCu JNS: (**a**) Overlay of Au (green) and Cu (red); (**b**) Cu map; (**c**) Au map. Figure S4: EDX-STEM elemental maps of the AuAgCu JNS: (**a**) Overlay of Au (green), Ag (blue), and Cu (red); (**b**) Cu map; (**c**) Ag map; (**d**) Au map. Figure S5: EDX-STEM line-scan profile: (**a**) AuAgCu PHNSs and (**b**) AuCu PHNSs. Figure S6: Histograms showing the pore size distribution of (**a**) AuAgCu PHNSs; (**b**) AuCu PHNSs. Figure S7: Histogram illustrating the atomic percentage of AuCu-based nanostructures as determined via EDS. Figure S8: Ag 3d XPS spectrum of AuAgCu PHNSs. Figure S9: TEM images of nanoparticles obtained using the same synthetic protocol as (**a**–**c**) AuCu PHNSs and (**d**–**f**) AuAgCu PHNSs, but with varied etching treatments: (**a**,**d**) $HAuCl_4$, (**b**,**e**) $HAuCl_4$ + KCl, and (**c**,**f**) $HAuCl_4$ + acetic acid. Figure S10: Determining the thermal transfer time constant (τ) of the system by plotting linear data from cooling times: (**a**) Au NPs; (**b**) AuCu JNSs; (**c**) AuCu PHNSs; (**d**) AuAgCu JNSs. Laser wavelength: 808 nm. Figure S11: Determining the thermal transfer time constant (τ) of the system by plotting linear data from cooling times: (**a**) Au NPs; (**b**) AuCu JNSs; (**c**) AuCu PHNSs; (**d**) AuAgCu JNSs. Laser wavelength: 1064 nm. Figure S12: The model schematics of (**a**) Model Au NPs; (**b**) Model AuCu JNSs; (**c**) Model AuAgCu JNSs; (**d**) Model AuCu PHNSs-I and (**e**) Model AuCu PHNSs-II. Table S1: XRD results of AuCu-based products in the current study. Table S2: Summary of the relative peak areas (%) for each split B.E. peak and the parameters used to fit the Cu 2p, Cu LMM, and Au 4f high-resolution XPS spectra. Table S3: Photothermal conversion efficiency of Au NPs, Au-Cu JNSs, Au-macro Cu JNSs, Au-Ag-Cu JNSs, and Au-Ag-meso Cu JNSs. Table S4: Comparative photothermal conversion performance of Au-based photothermal materials. References [40–47] are cited in supplementary materials.

Author Contributions: Q.Y.: conceptualization, methodology, investigation; Q.W.: software, validation, formal analysis, writing—original draft preparation; X.C.: data curation, visualization, writing—original draft preparation; X.S.: investigation, writing—original draft preparation; Y.W.: supervision, project administration, writing—reviewing and editing; X.W.: conceptualization, writing—reviewing and editing; Y.M.: resources, validation; P.Z.: methodology, supervision, writing—reviewing and editing; Y.Z.: conceptualization, supervision, funding acquisition, writing—reviewing and editing. All authors have read and agreed to the published version of the manuscript.

Funding: This work was financially supported by the Shandong Provincial Natural Science Foundation (grant No. ZR2025QC109 & ZR2022MB120), the Hundred Outstanding Talent Program of Jining University (grant No. 2020ZYRC05 & 2023ZYRC9), and the Science and Technology Innovation Team Foundation of Jining University (no. 23KCTD04 & 23KCTD05&24KCTD09). Additionally, support was provided by the Young Innovative Talents Introduction & Cultivation Program for Colleges and Universities of Shandong Province (granted by the Department of Education of Shandong Province, Sub-Title: Innovation Research Team on Organic Functional Molecules and Materials Design, No. 2023KJ277). This work is also supported by the University Feature Laboratory for Energy Conversion and Nanocatalysis of Shandong Province, the Suzhou Key Laboratory of Functional Nano & Soft Materials, the Collaborative Innovation Center of Suzhou Nano Science & Technology, the 111 Project, and the Joint International Research Laboratory of Carbon-Based Functional Materials and Devices.

Data Availability Statement: The data supporting this article have been included as part of the Supplementary Materials.

Conflicts of Interest: The authors declare no conflict of interest.

Use of AI and AI-Assisted Technologies: No AI tools were utilized for this paper.

References

1. Su, H.; Price, C.A.H.; Jing, L.; Tian, Q.; Liu, J.; Qian, K. Janus Particles: Design, Preparation, and Biomedical Applications. *Mater. Today Bio* **2019**, *4*, 100033. https://doi.org/10.1016/j.mtbio.2019.100033.
2. Wu, Z.; Li, L.; Liao, T.; Chen, X.; Jiang, W.; Luo, W.; Yang, J.; Sun, Z. Janus Nanoarchitectures: From Structural Design to Catalytic Applications. *Nano Today* **2018**, *22*, 62–82. https://doi.org/10.1016/j.nantod.2018.08.009.
3. Li, X.; Chen, L.; Cui, D.; Jiang, W.; Han, L.; Niu, N. Preparation and Application of Janus Nanoparticles: Recent Development and Prospects. *Coord. Chem. Rev.* **2022**, *454*, 214318. https://doi.org/10.1016/j.ccr.2021.214318.
4. Zhang, X.; Fu, Q.; Duan, H.; Song, J.; Yang, H. Janus Nanoparticles: From Fabrication to (Bio)Applications. *ACS Nano* **2021**, *15*, 6147–6191. https://doi.org/10.1021/acsnano.1c01146.
5. Li, Y.; Xia, M.; Zhou, J.; Hu, L.; Du, Y. Recent Advances in Gold Janus Nanomaterials: Preparation and Application. *Adv. Colloid Interface Sci.* **2024**, *334*, 103315. https://doi.org/10.1016/j.cis.2024.103315.
6. Li, C.-Y.; Duan, S.; Wen, B.-Y.; Li, S.-B.; Kathiresan, M.; Xie, L.-Q.; Chen, S.; Anema, J.R.; Mao, B.-W.; Luo, Y.; et al. Observation of Inhomogeneous Plasmonic Field Distribution in a Nanocavity. *Nat. Nanotech.* **2020**, *15*, 922–926. https://doi.org/10.1038/s41565-020-0753-y.
7. Wei, Y.; Qi, J.; Li, J.; Yu, C.; Zhao, J.; Pei, H. Precise Regulation of Surface Plasmonic Hotspots in an Au Split Nanoring Coupled System. *Results Phys.* **2024**, *61*, 107718. https://doi.org/10.1016/j.rinp.2024.107718.

8. Lu, Z.; Ji, J.; Ye, H.; Zhang, H.; Zhang, S.; Xu, H. Quantifying the Ultimate Limit of Plasmonic Near-Field Enhancement. *Nat. Commun.* **2024**, *15*, 8803. https://doi.org/10.1038/s41467-024-53210-8.
9. Zhang, D.; Chen, Y.; Hao, M.; Xia, Y. Putting Hybrid Nanomaterials to Work for Biomedical Applications. *Angew. Chem. Int. Ed.* **2024**, *63*, e202319567. https://doi.org/10.1002/anie.202319567.
10. Qiu, J.; Nguyen, Q.N.; Lyu, Z.; Wang, Q.; Xia, Y. Bimetallic Janus Nanocrystals: Syntheses and Applications. *Adv. Mater.* **2021**, *34*, 2102591. https://doi.org/10.1002/adma.202102591.
11. Li, Z.; Gong, J.; Lu, S.; Li, X.; Gu, X.; Xu, J.; Khan, J.U.; Jin, D.; Chen, X. Photothermal Lanthanide Nanomaterials: From Fundamentals to Theranostic Applications. *BMEMat* **2024**, *2*, e12088. https://doi.org/10.1002/bmm2.12088.
12. Zhang, M.; Ran, S.; Yin, X.; Zhang, J.; Sun, X.; Sun, W.; Zhu, Z. Mesoporous Polydopamine Nanoplatforms Loaded with Calcium Ascorbate for Amplified Oxidation and Photothermal Combination Cancer Therapy. *BMEMat* **2023**, *1*, e12041. https://doi.org/10.1002/bmm2.12041.
13. Chen, C.; Chu, G.; He, W.; Liu, Y.; Dai, K.; Valdez, J.; Moores, A.; Huang, P.; Wang, Z.; Jin, J.; et al. A Janus Au–Polymersome Heterostructure with Near-Field Enhancement Effect for Implant-Associated Infection Phototherapy. *Adv. Mater.* **2023**, *35*, 2207950. https://doi.org/10.1002/adma.202207950.
14. Xu, W.; Dong, C.; Hu, H.; Qian, X.; Chang, L.; Jiang, Q.; Yu, L.; Chen, Y.; Zhou, J. Engineering Janus Chemoreactive Nanosonosensitizers for Bilaterally Augmented Sonodynamic and Chemodynamic Cancer Nanotherapy. *Adv. Funct. Mater.* **2021**, *31*, 2103134. https://doi.org/10.1002/adfm.202103134.
15. Lv, Y.; Duan, S.; Wang, R. Structure Design, Controllable Synthesis, and Application of Metal-Semiconductor Heterostructure Nanoparticles. *Prog. Nat. Sci. Mater. Int.* **2020**, *30*, 1–12. https://doi.org/10.1016/j.pnsc.2019.12.005.
16. Zhao, T.; Chen, L.; Liu, M.; Lin, R.; Cai, W.; Hung, C.-T.; Wang, S.; Duan, L.; Zhang, F.; Elzatahry, A.; et al. Emulsion-Oriented Assembly for Janus Double-Spherical Mesoporous Nanoparticles as Biological Logic Gates. *Nat. Chem.* **2023**, *15*, 832–840. https://doi.org/10.1038/s41557-023-01183-4.
17. Yu, Y.; Lin, R.; Yu, H.; Liu, M.; Xing, E.; Wang, W.; Zhang, F.; Zhao, D.; Li, X. Versatile Synthesis of Metal-Compound Based Mesoporous Janus Nanoparticles. *Nat. Commun.* **2023**, *14*, 4249. https://doi.org/10.1038/s41467-023-40017-2.
18. Lv, K.; Hou, M.; Kou, Y.; Yu, H.; Liu, M.; Zhao, T.; Shen, J.; Huang, X.; Zhang, J.; Mady, M.F.; et al. Black Titania Janus Mesoporous Nanomotor for Enhanced Tumor Penetration and Near-Infrared Light-Triggered Photodynamic Therapy. *ACS Nano* **2024**, *18*, 13910–13923. https://doi.org/10.1021/acsnano.4c03652.
19. Peng, Z.; Huang, J.; Guo, Z. Anisotropic Janus Materials: From Micro-/Nanostructures to Applications. *Nanoscale* **2021**, *13*, 18839–18864. https://doi.org/10.1039/D1NR05499F.
20. Lu, Y.; Xu, R.; Liu, W.; Song, X.; Cai, W.; Fang, Y.; Xue, W.; Yu, S. Copper Peroxide Nanodot-Decorated Gold Nanostar/Silica Nanorod Janus Nanostructure with NIR-II Photothermal and Acid-Triggered Hydroxyl Radical Generation Properties for the Effective Treatment of Wound Infections. *J. Mater. Chem. B* **2024**, *12*, 5111–5127. https://doi.org/10.1039/D4TB00536H.
21. Li, S.; Zhu, J.; Shi, D.; Guo, P.; Wang, J.; Zhao, D.; Ma, Y. Interfacial Templating Strategy for Asymmetric Mesoporous Materials: Synthesis and Typical Applications. *Next Mater.* **2024**, *2*, 100144. https://doi.org/10.1016/j.nxmate.2024.100144.
22. Xia, X.; Xia, Y. Symmetry Breaking during Seeded Growth of Nanocrystals. *Nano Lett.* **2012**, *12*, 6038–6042. https://doi.org/10.1021/nl3040114.
23. Yang, T.-H.; Shi, Y.; Janssen, A.; Xia, Y. Surface Capping Agents and Their Roles in Shape-Controlled Synthesis of Colloidal Metal Nanocrystals. *Angew. Chem. Int. Ed.* **2020**, *59*, 15378–15401. https://doi.org/10.1002/anie.201911135.
24. Zeng, J.; Zheng, Y.; Rycenga, M.; Tao, J.; Li, Z.-Y.; Zhang, Q.; Zhu, Y.; Xia, Y. Controlling the Shapes of Silver Nanocrystals with Different Capping Agents. *J. Am. Chem. Soc.* **2010**, *132*, 8552–8553. https://doi.org/10.1021/ja103655f.
25. Xia, Y.; Gilroy, K.D.; Peng, H.-C.; Xia, X. Seed-Mediated Growth of Colloidal Metal Nanocrystals. *Angew. Chem. Int. Ed.* **2017**, *56*, 60–95. https://doi.org/10.1002/anie.201604731.
26. González-Rubio, G.; Mosquera, J.; Kumar, V.; Pedrazo-Tardajos, A.; Llombart, P.; Solís, D.M.; Lobato, I.; Noya, E.G.; Guerrero-Martínez, A.; Taboada, J.M.; et al. Micelle-Directed Chiral Seeded Growth on Anisotropic Gold Nanocrystals. *Science* **2020**, *368*, 1472–1477. https://doi.org/10.1126/science.aba0980.
27. Gao, C.; Goebl, J.; Yin, Y. Seeded Growth Route to Noble Metal Nanostructures. *J. Mater. Chem. C* **2013**, *1*, 3898–3909. https://doi.org/10.1039/C3TC30365A.
28. Xia, Y.; Xia, X.; Peng, H.-C. Shape-Controlled Synthesis of Colloidal Metal Nanocrystals: Thermodynamic versus Kinetic Products. *J. Am. Chem. Soc.* **2015**, *137*, 7947–7966. https://doi.org/10.1021/jacs.5b04641.
29. Zheng, Y.; Zeng, J.; Ruditskiy, A.; Liu, M.; Xia, Y. Oxidative Etching and Its Role in Manipulating the Nucleation and Growth of Noble-Metal Nanocrystals. *Chem. Mater.* **2014**, *26*, 22–33. https://doi.org/10.1021/cm402023g.
30. Liu, Y.-C.; Li, S.-Y.; Chen, X.-Y.; Chuang, Y.-C.; Wu, H.-L. Control of Oxidative Etching Rate of Cu Nanocubes in Synthesis of CuRu Nanocages and Nanoframes. *Chem. Mater.* **2023**, *35*, 136–143. https://doi.org/10.1021/acs.chemmater.2c02828.

31. Long, R.; Zhou, S.; Wiley, B.J.; Xiong, Y. Oxidative Etching for Controlled Synthesis of Metal Nanocrystals: Atomic Addition and Subtraction. *Chem. Soc. Rev.* **2014**, *43*, 6288–6310. https://doi.org/10.1039/C4CS00136B.
32. Makvandi, P.; Wang, C.-y.; Zare, E.N.; Borzacchiello, A.; Niu, L.-n.; Tay, F.R. Metal-Based Nanomaterials in Biomedical Applications: Antimicrobial Activity and Cytotoxicity Aspects. *Adv. Funct. Mater.* **2020**, *30*, 1910021. https://doi.org/10.1002/adfm.201910021.
33. Roper, D.K.; Ahn, W.; Hoepfner, M. Microscale Heat Transfer Transduced by Surface Plasmon Resonant Gold Nanoparticles. *J. Phys. Chem. C* **2007**, *111*, 3636–3641. https://doi.org/10.1021/jp064341w.
34. Rakić, A.D.; Djurišić, A.B.; Elazar, J.M.; Majewski, M.L. Optical Properties of Metallic Films for Vertical-Cavity Optoelectronic Devices. *Appl. Opt.* **1998**, *37*, 5271–5283. https://doi.org/10.1364/AO.37.005271.
35. Chen, X.; Qin, C.; Yang, L.; Li, X.; Wu, X.; Zhang, B. Triangular Pyramid Nanostructure Enhanced Photothermal Utilization of Noble Metal Nanoparticles. *Int. J. Therm. Sci.* **2024**, *200*, 108980. https://doi.org/10.1016/j.ijthermalsci.2024.108980.
36. Fu, X.; Tan, J.; Ma, Y.; Zhao, N.; Kong, Y.; Liu, F.; Zheng, Y.; Wang, Y.; Liu, M. *In Situ* Crumpling of Gold Nanosheets into Spherical Three-Dimensional Architecture: Probing the Aggregation-Induced Enhancement in Photothermal Properties. *Langmuir* **2022**, *38*, 1929–1936. https://doi.org/10.1021/acs.langmuir.1c03248.
37. Yang, Q.; Kong, H.; Tang, L.; Ma, Y.; Liu, F.; Liu, M.; Wang, Y.; Zhang, P.; Zheng, Y. Au–Cu Janus Nanostructures as NIR-II Photothermal Antibacterial Agents. *ACS Appl. Nano Mater.* **2024**, *7*, 20783–20792. https://doi.org/10.1021/acsanm.4c03673.
38. Zou, Y.; Qin, C.; Zhai, H.; Sun, C.; Zhang, B.; Wu, X. The Optical Characteristics of C@Cu Core-Shell Nanorods for Solar Thermal Applications. *Int. J. Therm. Sci.* **2022**, *182*, 107824. https://doi.org/10.1016/j.ijthermalsci.2022.107824.
39. Zou, Y.; Qin, C.; Yang, L.; Li, X.; Zhang, B.; Wu, X. Effect of Hollow Structure on Solar Thermal Applications of Au Nanodiscs. *J. Mol. Liquids* **2024**, *393*, 123528. https://doi.org/10.1016/j.molliq.2023.123528.
40. Jiang, T.; Song, J.; Zhang, W.; Wang, H.; Li, X.; Xia, R.; Zhu, L.; Xu, X. Au–Ag@Au Hollow Nanostructure with Enhanced Chemical Stability and Improved Photothermal Transduction Efficiency for Cancer Treatment. *ACS Appl. Mater. Interfaces* **2015**, *7*, 21985–21994. https://doi.org/10.1021/acsami.5b08305.
41. Bu, Y.; Huang, R.; Li, Z.; Zhang, P.; Zhang, L.; Yang, Y.; Liu, Z.; Guo, K.; Gao, F. Anisotropic Truncated Octahedral Au with Pt Deposition on Arris for Localized Surface Plasmon Resonance-Enhanced Photothermal and Photodynamic Therapy of Osteosarcoma. *ACS Appl. Mater. Interfaces* **2021**, *13*, 35328–35341. https://doi.org/10.1021/acsami.1c07181.
42. Song, Q.; Liu, Y.; Zhang, P.; Feng, W.; Shi, S.; Zhou, N.; Chu, X.; Shen, J. Au–Cu Bimetallic Nanostructures for Photothermal Antibacterial and Wound Healing Promotion. *ACS Appl. Nano Mater.* **2022**, *5*, 8621–8630. https://doi.org/10.1021/acsanm.2c02152.
43. Zhu, R.; Li, Y.; Zhang, X.; Bian, K.; Yang, M.; Cong, C.; Cheng, X.; Zhao, S.; Li, X.; Gao, D. Vapreotide-Mediated Hierarchical Mineralized Ag/Au Nanoshells for Photothermal Anti-Tumor Therapy. *Nanotechnology* **2019**, *30*, 055602. https://doi.org/10.1088/1361-6528/aaf0db.
44. Xu, M.; Lu, Q.; Song, Y.; Yang, L.; Ren, C.; Li, W.; Liu, P.; Wang, Y.; Zhu, Y.; Li, N. NIR-II Driven Plasmon-Enhanced Cascade Reaction for Tumor Microenvironment-Regulated Catalytic Therapy Based on Bio-Breakable Au–Ag nanozyme. *Nano Res.* **2020**, *13*, 2118–2129. https://doi.org/10.1007/s12274-020-2818-5.
45. Wang, Z.; Yu, N.; Li, X.; Yu, W.; Han, S.; Ren, X.; Yin, S.; Li, M.; Chen, Z. Galvanic Exchange-Induced Growth of Au Nanocrystals on CuS Nanoplates for Imaging Guided Photothermal Ablation of Tumors. *Chem. Eng. J.* **2020**, *381*, 122613. https://doi.org/10.1016/j.cej.2019.122613.
46. Sun, L.; Chen, Y.; Gong, F.; Dang, Q.; Xiang, G.; Cheng, L.; Liao, F.; Shao, M. Silicon Nanowires Decorated with Gold Nanoparticles via *in situ* Reduction for Photoacoustic Imaging-Guided Photothermal Cancer Therapy. *J. Mater. Chem. B* **2019**, *7*, 4393–4401. https://doi.org/10.1039/C9TB00147F.
47. Chen, M.M.; Hao, H.L.; Zhao, W.; Zhao, X.; Chen, H.Y.; Xu, J.J. A Plasmon-Enhanced Theranostic Nanoplatform for Synergistic Chemo-Phototherapy of Hypoxic Tumors in the NIR-II Window. *Chem. Sci.* **2021**, *12*, 10848–10854. https://doi.org/10.1039/d1sc01760h.